Paul Isaac Hagouel

X–Ray Lithographic Fabrication of Blazed Diffraction Gratings

Doctoral Dissertation

University of California, Berkeley
1976

hagouel@eecs.berkeley.edu

U·M·I Dissertation Services

A Bell & Howell Company

300 N. Zeeb Road, Ann Arbor, Michigan 48106
1-800-521-0600 313-761-4700

Printed in 1993 by xerographic process
on acid-free paper

INFORMATION TO USERS

This material was produced from a microfilm copy of the original document. While the most advanced technological means to photograph and reproduce this document have been used, the quality is heavily dependent upon the quality of the original submitted.

The following explanation of techniques is provided to help you understand markings or patterns which may appear on this reproduction.

1. The sign or "target" for pages apparently lacking from the document photographed is "Missing Page(s)". If it was possible to obtain the missing page(s) or section, they are spliced into the film along with adjacent pages. This may have necessitated cutting thru an image and duplicating adjacent pages to insure you complete continuity.
2. When an image on the film is obliterated with a large round black mark, it is an indication that the photographer suspected that the copy may have moved during exposure and thus cause a blurred image. You will find a good image of the page in the adjacent frame.
3. When a map, drawing or chart, etc., was part of the material being photographed the photographer followed a definite method in "sectioning" the material. It is customary to begin photoing at the upper left hand corner of a large sheet and to continue photoing from left to right in equal sections with a small overlap. If necessary, sectioning is continued again — beginning below the first row and continuing on until complete.
4. The majority of users indicate that the textual content is of greatest value, however, a somewhat higher quality reproduction could be made from "photographs" if essential to the understanding of the dissertation. Silver prints of "photographs" may be ordered at additional charge by writing the Order Department, giving the catalog number, title, author and specific pages you wish reproduced.
5. PLEASE NOTE: Some pages may have indistinct print. Filmed as received.

University Microfilms International
300 North Zeeb Road
Ann Arbor, Michigan 48106 USA
St. John's Road, Tyler's Green
High Wycombe, Bucks, England HP10 8HR

77-15,707

HAGOUEL, Paul Isaac, 1950-
X-RAY LITHOGRAPHIC FABRICATION OF BLAZED DIFFRACTION GRATINGS.

University of California, Berkeley,
Ph.D., 1976
Engineering, electronics and electrical

Xerox University Microfilms, Ann Arbor, Michigan 48106

X-Ray Lithographic Fabrication of Blazed Diffraction Gratings

By

Paul Isaac Hagouel

B.Eng. (New York University) 1972
M.S. (New York University) 1973

DISSERTATION

Submitted in partial satisfaction of the requirements for the degree of

DOCTOR OF PHILOSOPHY

in

Engineering

in the

GRADUATE DIVISION

of the

UNIVERSITY OF CALIFORNIA, BERKELEY

Approved: Andrew R. Neureuther
T. Van Duzer
Paul L. Richards

Committee in Charge

DEGREE CONFERRED DECEMBER 11, 1976

ACKNOWLEDGEMENTS

The author wishes to thank Professor A. R. Neureuther for his advise, support and understanding during the course of this work. He also thanks Professor T. Van Duzer for his advise and comments and Professor D. J. Angelakos for his encouragement over the years. Special thanks are due to the Air Force Office of Scientific Research for financial support.

This research has benefited from stimulating discussions with Bob Jewett, Miguel Schyfter, Mike O'Toole, Steve Shu-Kong Chang and Dr. Mike Morgan. Countless discussions non-technical and otherwise with Luis Figueroa, M. Kazem Shams, Dan Botez, T. R. "Rangu" Ranganath and S. Y. Wang provided, in many instances, the psychological springboard so important for completion of this work.

For their technical help, the author would like to thank Mrs. Dorothy McDaniel and Mr. Don Rogers of the Semiconductor Laboratory, Bob Hamilton of the Glass Shop, Don Faria of the Machine Shop, Maurice Bales of the Plasma Laboratory, and Wilfred Zeilinger, Department Engineer.

Thanks are also due to Dr. Bruce Kendall, Dr. Denis Tremain, Dr. Weys Wey-Chung Kuo, Dr. Robert Stovall, Hugh Kao, Shimon Coen, John Hunka, John Uyemura, Al Mathews, Henry Chang of the Electromagnetic group for their friendship through the years.

Special thanks are due to Professor S. Silver for his fatherly and scientific advise during the author's years at Berkeley.

Thanks are also due to my fiancee, Miss Nelly Issoua of Thessaloniki, Greece, for her love, understanding and patience during the final year of this work. Long distance communication with her did wonders for the author's work drive.

I take this opportunity to express my thanks and my deep love and appreciation to my two parents for their constant moral and financial support all those years spent away from home. Without their help and support, this work would not have been possible. This dissertation is affectionately dedicated to my father Leon-Avram and my mother Yvet-Sarrah.

TABLE OF CONTENTS

PAGE NOS.

APPENDIX

CHAPTER I

INTRODUCTION

In this thesis we study both experimentally and theoretically the feasibility of fabricating blazed diffraction gratings with x-ray lithography using holographically produced grating x-ray masks. Diffraction gratings are produced either by classical method of ruling or by interference (hologrpahically) [1] [2]. The advent of holographic gratings was possible after the development of lasers in the early sixties. Ruled gratings with up to 3600 grooves/mm and holographic gratings with up to 6000 grooves/mm are commerically available [1]. Small area ruled gratings with 7500 grooves/mm and holographic gratings with more than 10000 grooves/mm [3] have been produced.

Holographic gratings have certain advantages over ruled gratings: They can be produced much faster, do not generate ghosts, can be of large area with finer pitch [2] and it is possible to combine them with a lens function. An example of the later is comma, corrected grating. Holographic gratings are usually cheaper than ruled ones. The main disadvantage of the interference technique is that it allows rather less control over the groove profile than one has with the ruling process. Control over the groove profile is of fundamental importance, since it is the groove shape that determines the absolute efficiency which is defined as the percentage of incident energy of a given wavelength that is diffracted into the order of interest [2].

In order to obtain a better use of the grating it is desired to concentrate spectral energy into any one of the orders. The principle (for classically ruled gratings) is to rule the grating so that the reflecting elements (grooves), are tilted with respect to the grating surface. This profile is characteristic of blazed gratings. Figure 1.1 shows a typical blazed grating profile [1] [4] where b = a cos ϕ spectral energy is concentrated in the direction ϕ. ϕ is called blaze angle.

Blazed gratings are usually ruled. Blazed interference gratings of spectroscopic quality have only been produced for the ultraviolet spectral region and the techniques are still being further developed [2].

X-rays may be used for high resolution lithography since their wavelengths are much smaller than optical wavelengths. In particular a process similar to the x-ray lithography technique described by D. L. Spears and H. I. Smith [5] together with a holographically fabricated x-ray absorbing grating mask pattern can be used to fabricate diffraction gratings. In particular, blazed gratings can be produced by the multiple angle exposure technique sketched in Fig. 1.2. This process has potential advantages over both mechanically ruled and direct holographic grating fabrication techniques. Since the contact printing mask is itself a holographic grating the two advantages of small period (10,000 lines/mm) and large area uniformity can be preserved. The use of x-rays allows the planar pattern to be projected into the resist material without significant absorption or spreading due to scattering or diffraction. Upon chemical development this yields both deeper and more desirable groove shapes than those producible interfero metrically in photoresists. A very important process advantage is that a single mask can be used to replicate gratings with a variety of blaze angles.

In Chapter II, the principles of x-ray lithography are presented. We start with a brief review of x-rays. The theory of x-ray lithography and, in particular, the requirements for high-resolution lithography as

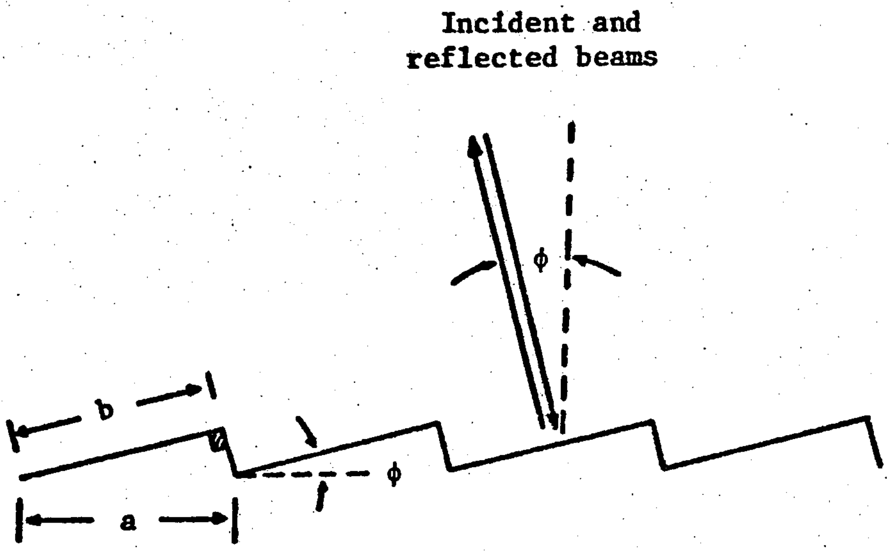

Fig. 1.1. Blazed grating profile.

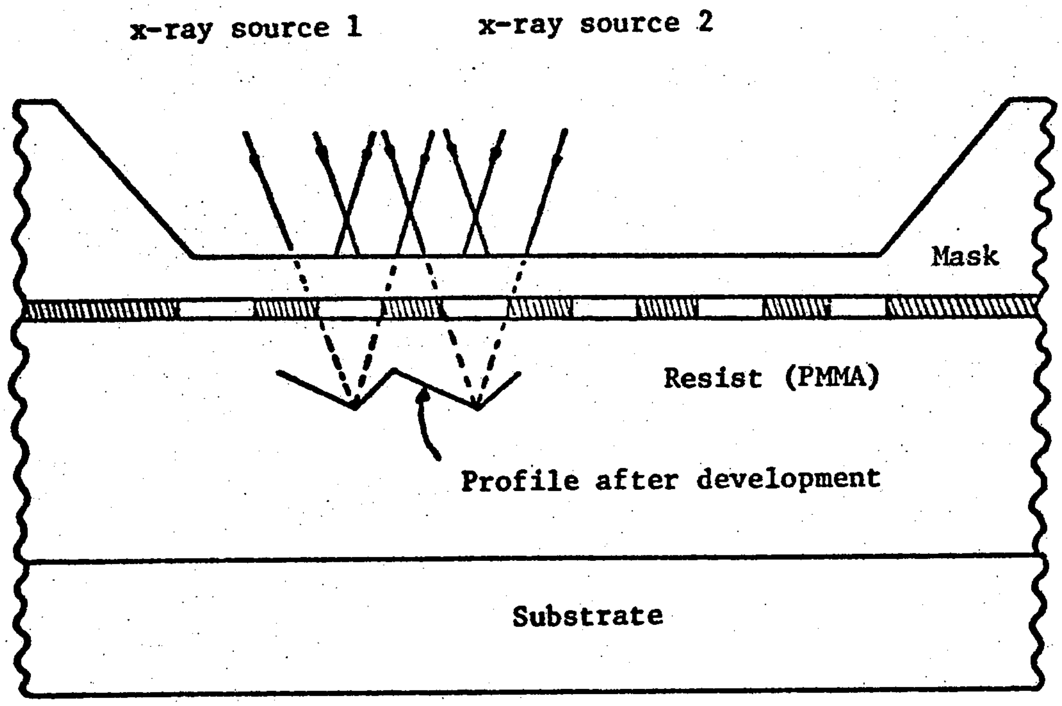

Fig. 1.2. Multiple angle soft x-ray contact printing of blazed gratings.

applied to the fabrication of blazed diffraction gratings are described. A simple algebraic model is presented along with curves for designing blazed gratings with specified blaze and groove angle. The fundamental limit on groove shape imposed by the fact that smaller-period gratings require thinner masks having lower exposure contrast is explored.

In Chapter III we describe our x-ray exposure system and a solid state x-ray detector.

In Chapter IV, the process for fabricating x-ray absorbing masks is described. The holographic fabrication of photoresist gratings, the subsequent fabrication of the gold grating absorbing mask pattern and the etching of the silicon substrate to produce an x-ray semitransparent thin silicon membrane are discussed in some detail.

In Chapter V our experimental results are presented and explained. Exposure dependent resist properties are also discussed, and in particular the thermal effects during exposure.

In Chapter VI, a rigorous simulation of the development process based on geometrical optics (ray tracing) is presented. Equations important for the algorithm are derived. Results are presented for cases of particular interest to this work such as grating profiles for various periods, source angles, developers and for different x-ray wavelengths. Results are also presented forother examples and they are compared with the ones obtained using different algorithmic approaches.

In Chapter VII, we discuss our results and present our conclusions.

CHAPTER II

THEORY OF X-RAY LITHOGRAPHY

In this chapter we present a brief account on x-rays and we describe the prinicples of x-ray lithography. In Section 1 we give a brief review on the theories of the generation and absorption of x-rays and of the efficiency of production of both characteristic and continuous x-rays. In Section 2 the principles of x-ray lithograph are described in detail, and in particular those aspects which are important for high-resolution lithograph.

2.1. X-Rays

X-rays are produced when rapidly moving electrons, which have been accelerated through potential differences of a few thousand volts up to hundred of thousands of volts, are allowed to strike a metal target. x-rays are electromagnetic radiation and they are governed by quantum relations in their interactions with matter. We speak of x-ray photons or quanta, the energy of such a photon given by the familiar relation $W = h\nu$ where h is Planck's constant and ν is the frequency of the radiation. Wavelengths of x-rays range from 10^{-10} to 10^{-6}cm. X-rays of long wavelength are called soft and those of short wavelength are called hard.

The production of a beam of x-rays requires an electron source, some means of accelerating the issuing electron beam and directing it on to the anode (target) and usually some sort of cooling for the target. The details of the system used to produce x-rays will be described in Chapter III.

Continuous x-rays are produced when the incident electrons are decelerated and scattered in close collision with nuclei of the atoms in the anode. This is a Coulomb interaction scattering. Although the electron does not lose energy to the nucleus because nuclei are so massive that they do not recoil appreciably, the electron sometimes does lose energy by electromagnetic radiation. This radiation constitutes the continuum x-ray spectrum.

When there are Coulomb interaction collisions between the incident electron and the electrons of the atoms in which the energy transfer is a large fraction of the energy of the incident electron and the energy is large enough, it is possible to excite an atomic electron of an inner shell from its highly negative energy level to one of the slightly negative or positive energy levels. This leaves the atom in a very highly excited state. The atom will eventually return to its ground state and in this process it emits a set of very-high-energy quanta which are members of its x-ray line spectrum.

For x-ray photon energies less than 5 MeV, the loss of x-ray beam intensity as it traverses matter, occurs both by absorption (which transfers energy to the absorber) and by scattering (which deflects it out of the beam). The absorbed energy is re-emitted either as secondary (fluorescent) radiation or as photo-electrons. When the energy of an x-ray photon is comparable or greater than the binding energy of atomic electrons, it can lead to the ejection of an electron. This is called the x-ray photoelectric effect and the ejected electron, a photoelectron [6]. The scattering may be either coherent, including Bragg diffraction, or incoherent, with change of wavelength (Compton Scattering). The degree of absorption of x-rays of given wavelength varies as a high power of the atomic number Z of an element and on the amount of it in the path of the beam. For a given element, absorption increases as a high power of the wavelength, with interruptions of the characteristic absorption edges corresponding to its emission lines.

We will now describe, in some detail, quantitative aspects of the production of x-rays and the x-ray absorption process.

2.1.1. Continuous X-rays

As mentioned earlier, the emission of electromagnetic radiation by a scattered electron constitutes the continuum x-ray spectrum. In this case, when the electron is an unbound scattered electron, classical theory is capable of describing quite well certain features of the production of continuum spectrum x-rays.

According to classical electromagnetic theory, a particle of charge, ze suffering an acceleration a, will emit energy in the form of electromagnetic radiation at the rate [6].

$$I_T = \frac{2}{3}\frac{(ze)^2 a^2}{c^3} \tag{2.1}$$

where c is the velocity of light. When the particle is scattered by a nucleus of charge Ze, it experiences a Coulomb force which is proportional to zZe^2 and, if the mass of the particle is m, its acceleration is proportional to zZe^2/m. Consequently the rate of emission of energy in electromagnetic radiation can be written

$$I_T \propto \frac{z^4 Z^2}{m^2} \tag{2.2}$$

From the factor $1/m^2$, it may be predicted that the emission of electromagnetic radiation is very much more important for electrons than it is for protons or other beam particles. This is true; the enegy emitted in continuum spectrum x-rays by a heavy charged particle in traversing matter is almost immeasurably small. The presence of the factor Z^2 shows that anodes of high atomic number are much more efficient producers of these x-rays. The Z^2 dependence also show that the radiation emitted in scattering from an atomic electron (i.e. $Z_1=1$) is negligible.

For incident electrons of non-relativistic energies, the angular distribution of the x-ray energy emitted in the continuum spectrum is given by [6][7]:

$$I(\Theta) \propto \sin^2\Theta \qquad (2.3)$$

where Θ is the angle between $\vec{r}$, the direction of the emitted x-rays, and $\vec{a}$, the acceleration of the incident electrons.

Experimentally it is found that the shape of the continuum spectrum depends only on the energy of the electrons incident on the anode, and not on the nature of the anode [8]. In particular, the short wavelength cutoff λ_c is inversely proportional to the incident electron kinetic energy E. The cutoff frequency $v_c = c/\lambda_c$ follows the empirical law

$$hv_c = E \qquad (2.4)$$

where h is in excellent numerical agreement with the value of Planck's constant.

The efficiency of production η_c of the continuous spectrum, as the ratio of energy in the x-ray beam to that in the incident electron beam, follows the empirical relation [7].

$$\eta_c = kZV \qquad (2.5)$$

where V is the electron beam accelerating voltage and k is a numerical factor. When V is in volts the value of k is given by Compton and

Allison [8] as $1.1\text{x}10^{-9}$; however, slight variations of the above are reported in the literature [7][9]. As the electron beam has power VI, where I is the target current, the power of the x-ray beam E_c is given by

$$E_c = kZV^2I \tag{2.6}$$

so long as the target is "opaque," i.e. thick enough to stop all electrons. This expression holds down to about 2kV. The number of quanta η_c emitted in the continuous spectrum from the high-frequency limit set by the beam voltage V to the lower limit, corresponding to a voltage V_c, beyond which quanta either do not escape from the target or fail to produce a response in the recording system, is given by [7].

$$\eta_c = 0.40(ekZI/h^2)(V-Vc)^{1.65}/Vc^{0.65} \tag{2.7}$$

where k is a constant e the electronic charge, h Planck's constant. The number of electrons falling on the target is I/e so that the quantum efficiency η_{cq} of the continuous spectrum is

$$\begin{aligned}\eta_{cq} &= 0.40(e^2h^2)\ kz(V-V_c)^{1.65}/V_c^{\ 0165} \\ &= 1.04\text{x}10^{-9}z(V-V_c)^{1.65}/V_c^{\ 0.65}\end{aligned} \tag{2.8}$$

Comparing the values of (2.7) and (2.8) it can be seen that the quantum efficiency is greater than the energy efficiency except at lower voltages close to V_c.

2.1.2. Characteristic X-rays

The characteristic or line radiation can be understood in considerable detail from the Bohr theory of the atom. The development of wave mechanics added to this understanding and enabled a detailed interpretation of the fine structure of specra to be built up. The classification of the orbital electrons into shells and the designation of individual electrons by means of quantum numbers are well-known features of the Bohr theory. Figure 2.1 [7] shows how the orbital electrons may be grouped together into the K, L, M, etc. shells of progressively decreasing binding energy, and it is seen that (with the exception of the K shell) each shell consists of several sub-shells of slightly different energy. Each shell is characterized by a Principal Quantum Number n, which has the values 1, 2, 3 etc. for the K, L, M etc. shells and it is this number which appears in the expression for the binding energy of electrons in the hydrogen-like atom [7]:

$$E_n = \frac{-2\pi^2 Z_{eff}^2 m_r}{h^2 n^2} \tag{2.9}$$

In this expression Z_{eff} represents the effective atomic number (Z) modified by the screening effect of the orbital electrons. Equation (2.9) is often written in the form

$$E = \frac{Rh_c Z_{eff}^2}{n^2} \quad \text{where} \quad R = \frac{2\pi^2 e^4 m_r}{ch^3} \tag{2.10}$$

The quantity R is the Rydberg constant, m_r is the reduced mass of the orbital electron, and should be written as mM/(M+m) where M is the atomic mass.

There are thus many distinct Rydberg constants, for nuclei of different mass, and these distinctions are observable in the optical spectra of light elements; however, the screening effect of orbital electrons imposes much greater departures from the simple formulas so we shall take m_r in Eq. (2.9) to be simply the mass of the electron. The Rydberg constant would be R_∞,

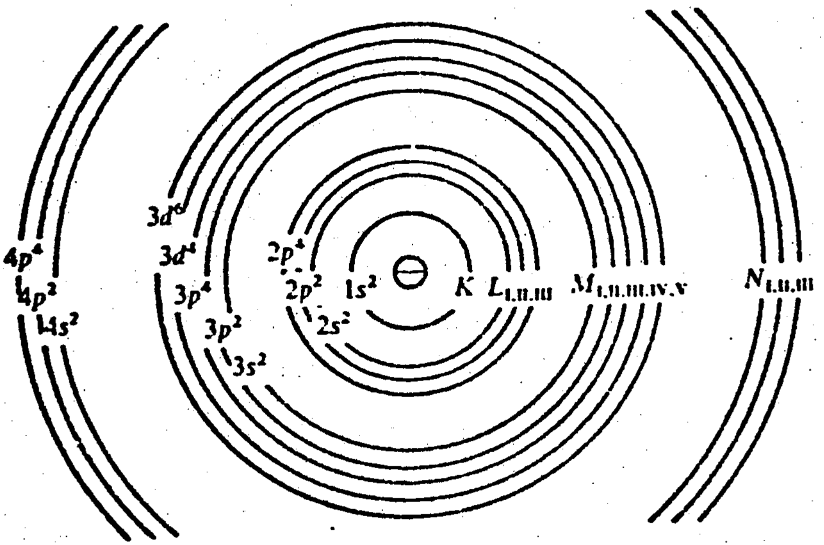

Fig. 2.1. The Bohr atom-shells and sub-shells of Krypton.

appropriate for an infinitely heavy nucleus.

In the wave-mechanical treatment the complete expression for the energy of a level (n,ℓ,j) where ℓ is the orbital angular momentum quantum number, j is the total angular momentum number and is given by $\pm s$ where $s(=\frac{1}{2})$ is the spin quantum number for an individual electron, is given by [7]:

$$E_{(n,\ell,j)} = Rhc \frac{M}{M+m}\left[\frac{(Z-\sigma)^2}{n^2} + \frac{\alpha^2(Z-\sigma')^4}{n^4}\left(\frac{n}{j+\frac{1}{2}} - \frac{3}{4}\right)\right] \tag{2.11}$$

Here σ and σ' are constants which have been introduced to allow for the partial screening of the nucleus by the orbital electrons. Each sub-shell (n,ℓ,j) can contain several electrons up to a maximum $2j+1$. This multiplicity of levels is of interest in that it affects the intensity of lines through its effect upon the transition probabilities between shells.

It is a central feature of the interpretation of x-ray spectra that observed lines correspond to transitions between two states. We may draw an energy level diagram in which each combination of n,ℓ and j gives rise to a distinct level. We may depict the energy levels of the atom as in Fig. 2.2 [7]. The removal of a strongly bound electron naturally gives rise to a level at the top of the digram and the emission of an x-ray photon corresponds to a transition from an upper level to a lower level. States corresponding to the removal of an electron are known as "hole-states." Not all transitions are possible. The selection rules which govern transitions between states are

$$\Delta\ell = \pm 1; \quad \Delta j = -1,\ 0,\ 1 \tag{2.12}$$

The transitions that obey (2.12) are shown in Fig. 2.2. The totality of x-rays which are emitted in these transitions constitute the x-ray line

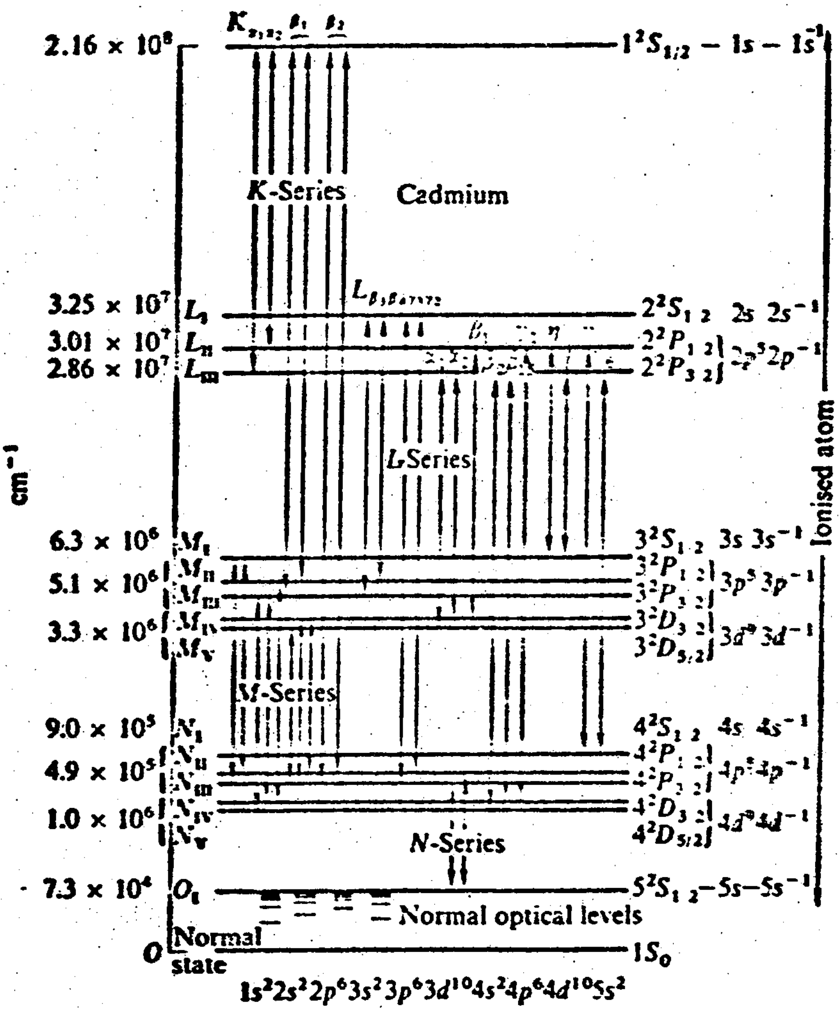

Fig. 2.2. Energy level diagram for cadmium.

spectrum of the atom. It is conventional to group those lines produced by transitions from the K shell into the so called K-series, from the L shell into the L series etc. In the L series, the strongest lines would be expected to be those which originate from the L_{III} atomic energy level (since this contains four electrons, anyone of which may be ejected by the initial ionization process) and which terminate in the M_{IV} and M_V levels. These lines are designated L_{α_2} and L_{α_1} respectively.

In order for a photon to be emitted, an atom has first to be ionized in the appropriate shell, and this may be achieved by several means. The material in which ionization is required may be in the form of a target which is then bombarded by electrons (the usual procedure for generating x-rays) with an energy in excess of the required excitation energy. This energy must be sufficient to either remove the electron altogether from the target, or at least sufficient to put it into a vacant outer level or into the conduction band in the case of a metal or semiconductor. Alternatively the material may be ionized by radiation with x-rays or gamma rays of sufficient energy to be absorbed by the photoelectric effect. Following the ionization, an electron has to "fall in" from an outer shell, but it should be noted that this energy is not always emitted in the form of an x-ray photon. The alternative process is known as the Auger effect. The Auger effect is a radiationless transition in which the available energy is used to release an electron from the outer shell. This electron is known as an Auger electron. It is readily seen that an atom which has emitted an Auger electron now has two vacancies, neither of which is the same as the vacancy created by the initial ionizing event. An Auger transition thus involves two orbital electrons and three electron orbits. The fluorescence yield is defined as $\omega_n = X_K/(X_n+A_K)$, for the k shell, where X_n is the number of emitted x-ray photons of the K-series, and A_N is the number of K Auger electrons.

If a photon is emitted when an electron falls from an outer shell to an inner one there will be one vacancy in the outer shell remaining to be filled.

The frequency ν of an emitted photon bears the usual relation to the energy E which it carries; E = hν; therefore, if we have a transition from an initial (excited) state (n_i, ℓ_i, j_i), to a final energy state (n_f, ℓ_f, j_f) the frequency ν of the emitted phonon is given by

$$\nu = \frac{1}{h} [E_{(n_f, j_f, \ell_f)} - E_{(n_i, j_i, \ell_i)}] \tag{2.13}$$

In practice the contribution of the line to the total spectral energy is always less than that from the continuous but the ratio rises as the target voltage is raised above the minimum needed to excite a given line. We shall consider only the energy in the K_α-line since the information on the L lines is very scant. In first approximation experiment establishes the simple relation [8]:

$$E_k \propto (V - V_k)^{1.65} \tag{2.14}$$

for the energy in the K_a-line, if V_k is the minimum voltage needed for its excitation and V_1 is the beam voltage. On theoretical grounds [9] the relation is

$$E_k = AZVV_k I[\ n(V/V_k) - (1 - \frac{V_k}{V})]\ R_k \omega_\alpha \tag{2.15}$$

where A is a constant, I is the beam current, ω the fluorescent yield for K_α radiation, and R_k the ratio of the probability for K ionization to that for the production of a quantum of energy greater than V_k in the continuum. The value of R_k varies somewhat with atomic number and is equal to 3.5 for copper; it has been shown to be constant over a wide range of voltage. Comparison with experimental measurements shows that (2.15) can be closely approximated to the accuracy quoted in connection with the continuous spectrum, by the following expression [7]

$$E_k = 1.04\text{x}10^{-9} ZIR\omega_\alpha (V-V_k)^{1.65} V_k^{0.35} \qquad (2.16)$$

Comparison of (2.16) and (2.6) now gives the ratio of the energy in the K_α-line to that in the continuous spectrum as a whole. For copper, with the value of 0.395 for ω_α, we have [7]

$$\begin{aligned} E_k/E_c &= 1.1\ V_k^{0135}(V-V_k)^{1.65}/V^2 \qquad (2.17) \\ &= 1.1(U-1)/U^2 \end{aligned}$$

on writing $U = V/V_k$. Hence the energy in the K_α-line is less than that from the continuous spectrum as a whole. Equation (2.17) must be regarded as an empirical relation because its derivation rests on experimental values for this power law, for R_k, and for ω_α.

The ratio of the energy efficiency for the K_α-line η_{ke} to that for the continuous spectrum η_{ce} is the same as the ratio of the actual energies, so that the value of η_{ke} can be found by substituting (2.5) into (2.17). The quantum efficiency η_{kq} for K production is a more important factor; with n_k and n_e for the number of k_α-quanta and electrons respectively, it is given by

$$\begin{aligned} \eta_{kq} &= n_k/n_e = \eta_{ke} V/V_k \qquad (2.18) \\ &= 1.04\text{x}10^{-9} ZR\omega_\alpha V_k (U-1)^{1.65} \end{aligned}$$

It follows from this discussion that in all circumstances the efficiency, whether measured in terms of energy or quanta, remains of order 10^{-4} to 10^{-2}, being higher for elements of high Z and at high voltage; however, if the target reabsorption of the emitted x-rays is taken into account, there is a practical upper limit to the accelerating voltage V for maximum efficiency of production. This topic is discussed in detail by Green [10] and also by Dyson [7]. For soft x-rays (8.34 Å) and for accelerating potential around 7kV the quantum efficiency is around 10^{-4} photons per electron per steradian.

2.1.3. X-ray Absorption

When a collimated beam of x-rays passes through a thickness t of a particular element it is found that its intensity is reduced from the initial value I_o to a value I according to an exponential relation (Lambert's Law):

$$I = I_o e^{-\mu t} \tag{2.19}$$

where μ is a constant, the value of which depends on the atomic number of the element and on the wavelength of the x-rays. It has the dimensions of a reciprocal length and is known as the linear absorption coefficient. Equation (2.19) implies that, in passing through successive elementary layers of thickness dt, the beam loses a constant fraction of its intensity in each layer:

$$dI/I = -\mu dt \tag{2.20}$$

The value of the linear absorption coefficient depends on the number of atoms in the path of the beam and hence on the state of aggregation of the element. Division by its density (ρ) gives a more practically useful quantity (μ/ρ), which is independent of the physical state. It is known as the mass absorption coefficient ($\mu_m = \mu/\rho$) and has dimensions of area over mass (cm^2-gm^{-1}). Absorption is thus referred to the amount of matter in the path of the beam, measured as the mass per unit area or "mass-thickness" m, and since $m = \rho t$, (2.19) becomes

$$I = I_o e^{-\mu_m m} \qquad (2.21)$$

Similarly, division of μ by the number of atoms per unit volume ($\rho N/A$) defines the absorption coefficient per atom

$$\mu_a = \mu_m A/N \qquad (2.22)$$

where A is the atomic weight of the absorbing element and N is Avogadro's number. Since absorption is primarily concerned with the inner electron shells of the atom, μ_a is almost entirely independent of the physical state and mode of chemical combination of the absorbing element.

As mentioned earlier the variation of the absorption coefficient with atomic number and wavelength is complicated by the fact that loss of beam intensity occurs both by absorption (photoelectric absorption or fluorescence) and by scattering. To this, if the photon energies are larger than 5 MeV, we should add the loss of beam intensity due to electron-positron pair production which can take place in the Coulomb field of an atom of the absorbing material; however, for photon energies of interest, we can disregard the pair production completely. The experimentally determined mass absorption coefficient will thus be composed of two terms

$$\mu_m = \frac{\mu_{ph}}{\rho} + \frac{\mu_{sc}}{\rho} \qquad (2.23)$$

where $\frac{\mu_{ph}}{\rho}$ represents absorption by photoelectric emission and fluorescence and μ_{sc}/ρ is the mass scattering coefficient. For the wavelengths used in our work, the mass scattering coefficient is negligible compared to that for absorption.

The value of μ_{ph}/ρ varies both with wavelength and atomic number Z. If we are away from characteristic absorption edges (to be discussed below) then μ_{ph}/ρ is given approximately by [8]

$$\mu_{ph}/\rho = C\lambda^{r}z^{s} \tag{2.24}$$

where C is a constant to within a narrow range of λ and z. For wavelengths in the range of 1-10 Å, the value of r and s is 3.

A striking feature of plots of the mass absorption coefficient vs. wavelength is the apparently discontinuous jumps at various wavelengths characteristic of the absorbing element. These can be explained as follows. When the energy of an x-ray photon is increased, the photon becomes more penetrating, i.e. less absorbed by the absorbing material; however, when its energy exceeds that required for the ejection of an electron from an inner shell, this will correpsond to energy being transferred to the absorber (for the ejection of the electron) with a corresponding increase in the mass absorption coefficient. The jumps occur at wavelengths close to those corresponding to the emission of characteristic x-ray lines. Since the photoelectric effect is the ejection of an electron of a shell entirely from the atom, and the characteristic lines arise from transitions from one shell to another, it is seen that the energy of the photon needed to eject an electron from a particular shell is slightly larger than the energy of the corresponding characteristic x-ray line; therefore, a material is always a bad absorber of its own characteristic radiation. Figure 2.3 shows qualitatively the shape of part of the curve of the mass absorption coefficient vs. wavelength. The wavelength of the characteristic line corresponding to the jump shown will be situated near the jump on the long wavelength side.

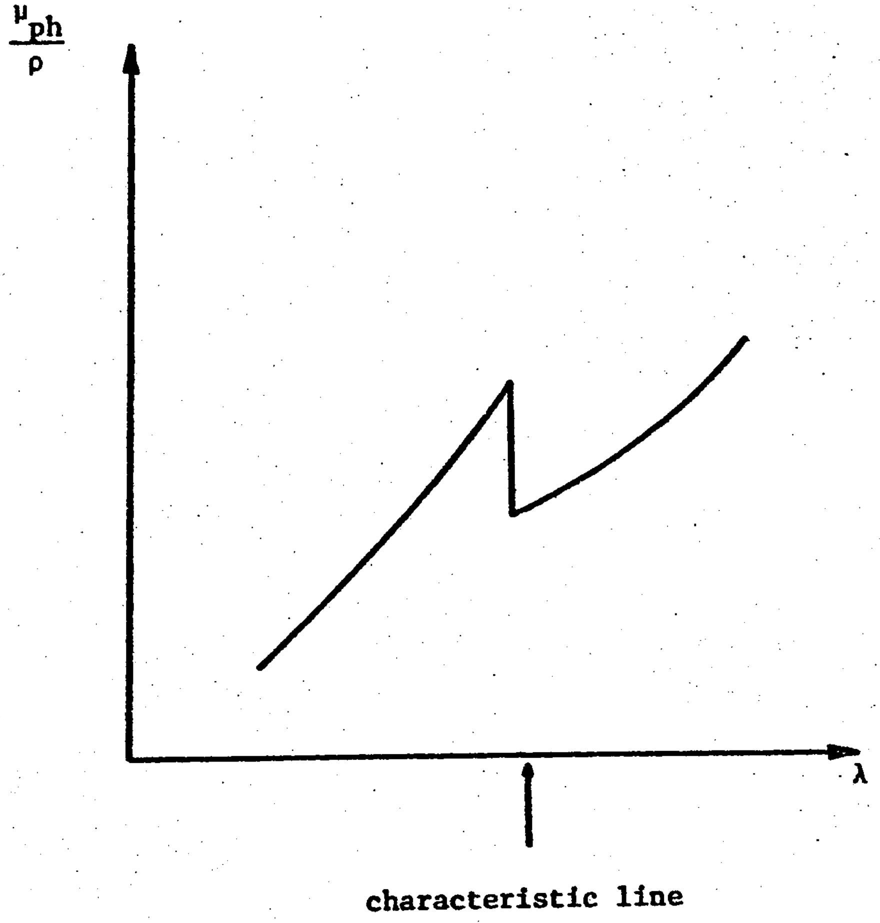

Fig. 2.3. X-ray absorption coefficient vs. wavelength.

2.2. Principles of X-ray Lithography

In Chapter I, we introduced the concept of soft x-ray contact printing by projection of an absorbing gold mask pattern into resist material (poly-methylmethacrylate). The three major requirements for x-ray lithography are the fabrication of an absorbing mask on a suitable semitransparent substrate, a soft x-ray exposure system and x-ray resists with comparison chemical developers. A description of the soft x-ray exposure system is given in Chapter III, and the fabrication procedure for x-ray masks is given in Chapter IV. In this section we present the theory of x-ray lithography and in particular the requirements for high-resolution lithography as applied to the fabrication of blazed diffraction gratings.

2.2.1. Soft X-ray Exposure

Figure 2.4 illustrates the x-ray lithography technique. The mask consists of a highly absorbing pattern on top of a semitransparent membrane. This is in contact (or off contact) with a substrate coated with a polymer film sensitive to x-ray irradiation. X-rays are produced by electron bombardment of a metallic target. A foil which is a combination of a heat and stray electron shield and x-ray filter, is placed between the mask substrate system and the x-ray source. The foil is semitransparent to x-rays. For this scheme, the choice of x-ray wavelengths for efficient and quick exposure of the sensitive polymer film (x-ray resist) is limited by the availability of sensitive x-ray resists and highly transparent mask substrates and x-ray filter foils. Gold, being an excellent absorber of x-rays in wavelength regions far from its characteristic absorption edges, is used for the fabrication of the absorbing mask pattern.

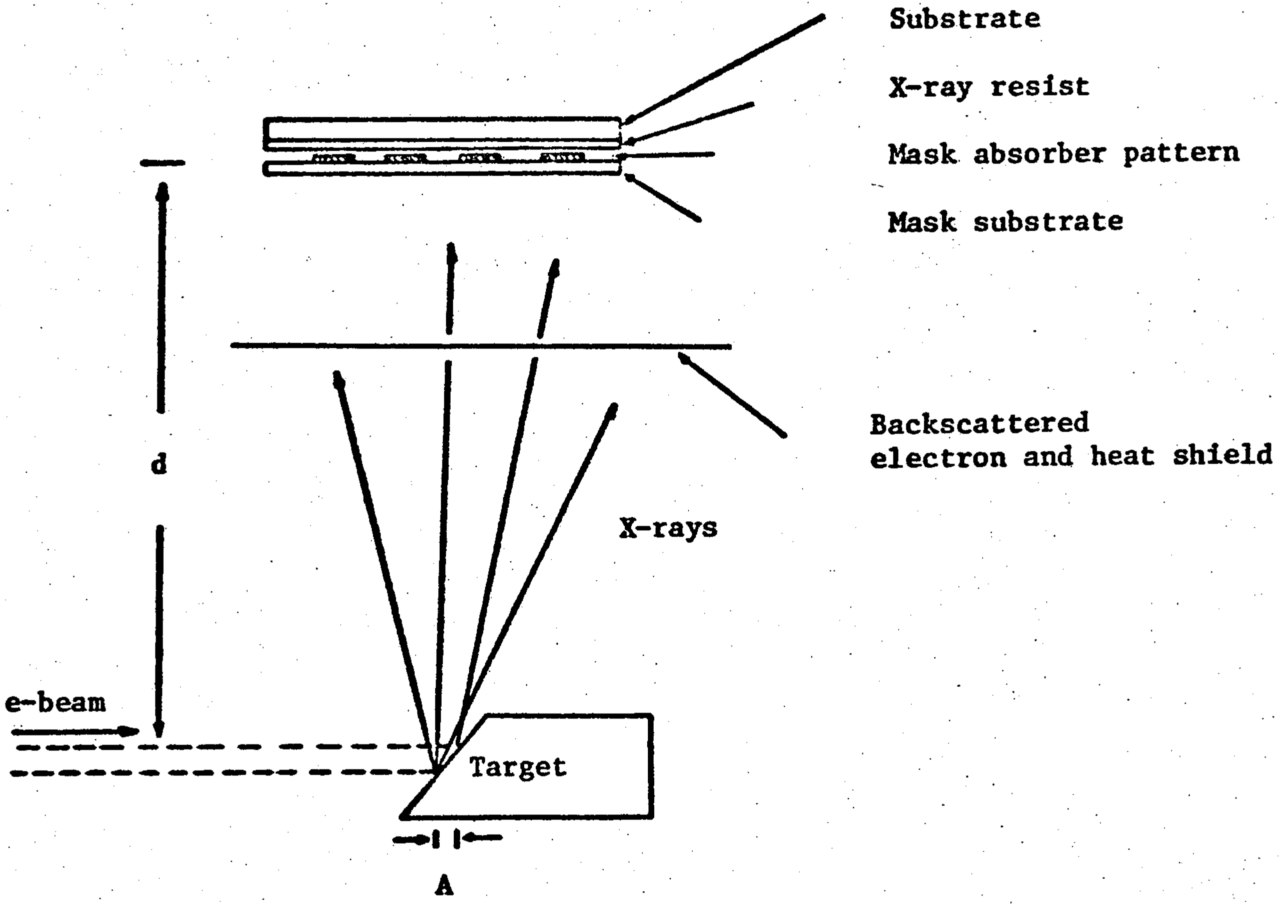

Fig. 2.4. X-ray lithography technique.

The x-ray flux at the resist substrate surface (originating from a monochromatic source) is given by

$$\phi_s = \frac{I\epsilon' h\nu}{qd^2} A \left(\frac{W}{cm^2}\right) \qquad (2.25)$$

where I is the electron beam current, d is the source-to-substrate distance, ϵ' is the x-ray yield measured in photons per electron per steradian, q is the electronic charge and ν is the frequency of radiation. A is a factor proportional to the transmission of the filter foil and of the mask substrate (without taking into account the absorbing pattern), and it is given by

$$A = e^{-\alpha_f t_f - \alpha_s t_s} \qquad (2.26)$$

where α_f and α_s are the linear absorption coefficients of the foil and the mask substrate respectively and t_f and t_s are their respective thicknesses α_f and α_s are highly wavelength dependent.

The x-ray flux passing through the resist film is attenuated according to the relation

$$\phi = \phi_s e^{-\alpha_r z} \left(\frac{\omega}{cm^2}\right) \qquad (2.27)$$

where ϕ_s is the incident flux, ϕ is the transmitted flux, α_r is the resist linear absorption coefficient, and z is the resist thickness. The total energy dose absorbed in the resist per unit volume is

$$D = \frac{t}{z}(\phi_s - \phi) = \frac{t}{z}\phi_s(1 - e^{-\alpha_r z}) \left(\frac{Joules}{cm^3}\right) \qquad (2.28)$$

where t is the total exposure time. For poly-methylmethacrylate (PMMA) $\alpha_r \approx 1000\ cm^{-1}$ at the $A\ell_{k_\alpha}$ line (8.34 Å). Therefore, for z small ($<2x10^{-4}$cm)

(2.28) becomes

$$D \cong t\phi_s \alpha_r \tag{2.29}$$

i.e. the power dissipated is uniform throughout the resist thickness.

The above relations are valid for a monochromatic source of x-rays. Monochromatic radiation is not essential for exposure of the resist; however, the highest intensity is obtained by exciting characteristic K or L radiation at a voltage which exceeds the minimum voltage required for excitation by a factor of two or more [11]. For efficient x-ray exposure the mask substrate and the filter foil should be highly transparent to the incident "monochromatic" radiation and simultaneously filter out the continuum. Also, the wavelength of the incident radiation should be such that it is absorbed by the resist film and exposes it. For a thin silicon membrane mask, a thin aluminum foil-filter and PMMA resist, the optimum wavelength for the shortest exposure is the $A\ell_{k_\alpha}$ line (8.34 Å) [11][12]. Due to the aluminum absorption edge at 7.9 Å, the foil acts as a strong filter for any continuum x-rays with wavelengths below 7.9 Å. The thin silicon membrane with a K-absorption edge at 6.7 Å does the same. On the long-wavelength side of 8.34 Å, the absorption coefficient of both aluminum and silicon varies as $\lambda^{2.73}$ [12] and any long wavelength continuum x-rays are strongly attenuated; therefore, with an aluminum target operated at 7.5 kV, we can assume that the radiation incident on the polymer film is almost entirely the $A\ell_{k\alpha}$ line at 8.34 Å. For aluminum the linear absorption coefficient (cm^{-1}) is given by $40.18\ \lambda^{2.78}$ for $\lambda < 7.95$ Å and by $3.19\ \lambda^{2.73}$ for λ between 7.95 and 114 Å. For silicon it is given by $43.11\ \lambda^{2.77}$ for $\lambda < 6.75$ Å and by $3.59\ \lambda^{2.73}$ for $6.75 < \lambda < 82$ Å. The use of the Cu_{L_α} line at 13.3 Å is suitable only with an aluminum oxide mask because of the severe attenuation that the radiation experiences in passing through the thin silicon membrane-foil combination. For a 3 μm silicon membrane only 30% of the incident $A\ell_{k_\alpha}$ irradiation (8.34 Å) is absorbed as it traverses it. For Cu_{L_α} irradiation (13.5 Å) 73% is absorbed. This makes exposure times extremely long. The major advantage of the Cu_{L_α} line over the $A\ell_{k_\alpha}$ line is that Cu_{L_α} x-rays are more severely attenuated than $A\ell_{k_\alpha}$ x-rays for the same gold thickness of the absorpting mask pattern, therefore, providing a much higher contrast between the partially exposed and the completely exposed region directly beneath the mask pattern.

2.2.2. Local Development Model

During irradiation, positive working x-ray resist will degrade from a high average molecular weight $\bar{M}_n$ to a lower one $\bar{M}_f$. For PMMA, this is accomplished by random chain scission [13]. The dependence of $\bar{M}_f$ on the obsorbed energy density D has been shown to be [14,15]:

$$\bar{M}_f = \frac{\bar{M}_n}{1 + \frac{gD\bar{M}_n}{\rho A_o}} \qquad (2.30)$$

where g is the efficiency factor proportional to the radiation chemical yield, A_o is Avogadro's number and ρ is the resist density. For PMMA $\rho = 1.2$ gm/cm^3 and $g = 1.9\text{x}10^{-2}$ events/eV. g is assumed the same for both e-beam energy and x-ray energy. It has been shown [17] that the development rate of PMMA is essentially independent of the nature of the ionizing radiation, and depends only on the energy dissipated permit volume.

A key assumption is that during chemical development of irradiated PMMA, it can be modeled by a surface etching process. That is, the developer action is confined to the active surface and the developer solution has a strength which is independent of the relative amount of previously dissolved material. PMMA development measurements by Greeneich tend to show a surface-etching process for electron-beam exposure [14]. The surface-etching rate during development depends on the developer used and it is a function of the average fragmented molecular weight $\bar{M}_f$. The rate R is given by [14,16]

$$R = R_o + \beta \bar{M}_f^{-\alpha} \tag{2.31}$$

(usually in Å/min) where R_o is the background etch rate and β and α are characteristic constants of the developer used. For developers with $R_o = 0$ we note that R is inversely proportional to the average fragmented molecular weight $\bar{M}_f$. Data reported [14,17] for a number of developers is summarized below.

Developer	α	β	R_o
1:3 MlBk:IPA	3.86	9.332×10^{14}	0
1:2 MlBk:IPA	3.4	5.24423×10^{14}	0
1:1 MlBk:IPA	1.188	6.645×10^{6}	0
MlBk	1.5	3.14×10^{8}	84(Å/min)

MIBK denotes methyl isobutyl ketone and IPA denotes isopropyl alcohol. The above relation (2.31) is valid over a large range of molecular weights and only β is temperature dependent [16].

From (2.30) and (2.31) the dependence of R on D is given by

$$R = R_o + \frac{\beta}{(\bar{M}_n)^{\alpha}} \left(1 + \frac{gD\bar{M}_n\sigma}{\rho A_o}\right)^{\alpha} \tag{2.32}$$

where σ is the transmission factor of the absorbing mask. σ varies from 0 (perfect mask) to 1 (no mask). A contrast ratio Γ is defined as $\Gamma = 1-R_s/R_f$ where R_s is defined as the slow etch rate ($0 \leq \sigma < 1$) and R_f is the fast etch rate ($\sigma = 1$). Γ varies from 0 to 1. R_s/R_f is given by

$$\frac{R_s}{R_f} = \frac{R_o + \frac{\beta}{(\bar{M}_n)^\alpha}\left(1 + \frac{gD\bar{M}_n\sigma}{A_o}\right)^\alpha}{R_o + \frac{\beta}{(\bar{M}_n)^\alpha}\left(1 + \frac{gD\bar{M}_n}{\rho A_o}\right)^\alpha} \tag{2.33}$$

We note that for a given resist and exposure conditions (i.e. constant g and D) decreasing σ higher values of contrast Γ can be achieved.

For electron-beam exposure, D is given by [14]

$$D = \left(\frac{Q}{q}\right)\left(\frac{E_o}{R_G}\right)\lambda(f) \tag{2.34}$$

where Q is the total incident charge per unit area, E_o is the beam energy and $\lambda(f)$ is a normalized dose function. Due to $\lambda(f)$, ε is non-uniform with depth except for high incident energies (E_o) and thin resist films. The non-uniform absorption of energy is mainly due to the finite range of electrons in the resist and the backscattering of electrons from both the substrate and the resist film. However, this problem is not present in x-ray exposure where to a good approximation the dose is independent of the distance the ray has traveled in the resist as it was shown earlier.

To explore the effects of x-ray exposure on contrast Γ and development time it is convenient to use the exposure energy in Joules/cm^3. In Figure 2.5 the contrast Γ is plotted vs. D for the developers MIBK and 1:3 MIBK:IPA. The nonzero background development rate for MIBK requires an exposure of about 250 J/cm^3. For a thin mask allowing up to 50% transmission, the required exposure can be as large as 600 J/cm^3 for

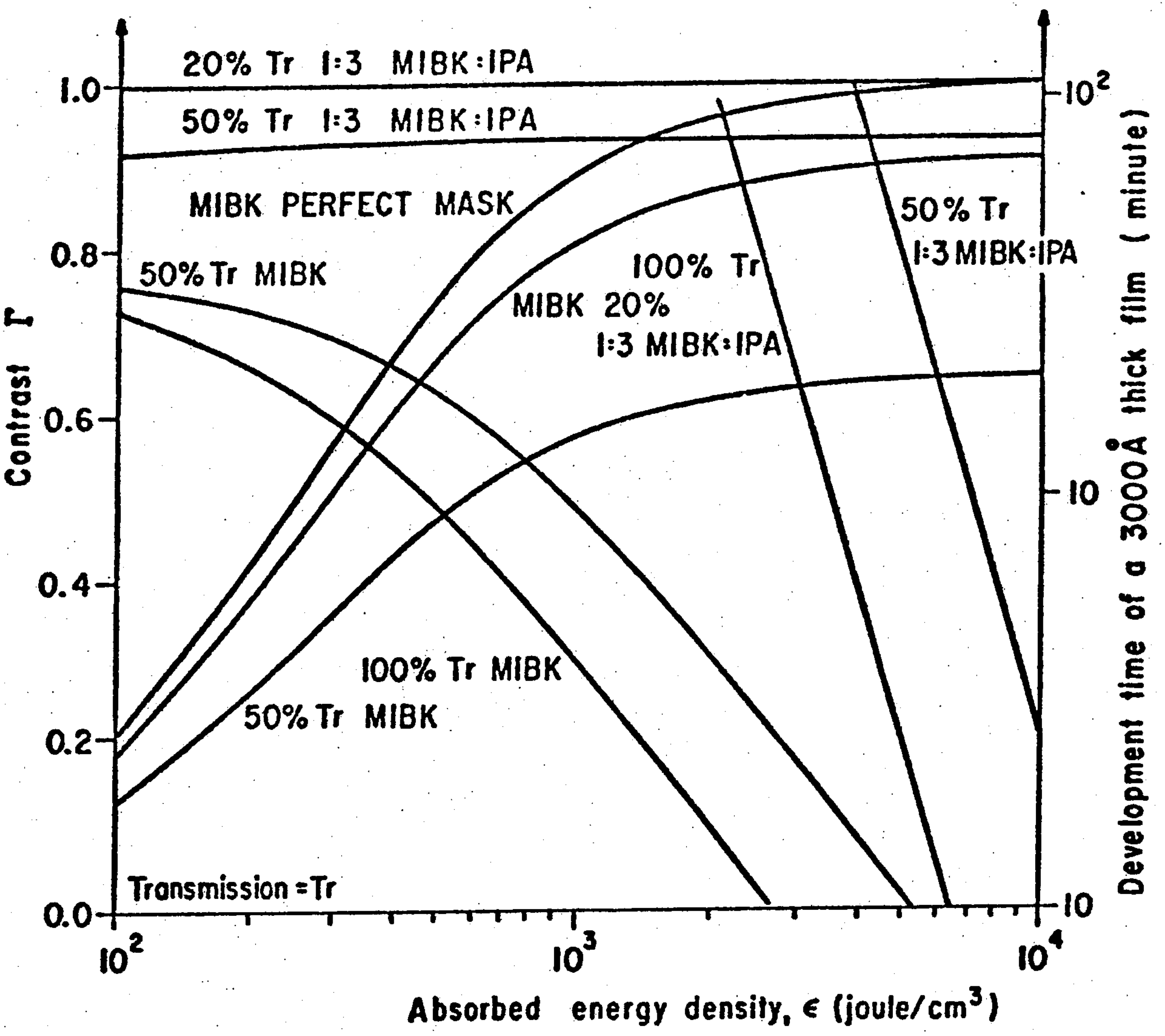

Fig. 2.5. The contrast Γ vs. absorbed energy density ε (positive slope) for two developers and three transmission factors. The development time for a 3000 Å film vs. ε (negative slope) for two developers and two transmission factors.

$\Gamma = 0.5$. The time required to develop a 3000 Å film is also shown in Fig. 2.5. For MIBK, contrast imposes the primary consideration for exposure. For developer mixtures having $R_o = 0$ such as 1:3 MIBK:IPA, the contrast Γ for a perfect mask is always equal to unity. However, even for moderate development times (10 to 20 minutes for a 3000 Å film) the energy required for exposure will necessitate long exposure times. The primary constraint on exposure for these developers is the development rate. In Fig. 2.6 the development rate vs. D is shown for the three developers: MIBK, 1:1 MIBK:IPA and 1:3 MIBK:IPA. The developer MIBK is the obvious choice for moderate contrast. For thin masks the use of Cu_{L_α} (13.3 Å) instead of $A\ell_{k_\alpha}$ (8.3 Å) x-rays will reduce mask transmission and increase the contrast.

2.3. Blazing with Non-threshold Development

In Chapter I we introduced the principle of multiple-angle soft x-ray contact printing of an absorbing (gold) grating mask pattern for the fabrication of blazed gratings (Fig. 1.2). An important problem is introduced by the finite transmission of the mask ($\sigma > 0$) and the fact that the development rate does not show a sharp threshold behavior with respect to exposure energy. The mask transmission leads to low exposure contrast ratios (2:1). The non-threshold development behavior implies that the development effects in the shadowed or partially shadowed region lead to significant groove shape changes.

The exposure process is modeled approximately as follows (A more rigorous approach is described in Chapter VI): We calculate a finite gold transmission factor based on the thickness and angle of incidence. The attenuation in the PMMA ($e^{-\alpha_r z}$, $\alpha_r \approx 1000\ \mathrm{cm}^{-1}$) is neglected and absolute exposure levels were not considered as the development process effects depend only on relative exposure ratios provided the total exposure dose is such that we are on the linear portion of the etch rates curves for the various developers as shown in Fig. 2.6. The basic approximation is that of a zero thickness, but finite absorption, mask. With this assumption we can disregard geometries involving mask edge profiles, in which case the determination of the exposure profile in the resist is more complicated. A modification of the mask opening, d, to an effective opening, d_{eff}, to compensate for our earlier assumption of zero thickness (planar) mask is added. This is shown in Fig. 2.7.

The above model predicts a planar front etching phenomenon. A sketch of how the planar etching front occurs is shown in Fig. 2.8. In this case a single exposure results in distinct regions having exposed and background etch rates R_E and R_B, respectively. When the developer is applied to the top surface the locus of the developer front can be found by using a technique anologous to Huygen's principle for electromagnetic theory. At any time t, each point on the developer front can be thought of as an etching center about which a sphere (or cylinder in two dimensions) of radius $R\Delta t$ is produced, where R is the etch rate at the center of each sphere. The envelope of the intersecting spheres forms the developer front at $t + \Delta t$. Due to the fact that R depends on position the appropriate limits on Δt discontinuities of R at shadow boundaries must be considered.

For the exposure profile shown in Fig. 2.8, the development process can be solved analytically. The planar surface of the exposed and background regions translate vertically at rates R_B and R_E respectively. For an exposure at an angle θ_i, the horizontal planar front in the R_E region intercepts a point on the shadow boundary of the mask which moves at a

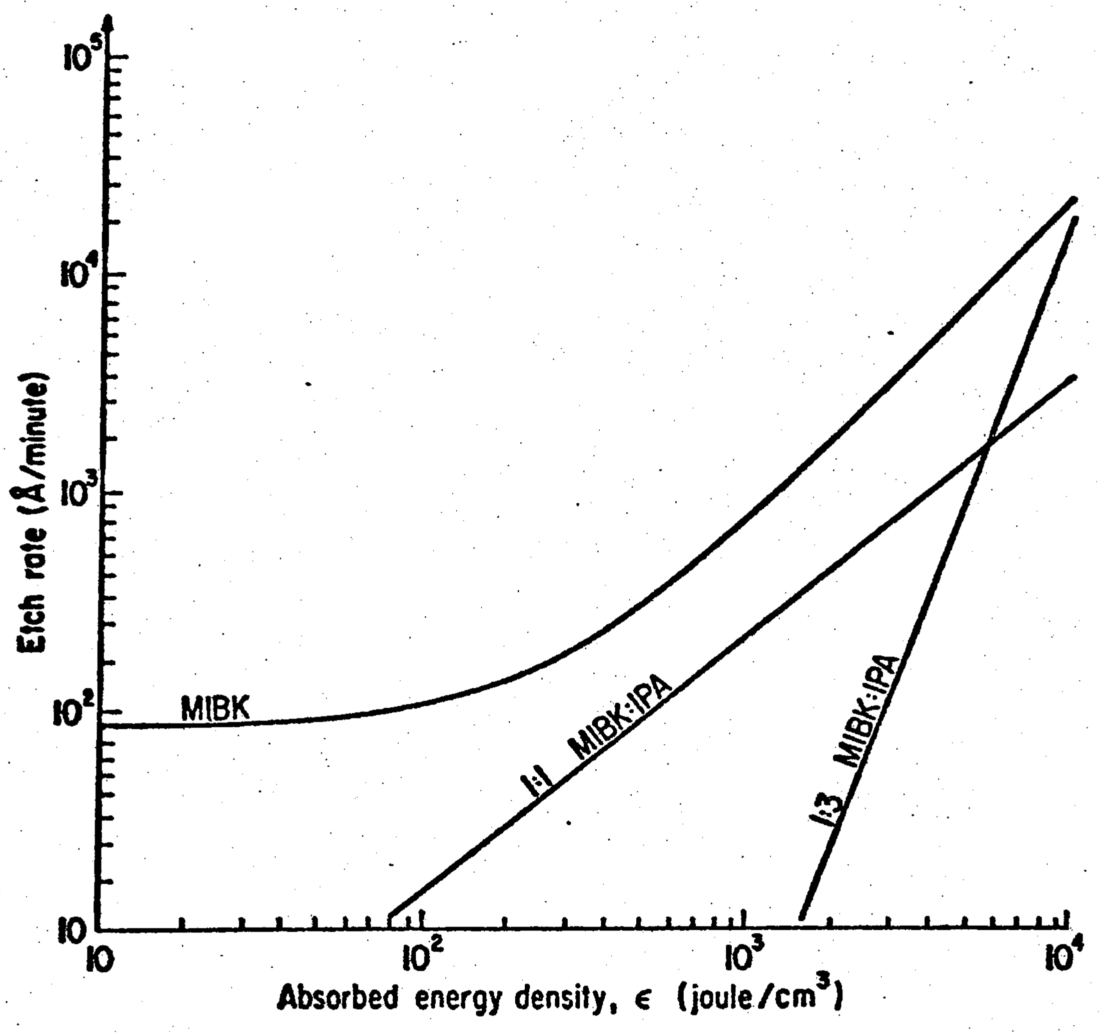

Fig. 2.6. The solubility (etch) rate vs. absorbed energy density ε for three different developers.

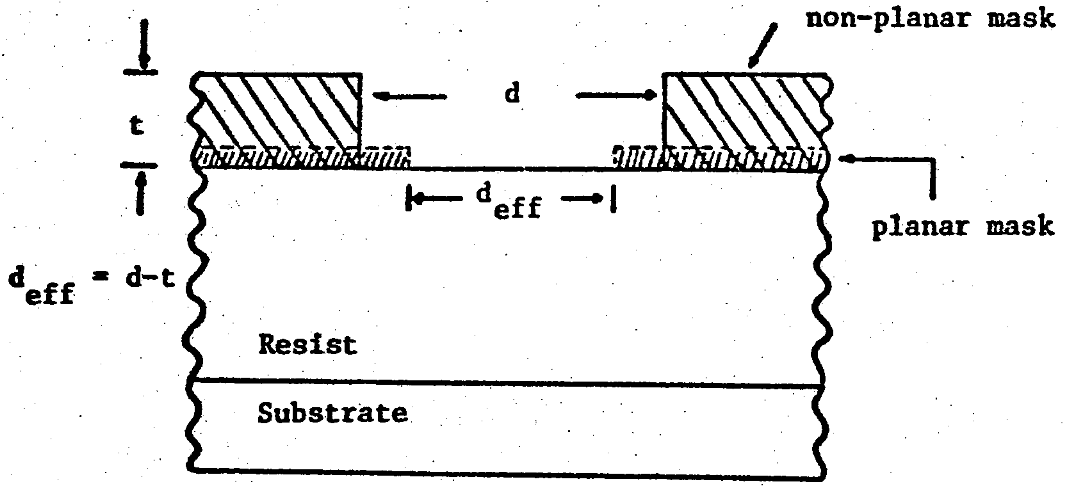

Fig. 2.7. Planar and non-planar mask profile.

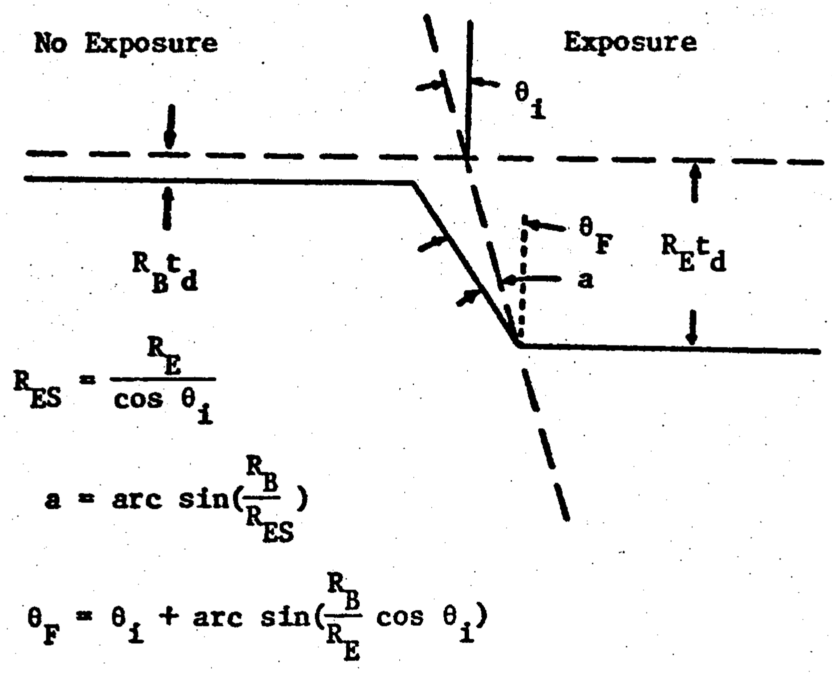

$$R_{ES} = \frac{R_E}{\cos\,\theta_i}$$

$$a = \arc\sin(\frac{R_B}{R_{ES}})$$

$$\theta_F = \theta_i + \arc\sin(\frac{R_B}{R_E}\cos\,\theta_i)$$

Fig. 2.8. Isotropic etching model showing planar etching front phenomenon.

velocity $R_{ES} = R_E/\cos\theta_i$. This moving interception point generates a continuous sequence of etching centers whose spheres move into the background region at a rate R_B. The largest of these spheres move into the background region at a rate R_B. At time t the envelope of the sequence of interception point generated spheres is a new planar front tangent to the largest sphere and passing through the transition point a distance $R_{ES}t$ down the mask shadow boundary. This new planar front forms an angle $\alpha = \arcsin(R_Bt/R_{ES}t)$ with respect to the interface. The net planar front angle is thus $\theta_F = \theta_i + \arcsin(R_B\cos\theta_i/R_E)$.

Figure 2.9 shows a complete line shape where for clarity the absorbing mask has not been removed. Normal incidence of x-rays is assumed. The minimum sidewall angle(based on some application criterion such as for IC lithography or a minimum groove half angle, $\theta_G/2$ for diffraction grating fabrication) is also shown. This angle ($\theta_G/2$) is given by $\theta_G/2 = \arcsin R_s/R_f$ or arc sin (L-Γ) where R_s is the etch rate in the shadowed region and R_f is the etch rate in the exposed region. Through Γ, mask absorption can be related to the minimum feature resolution. It should be noted that the profile shown in Fig. 2.9 is exact since the exposure does not depend on mask edge profile for this configuration. The minimum sidewall angle vs. D for various developers and different σ is shown in Fig. 2.10.

Our PMMA was obtained commercially [18] and its initial average molecular weight is approximately 150,000 [19]. This is the value used ($\bar{M}_n$=150,000) in calculating the curves for Figs. 2.5, 2.6 and 2.11 PMMA with a higher initial average molecular weight ($\bar{M}_n$=950,000) is available commercially [17]. For $\bar{M}_n$ = 150,000, the minimum sidewall angle vs. D for various developers and different σ is shown in Fig. 2.11. For the same developer and mask transmission the resulting $\theta_G/2$ for the two different

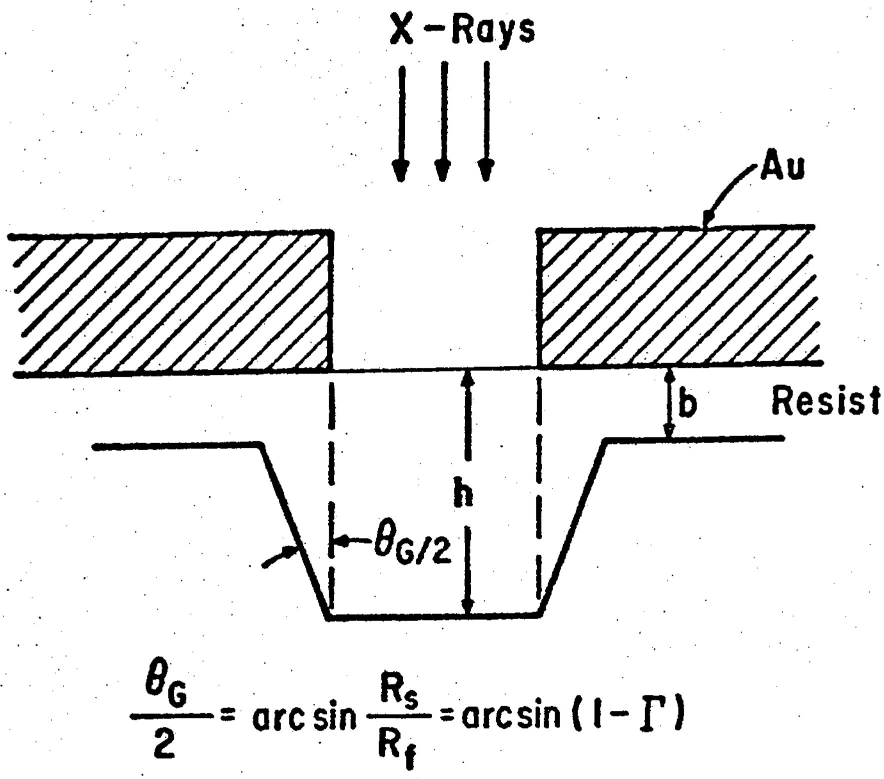

$$\frac{\theta_G}{2} = \arcsin\frac{R_s}{R_f} = \arcsin(1-\Gamma)$$

Fig. 2.9. Mask-resist system with a characteristic development profile.

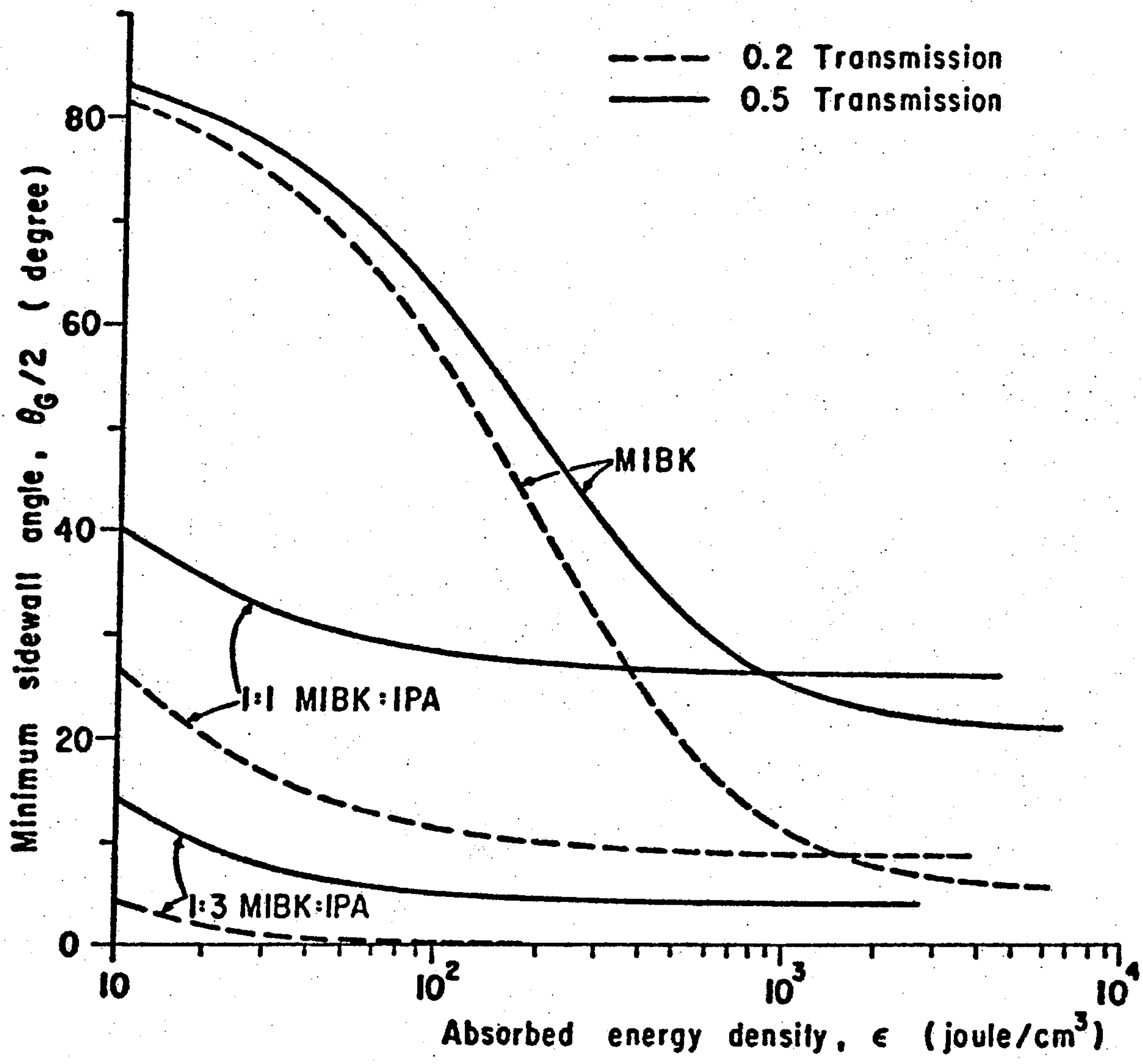

Fig. 2.10. The minimum sidewall angle, $\frac{\theta_G}{2}$ vs. absorbed energy density ε for three developers and two transmission factors.

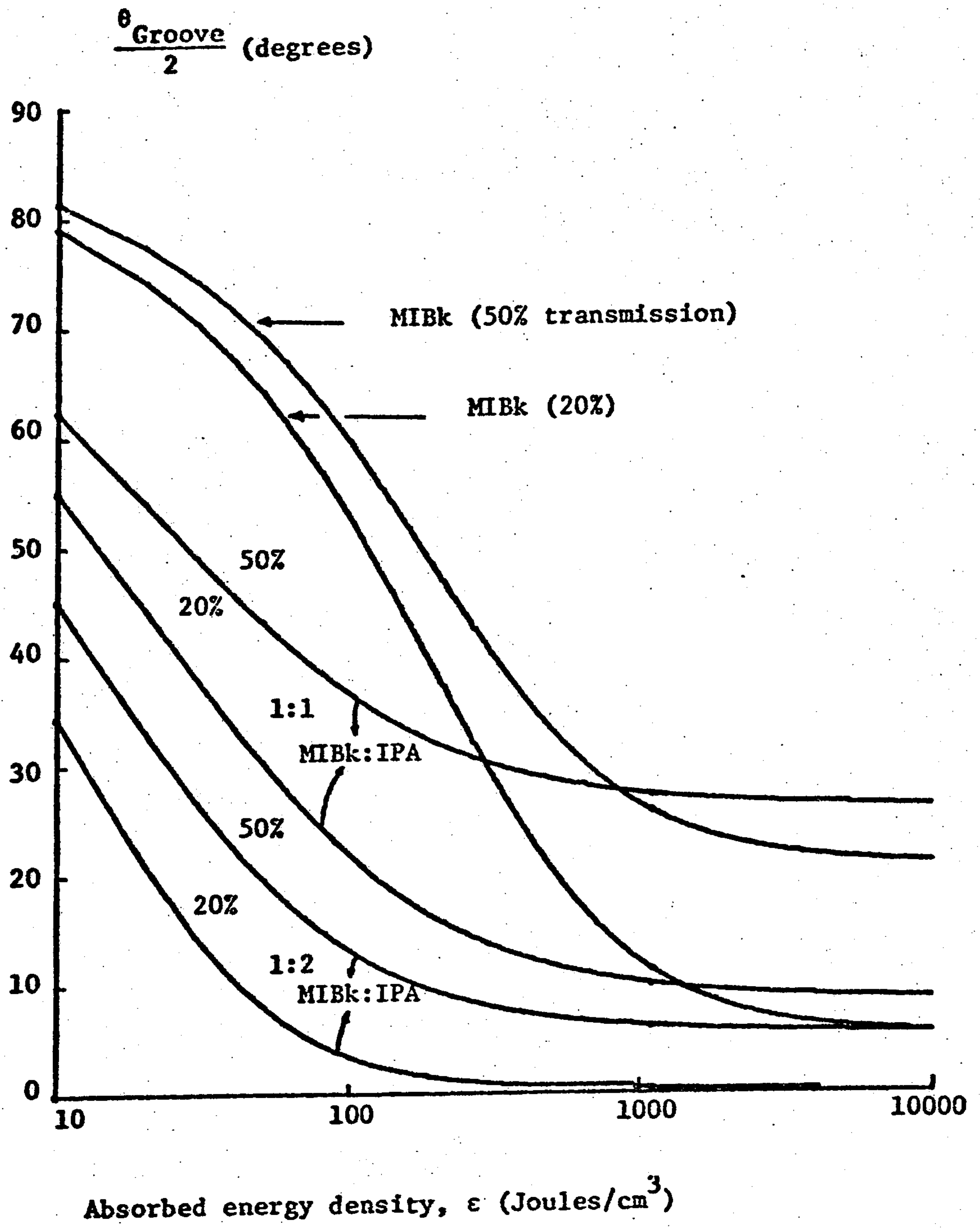

Fig. 2.11. The minimum sidewall angle, $\frac{\theta_G}{2}$ vs. absorbed energy density ε for three developers and two transmission factors. ($\bar{M}_n$ = 150,000).

values of $\bar{M}_n$ is shown in Fig. 2.12. We note that for an energy dose $D < 1000$ Joules/cm^3, the minimum sidewall angle $\theta_G/2$ depends on the intitial average molecular weight $\bar{M}_n$. The final average molecular weight $\bar{M}_f$ vs. initial average molecular weight $\bar{M}_n$ for $D = 1000$ Joules/cm^3 is shown in Fig. 2.13.

The planar-front phenomenon makes blazing of gratings possible even when development can occur in partially or totally shadowed regions. Two exposure techniques for blazing gratings are shown in Fig. 2.14. The single source approach uses planar fronts on both sides and the exposed shaft is removed at a rate R_E. A groove angle $\theta_G = 2 \arcsin(R_B/R_E)$ is produced. This is the smallest possible groove angle and can be used to estimate the ultimate capabilities of x-ray lithography. The minimum groove angle vs. period for various mask (gold) thickness to period ratios and for the developer 1:2 MIBk:IPA is shown in Fig. 2.15 where $A\ell_{k_\alpha}$ (8.34 Å) irradiation is assumed.

As the period is decreased and hence the gold thickness is also decreased, the mask transmission increases which in turn increases the ratio of R_B/R_E and consequently increases the minimum groove angle. The curves for various gold thickness to period ratios emphasize the importance of mask thickness. The angle of incidence changes the apparent mask thickness but this is only a relatively minor effect.

The more flexible two source exposure technique shown in Fig. 2.14, which also takes advantage of the planar etching-front phenomenon, is also treated analytically. In this case the exposure at θ_i and θ_R creates regions having etch rates R_B, R_1, R_2 and R_{12} corresponding to partial exposure by both source 1 and 2, source 2 and partially source 1, source 1 and partially source 2 and both source 1 and 2 respectively. Planar etching

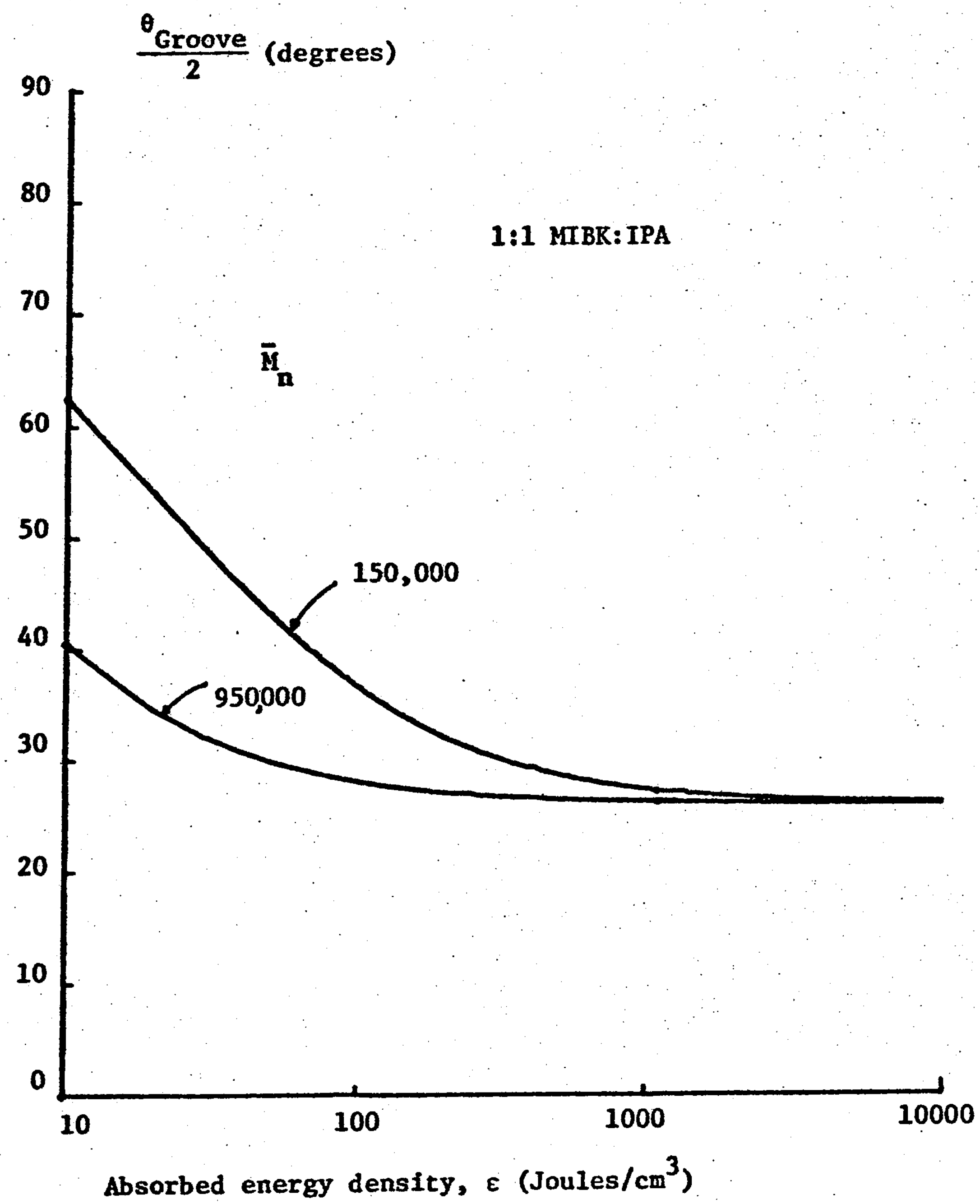

Fig. 2.12. The minimum sidewall angle, $\frac{\theta_G}{2}$ vs. absorbed energy density ε for two different values of initial average molecular weight $\bar{M}_n$.

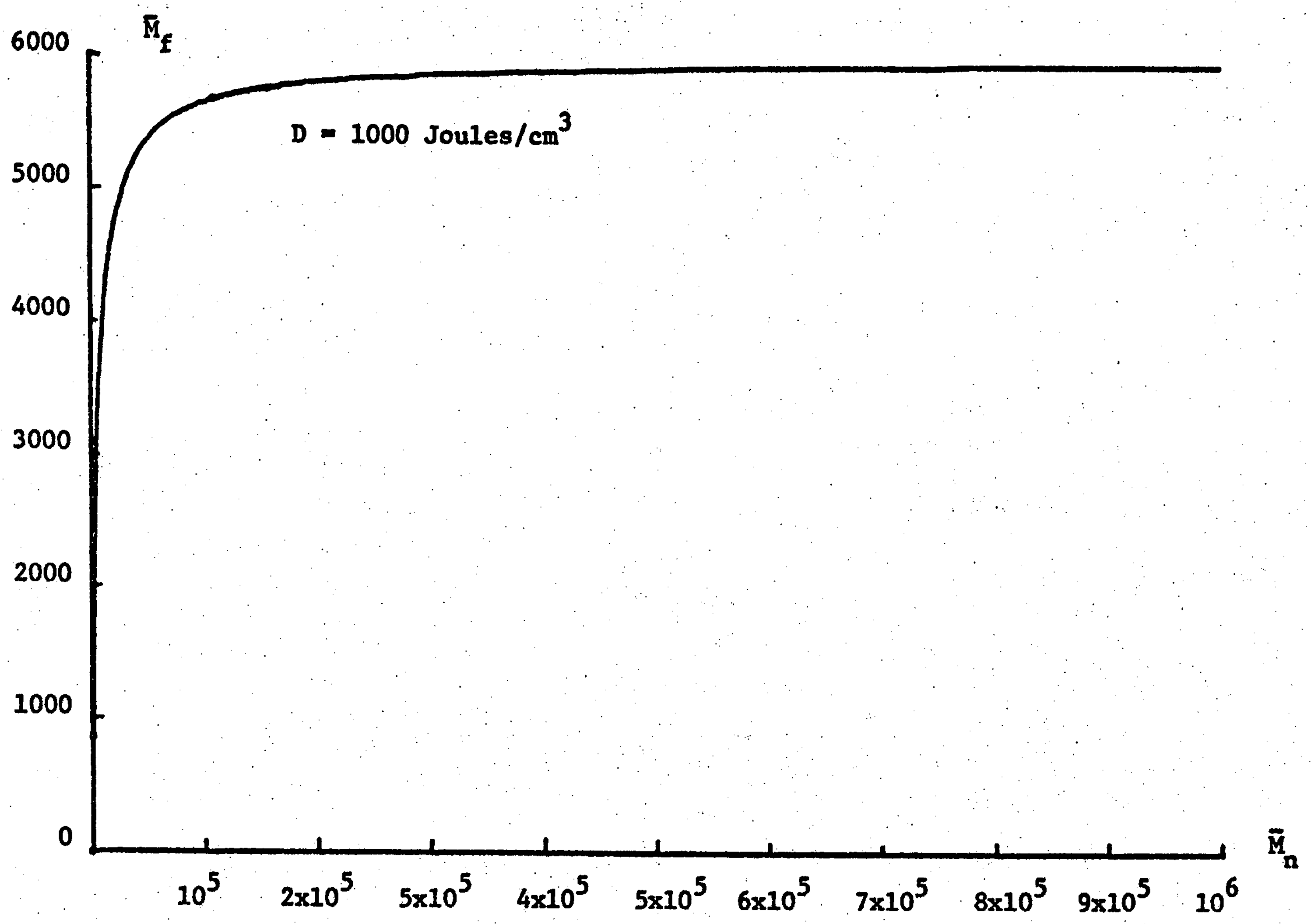

Fig. 2.13. Final average molecular wieght $\bar{M}_f$, vs. initial average molecular weight, $\bar{M}_n$ for ε = 1000 Joules/cm^3.

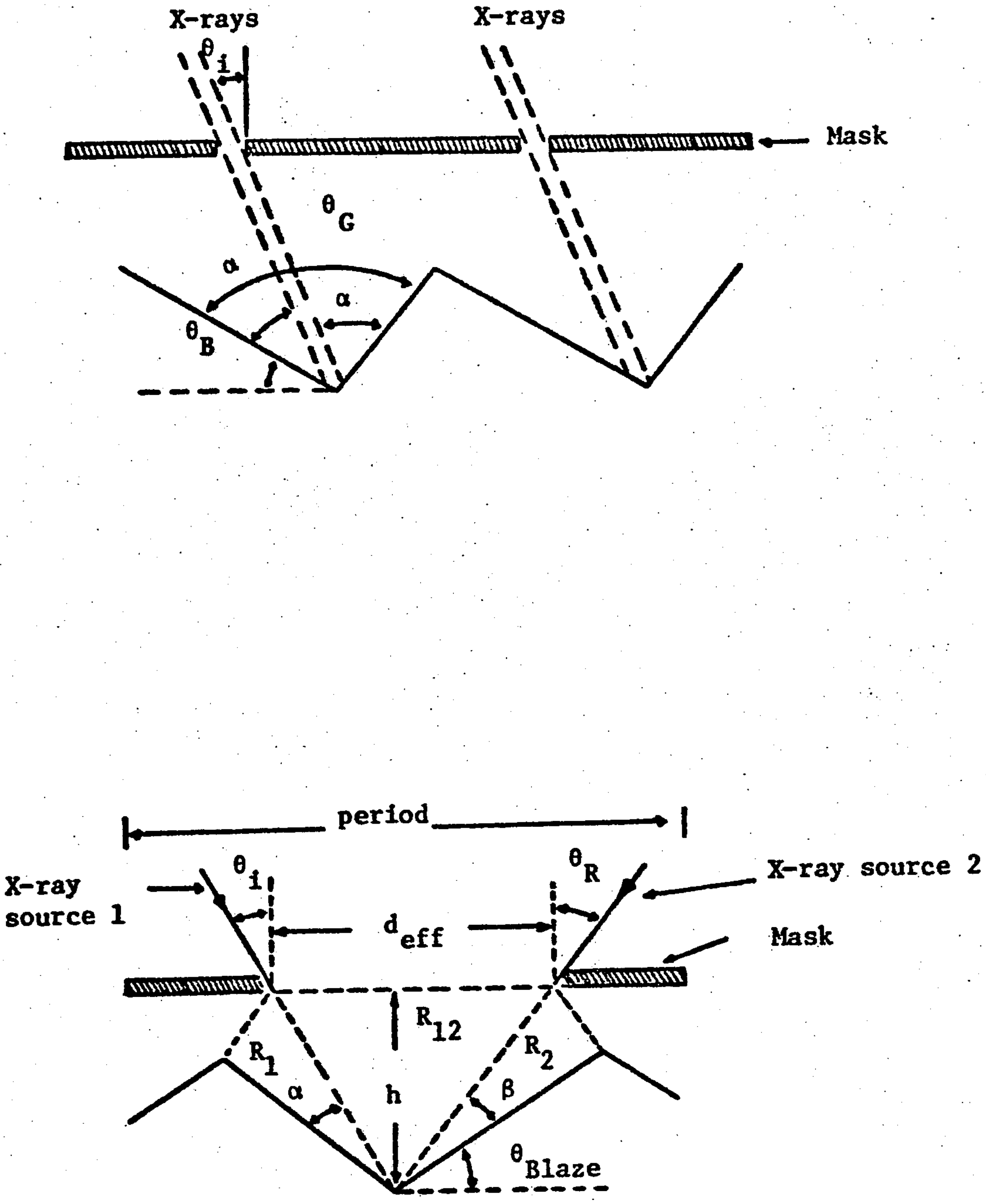

$$\theta_{Groove} = \theta_i + \theta_R + \alpha + \beta$$

Fig. 2.14. Single source and double source exposure technique.

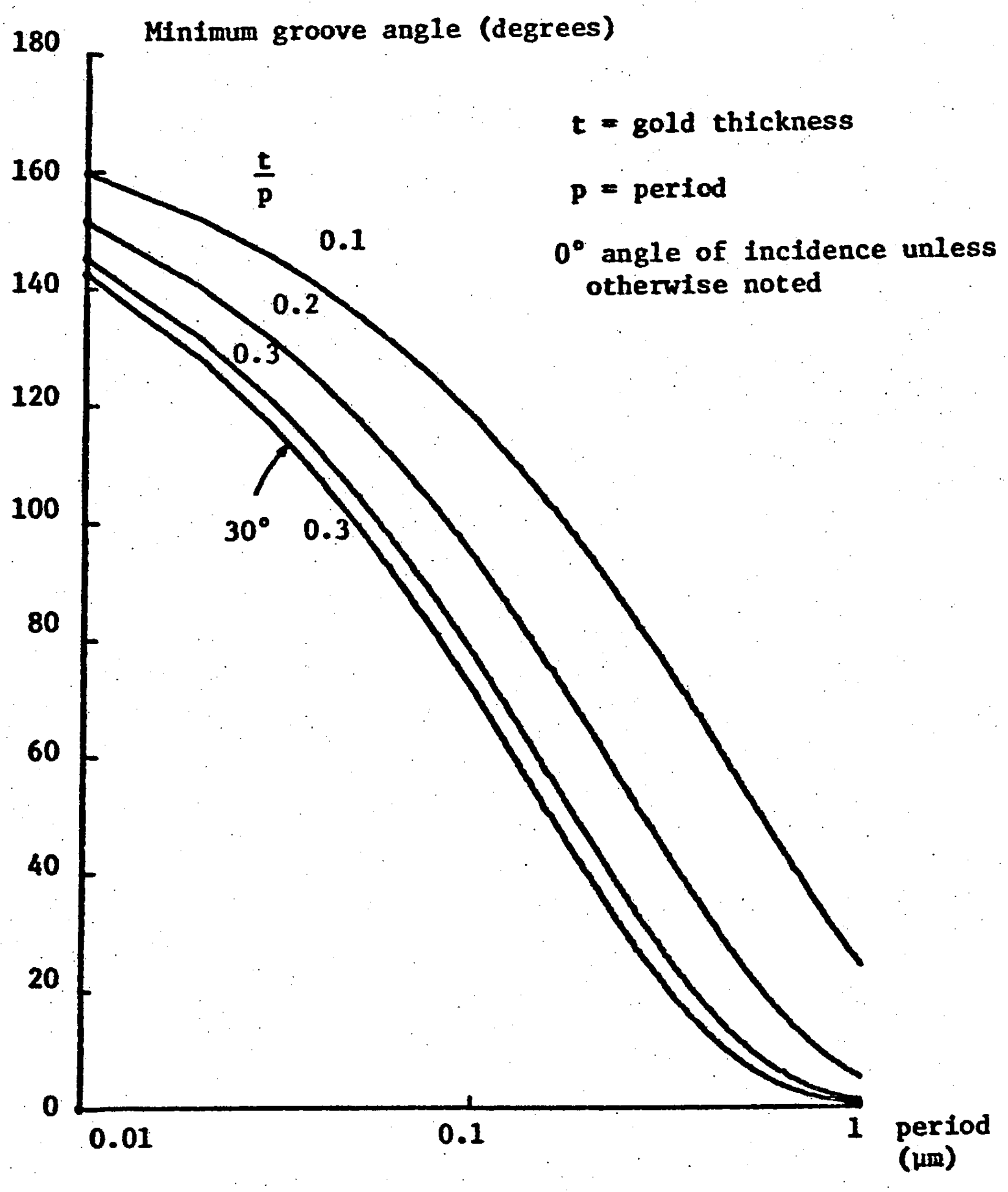

Fig. 2.15. Minimum groove angle vs. period for three mask thickness to period ratios.

fronts along the shadow boundaries which intersect at an angle θ_G deep in the resist form the grating facets. It is necessary to stop the development process when the direct vertical etching of the region exposed to both source 1 and 2 reaches the intersection $t_d = R_{12}/h$. The actual grating height will necessarily be less than h. The blaze angle is $\theta_B = 90°-\theta_R-\beta$.

The effective mask opening d_{eff} is typically equal to $(p/2)-t$ where p is the grating period and t is the thickness of the mask. For the shadow boundaries to intersect at depth h, θ_R is given by

$$\theta_R = \arctan\left(\frac{d_{eff}}{h} - \tan\theta_i\right) . \tag{2.35}$$

Let α_g denote the linear absorption coefficient for gold (α_g=4.60517 μm^{-1} at 8.34 Å) and a' denote the developer parameter α defined earlier. The groove and blaze angles are then given by

$$\theta_G = \theta_i + \theta_R + \alpha + \beta \tag{2.36a}$$

$$\theta_B = 90° - \theta_R - \beta \tag{2.36b}$$

where

$$\alpha = \arcsin\left[\frac{(1 + e^{-\alpha_g t/\cos\theta_i})^{a'}}{2^{a'}} \cos\theta_i\right] \tag{2.37a}$$

and

$$\beta = \arcsin\left[\frac{(1 + e^{-\alpha_g t/\cos\theta_R})^{a'}}{2^{a'}} \cos\theta_R\right] \tag{2.37b}$$

The determining parameters are d_{eff}/h and t.

Information for the design of blazed gratings in the presence of non-threshold development effects can be obtained from the above equations.

Figure 2.16 shows that for a given d_{eff}/h and t, the groove anlge θ_G is a relatively insensitive function of θ_i. The thickness of the mask is chosen to be a small percentage of the grating period and the appropriate d_{eff}/h value is read from the curves. The blaze angle dependence on θ_i is shown in Fig. 2.17. Given the desired θ_B the required θ_i is read from the particular t and d_{eff}/h curve selected previously. A final important consideration is the selection of the d_{eff} value, which can be different from p/2–t. It depends on the actual fabrication of the mask. It is chosen such that the two facets forming the peak of the groove profile intersect at the intersection of the shadow boundaries for the two exposures as shown in Fig. 2.18.

Figure 2.18 as an example of the designing technique just described. The period is equal to .5 μm. For $\theta_B = 37°$ and $\theta_G = 96°$ we first select a gold thickness of .2 μm. Figure 2.17 indicates that $d_{eff}/h = .8$ and $\theta_i = 18°$. This given $\theta_G = 96°$ from Fig. 2.16, $\alpha = 25°$, $\beta = 27°$ and $\theta_R = 26°$. The resulting profile is shown in Fig. 2.18.

In Chapter VI, a more rigorous approach is described for predicting groove shapes.

2.4. Geometric Considerations

For the x-ray lithography configuration as shown in Fig. 2.4, the finite source size A and the finite mask-to-substrate gap s lead to the penumbral shadowing which leads to a line edge uncertainty $\delta = \frac{s}{d} A$ where d is shown in Fig. 2.4 and δ is shown in Fig. 2.19a. Figure 2.19b shows the geometric distortion $\gamma = \frac{s}{d}\frac{w}{2}$ where w is the substrate wafer diameter.

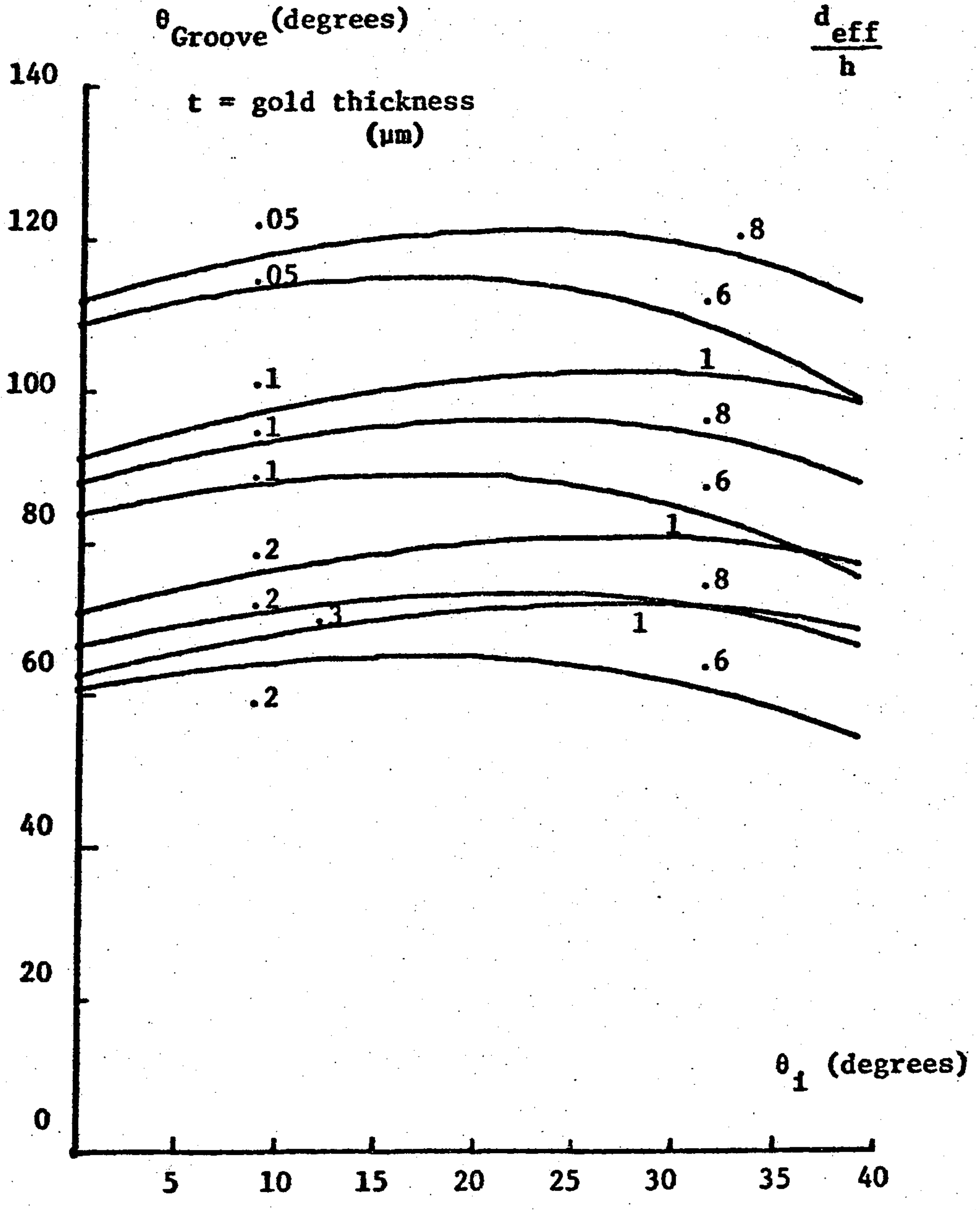

Fig. 2.16. Groove angle, θ_G vs. θ_i for different mask thickness and d_{eff}/h.

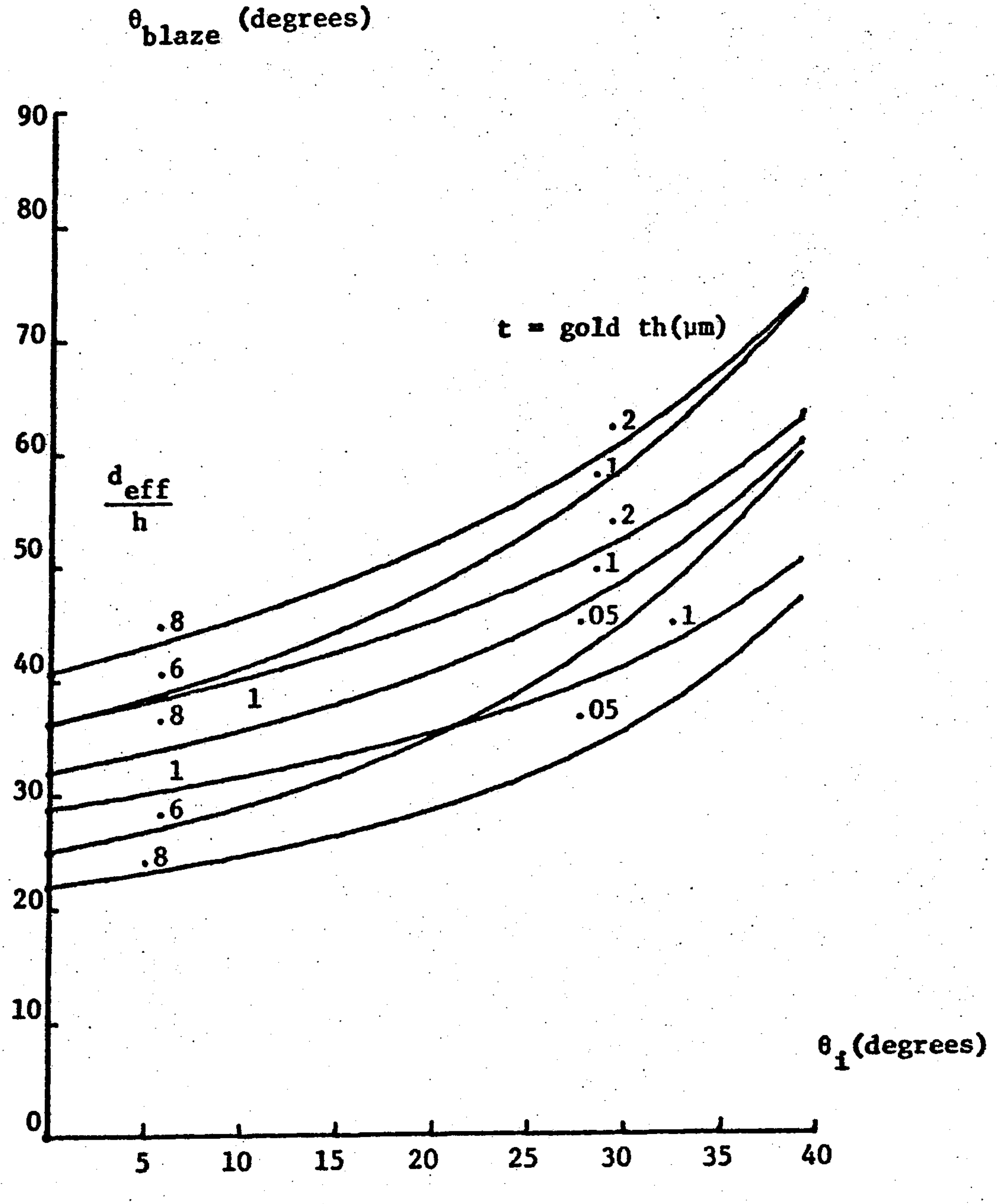

Fig. 2.17. Blaze angle, θ_B vs. θ_i for different mask thickness and d_{eff}/h.

Gold thickness = 0.1 μm, $d_{eff}/h = 0.8$

$\theta_{Groove} = \theta_i + \theta_R + \alpha + \beta = 96°$

$\theta_i = 18°$

$\theta_R = 25°$

$\beta = 27°$

$\alpha = 25°$

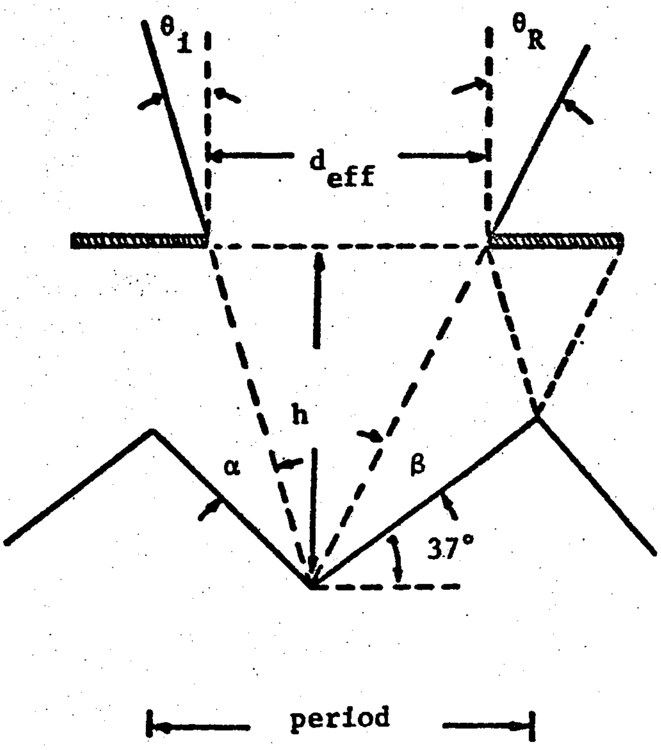

Fig. 2.18. Exposure, masking and etching geometry for producing etypical optical grating with $\theta_G = 96°$, $\theta_B = 37°$ and period of 0.5 μm.

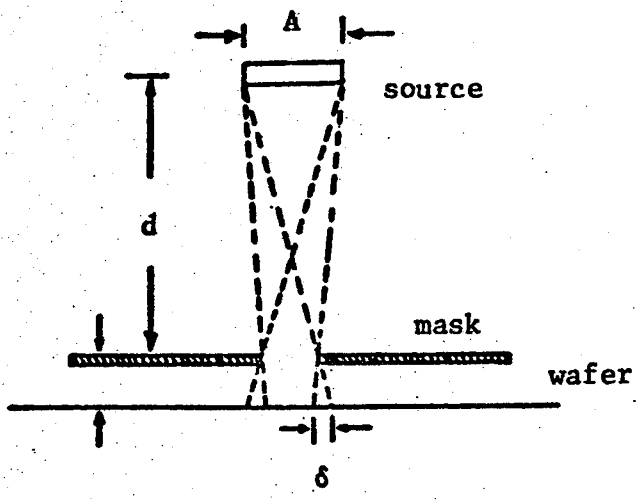

Fig. 2.9a. Definition of the penumbra δ.

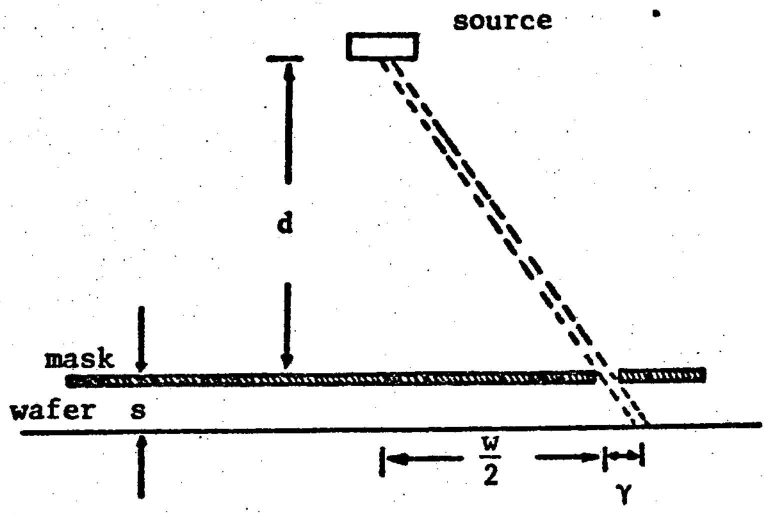

Fig. 2.9b. Definition of the geometric distortion γ.

CHAPTER III

X-RAY EXPOSURE SYSTEM

In Section 1 of this Chapter, we describe the x-ray expsoure system used for x-ray lithography. In Section 2 we give a brief description of a solid state x-ray detector.

3.1. X-ray Exposure System

The soft x-ray source consists of an electron evaporator gun assembly, a water-cooled target, a substrate holder and a water cooled substrate holder for long exposures, both situated above the x-ray source. The above are incorporated in a vacuum system shared with other experiments. A general view of the system is shown in Fig. 3.1 and a schematic of the system in Fig. 3.2. A high voltage power supply is a separate unit and provides the accelerating potential for operation of the x-ray system. A description of the various system components is given below.

3.1.1. Electron gun, power supply and x-ray target

The electron gun used in our system is a commercially available evaporator gun [20]. It had been used previously for metal evaporation. The gun has the following characteristics:

1. It is a straight gun. Originally it was a 90° gun but the focussing magnet was removed.

2. Its cathode consists of a spiral tangsten filament. The diameter of the filament is 4 mm. A 6 volts DC potential is applied across the filament. Maximum current through the filament is 12 A.

3. The emergent electron-beam is accelerated by a high negative

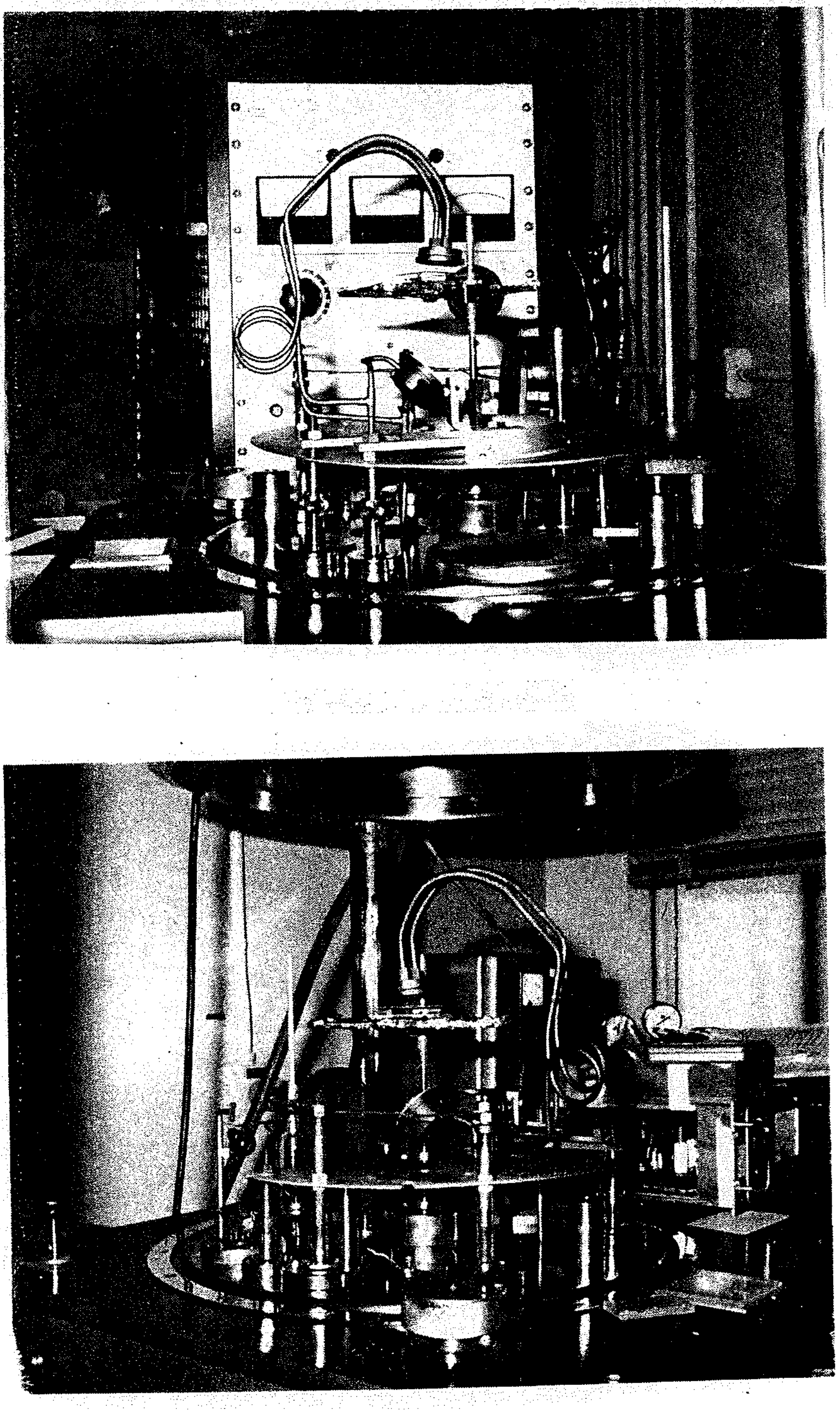

Fig. 3.1. Two views of the x-ray exposure system sharing vacuum chamber with other systems. Top picture shows high voltage power supply in background.

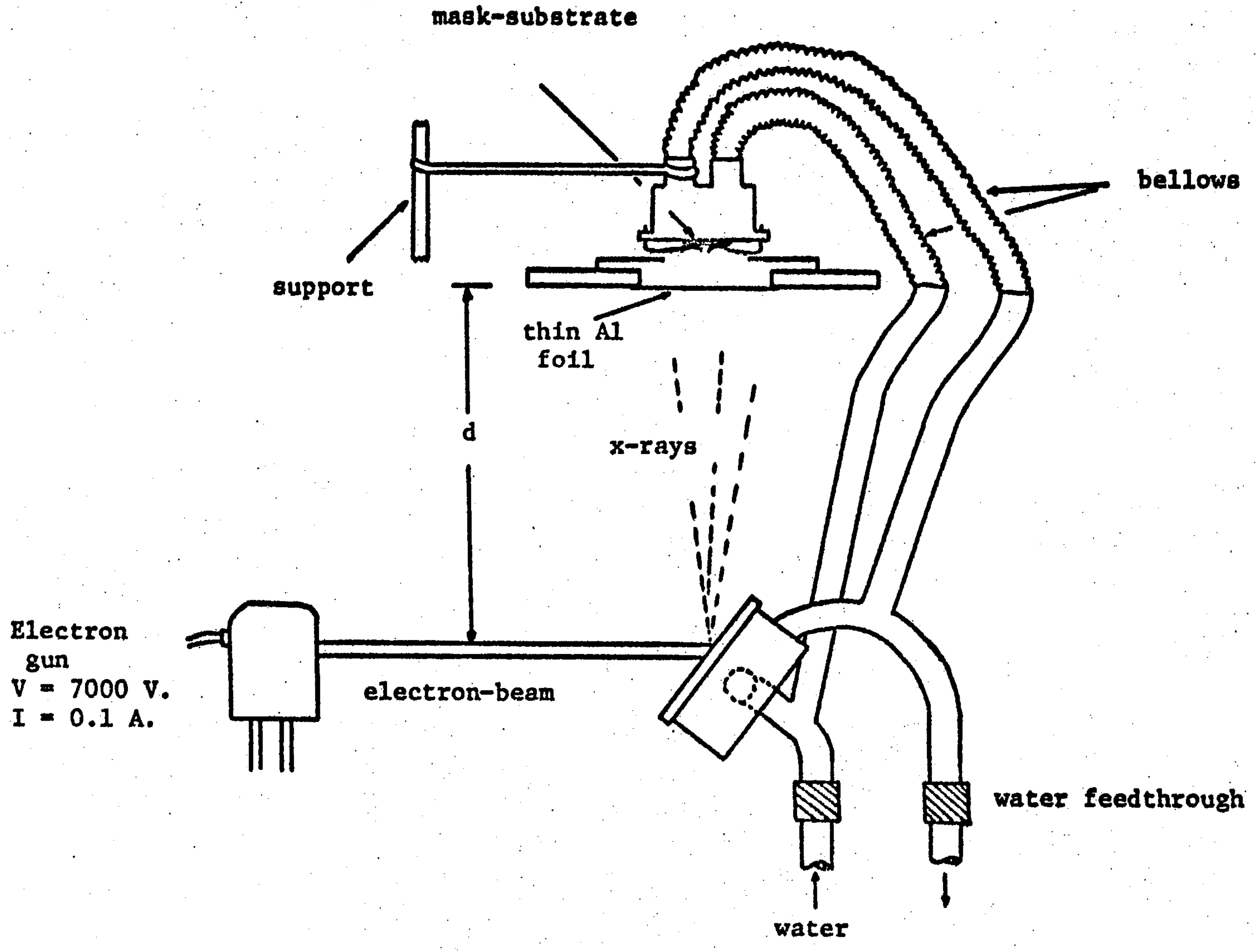

Fig. 3.2. Schematic of the x-ray exposure system

potential applied to the cathode and to the focussing cup. The nominal value of the beam diameter is 3 mm;however, experimental results indicate that the beam diameter is closer to 5 mm [20].

4. There is no provision for removal of the cathode heat (maximum power: 70 watts). Under high-vacuum conditions, it is radiated away from the cathode and increases the temperature of the substrate holder and the mask-resist-substrate system. Figure 3.3 is a schematic of the electron gun.

The vacuum system, where the x-ray apparatus is incorporated, can reach an ultimate pressure of 10^{-5} Torr, in 45 minutes from atmospheric pressure. It has a manual high vacuum valve with no automatic shut off if the pressure in the chamber rises above a certain value. The high voltage power supply is also commercially available [21]. There exists an interlock between the high-vacuum valve and the power supply.

Figure 3.4 shows a diagram of the x-ray target. This configuration was machined to our own specifications in order to meet the particular needs of our x-ray lithographic system. As shown in Fig. 3.2, the target makes an angle of 45° with the incident electron-beam. Its main features are the following:

1. It has a demountable metal plate target. An aluminum plate is used when the $A\ell_{k_\alpha}$ line (8.34 Å) is desired, and a copper one when the Cu_{L_α} line (13.3 Å) is desired. The plate is 1.5 mm thick and 50 mm in diameter. A Viton gasket makes a vacuum tight seal between the front and the back surfaces of the metal plate. The main advantage of this scheme is the ease of removal if the target plate. This allows for quick interchange between targets of different materials of a different characteristic x-ray line is desired.

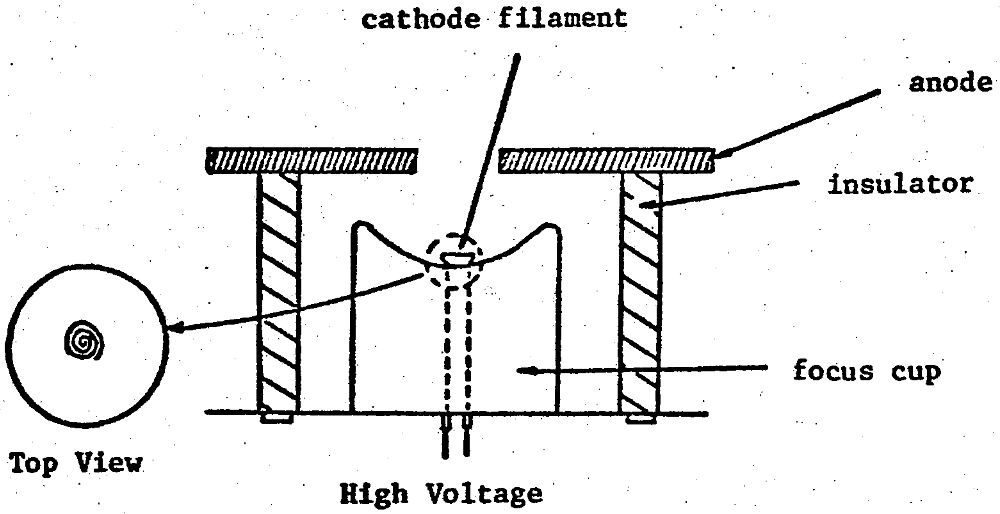

Fig. 3.3. Schematic of a BTI 777 electron gun.

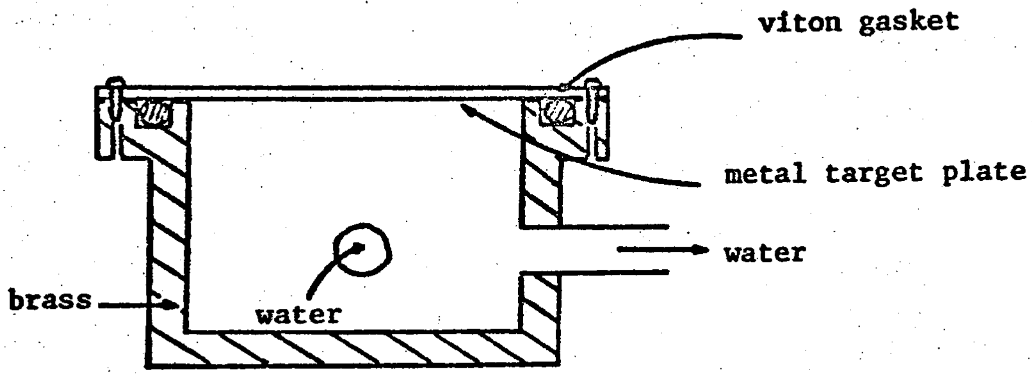

Fig. 3.4a. Schematic of the x-ray target.

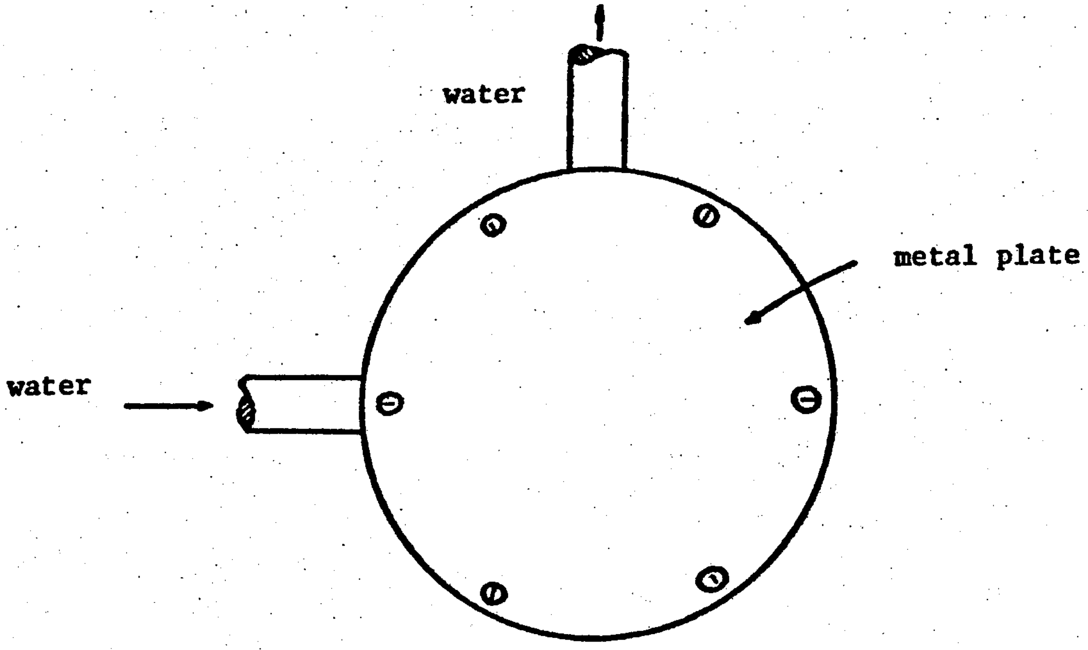

Fig. 3.4b. Top view of the x-ray target.

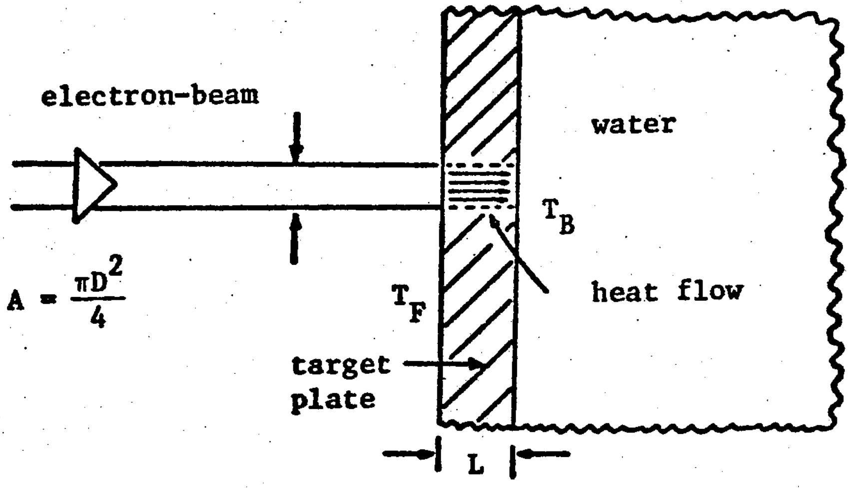

Fig. 3.5. Linear model of heat conduction.

2. Water cooling. This is very important for heat dissipation, due to beam power striking the target, so that the system can be operated at high power levels. Quantitative results will be mentioned below.

A major problem is that the accumulation of even very thin layers of tungsten contamination (from the filament) at the tartet (anode) can greatly reduce the intensity of the emitted soft characteristic radiation from the underlying light element target material [7]. Since it is impossible to avoid this, given the design of our system, each time an exposure is to be made, the metal target plate should be cleaned as follows:

1. Polish both surfaces of the target plate. In particular it is important that no scratches remain on the side which is in contact with the Viton gasket.

2. Degrease in hot trichloroethylene (60° C) for 10 minutes.

3. Rinse in acetone and blow dray with N_2.

4. Mount the target.

For a worst case analysis for heat dissipation in the target we may assume the heat flow to be linear across the target plate as shown in Fig. 3.5. The magnitude of the heat current in the steady state is then given by

$$H = kA \frac{T_F - T_B}{L} \left(\frac{\text{calories}}{\text{second}}\right) \tag{3.1}$$

where k is the thermal conductivity given in calories per second, per cm per degree (.49 for Aluminum, .92 for copper), A is the cross section of the electron-beam, L is the plate thickness, T_F is the temperature on the front surface of the target and T_B is the temperature of the water cooled surface (3.1) can be written

$$\Delta T \equiv T_F - T_B = \frac{LH}{kA} \qquad (3.1a)$$

For a 5 mm beam diameter and a total beam power of 800 watts (7.3 KV accelerating voltage, 110 mA beam current), and for an aluminum target; ΔT is equal to 300°C. If a copper target is used ΔT = 160°C. For $T_B = 70°C$, T_F is still well below the melting point of both metals (660°C for Aluminum and 1083°C for copper). Since the target thickness is not large compared to the beam spot size, we can not assume that the heat flow is radial into the hemisphere of which the spot is the center and furthermore assume a semi-infinite block of material [9]; nevertheless a calculation based on this wrong assumption, yields values of ΔT lower than the ones derived from the linear model.

3.1.2. Substrate Holders - Backscattered Electron Shield

Figure 3.6 shows the layout of the two substrate holders. The rigid one can move vertically so that the distance, d, between x-ray source and the mask substrate can be increased or decreased at will.

A thin aluminum foil (2.5 μm thick) [22] serves both as a shield for backscattered electrons and as an x-ray filter. For an electron-beam incident at 45° to the normal on an aluminum target, the fraction of backscattered current is 0.3. The fraction of primary beam energy which is carried away by the backscattered electrons is 0.13 and it is independent of beam voltage [23].

The flexible substrate holder was machined to our own specifications. It is water cooled and it shares the same water feedthroughs as the x-ray target. Restrictors in the pipes divert most of the water flow to the x-ray target where cooling is extremely important. The flexible bellows pipes allow for the rotation of the substrate holder so that its surface

Rigid substrate holder

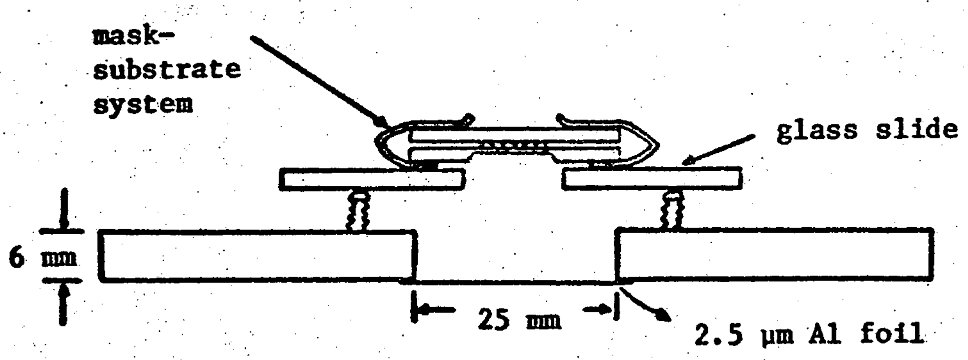

Flexible substrate holder. This holder is positioned on top of the rigid substrate holder.

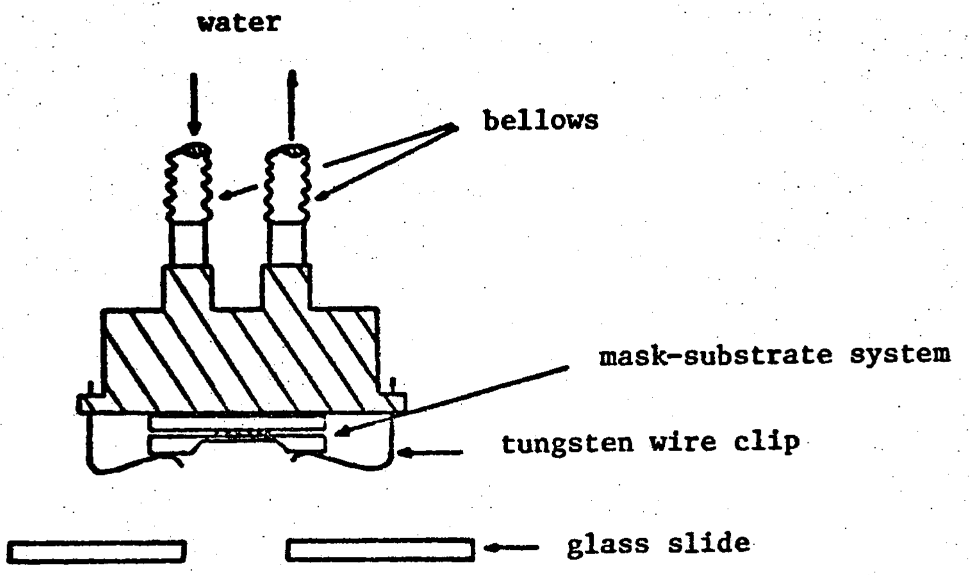

Fig. 3.6. Substrate holders.

makes an angle with the surface of the rigid holder. This in effect provides for an exposure of an angle. The mask-resist-substrate system is retained with clamps (.024" tungsten gauge wire) which provide the necessary contact between the mask and the resist substrate. A thin layer of silicon grease between the back surface of the substrate and the surface of the holder provides a conduction path and good thermal contact between the surfaces for efficient cooling of the system. During the flexible holder is retained into position using clamps.

3.2. X-ray Solid State Detector System

The x-ray detector system uses a silicon PIN Schottky barrier photodiode (United Detector Technology PIN 10UV enhanced) in order to measure x-ray flux (W per cm^2). It does not measure photons per cm^2 per second; therefore, it is particularly sensitive to high-energy continuum radiation that reaches its active surface. More than 50% of the energy that reaches the detector is due to the continuous radiation for a copper target. In order to measure only characteristic x-rays (either the $A\ell_{k_\alpha}$ or the Cu_{L_α} lines depending on the target material used) it would require a flowing gas proportional detector and a pulse-height discriminator. Below we give a brief description of the Schottky barrier silicon PIN photodiode, the electronics of the detector system and our measurements using the detector.

3.2.1. PIN and Schottky barrier PIN photodiodes.

Both the PIN and the Schottky barrier PINphotodiodes are depletion-layer photodiodes. Depletion layer photodiode consist, in essence, of a reverse biased semiconductor diode whose reverse current is modulated by the electron-hole pairs produced in or near the depletion layer by the absorption of light. One of the key factors that determines wavelength response is the absorption coefficient α. Figure 3.7a [24] shows the intrinsic absorption coefficients for Si as a function of wavelength. The short wavelength cutoff of the photoresponse comes about because the values of α for short wavelengths are very large ($\sim 10^5 cm^{-1}$) and the radiation is absorbed very near the surface where the recombination time is short so they recombine before they are swept out. The long wavelength cutoff is established by the energy gap of the semiconductor since for longer wavelengths than the cutoff λ_c, α is too small for appreciable absorption. The cutoff λ_c is equal to h/E_g where h is Planck's constant and E_g is the energy gap for a particular semiconductor.

Figure 3.8 [25] shows the spectral response of the photodiode [PIN10UV]. The responsivity, R, is defined as the signal current out of the photodiode over the input light intensity for a particular wavelength. Figure 3.7b [11] shows the attenuation coefficient as a function of x-ray wavelength for gold, silicon and beryllium. In the soft x-ray region (5-20 Å), the linear absorption coefficient of silicon as shown in Fig. 3.7b comparable to the values shown in Fig. 3.7a; therefore, the photodiode can be used as an x-ray detector where, for a particular wavelength in the soft x-ray region of interest, the responsivity R has the value that corresponds to the optical wavelength R with the same absorption coefficient as the x-ray wavelength. For the x-ray wavelength of interest (5-15 Å) all of the absorbed energy produces carrier pairs since the absorption is accomplished by photoelectric emission (Chapter II).

Figure 3.9a is a schematic of a Schottky barrier PIN photodiode, Fig. 3.9b shows the energy band diagram of a metal-semiconductor barrier, and Fig. 3.9c shows a band-to-band excitation of electron-hole pairs ($h\nu > E_g > q\phi_{Bn}$ where E_g is the energy gap, hν is the energy of the incoming

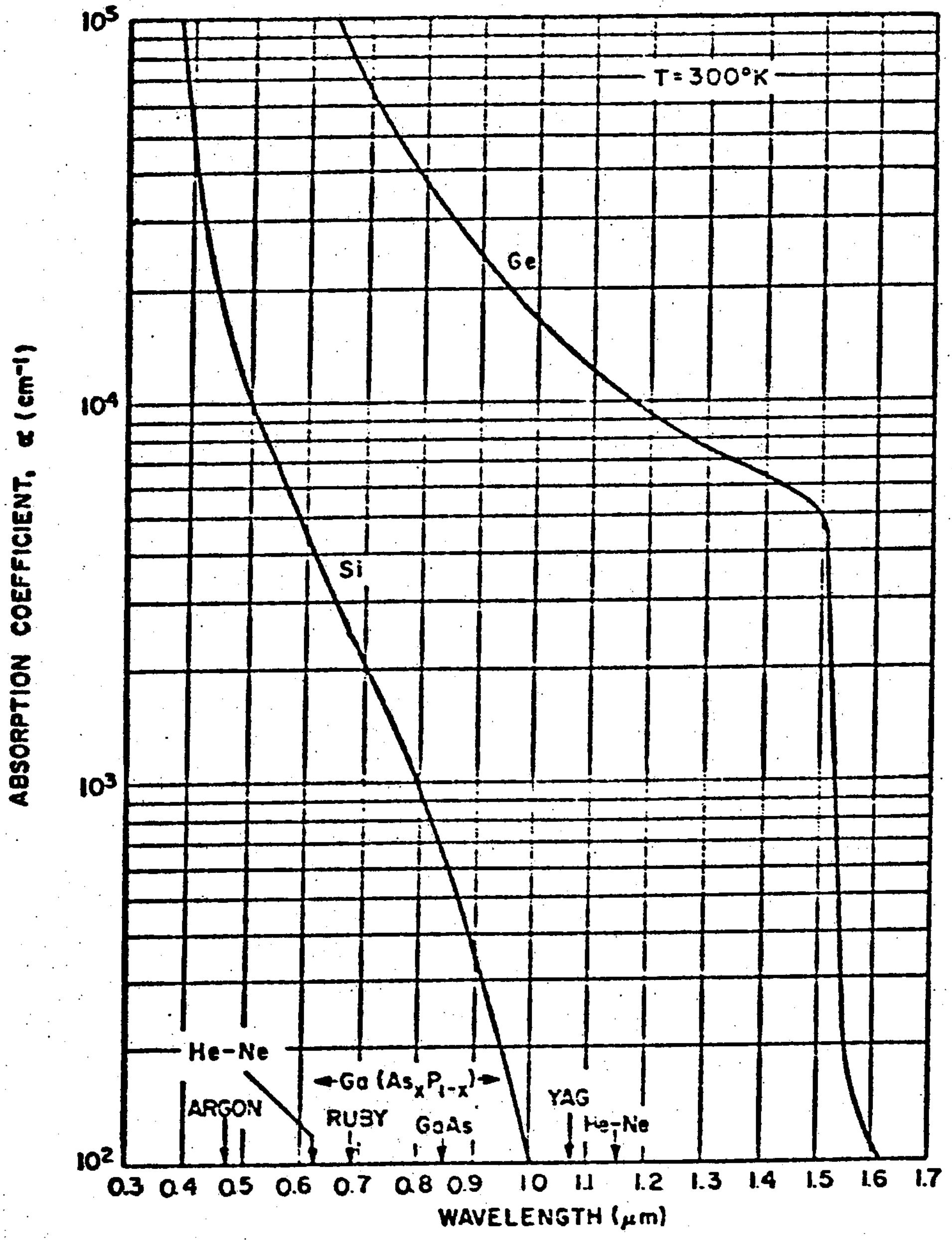

Fig. 3.7a. Absorption coefficient versus wavelength for Ge and Si at 300°K.

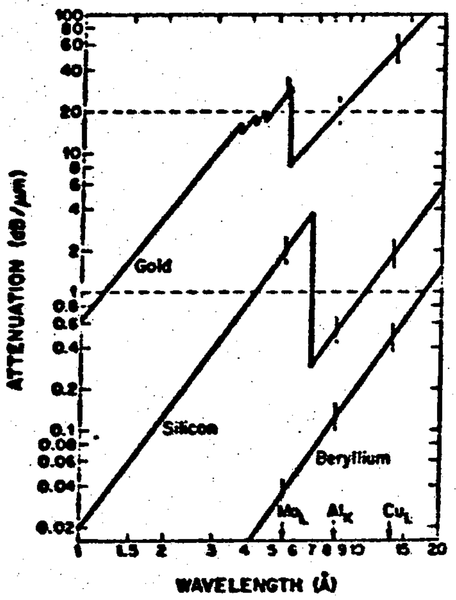

Fig. 3.7b. Attenuation coefficient vs. wavelength for gold, silicon and beryllium.

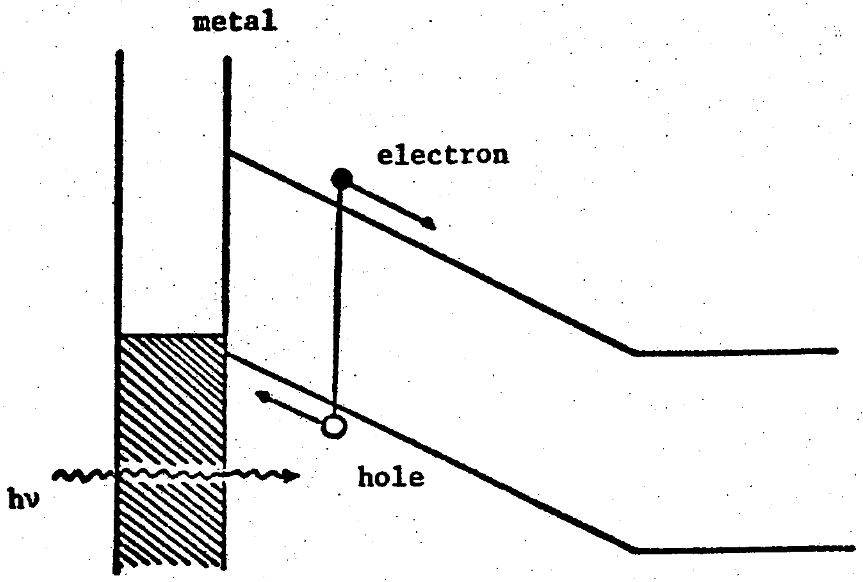

Fig. 3.9c. Band-to-band excitation of electron-hole pairs.

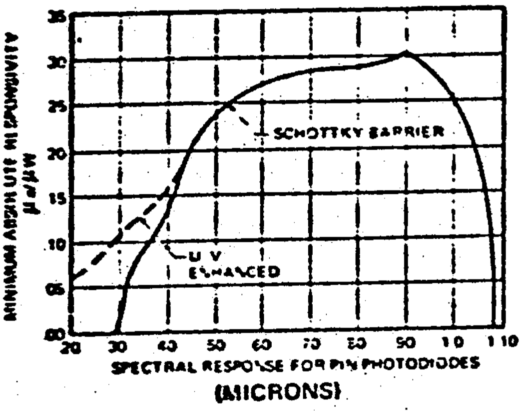

Fig. 3.8. Responsibility of the PIN10UV photodiode.

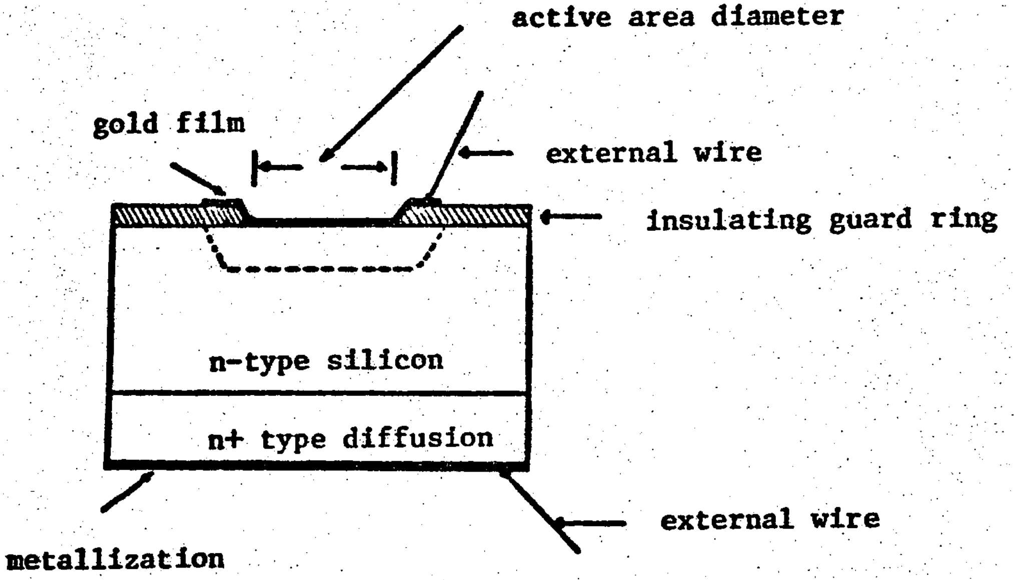

Fig. 3.9a. Schematic of a Schottky barrier PIN photodiode.

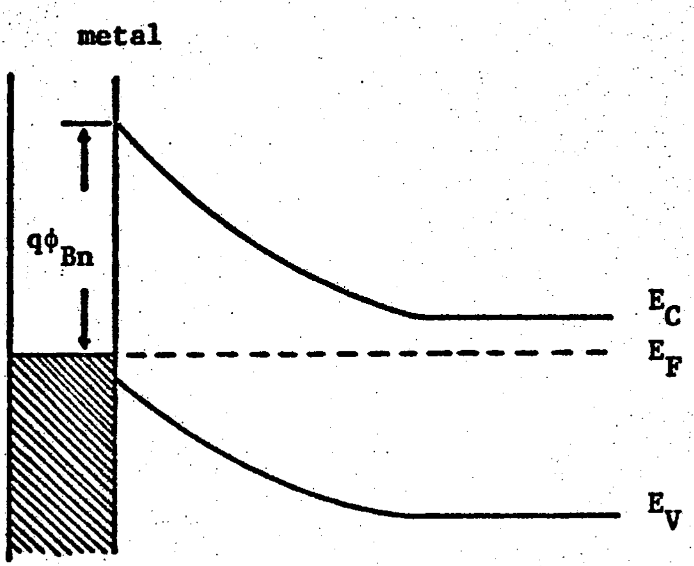

Fig. 3.9b. Energy band diagram of a metal-semiconductor barrier.

photon and ϕ_{B_n} is the Schottky barrier height on the n-type semiconductor).

For the case depicted in Fig. 3.9c, the general characteristics of the diode are very similar to those of a PIN photodiode. Under steady-state conditions the total current density through a reverse-biased depletion layer is given by

$$J_{tot} = J_{dr} + J_{diff} \tag{3.2}$$

where J_{dr} is the drift current due to carriers generated inside the depletion region and J_{diff} is the diffusion current density due to carriers generated outside the depletion layer in the bulk of the semiconductor and diffusing into the reverse-biased junction. The total current density is given by [24].

$$J_{tot} = q\Phi_o \, [1 - \frac{e^{-\alpha W}}{1+\alpha L_n}] \tag{3.3}$$

where Φ_o is the total incident photon flux in photons per cm^2 per second, α is the absorption coefficient, W is the width of the depletion region and L_n is the diffusion length. We note that the total photocurrent is proportional to the photon flux density.

3.2.2. Detector System

The Schottky barrier PIN photodiode is used in combination with a FET input operational amplifier (signetics NE 536) and this combination constitutes the x-ray detector system. Figure 3.10a shows the hookup configuration used. There is no reverse bias applied to the diode (V_B=0). The 1-V characteristics of this hookup are those of the photovoltaic region [25]. In order for the photodiode response to be linearly dependent on the input x-ray intensity when operated in the photovoltaic

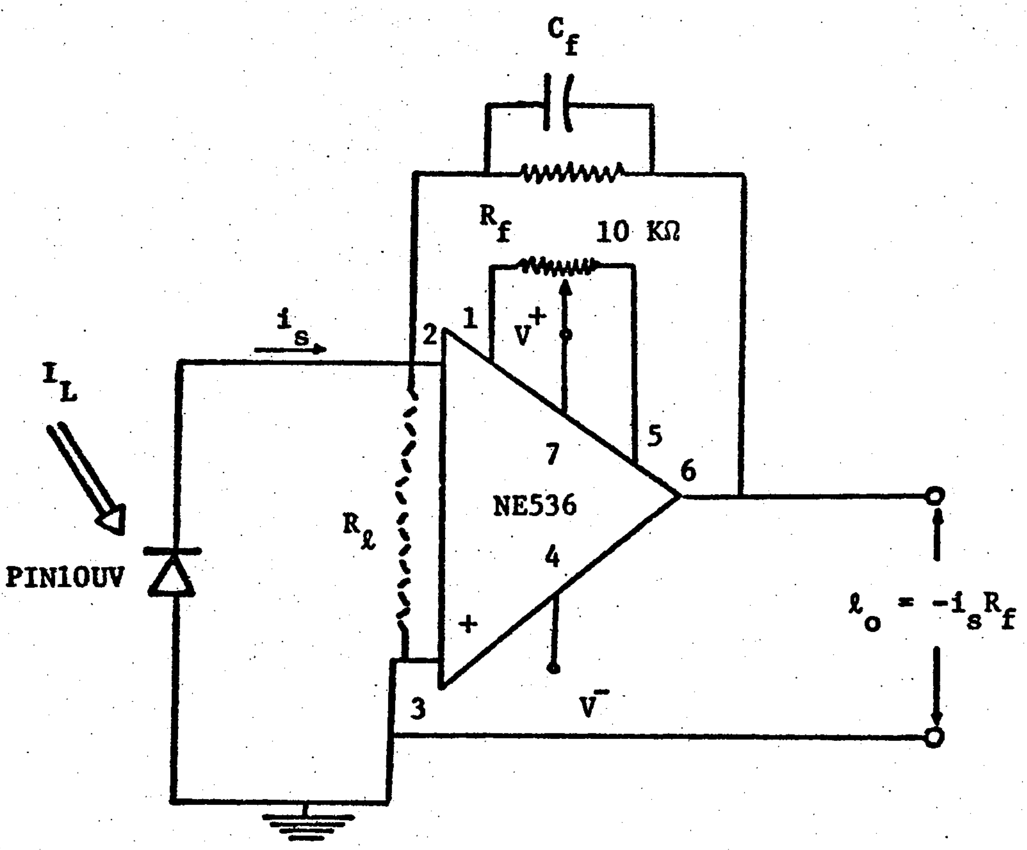

Fig. 3.10a. Hookup configuration of the photodiode with the operational amplifier

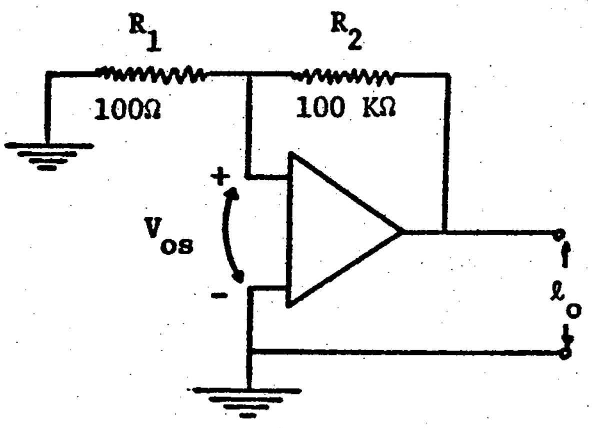

$$\ell_o = -\frac{(R_1+R_2)}{R_1} V_{os}$$

$$V_{os} = -\frac{\ell_o}{1001}$$

Fig. 3.10b. Input offset voltage test circuit.

region, the load resistance R_ℓ should be as small as possible. R_ℓ is given by R_f/A where R_f is the feedback resistance. For $R \leq 10$ ohms, R_f should be less than or equal to 1 MΩ. The linear relationship between the signal current out of the photodiode and the output x-ray intensity is given by

$$i_s = RI_L \tag{3.4}$$

where R is the responsivity of the photodiode in amperes per watt, and I_L is the input light intensity in watts.

The voltage out of the opamps is the product of the current in the feedback loop and the feedback resistance R_f. Since the open loop gain A is much greater than 1, the feedback current and input signal current are equal, and the opauys output voltage is

$$e_o = i_s R_f \tag{3.5}$$

If we combine (3.4) with (3.5) we get

$$e_o = RR_f I_L \tag{3.6}$$

To adjust the output offset voltage to zero, a 10 kΩ potentiometer is connected to the opamp between points 1 and 6. V^+ and V^- are +15 and -15 volts respectively. Figure 3.10b shows the hookup for the input offset voltage (V_{os}) test circuit used to minimize it. Its value is negligible. The feedback capacitor C_f in parallel with the feedback resistance stabilizes the circuit and lowers the noise by rolling off the high frequency response at $1/2\pi R_f C_f$.

3.2.3. X-ray Intensity Meausrements

Figure 3.11 shows the x-ray detector set up in the vacuum system

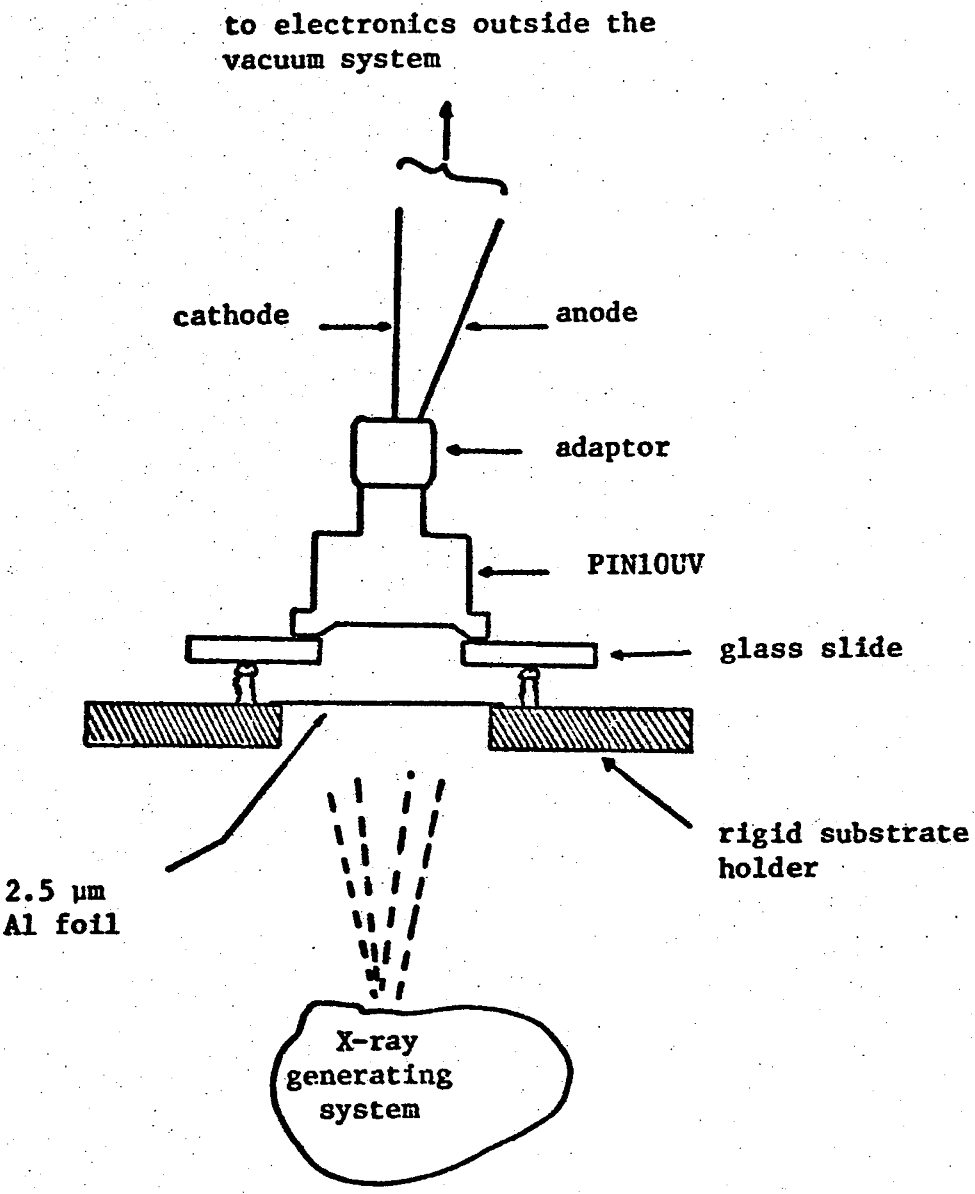

Fig. 3.11. X-ray detector setup.

for x-ray detection and measurement. The reason for use of both the thin aluminum foil and the thicker one surrounding the diode is to prevent light from reaching the detector and generating current. Light is produced both by the filament of the electron gun and, in some cases, by luminescence in samples and particles exposed to electron or x-ray bombardment. The later case was verified optically. Furthermore, the thin aluminum foil acts as a shield for backscattered electrons that might cause damage to the diode; however, the above was not adequate enough in shielding the light completely.

A copper target was used for our measurements. The accelerating voltage was kept at 7.6 kV. This is below the threshold for the excitation of copper K_{α} radiation (8.027 keV). The value of R_f is 98,470 ohms and a typical value of 150 Å for the fold layer of the diode active region was assumed [25]. The distance d between source and detector was 9.8 cm ($\pm$1mm).

Figure 3.12 is a plot of e_o (the opamp output voltage) and the cathode ray current. During measurements the vacuum was kept at 2×10^{-5} Torr. For zero cathod ray current, the background output voltage was .0179 volts. We notice the linearity of the relationship between output voltage and cathode ray current. This follows since, for a constant accelerating voltage, the total power of the x-ray beam due to the continuous spectrum is linearly dependent on the electron-beam current (Eq. (2.6)) and the same holds true for the total energy of the characteristic line ($Cu_{L_{\alpha}}$ at 13.3 Å) (Eq. (2.26)). A linear regression was performed on the data and the coefficient of determination was calculated to be 0.99 where 1 denotes a perfect fit.

In order to be able to discriminate between the power input due to

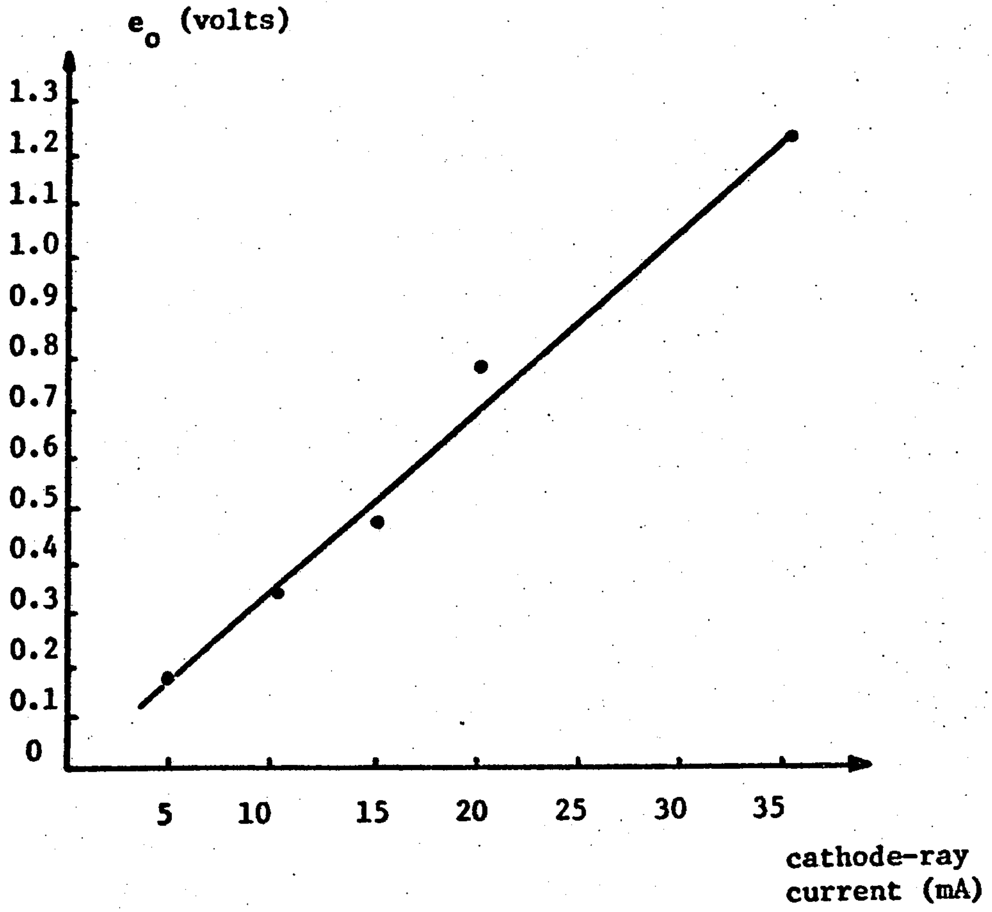

Fig. 3.12. Plot of operational amplifier output voltage vs. electron-beam current.

the continuous radiation and that of the characteristic line, the continuuous spectrum profile should be known so that different absorption of various wavelengths in the thin aluminum foil and the gold layer can be taken into account. The diode should also be calibrated against an NBS standard however, that doesn't remove the requirement of accurately measuring the continuous spectrum.

For a first-order approximation we assume the following:

1. The total transmitting factor (gold + aluminum foil) and the diode responsivity for the whole continuous spectrum are equal to the ones corresponding to the Cu_{L_α} characteristic line (13.3 Å).

2. No loss of input electron-beam energy due to backscattered electrons.

3. The target reabsorbtion factor is taken equal to 1, and isotropic angular distribution for the continuous radiation.

The value of the quantum efficiency for the Cu_{L_α} line (13.3 Å) is 1.35×10^{-4} quanta per electron per steradian [26]. The total calculated power reaching the detection is $4.4086 \times 10^{-4}/d^2$(W) for a 5 mA cathode ray current. The detection reading is $3.9063 \times 10^{-6} \frac{W}{cm^2}$. From those values we calculate d to be equal to 10.62 cm. Even though this value of the distance between source and detector is very close to the actual one, it has to be accepted with reservations.

There was no noticeable change in diode sensitivity with time. The x-rays used were too soft to cause any significant radiation damage to the detector.

A 50 Å change in the gold thickness will increase the signal current less than 8%. The overall sensitivity is approximately 30000 V/W.

In conclusion, the x-ray detector is a good indicator of relative exposure dose changes as a function of fluctuations in electron-beam accelerating voltage, changes in beam current, beam location on the target and the distance between source and substrate holder.

CHAPTER IV

MASK FABRICATION

4.1. Introduction

A very important step for x-ray lithography is the fabrication of the absorbing mask pattern to be replicated on an x-ray semitransparent membrane. In this chapter we give the actual steps in fabricating x-ray masks in sufficient detail so that the process could be easily reproduced. A summary of steps in outline form is given at the end of the chapter.

To date three kinds of membranes have been used as mask substrates. Thin silicon membranes [17][27], mylar membranes [28] [29] and aluminum-oxide membrane [12][30]. A schematic of the three different mask-membrane combinations is shown in Fig. 4.1. For our mask we chose the thin silicon membrane for the following reasons:

1. Good dimensional stability and sturdiness of the membrane. This is of paramount importance when distortion of the gold grating mask pattern might be particularly important in incorporating a replicated grating (in PMMA) into a standard optical or integrated optics device.

2. Fabrication processes and equipment peculiar to our laboratory, are compatible with silicon technologies.

3. For optimum exposure time when the $A\ell_{k_\alpha}$ (8.34 Å) line is used, the thin silicon membrane is the best choice.

The fabrication steps of x-ray masks by placing gold patterns on thin silicon membranes have been described by McCoy and Jullivan [27], and by Cohen et al. [31]. Here we describe the fabrication process used in our laboratory and, in particular, the steps that differ from those described elsewhere [27][32].

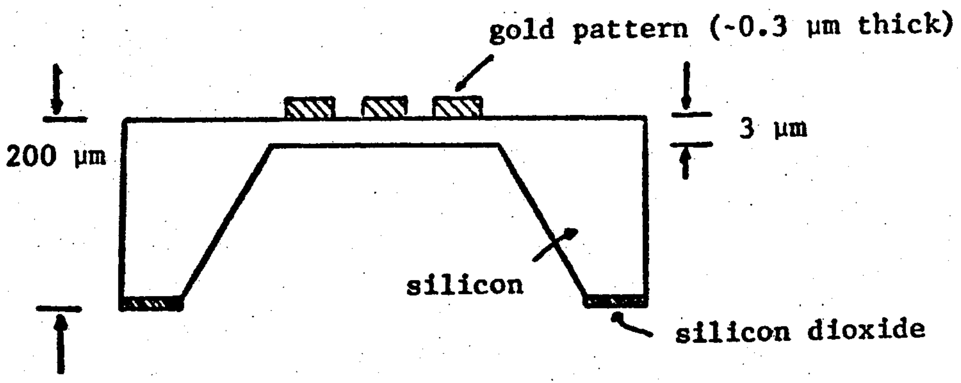

Thin silicon membrane mask

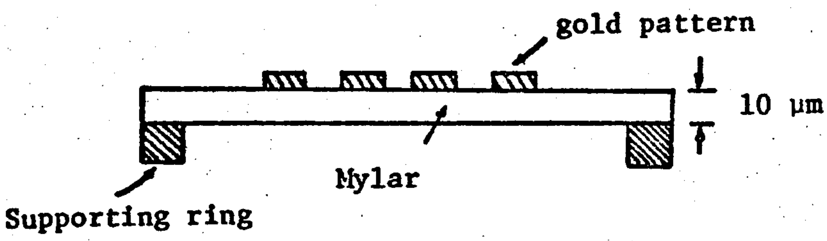

Mylar mask

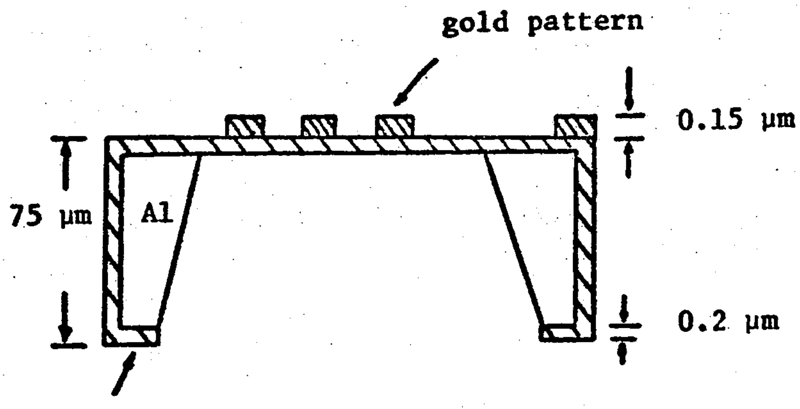

Aluminum oxide mask

Fig. 4.1. Schematic of three different mask-membrane combinations.

4.2. Initial Processing

4.2.1. Initial Wafer Preparation

The wafers used for mask fabrication were obtained commercially with the following specifications:

Diameter:	1-1/4 inches
Resistivity:	4.8-7.2 ohms-cm
Flat width:	.25-.5 inches
Orientation:	<100>
Thickness:	.008-.012 inches
Doping:	phosphous n-type

Polished one side

The wafer was cleaned as follows:

1. Degreasing by dipping in 60°C trichloroethylene (TCE) for 12 minutes. This removes gross organic contaminants. Upon removal from the hot TCE bath, the wafer is immediately immersed in acetone for 2 minutes. The wafer is then rinsed with dionized (Dl) H_2O for 1 minute.

2. The wafer is then immersed in a 75°C solution of 5 parts H_2O, 1 part NH_4OH and 1 part H_2O_2 for 12 minutes. This solution removes organic contaminants. Upon removal the wafer is rinsed in DI H_2O for 1 minute. At this point the wafer should be hydrophylic.

3. The wafer is then immersed in a 75°C solution of 6 parts H_2O, 1 part HCL and 1 part H_2O_2 for 12 minutes. This solution removes inorganic contaminants and metal traces [32]. The wafer is rinsed in DI H_2O upon removal from the solution for 1-1/2 minutes. It should be hydrophylic at this stage. It is then blown dry with N_2.

A thermal oxide is grown in a wet atmosphere in an oxidation furnace.

The oxidation temperature is 1100°C. A flow of .4 lit/min of O_2 is introduced into the furnace through an H_2O bubbler after the furnace temperature has stabilized. The wafer is introduced into the furnace 10 minutes after the initiation of the O_2 flow. A 1-1/2 hours of oxidation results in a .8 μm thick layer of SiO_2 on both sides of the wafer. This is verified optically with the thermally grown oxide color chart.

4.2.2. Oxide Striping

The oxide layer on the front surface of the wafer has to be removed next. The oxide will mask the back surface during a subsequent boron predeposition. The oxide can be removed by photoresist method as described by Huang [33], or with a cotton swab, or with a wax technique. We briefly describe the swab technique and in more detail the wax technique.

The swab technique consists of depositing droplets of concentrated HF on the center of the wafer front surface and gradually with a circular motion cover the surface with a layer of HF. Care should be taken not to cover the edges of the wafer or else there is a possibility of HF attacking the back surface oxide layer. The wafer is then rinsed in DI H_2O. If the oxide has been etched the surface will be both hydrophobic and HF-phobic. The main disadvantage of this approach is the possible scratching of the surface with the swab.

The steps involved in the oxide removal with wax technique are the following:

1. Place a glass slide on a hot plate and touch a stick of black wax to the slide until it melts and coats a large area of the slide.

2. Place the wafer, back side (unpolished) facing the molten wax layer, on the wax. Press the edges slightly with a cotton swab and

immediately slide the wafer parallel to the slide surface and off the slide.

3. Visually check if the back surface is coated completely. Let dry for 15 seconds and then immerse in concentrated HF. Complete removal of the oxide takes place in less than 2 minutes. Rinse in DI H_2O.

4. Immerse the wafer in a beaker with TCE which is agitated by an ultrasonic cleaner. This will remove the wax from the back surface.

The wafer is again cleaned as in 4.2.1. After the recleaning, the wafer is ready for a boron predeposition.

4.2.3. Boron Predeposition and Drive-in

Boron predeposition occurs in an open tube furnace under the following conditions:

Temperature: 1100°C

N_2 flow: 1.3 ℓ/min

O_2 flow 13 cc/min

B_2H_6 flow: 260 cc/min.

The flow of the gases was started at least 15 minutes before the wafer was introduced into the furnace so that the gas atmosphere stabilized. The wafer was placed flat on a quartz boat, polished side facing up. This is so that a more even deposition occurs on the front surface. The predeposition takes 6 hours. At the end of the predeposition time the wafer is slowly removed from the furnace.

The large boron surface concentration ($\geq 7\text{x}10^{19}\text{cc}^{-1}$) coupled with field aided diffusion [34] and enhanced diffusion by induced lattice strain [35] results in a boron distribution which is not represented as a complementary error function but has the profile shown in Fig. 4.2 [35].

The long predeposition time leads to layers of different composition

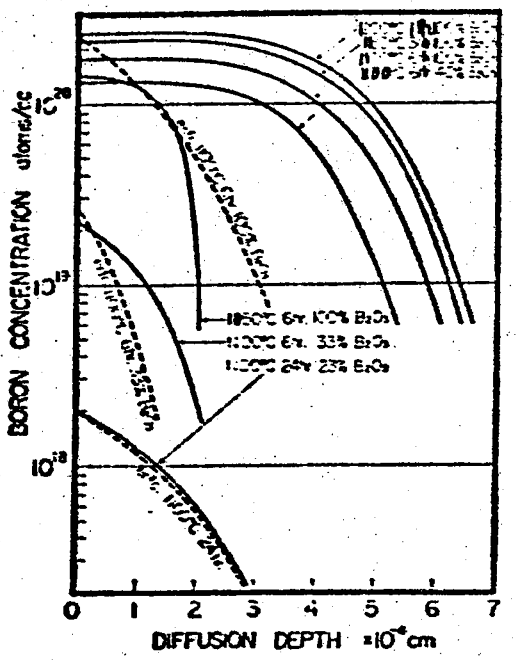

Fig. 4.2. Concentration distributions of boron.

on both the front and back surface of the wafer. On the front surface of the wafer there exist a Si-B interface on top of the Si surface and a silicon glass-boron glass layer on top of the Si-B phase. On the back surface, a Si-B glass layer exists.

In order to remove those layers, a low temperature oxidation and drive-in was done at a temperature of 350°C for three hours under the same conditions as those of the initial oxidation in 4.2.1.

Removal of the layer takes place upon immersion of the wafer in concentrated HF for 6 minutes. Again the surface of the wafer should be hydrophobic upon complete removal of the oxide and Si-B phases.

4.2.4. Gold Deposition

A thick film of SiO_2 was first sputter deposited on the undoped surface of the wafer as follows. The wafer was placed at the center of the sputtering system substrate holder on top of a glass slide. Centering provides for the most uniform film and protection of the front surface from possible damage by the roughness of the substrate holder plate surface. The system was pumped down to $3x10^{-7}$ Torr. This low pressure assures a certain degree of cleanliness even though extreme cleanliness is not very important for this phase of the mask fabrication process. Argon was then introduced to the system at a pressure of $6-8x10^{-3}$ Torr. Before the actual sputtering process was initiated, the system was left with argon flowing for 15 minutes in order that any residual gases would be flushed. A note of caution: Usually a mixture of both argon and oxygen is used when sputtered deposition of SiO_2 is desired [36]. This prevents the deposition of a mixture of $SiO-SiO_2$ instead of SiO_2, where the SiO is rather difficult to etch [37]; however, we have found no difficulty in etching sputter deposited oxide films when only argon was introduced during the actual sputtering. Sputtering takes place under the following conditions:

Forward power:	320 watts
Reflected power:	maximum (~3-4 watts)
Target Bias:	2120 volts.

After two hours of sputtering, the thickness of the film obtained is around 12000 Å. For ultra-clean and uniform films the following procedure should be followed:

1. Ten minutes before sputtering on the wafer, sputter on a dummy substrate. This cleans the SiO_2 target from contaminants and during this brief period the sputtering parameters stabilize.

2. After one hour of sputtering (for a total of two hours of sputtering), stop the sputtering and rotate the wafer. Repeat the previous steps for the remaining hour. This prevents pinholes in the oxide and also results in a more uniform layer [23].

A 1000 Å-1500 Å SiO_2 film is sputter deposited on the doped surface of the wafer next. The purpose of this film is to provide an interface between the silicon surface and the NiCr-Au layer to be deposited next.

A thin layer (~300 Å) of nichrome is deposited on the doped surface of the wafer by evaporation. The evaporation is done when the vacuum system has reached a pressure of 4×10^{-7} Torr. This thin NiCr layer is used for adhesion during the subsequent gold evaporation.

Under the same vacuum conditions, a 2000 Å thick Au film is deposited by evaporation. It is very important that the wafer be at least 20 cm away from the evaporation source; otherwise, the gold film deposited has a dull and frosty appearance. Occasionally globules of gold (25-50 μm) appear on an otherwise very good quality gold surface. It is very important to have a very flat gold film for good contact between mask and resist-substrate during an x-ray exposure.

Glass slides which were used to cover remaining openings of the evaporation chimney and have a deposited gold film on them are kept in order to be used later as monitors.

4.3. Holographic Grating Fabrication

Gratings are produced interferometrically on the gold layer via photoresist [3]. The use of a helium-cadmium laser (λ=3250 Å) was preferred instead of an argon laser (λ=4880 Å) because gold is much less reflective at 3250 Å than at 4880 Å. Table 1 [38] shows the reflection coefficient of gold for various wavelengths. Highly reflective substrates create standing waves in the photoresist with substantial broadening of the lines and appearance of standing-wave effects [39].

The photoresist used for our exposure was Shipley AZ1350J. It was thinned to a mixture of one part thinner (Shipley AZ thinner) - one part photoresist at full strength. It was not found necessary to filter the solution. The initial preparation of the wafer for subsequent holographic exposure is as follows:

1. Blow with N_2. This will remove dust particles on the polished surface of the wafer. Place the wafer on the spinner head.

2. Flood the wafer with the 1:1 mixture of the photoresist. Spin for 30 seconds.

3. The following rpm are used: 5000 rpm and 4000 rpm. The first results in a photoresist layer thick enough to be suitable for the

Metal	Wave-length, µm	Index of refraction n	Extinction coefficient k	Reflectance calculated
Gold, evaporated	0.140	1.357	1.070	0.1899
	0.145	1.386	1.089	0.1941
	0.150	1.419	1.102	0.1967
	0.155	1.450	1.108	0.1978
	0.160	1.463	1.106	0.1971
	0.165	1.512	1.093	0.1941
	0.170	1.519	1.070	0.1888
	0.175	1.500	1.070	0.1886
	0.180	1.470	1.085	0.1921
	0.185	1.442	1.107	0.1976
	0.190	1.427	1.135	0.2049
	0.195	1.424	1.170	0.2138
	0.200	1.427	1.215	0.2251
	0.450	1.40	1.88	0.397
	0.500	0.84	1.84	0.504
	0.550	0.331	2.324	0.815
	0.600	0.200	2.897	0.919
	0.650	0.142	3.374	0.955
	0.700	0.131	3.842	0.967
	0.750	0.140	4.266	0.971
	0.800	0.149	4.654	0.974
	0.850	0.157	4.993	0.976
	0.900	0.166	5.335	0.978
	0.950	0.174	5.691	0.979
	1.000	0.179	6.044	0.981
Gold, crystalline	0.4400	1.5778	1.9077	0.3863
	0.4600	1.4843	1.8257	0.3754
	0.4800	1.2543	1.7301	0.3787
	0.5000	0.8031	1.8180	0.5100
	0.5200	0.5264	2.1277	0.6929
	0.5400	0.3772	2.4520	0.8032
	0.5600	0.3054	2.7501	0.8692
	0.5800	0.2524	3.0106	0.9050
	0.6000	0.2113	3.2411	0.9294
	0.6200	0.1906	3.4621	0.9431
	0.6400	0.1667	3.6902	0.9555
	1.0000	0.2200	6.7100	0.9811
	1.5000	0.3600	10.4000	0.9869
	2.0000	0.5500	13.9000	0.9888
	2.5000	0.8200	17.3000	0.9892
	3.0000	1.1700	21.0000	0.9895
	4.0000	2.0400	27.9000	0.9896
	5.0000	3.2700	35.2000	0.9896
	6.0000	4.7000	35.2000	0.9896
	8.0000	7.8200	54.60000	0.9898
	10.0000	11.5000	67.5000	0.9902
	12.0000	15.4000	80.5000	0.9909
	1.0000	0.3100	5.5800	0.9823
	2.0000	0.5400	11.2000	0.9831
	3.0000	0.9300	16.7000	0.9868
	4.0000	1.4900	22.2000	0.9881
	5.0000	2.1900	27.7000	0.9887
	6.0000	3.0100	33.0000	0.9891
	7.0000	3.9700	38.3000	0.9894
	8.0000	5.0500	43.5000	0.9895
	9.0000	6.2100	48.6000	0.9897

Table 1. Optical constants of gold.

subsequent holographic fabrication of .6 μm period gratings. 4000 rpm are used when 1 μm period gratings will be fabricated.

4. Bake the wafer for 8-10 minutes in a 88°C oven. Care should be taken in not exposing the resist to light before the holographic exposure. The resist-coated wafer should be exposed no later than 48 hours.

Occasionally the photoresist film will have a spotty appearance. When this occurs, the photoresist film should be stipped by dipping in acetone for 30 seconds. Then the wafer should be rinsed in DI H_2O, blown dry with N_2 and placed under an infrared lamp for 5 minutes. After it cools down, it can be coated again following all of the previous steps

Figure 4.3 shows a schematic of the holographic exposure set up. For the Liconix 301 Laser, the total beam path lengths $\overline{OBE}$ and $\overline{OAE}$ should be to within 2 to 3 cm from each other, otherwise the quality of the gratings obtained will not be good. A filter-beam expander collimator is more desirable than the lens-iris combination. The rim of the iris diffracts the beam and the pattern is recorded on the photoresist.

The groove spacing a of a holographically recorded diffraction grating is given by

$$a = \frac{\lambda}{2n \sin \alpha} \tag{4.1}$$

where λ is the laser wavelength, α is the angle of incidence of the laser beam as shown in Fig. 4.3 and n is the index of refraction if a liquid immersion is used. Using refractive index liquids as explained by C. V. Schank and R. V. Schmidt [3], periods of the order of 1800 Å and 1000 Å can be achieved with the argon and helium cadmium lasers, respectively.

Figure 4.4 shows the diffraction grating formula [1]. The formula is given by

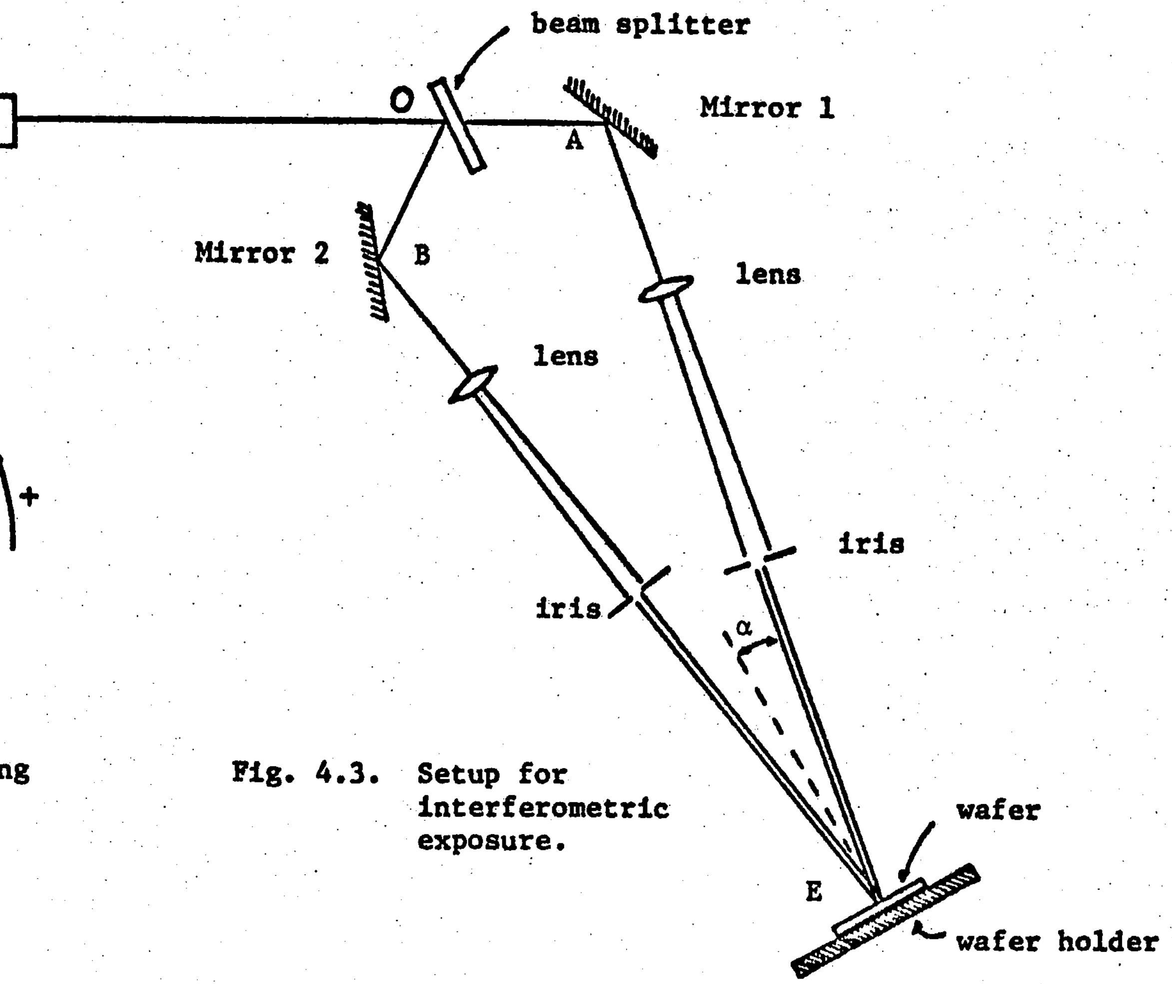

Fig. 4.3. Setup for interferometric exposure.

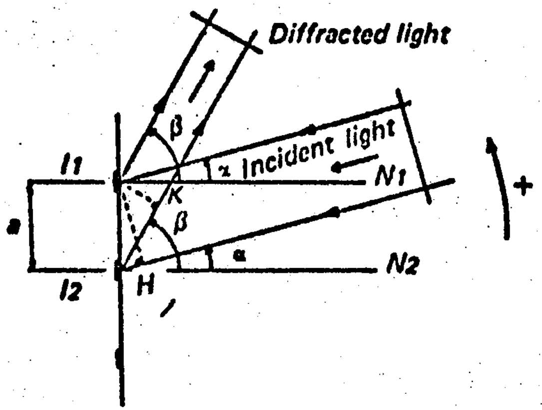

Fig. 4.4. Diffraction grating formula.

$$\sin \alpha + \sin \beta = \frac{k\lambda}{a} \tag{4.2}$$

The formula gives, for each value of α, all the possible values of β where a maximum of intensity for wavelength λ is found (one maximum for each value of k). For the shortest visible wavelength ($\lambda \sim 4000$ Å-violet) the smallest value of the grating period a for which there can be visual observation of the diffracted beam is given by

$$a = \frac{\lambda}{\sin 90^{\circ -} + \sin 90^{\circ -}} \cong \frac{4000}{2} \sim 2000 \text{ Å} \tag{4.3}$$

where $90^{\circ -}$ denotes a surface grazing angle; however, the color observable from a 3000 Å periodicity grating at a grazing viewing angle is deep purple [40]. For the periodicities of interest [.6 μm and 1 μm] the whole color spectrum is obserable and the periodicities are well within the optical microscope resolution limit. The following method is suggested for determination of the optimal exposure times and photoresist layer thickness. Due to the slowly decreasing power output of helium-cadmium laser during its lifetime exposure times cannot be quoted.

1. The resist thickness should be smaller or comparable to the grating period being produced.

2. Expose different portions of a photoresist coated test wafer for different times.

3. Develop in a 1:1 mixture of AZ1350 Developer: H_2O for 25-30 seconds. Rinse in DI H_2O to stop the developer action and blow dry with N_2. Check the wafer for diffraction under yellow light. If the grating has opened down to the gold, it will diffract much more than if it has not. Here more diffraction is more brightness. This is because the refectivity of gold, the surface of which now forms part of photoresist-gold relief

structure, at visible optical wavelengths in big (See Table 1).

When the grating is viewed under an optical microscope under complete phase contrast view field, if the grating has opened down to the gold surface, a light green to medium dark beige should be observed together with the delineation of the grating structure. If the grating has not reached the gold completely, the color observed will be brown. A dark brown color (still under phase contrast view field) denotes no grating area (or a very light resist surface perturbation) and just photoresist which covers the gold completely. In the next section, a second method for determining optimum exposure times and resist thickness will be described. This method will be also applicable to smaller period gratings.

The gratings obtained had a diameter of 6 mm and were uniform over the whole area.

4.4. Gold Gratings

The postbaking of the developed resist profile is critical for two reasons: The resist has to hold and not flow during radio-frequency (r.f.) sputter etching of the gold layer. This requires a rather elevated (postbaking) temperature. Also the preservation of the developed resist profile (a micron or submicron period grating structure) during postbaking imposes the opposite requirement, i.e. a low postbaking temperature. We chose a two-step process where the wafer is postbaked first at a low temperature (88-90°C) for 20 minutes for outgassing and immediately afterwards at a higher temperature (110°-115°C) for 30 minutes. The postbaking should be done no later than 24 hours after exposure. This is to avoid deterioration of the developed resist profile which will result in rippled line edges (and rippled, curvy lines) both during postbaking and r-f sputter etching.

Both r-f sputter etching and wet (chemical) etching have been used to produce the gold pattern on the front side of the wafer; however, due to edge resolution and undercutting of chemical etching, r.f. sputter etching is preferred over chemical etching. Figure 4.5 show a 1 μm period gold grating obtained after chemical etching. It was fabricated by dipping the wafer in concentrated aqua regia (1:3, HNO_3:HCl) and the resist profile provided the necessary masking. After the etching the photoresist was easily removed by dipping in acetone. For chemical etching, the resist pattern need only to be postbaked at 90°C for 15 minutes.

The major constraint in increasing the gold mask thickness for a better exposure contrast is the fact that the sputter etch rate of the photoresist (AZ1350J) is comparable to that of gold. During r-f sputter etching, liftoff of the resist has been observed before complete etching of the gold pattern.

For r-f sputter etching the wafer is placed at the center of the water cooled substrate electrode of the r-f sputtering system. Excessive heating of the substrate being etched is appreciable so, for a better heat conduction path between wafer and the water cooled electrode surface, gallium is spread on the back surface of the wafer (the gallium spreads and sticks much better on the SiO_2 covered backsurface than it does on a bare silicon surface) and then pressed on the electrode surface. The gallium will provide the necessary heat conduction path. This cooling is important since even with the previous postbaking process, resist lines occasionally would flow during etching. A glass slide which was partially coated with gold when it was used to cover the evaporation chimney during gold

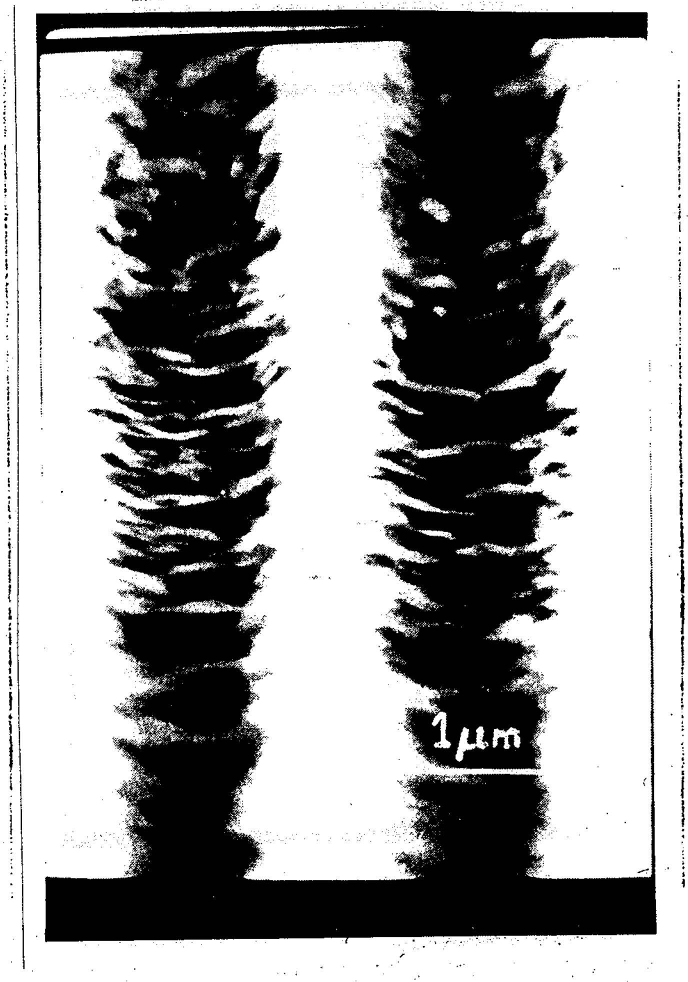

Fig. 4.5. Picture of 1 μm period gold grating with aqua regia.

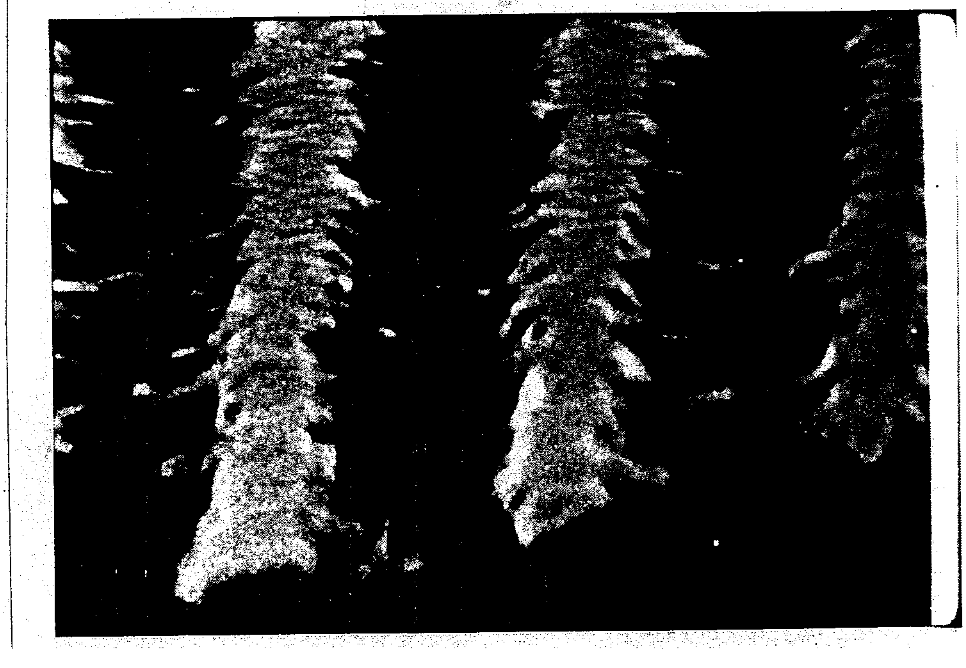

deposition, is placed next to the wafer on the electrode. It acts as an etch monitor since the thickness of the gold layer on it is almost equal to that on the wafer. Visual observation will determine when the gold has been etched.

The r-f sputtering system was first pumped down to a pressure of $5x10^{-5}$ Torr and argon at a pressure of $2x10^{-2}$ Torr was introduced in the system of least 10 minutes before actual sputter etching of the substrate. Oxygen will hasten the removal of the photoresist due to oxidation; therefore, it is desirable to have a relatively oxygen-free atmosphere. The actual sputter etching is done at low power. This prevents the resist from polymerizing, something that makes removal of the resist extremely difficult. Upon removal from the electrode (if the gallium is solidified, the wafer electrode system should be heated up with a heat gun for easier removal of the wafer) the wafer is placed with its back surface facing up. Removal of the gallium is accomplished as follows:

1. Wet the cotton tip of a swab with concentrated HCl. Touch the qallium with the wet tip. If the gallium is in liquid phase it will be instantaneously removed.

2. Small globules of gallium should be thrown off the wafer with a quick radial movement using the tip of a dry cotton swab. It is important that no gallium gets deposited on the front (gold) surface of the wafer. It will stick on the gold.

3. Rinse in DI H_2O and blow with N_2.

Removal of the remaining photoresist layer is best accomplished with a plasma asher (plasma oxidation). This system is not currently available. It is impossible to remove the resist with regular resist strippers commercially available. Partial removal of the photoresist layer is accomplished with immersion in hot acids. The process (described below) is uncontrollable to a degree and visual observation of the wafer surface during actual immersion in the acid bath is very important for immediate withdrawal of the wafer before damage is done to the pattern.

The wafer is immersed in a 5:1 freshly made solution of concentrated H_2SO_4 and concentrated H_2O_2. It is very important that the solution is thoroughly mixed before immersion of the wafer, so that concentrated H_2O_2 does not attack the surface. (The acid mixture will etch gold at spots where gallium is present). When lift off is imminent (this becomes apparent when gold starts lifting off at the edges of the wafer and swelling of gold starts in various parts of the wafer) the wafer should be immediately withdrawn from the solution, rinsed in DI H_2O and blown dry with N_2. Figures 4.6 up to 4.14 show gold grating mask patterns. Details are given under the figure captions.

The second method for determining optimum expsoure times and resist thickness (the first one was described in Section 3) again makes use of a test wafer where gratings have been fabricated holographically at various exposure times. The wafer is r-f sputter etched following the sequence of steps just described. The resist is stripped by immersion in the 5:1 solution of H_2SO_4:H_2O_2. At grating spots where the resist grating groove had not opened down to the gold surface during development, the gold surface will be unperturbed (it will reveal no etching) except if the resist grating groove was originally very close to the gold surface; however at spots where grating grooves have reached the gold surface, a gold grating will be present upon removal of the resist. SEM studies can be used to measure the opening of the gold grating.

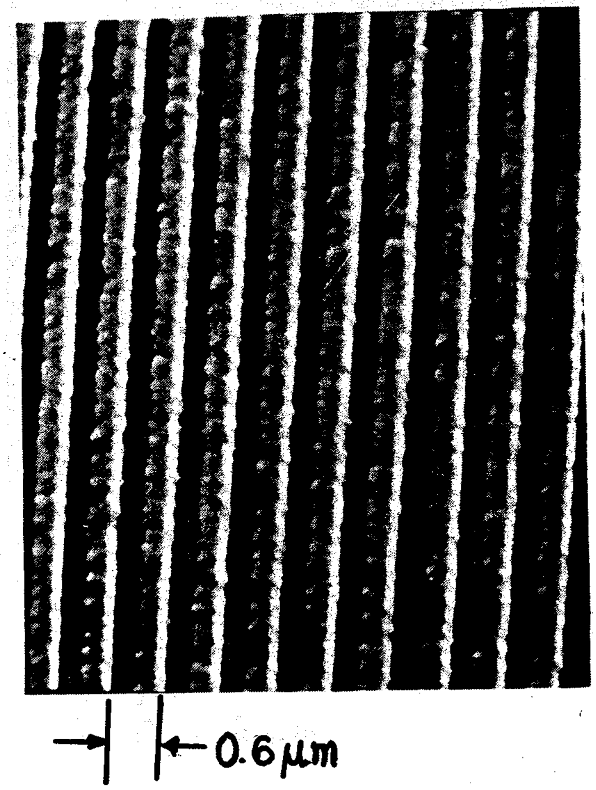

Fig. 4.6. 0.6 µm period gold grating.

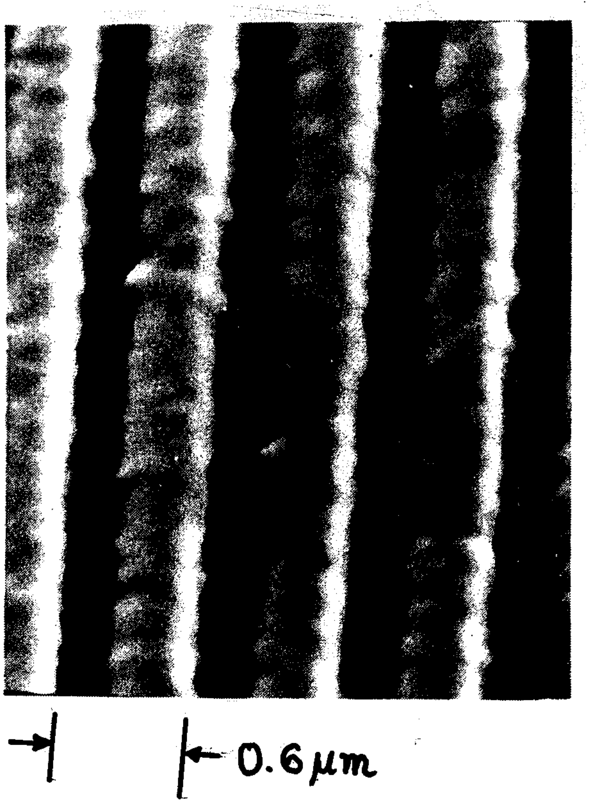

Fig. 4.7. Close up of a 0.6 μm period gold grating mask showing roughness related to developed photoresist roughness.

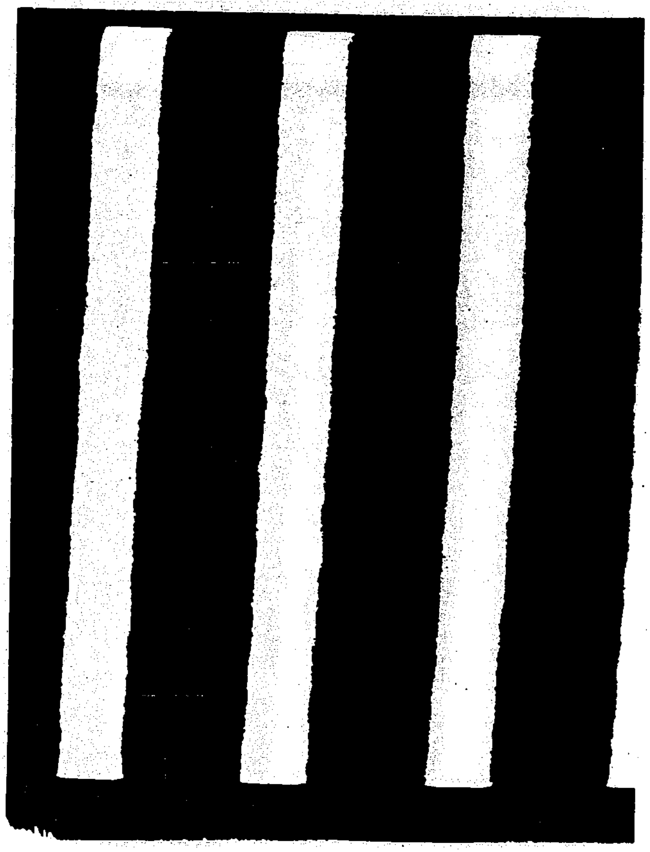

Fig. 4.8. 1 μm period gold grating mask pattern. Notice the large mask opening to period ratio.

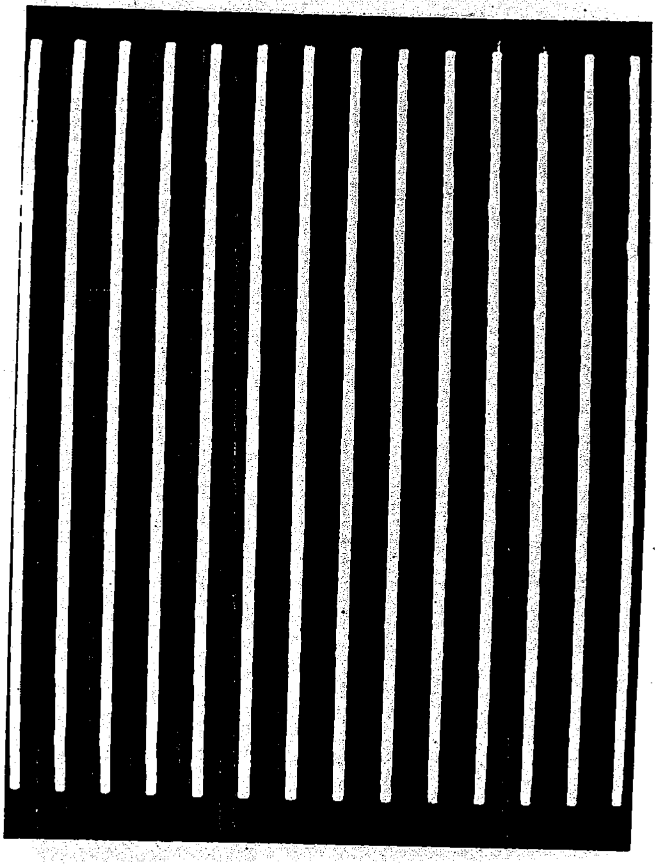

Fig. 4.9. 1 μm period gold grating mask pattern. Same mask as in Fig. 4.9 but lower magnification.

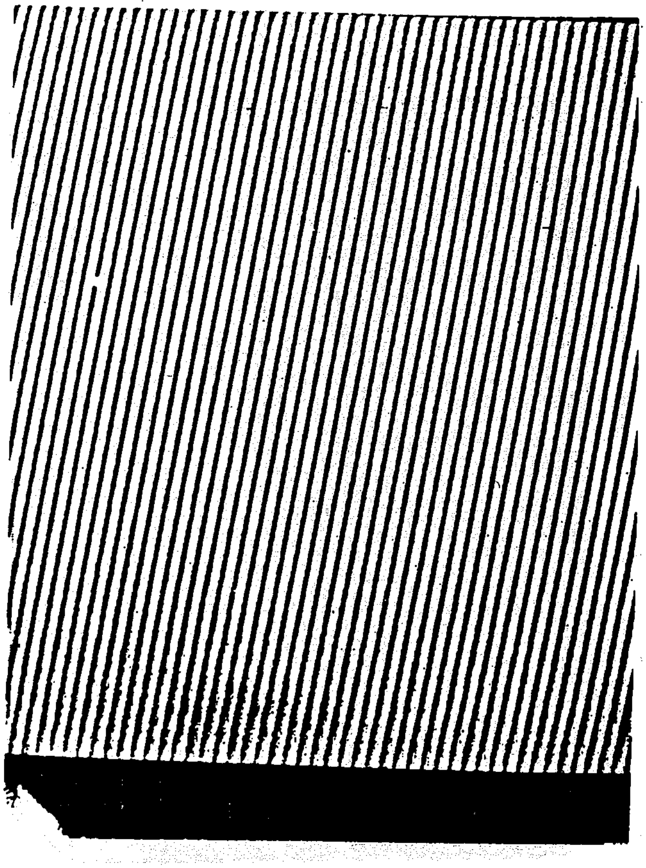

Fig. 4.10. 1 μm grating. Low magnification reveals large area uniformity. The area shown is typical of the grating as a whole. Tilt 5°.

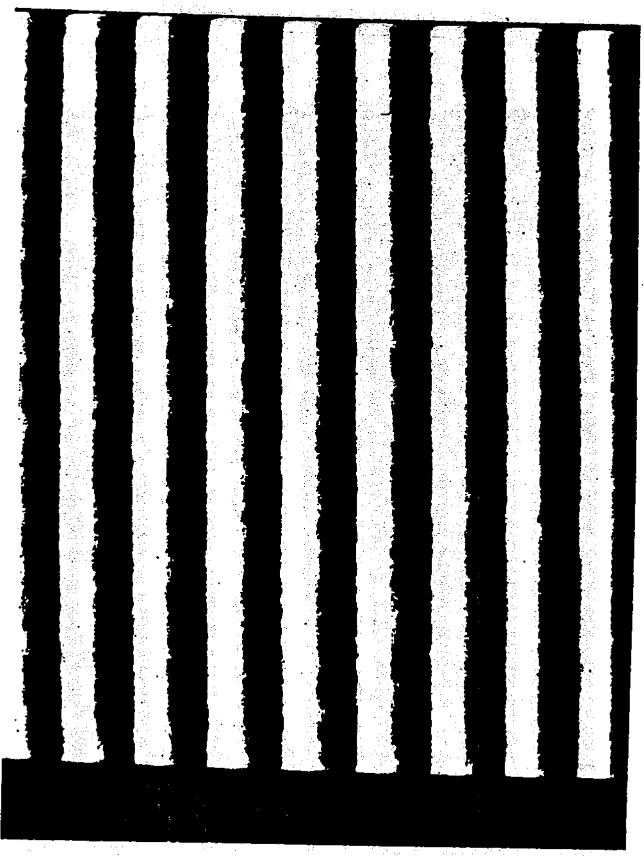

Fig. 4.11. 1 μm grating structure. Same area as in Fig. 4.10 but higher magnification. 5° Tilt.

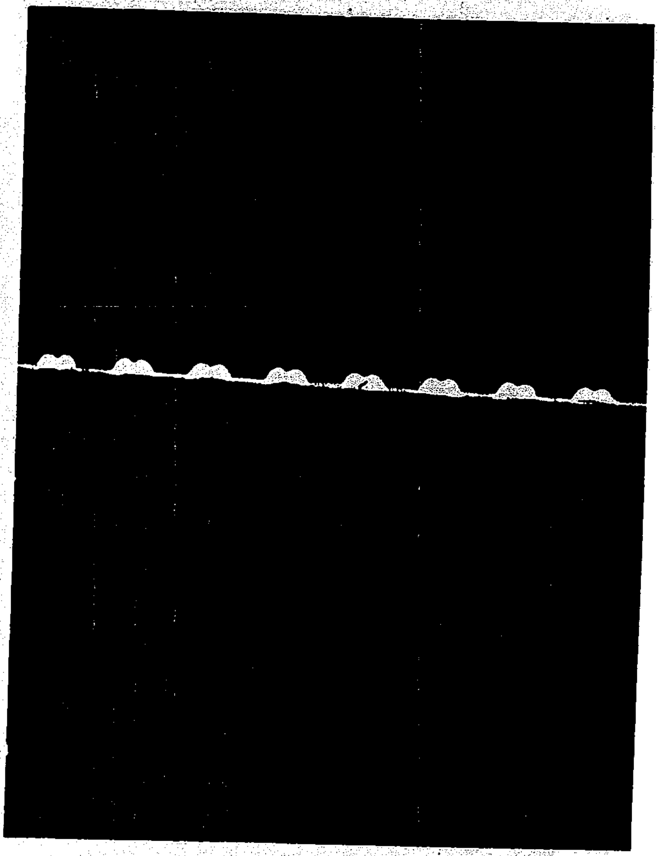

Fig. 4.12. Edge view (90° tilt) of the 1 μm period gold grating.

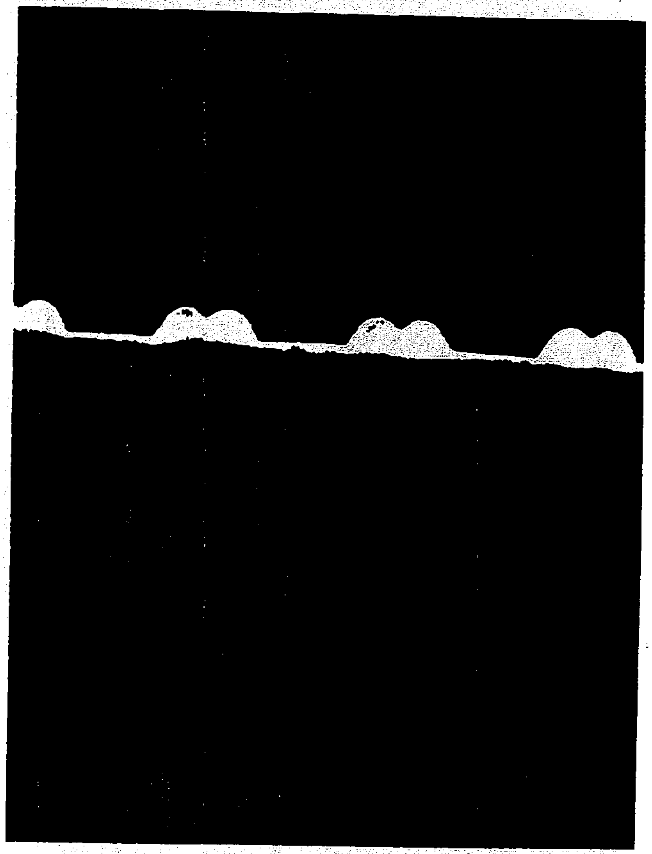

Fig. 4.13. High magnification electron micrograph of the edge view of a 1 μm grating mask pattern. For this particular mask, the mask opening is half the period. The gold thickness was measured to be 2000 Å. The depression at the center of the gold bars is most probably due to the photoresist profile after development.

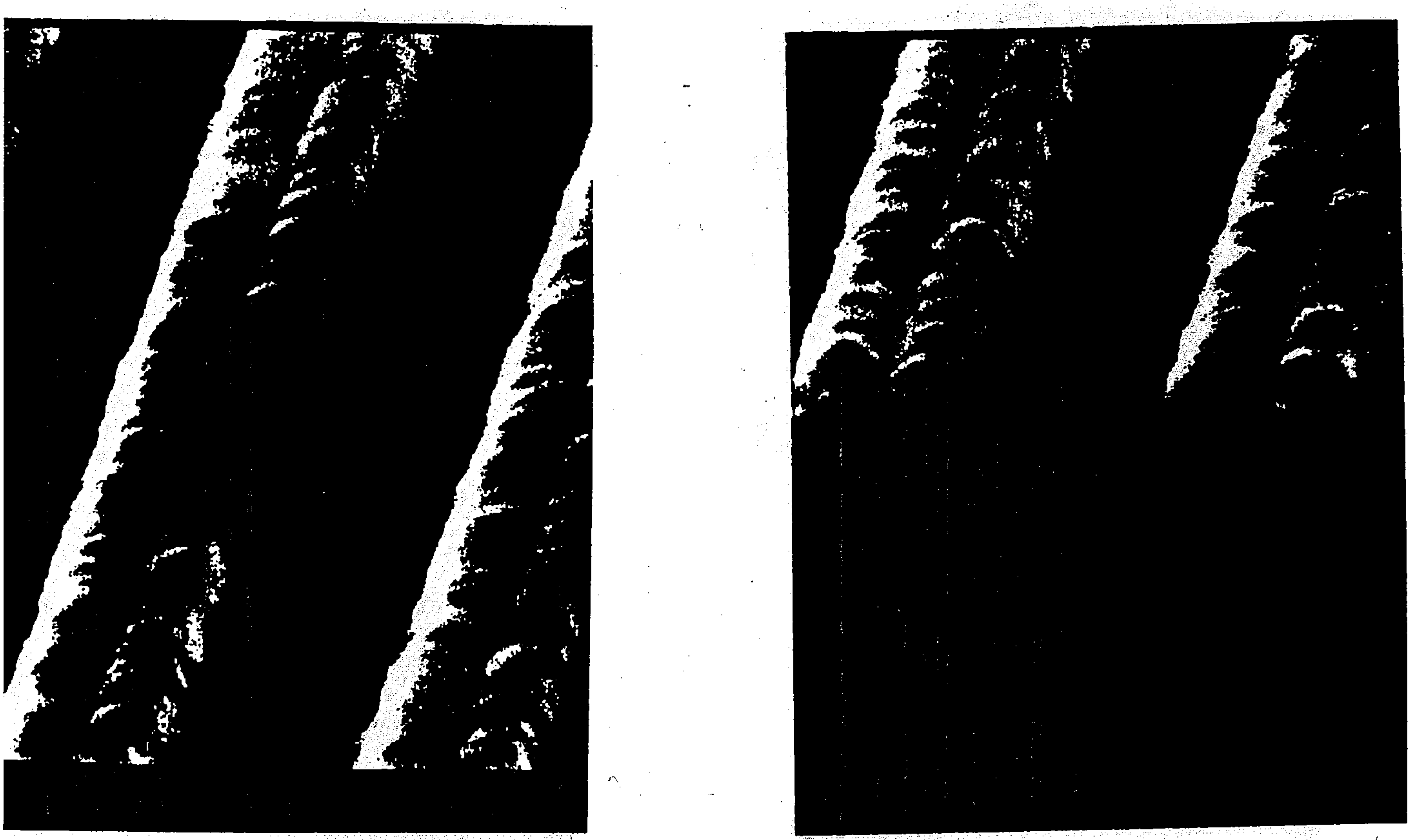

Fig. 4.14. A 72 both the
depr the edge
res

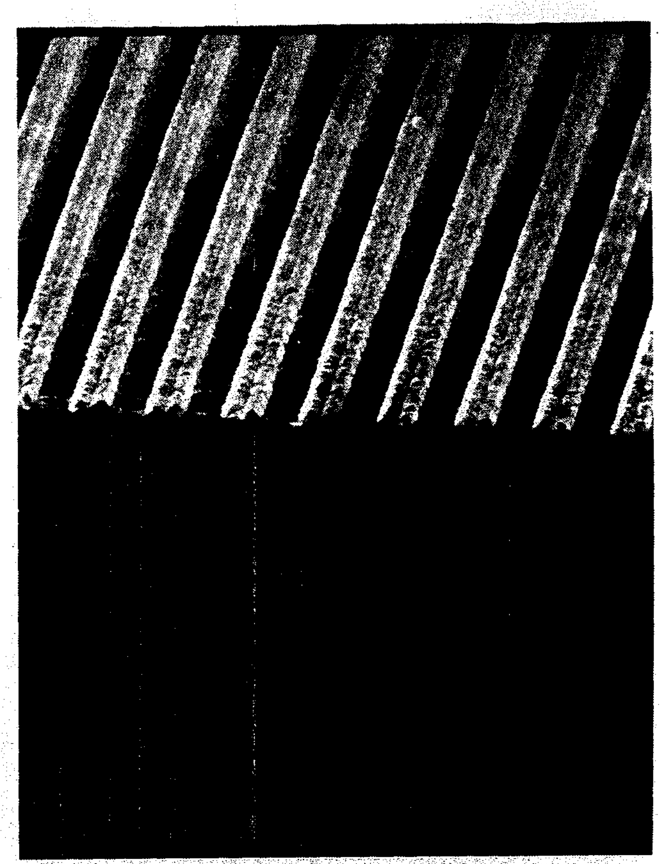

Χρυσό Φράγμα Παράθλασης 1 μm (72° κλίση)
1 μm Gold Diffracton Grating (72° tilt)

4.5. Thin-Silicon Windows

In this section we describe the fabrication process of the thin silicon membranes. The fabrication process is based on the following facts:

1. The ethylenediamine-pyrocatechol-water mixture shows preferential etching of a p^+n junction and anisotropic etching of bulk silicon [41][42]. Using a solution composed of 255 ml of ethylenediamine ($NH_2(CH_2)_2NH_2$), 120 ml of DI H_2O and 45 grams of pyrocatechol ($C_6H_4(OH)_2$) or lower concentrations but of the same ratios, the etch ratios for <111>, <110> and <100> oriented silicon are approximately 3:30:50 [41]. The mixture will etch the n-type bulk silicon and will abruptly stop at a boron concentration (p-type) of $7\times10^{+19}$ atoms/cm^3 [43]. The value of $2\times10^{+19}$ atoms/cm^3 was also reported [31].

2. The above etchant has an extremely slow etch rate for SiO_2 films (~200 Å/hour) so they are used as etching masks.

3. At a temperature of 115°C the etch rate for <100> oriented silicon is approximately 50-60 μm/hour [41]. The etch rate varies considerably with even minute changes of the mixture rations as well as with temperature as reported by R. M. Finne and D. L Klein [41] and verified experimentally. A freshly prepared solution has slightly higher etch rates than one a few hours old.

The thickness of membranes obtained can be measured with various techniques. For membranes 2000 Å thick or less, a color chart is available [33] for visual determination of the thickness. SEM measurements of the edges of broken membranes are also quite accurate. For thick membranes ($\geq$1μm) an optical interference method using the concept of the Fabry-Perot resonance observed when a light beam is transmitted through a transluscent film and the spectral output is measured, has been used to measure membrane thickness [44]. This method is accurate to ±10%. A third method which gives satisfactory results with an uncertainty of ±15% makes use of the groove and stain procedure to measure the junction depth in combination with the four-point probe technique in measuring the average resistivity $\bar{\rho}$ of a diffused layer [34]. In brief the technique is as follows:

1. A set of measurements (voltage and current) are taken using the four-point probe.

2. The junction depth is determined by grooving and staining. A set of measured values of the junction depth x_j was averaged to the value $x_{j_{av}}$.

3. For diffused layers whose lateral dimensions are large and whose width x_j is small in comparison to the spacing of the probe, the average resistivity $\bar{\rho}$ is given by [34].

$$\bar{\rho} = \frac{\pi}{\ell n 2} \frac{V}{I} x_{j_{av}} = 4.532 \frac{V}{I} x_{j_{av}} \tag{4.4}$$

To a first order approximation a "box" distribution was assumed. The "box" distribution is a valid approximation for the cases where both the boron surface concentration and the predeposition temperature are large as shown in Fig. 4.2. Figure 4.15 [34] shows the surface concentration vs. average resistivity with a box impurity distribution. C_S is the surface concentration and C_B is the bulk silicon concentration. For our predeposition time (6 hours) and temperature (1100°), the groove and stain procedure yields a value of 3.34 μm for $x_{j_{av}}$, and the four point probe measurements yield a value $\bar{\rho} = 1.178\text{x}10^{-3}$ ohm-cm. Figure 4.15 yields a value of $1.2\text{x}10^{20}$ cm^{-3} for C_S. A plot of concentration vs. depth where $x_{j_{av}} = 3.34$ μm and $C_S = 1.2\text{x}10^{20}$ atoms/cm^3 and which follows

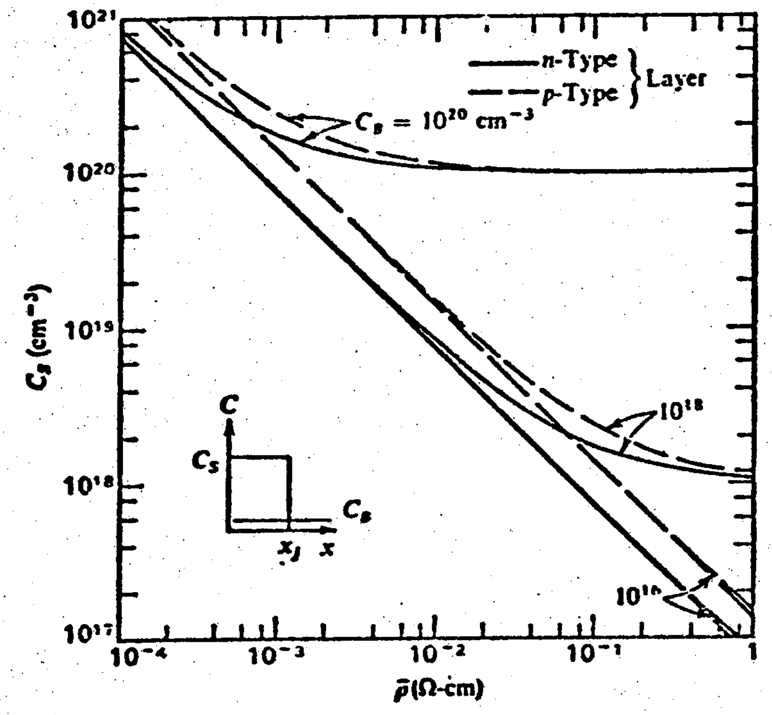

Fig. 4.15. "Box" distribution surface concentration vs. average resistivity.

approximately a "box" distribution yields a value for the membrane thickness d equal to 2.75 μm ±10%. (A boron concentration of $2\text{x}10^{19}\text{cm}^{-3}$ was assumed sufficient to stop the etching). This is shown in Fig. 4.16. Measurements made using the optical interference method indicate a membrane thickness between 2.5 μm and 3 μm.

The preferential etchant of silicon (ethylenediamine-pyrocatechol-water) will attack the gold surface of the wafer after 4 or 5 hours of continuous etching. After 5 hours the gold surface would aquire a frosty appearance which is due to swelling of the thin gold film; however, the grating lines would be literally ripped off almost immediately upon immersion in the etching solution. Before opting for the fabrication procedure described below, two alternative procedures for protecting the gold pattern during etching were examined.

The first one, proposed by Cohen et al. [31] was to use a teflon fixture so that only one side (backside) of the wafer is in contact with the etchant however, our fixture could only accommodate a certain size circular wafer (1" diameter) and it was difficult to handle a variety of wafer sizes and pieces of various shapes. Figure 4.17 is a schematic of our teflon wafer holder. The preferential ethant does attack and etch rubber, but not teflon.

Another procedure was to fabricate the thin silicon membrane first and then deposit the gold mask. The difficulty of this approach was that the handling of the wafer through the remaining process steps had to be extremely careful.

A variety of different resist and wax films were tried for protection during etching, but they were almost immediately lifted off upon immersion in the etching solution. One known material that etches very slowly is

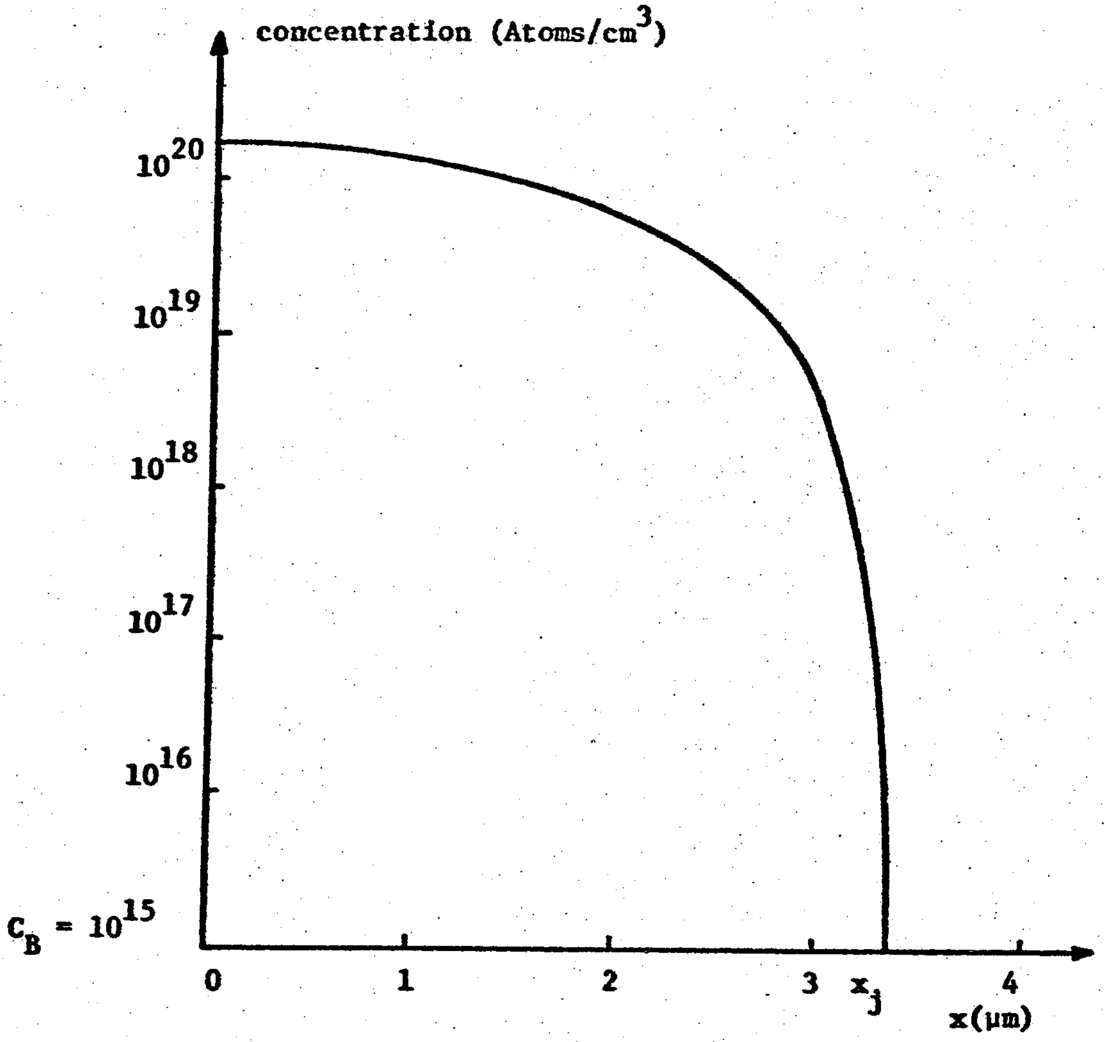

Fig. 4.16. Boron concentration vs. depth.

Fig. 4.17. Cross-section of teflon wafer holder.

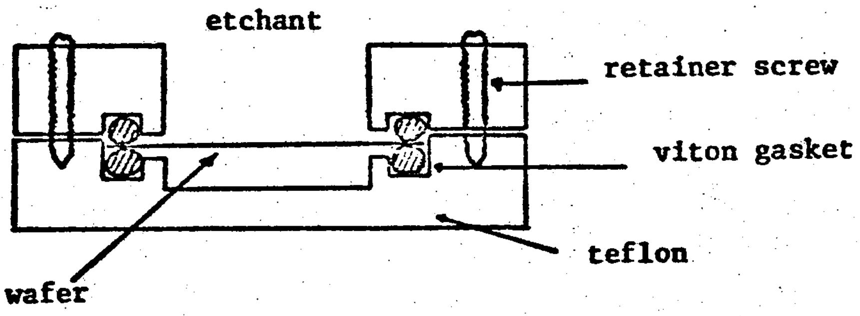

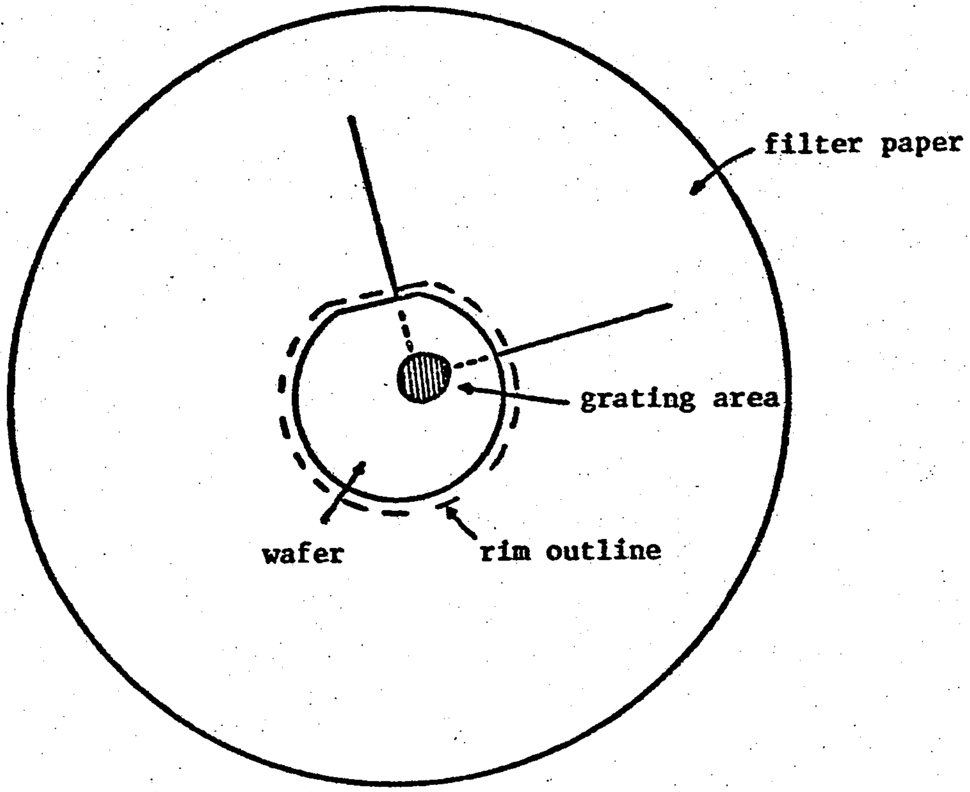

Fig. 4.18. Mask aligning scheme.

SiO_2, therefore, it was decided to use SiO_2 as a protective film. The remaining mask fabrication steps are as follows:

A. A thin film (~3000 Å) of nichrome was evaporated on the gold relief structure. This film is used as a convenient adhesive interface between gold and SiO_2. Tests indicate that nichrome etches much faster in a 1:1 mixture of concentrated $HCl:H_2O$ than it does in a 1:1 mixture of concentrated $HNO_3:H_2O$. Glass slides covering the evaporation chimney and covered with nichrome can again be used as etch monitors during a later removal of the thin nichrome film.

B. Following the nichrome evaporation, a thick film of SiO_2 (~1.2 μm) was sputter deposited on top of the nichrome film. The same procedure was used as when the SiO_2 film was deposited on the back surface of the wafer (see Section 4.2.4.). This film protects the gold pattern during the preferential etching of silicon.

C. The next step was the opening of the SiO_2 window on the back surface directly beneath the gold grating pattern. The procedure is as follows:

1. Spincoat the front side of the wafer with undiluted AZ1350J at 3000 rpm for 30 seconds. Prebake at 88°C-90°C for 10 minutes. This thick coat of photoresist (~2 μm) will protect the gold grating pattern from scatching during the rest of the process when the wafer is laid on its front surface.

2. Spincoat the back side of the wafer with undiluted AZ1350J at the same conditions as in 1. Prebake at 88°C -90°C for 10 minutes.

3. The wafer is laid flat on its back surface on top of a piece of white paper (preferably filter paper). The wafer rim is outlined on the paper as shown in Fig. 4.18 and two lines perpendicular to each other are

drawn. Their extensions intersect at the center of the grating structure. Overturning the filter paper, the outline of the wafer and the straight lines are graphed again.

4. Lay the overturned filter paper directly beneath a sun lamp (650 watts). The distance between the lamp and the filter paper is 20 cm. The wafer is then placed front side down on top of the filter paper and within the graphed rim outline. A contact mask with just a transparent square (7 mm x 7 mm) is placed onto the wafer. By visual observation the sides of the square should be perpendicular to the two drawn lines and the intersection of the extension of the lines should roughly coincide with the center of the mask square. The wafer mask system is exposed for 30 seconds. Development is accomplished in less than one minute by dipping in a 1:1 mixture of AZ1350 Developer: DI H_2O. The wafer is then rinsed with DI H_2O and blown dry with N_2. It is not critical for the square side to be aligned with the flat edge of the wafer since a smooth window side edge is not important; however, the square edges were roughly aligned either perpendicular or parallel (depending on the side) to the wafer flat edge.

5. The wafer is postbaked at 165°C for 15 minutes. This will harden the resist so that it will stay during the subsequent etching of the SiO_2.

6. In order to prevent photoresist liftoff and etching of the SiO_2 at places where the resist lifted off (besides the window area) drops of the buffered HF etchant (one part concentrated HF, five parts NH_4F) were deposited only on the window area to be etched using a cotton swab. The etchant wets the SiO_2 but not the photoresist. The etching of the 1.2 μm thick SiO_2 layer takes about 10 minutes. If, on the touch of a

dry cotton tip on the etchant, the film breaks immediately, then the etching is complete. The window area should have a silvery color. Rinse with DI H_2O. If the window area is hydrophobic then the etching is complete. It should be noted that usually, due to incomplete weting, the corner areas of the square SiO_2 opening will require additional time (~3 minutes) for complete etching and supplemental weting may be required.

D. The wafer is now ready for immersion in the preferential etchant of silicon. The etchant consists of a mixture of 130 ml of ethylenediamine, 60 ml of H_2O and 22.5 grams of pyrocatechol. The wafer is immersed in the solution which is then heated up to 110°C-115°C. The wafer-solution system forms part of a gas refluxing system in order to conserve volatile water, as shown in Huang [33]. N_2 is bubbled in the solution for agitation and mixing. Initially, when the solution reaches 75°C-80°C, bubbles should start emanating from the window area. This heralds the onset of etching. The thick photo-resist layer that was covering both sides of the wafer is also lifted off. Figure 4.19 shows the wafer topology for nichrome SiO_2 protection of the gold mask during the window etching. Complete etching takes place anywhere from 3 hours to 5 hours for a 220 μm thick silicon wafer. This is due to the sensitivity of the etchant to factors described above. When the window surface area has been smoothed by the etchant which has reached the high boron concentration, the etching should be maintained for half an hour more; otherwise, small crystallites will be present on the surface of the window upon removal from the solution. The solution should be cooled to 60°C before removal of the wafer [31]. Figure 4.20 shows a picture of a window.

E. Upon removal, the wafer should be immediately immersed in warm (50°C) methanol for 1 minute and rinsed with DI H_2O. It should be handled

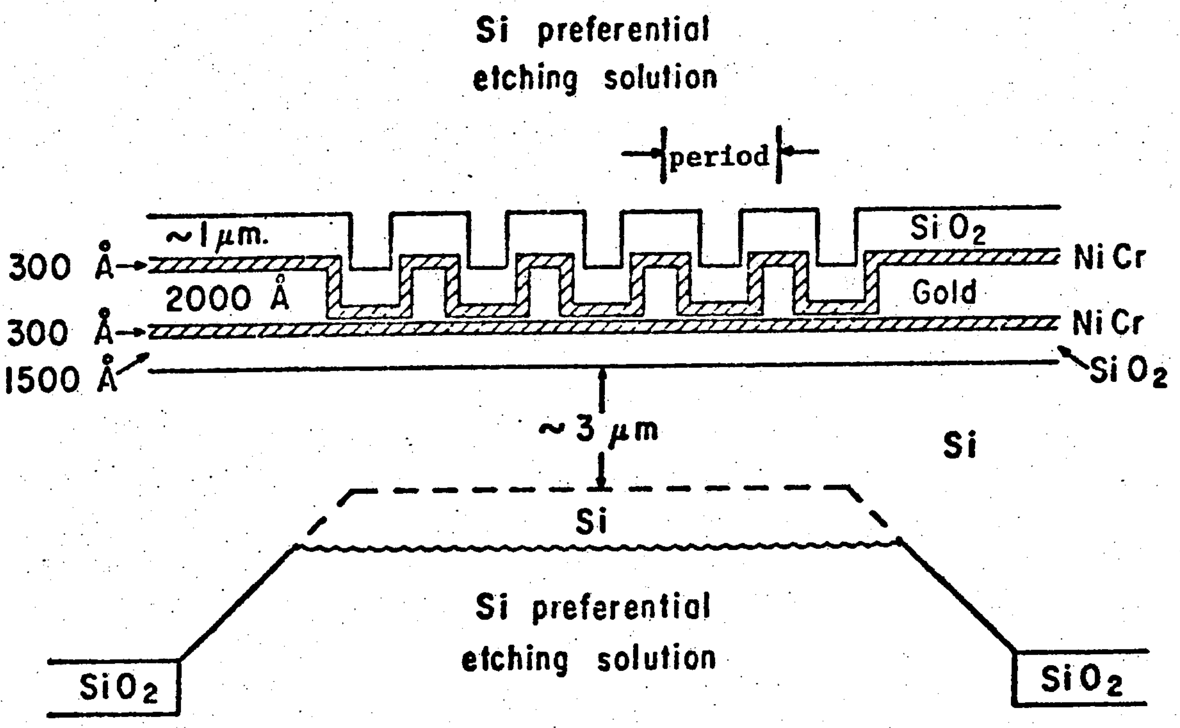

Fig. 4.19. Wafer topology for nichrome - SiO_2 protection of the gold mask during anisotropic etching of silicon.

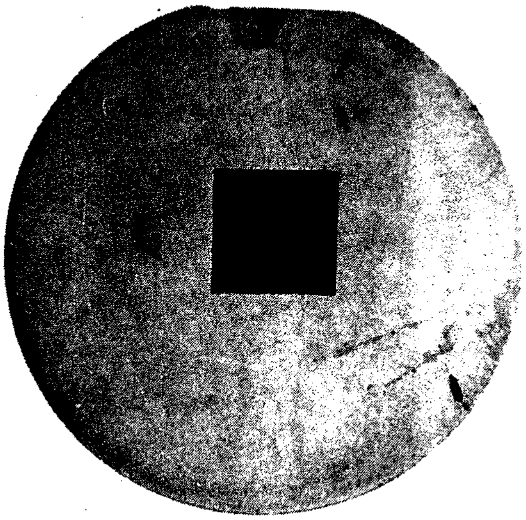

Fig. 4.20. Picture of window. The dark spots on the membrane are due to coloring.

with extreme care. It should be dried both with the application of filter paper to remove gross quantities of H_2O and by blowing it with a very gentle stream of N_2 always parallel to the window surface. At this stage the membrane is wavy, i.e. it is not stretched flat. This is due to the thick (1.2 μm) SiO_2 film still present on top of the gold relief pattern.

F. Removal of the SiO_2 layer should be done with extreme care. Immersion of the wafer (no agitation) in a 3:1 mixture of concentrated NH_4F and concentrated HF will remove the SiO_2 layers from both sides of the wafer. The thickness being the same for both layers, visual observation of the color change of the back surface (i.e. to a shiny silver color when all the SiO_2 has been removed) and a change from an HF-phylic surface to an HF-phobic and hydrophobic will herald the complete etching of all the SiO_2. If smallcrystallites are present on the back surface of the membrane, they will be colored red by the SiO_2 etchant along with the surrounding smooth area; however, if the surface is really smooth and shiny with no obvious crystallites no coloring will occur. The coloring has no detrimental effect on the mask; therefore, it can be tolerated. The wafer is then rinsed with DI H_2O and dried as in E. The membrane should now be well stretched. This is due to the tensile stressexisting in the silicon membrane as a result of boron doping which is a substitutional impurity with a lattice missfit ratio, Γ, of 0.746 [27]. This introduces the stress. Also the gold layer is under tensile stress [45]. If the membrane is removed from its bulk silicon support structure, it will curl up. If, at the center of the membrane a spot exists with no gold the membrane will be dimpled toward the gold side in that area. This is due to the stress exerted by the surrounding gold.

G. The thin nichrome film present on the gold relief pattern can be removed by dipping of the wafer in a 1:1 solution of concentrated HCl and H_2O; however, if desired it may be left on top of the gold pattern since it will not contribute to any loss in resolution or mask contrast. If removal is desired, the gold should not be etched all the way to the first nichrome layer (Fig. 4.19) so that accidnetal lift off of the gold pattern is avoided.

4.6. Summary of Steps

In this section we present the mask fabrication process steps in an outline form.

a. Clean a <100> orientation n-type silicon wafer (degrease-RCA1-RCA2).

b. Grow an 0.8 μm SiO_2 layer (wet atmosphere, O_2, 1100°C, 1-1/2 hours).

c. Strip oxide from front surface (HF).

d. Reclean wafer (as in a.)

e. Deposit boron into the front surface (B_2H_6, N_2, O_2, 1100°C, 6 hours).

f. Boron drive-in (wet atmosphere, 950°C, 3 hours, O_2).

g. Sputter deposit a 1.2 μm SiO_2 film on the back surface and a 1000 Å film on the front surface.

h. Evaporate a 300 Å layer of nichrome and 2000 Å of gold on the front surface.

i. Holographic grating fabrication on the wafer via photoresist.

j. R-f sputter etch gold grating mask pattern.

k. Sputter deposit a 1.2 μm SiO_2 film on the gold pattern subsequent to a 300 Å nichrome evaporation.

l. Open a SiO_2 window directly beneath the gold grating pattern.

m. Etch the silicon for fabrication of the thin silicon membrane.

n. Remove the SiO_2 layers (HF).

o. Remove the NiCr layer (HCl).

The above steps may be modified if the mask pattern being fabricated is that of an IC instead of a grating. The pattern, besides being fabricated holographically (grating), can be made with optical lithography, electron-beam lithography [11] [27] and x-ray lithography.

CHAPTER V

X-RAY EXPOSURE AND DEVELOPMENT RESULTS

In this chapter we present our experimental results. In Section 1, exposure-dependent resist properties are briefly discussed. In Section 2, the experimental results are presented.

5.1. Exposure-dependent Resist Properties

If no cooling of the resist-substrate system is taking place during exposure, heat generated by the gun cathode filament will raise the resist temperature. Heat is generally detrimental but in some particular instance it can be beneficial. In particular we noted that the pattern was visible in some cases immediately after exposure. The explanation is related to the type of scission events taking place during exposure.

It is well known that PMMA exhibits predominantly random chain scission upon x-ray exposure with a subsequent decrease in the initial average molecular weight. The final average molecular weight after exposure in inversely proportional to the radiochemical yield G for main chain fracture. This can be utilized so that exposure time may be decreased in typical x-ray lithographic applications by increasing the ambient temperature of the x-ray exposure system or by incorporating small amounts of acrylonitrile in the PMMA resist [46].

Polymers used for x-ray resists are also degraded by other types of process such as thermal degradation (Pyrolysis) [13]. Thermal degradation can be divided roughly into two general categories: random chain scission and depolymerization. The latter is essentially a depolymerization process in which monomer units are released from the chain ends. In this type of degradation, the molecular weight of the residual polymer remains almost equal to the initial average molecular weight.

For low average molecular weight PMMA thermal degradation consists almost exclusively of depolymerization. Volatile monomer (methylmethacrylate) is almost the exclusive produce [47]. The simultaneous radiation degradation and thermal depolymerization can be useful in x-ray lithography since x-ray-thermal exposure is effectively a simultaneous exposure and development process.

Figure 5.1 shows the thermal degradation of PMMA samples of varying molecular weight as indicated in the relationship of the percent of the original molecular weight of the polymer residue to thr percent degradation to monomer. Sample A, molecular weight 94,000; sample B, molecular weight 725,000 [13]. Line A_oB denotes only random chain scission and line A_oC only depolymerization.

5.2. Exposure Results

Comercially available nickel grids with 10 μm and 6 μm linewidth were contact printed in PMMA on flexible glass. As was mentioned earlier, we noted that profiles were visible in some cases immediately after exposure; however the contrast was low. Subsequent development in a mixture of 60% isopropylalcohol and 40% methyl-isobutyl ketone for 50 minutes increased the contrast substantially, by deepening the pattern in the exposed regions. This validated the concept of simultaneous radiation degradation and thermal depolymerization effect. Figure 5.2a is a photomicrograph of the 10 μm minimum-linewidth grid replicated in PMMA. Figure 5.2b is an SEM picture of the same grid. Figure 5.3a is a photomicrograph of the 6 μm grid and Fig. 5.3b is the same pattern replicated in PMMA.

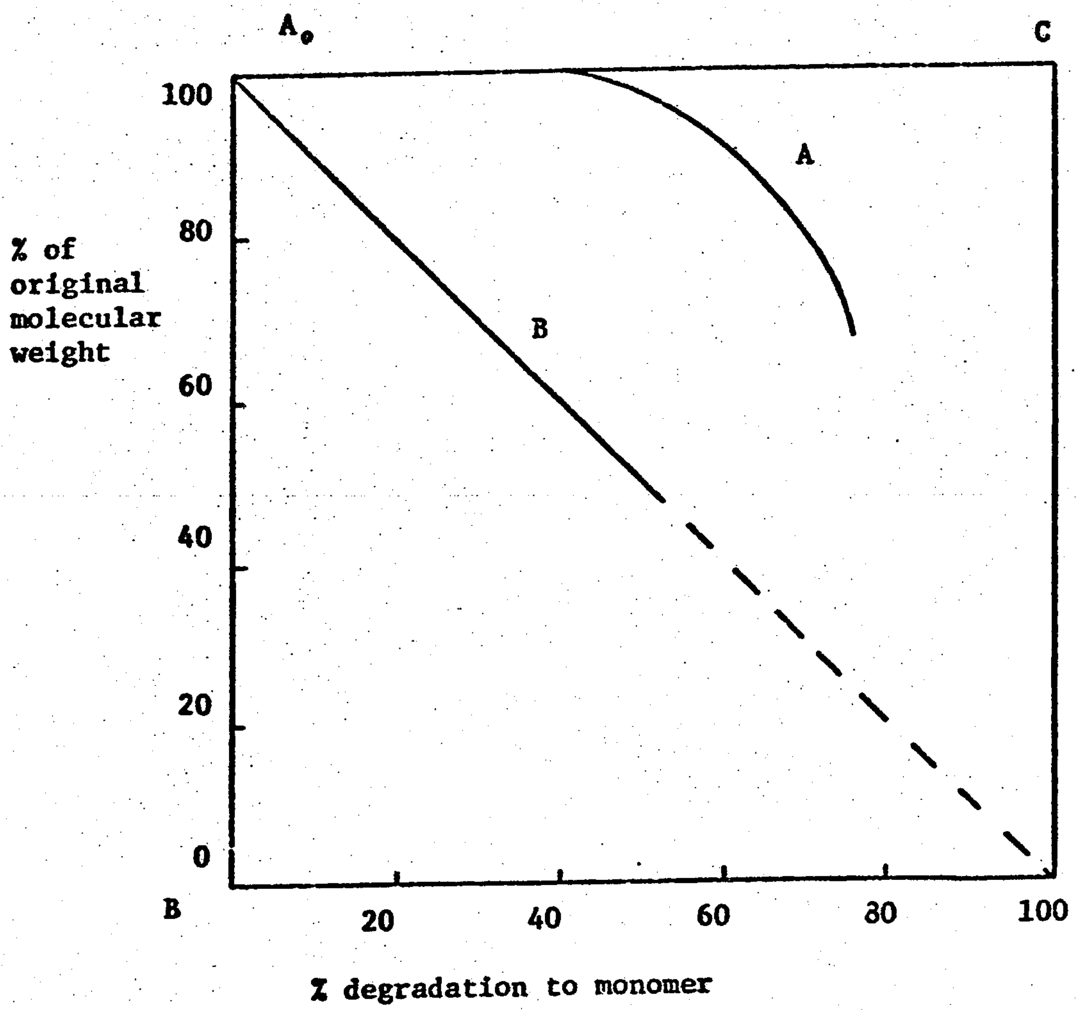

Fig. 5.1. Thermal degradation of polymethyl methacrylate samples of varying molecular weight.

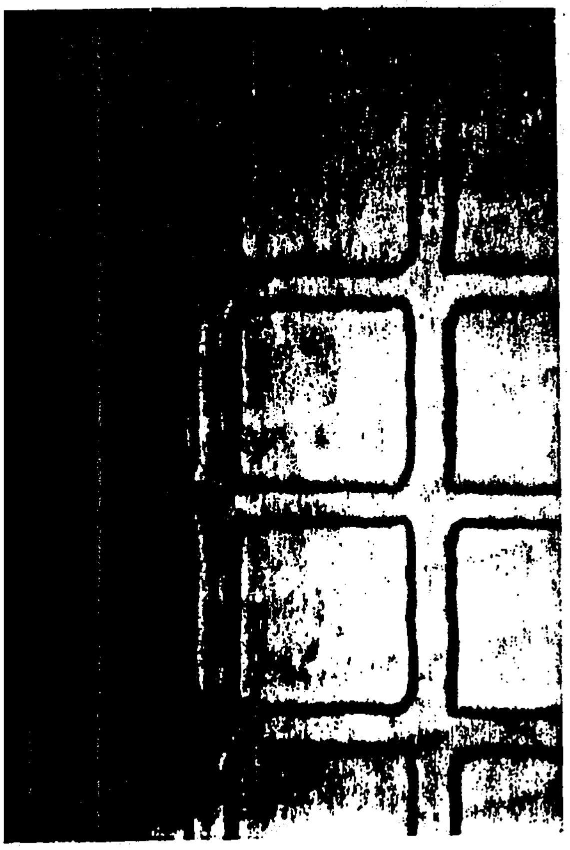

Fig. 5.2a. 10 µm minimum-linewidth grid replicated in PMMA.

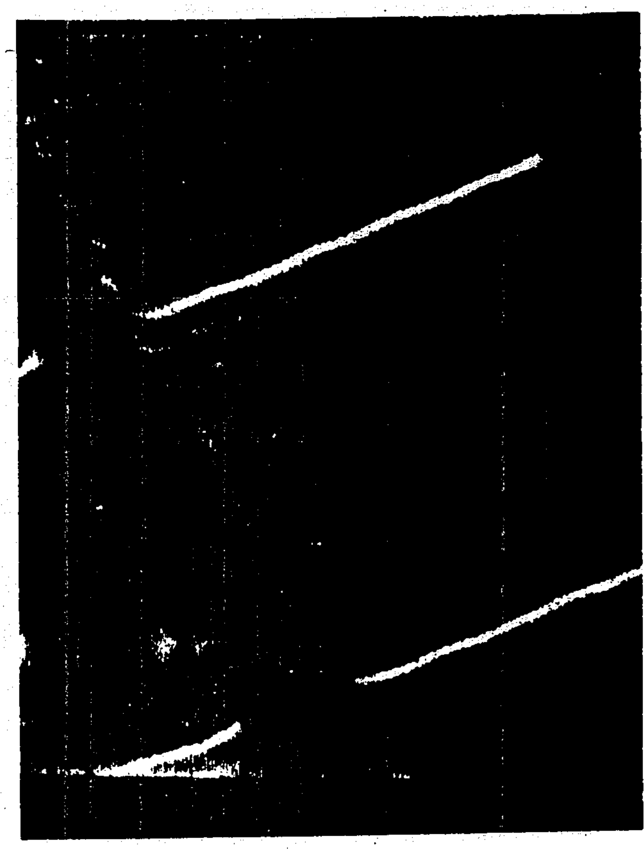

Fig. 5.2b. Electron micrograph of the 10 µm grid.

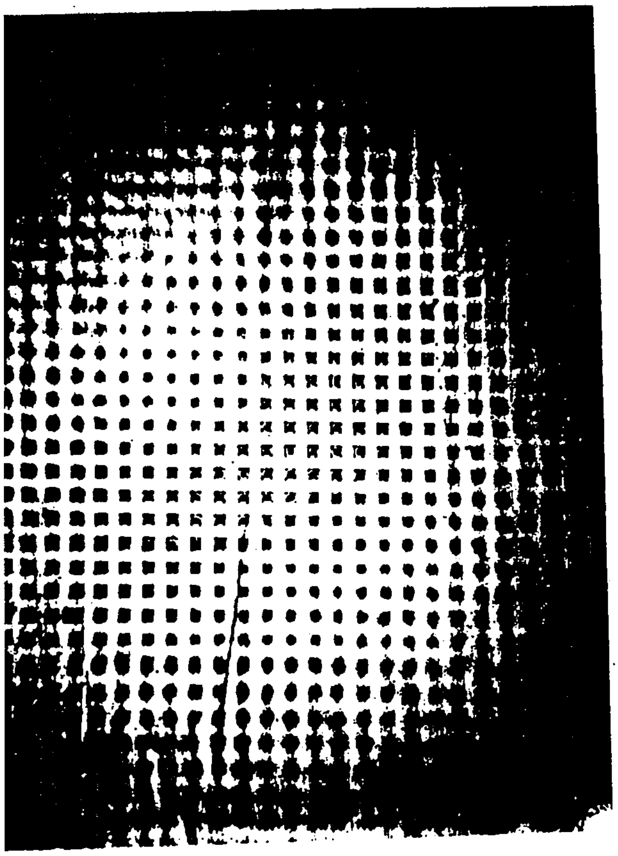

Fig. 5.3a. Photomicrograph of the 6 μm nickel grid.

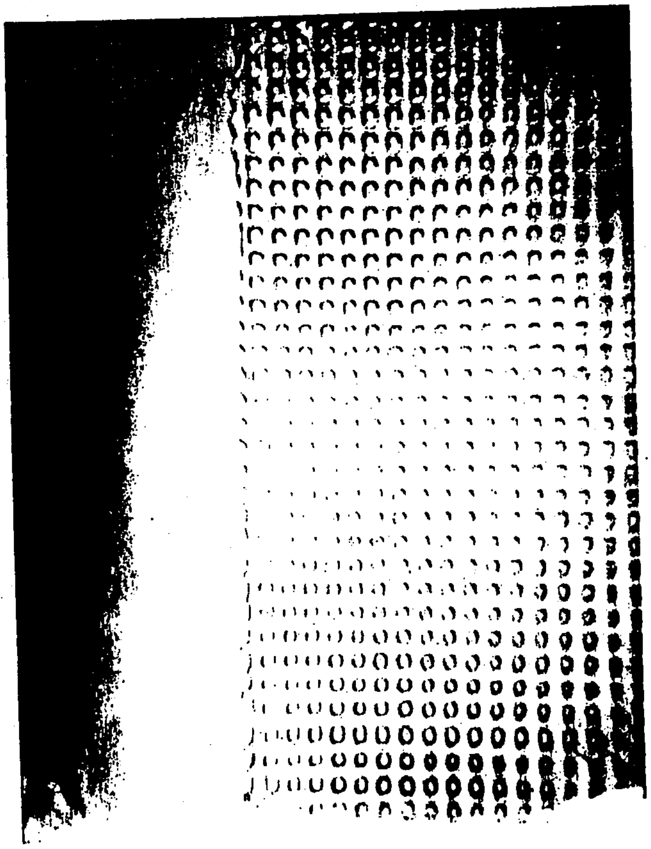

Fig. 5.3b. 6 μm pattern replicated in PMMA.

The 10 μm grid was also contact printed in PMMA using a two source exposure as follows: first the mask-substrate system was positioned at an angle of 35° with respect to the horizontal and exposed for 20 minutes at a source to substrate distance of 8 cm and a beam current of 100 mA. Then the mask substrate system was rotated around its axis of rotation so that the angle of the second use was -55°. It was again exposed for the same time.

This exposure scheme produced three distinct regions of exposure.

A. A region where the exposure was maximum (effectively a 40 minute exposure).

B. A region where one exposure was partially attenuated due to the mask.

C. A region where both exposures were partially attenuated.

The results after development in Fig. 5.4 show a distinct 3 step structure due to the different etch rates in the different regions of exposure. The visible edge ripple of the replicated grid bars is due to the exact reproduction of the original nickel mask which had rippled edge.

A submicron period (.6 μm) gold grating on top of a thin silicon window was replicated at an angle of 10°. The diameter of the grating area was 6 mm. Total exposure time was 60 minute at an accelerating potential of 7.3 kV and electron-beam current of 100 mA. Excessive heating of the mask substrate system (no cooling of the resist substrate) imposed a severe limitation on the total exposure time. For maximum exposure the source to substrate distance was 6 cm; however at this distance the thin aluminum foil gets destroyed and the penumbra increases. If a 4 μm spacing exists between mask and resist substrate, the penumbra is equal to 0.33 μm. The large value of the penumbra is mainly due to

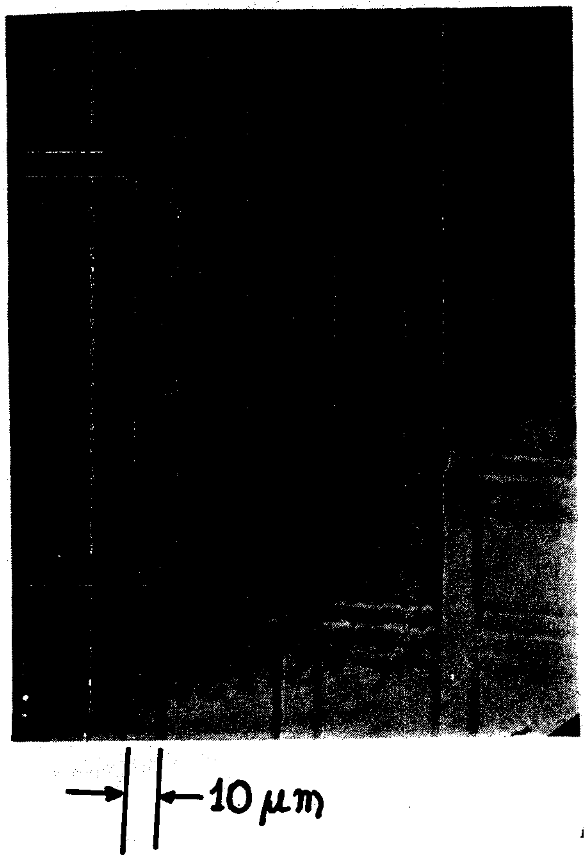

Fig. 5.4. Two source exposure.

large value of the source diameter A (= 5mm). Total development time was 50 min in a 60:40 mixture of IPA:MIBK. Due to the penumbra the grooves of the replicated grating in PMMA shown in Fig. 5.5 are wider than the originals of the gold grating and the groove depth to period ratio is small.

A 1 μm period grating mask (Chapter IV) was replicated a number of times. Typical exposure and development parameters are as follows: Total exposure time: 120 minutes, source to substrate distance: 10 cm and total development time: 16 minutes in a 60:40 mixture of IPA and MIBK. The total energy density absorbed by the resist during exposure was approximately 900 Joules/cm^3. This was calculated using Eqs. (2.26) and (2.30) of Chapter II where the following values were used for $A\ell_{k_\alpha}$ irradiation (8.34 Å): $\eta = 1$, $\varepsilon = 1.35 \times 10^{-4}$ photons/electron/steradian [23] [48] for an accelerating potential of 7.3 kV, I = 115 mA and a = .52 where $a \equiv a_1 a_2$ and $a_1 = .768$ is the transmission factor of the thin aluminum foil and $a_2 = .68$ is the transmission factor of the silicon membrane. The development rate of the exposed PMMA is approximately 130 Å/min [17]. The following are representative of the exposure and development results. Figure 5.6 is an SEM picture (65° tilt angle) of the 1 μm grating mask replicated in PMMA. The x-rays were incident normal to the mask-resist substrate system. The resist substrate was water cooled during exposure in order to avoid damage of both mask and resist due to excessive heating. The total exposure time was limited to two hours due to tungsten deposition on the aluminum x-ray target. This thin layer of tungsten severly attenuated the emergent characteristic $A\ell_{k_\alpha}$ x-rays. A three hour exposure yielded the same results confirming the detrimental effect of tungsten contamination. Development time was

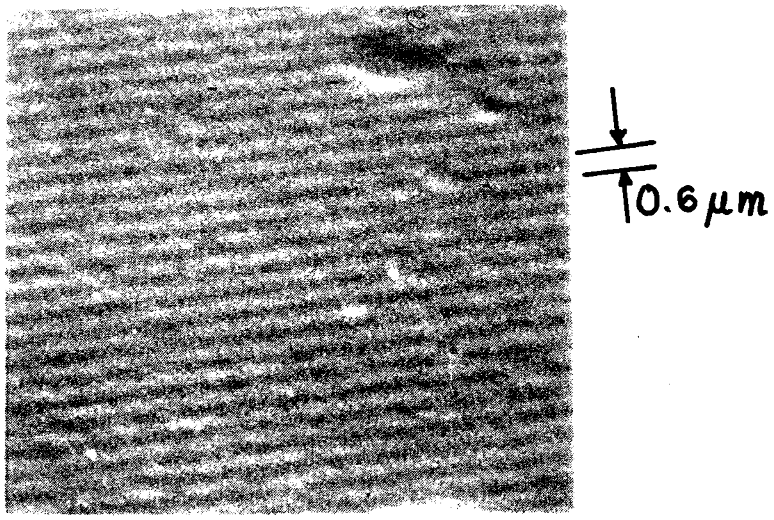

Fig. 5.5. 0.6 μm period grating.

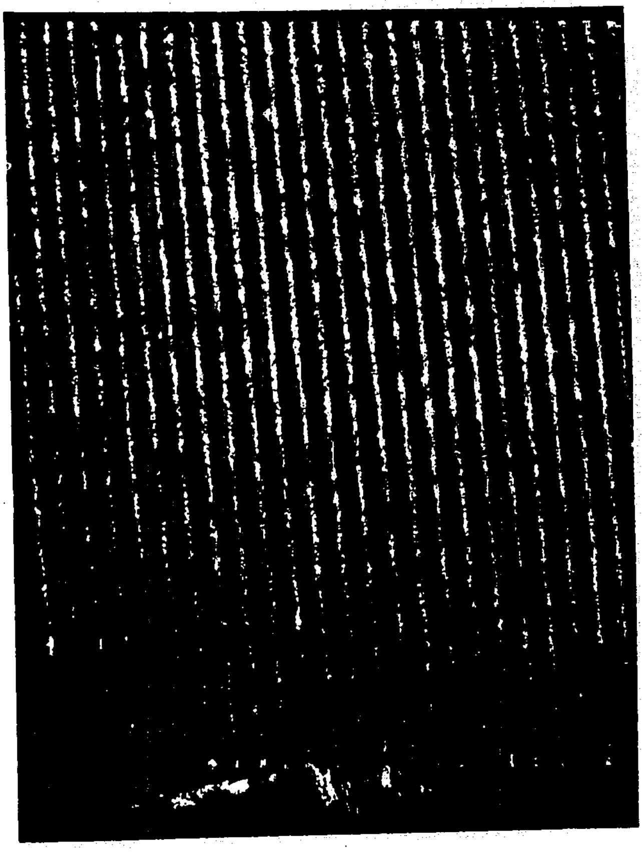

Fig. 5.6. 1 μm period grating.
65° Tilt.

limited to 15 minutes due to deterioration of the resist if the substrate was left longer in the developer. A freshly made resist was tried with the same results. The groove opening of the replicated grating is greater than the one of the original gold mask. This is due to the penumbra.

Figure 5.7a and 5.7b are SEM pictures (62° tilt angle) of the replicated pattern in PMMA of the same mask as before. During exposure, the mask-resist substrate system was positioned at an angle of 20° with respect to horizontal. At an earlier trial run, the mask was broken and two cracks perpendicular to each other were created. Due to the gold tensile strain, one of the broken edges of the silicon membrane curved upwards. This provided the necessary contact when the resist substrate and the mask were clamped together during exposure. In Figures 5.7a and 5.7b we notice three distinct regions.

A. A region with no grating structure. This is due to the bad contact between mask and resist substrate.

B. A deep groove in the middle. This is due to the mask crack opening. Exposure of the grating area was 68% of that in the groove due to the attenuation suffered by the beam as it passed through the silicon membrane. Subsequent development differentiated between the regions that received different exposure doses.

C. A region where the grating structure is clearly visible. Contact provided by the curved membrane edge minimized the penumbra.

As we move away from the crack, the mask-substrate separation becomes increasingly larger. This in turn increase the penumbra and the replicated pattern becomes less and less pronounced until it disappears completely.

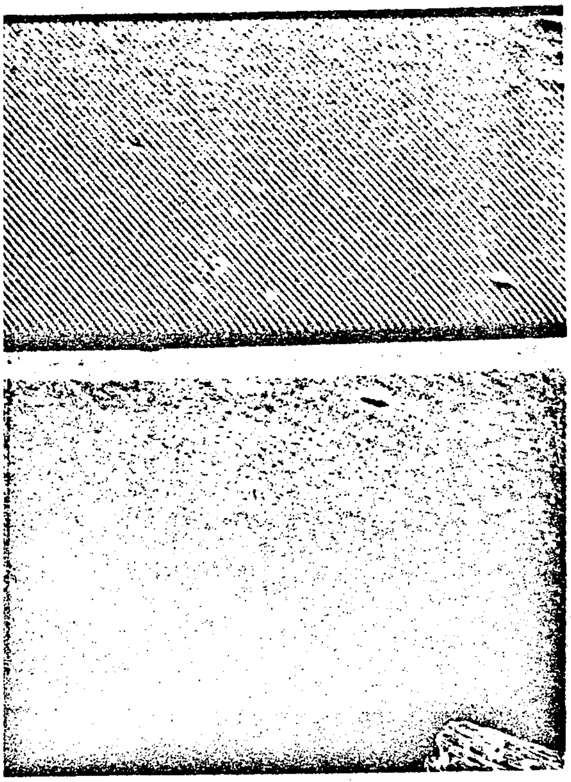

Fig. 5.7a. 1 µm period grating. 62° Tilt.

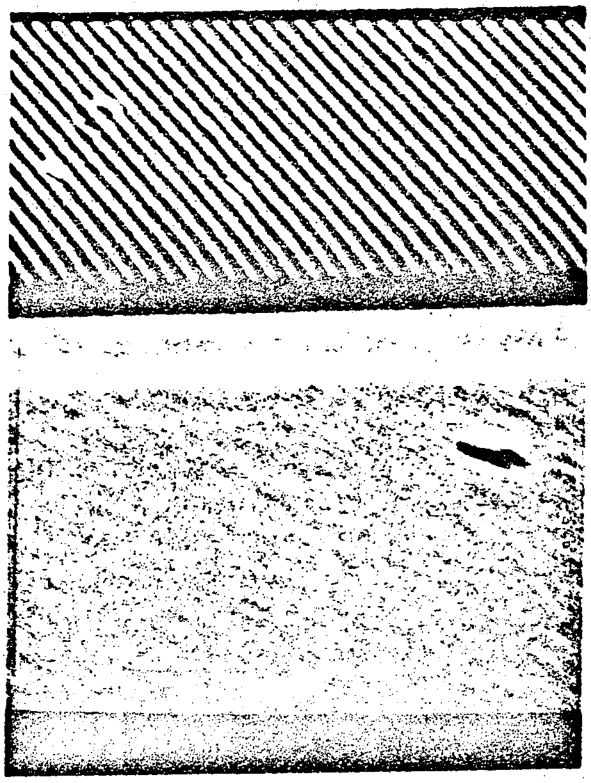

Fig. 5.7b. 1 µm period grating. Larger magnification at 62° Tilt.

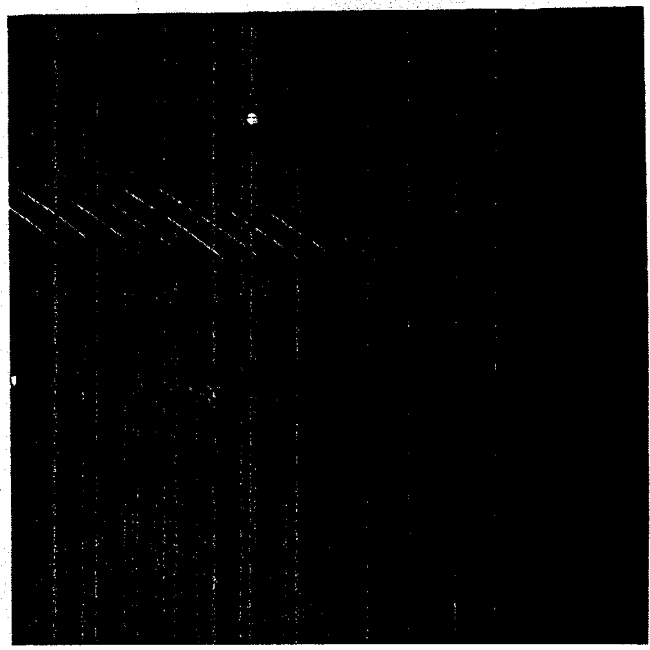

Figure 5.8 is an SEM picture (70° tilt angle) of the 1 μm grating mask pattern replicated in PMMA where the mask-resist substrate system was positioned at an angle of 30° with respect to the horizontal during exposure. Figures 5.9a and 5.9b are SEM pictures (72° tilt angle) of the same replicated grating pattern after it was cleaved. Figures 5.10a and 5.10b are SEM pictures (90° tilt angle) of the edge view of the replicated pattern. Notice that the left groove facet is longer than the right one. The left facet is the one corresponding to the angle exposure. The large sloping of the facets is due to the penumbra. The depression in the middle of the gold mask rib (Chapter IV) had no noticeable effect on the profile after development.

A simple experiment was performed as follows: The PMMA grating was positioned perpendicularly to the path of an argon laser beam (4880 Å). The intensities of the 1 and -1 order were found to be different by 25%. This is a further indication of the assymetry of the grating profile due to the angle exposure.

The difference in height between the peak of the grating groove and the valley is approximately 2000 Å (SEM measurement). This corresponds to within 10% of the calculated development rate since
2000 Å/15 min = 133 Å/min.

Figures 5.11a and 5.12b show results of replication of a 1 μm grating structure with no cooling of the substrate during exposure. Due to heat, intimate contact was achieved between mask and substrate at various regions. The uneven profile of the lines is due to the wiggly gold lines of the mask. The mask used had a large (~ 1/2) mask opening to period ratio.

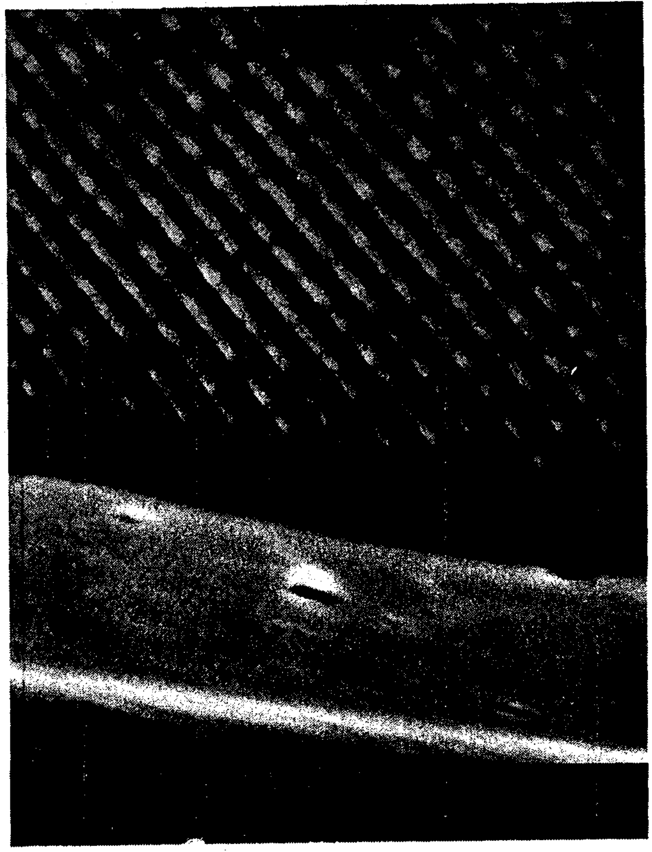

Fig. 5.8. 1 µm period grating. 70° Tilt. It was exposed at an angle of 30°

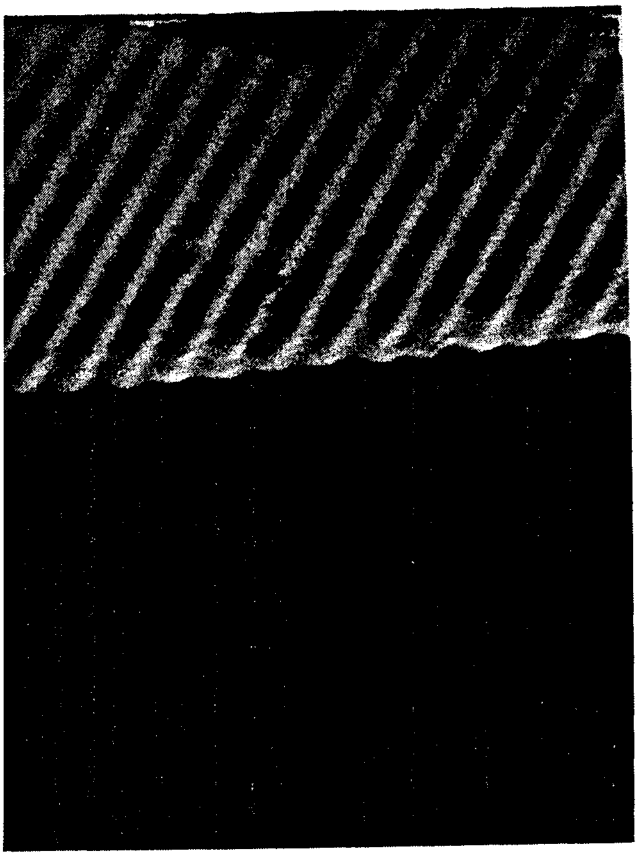

Fig. 5.9a. Same grating area as in Fig. 5.8. 72° Tilt.

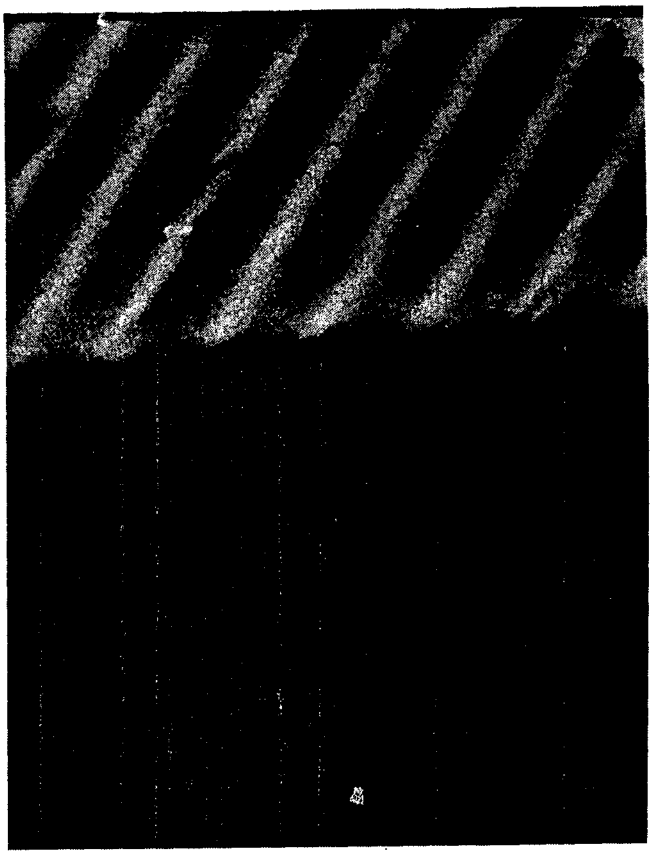

Fig. 5.9b. Higher magnification of the same area as in Fig. 5.9a.

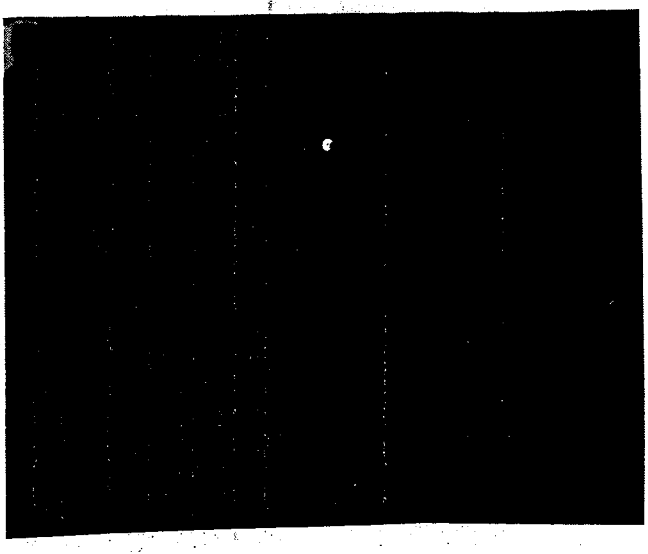

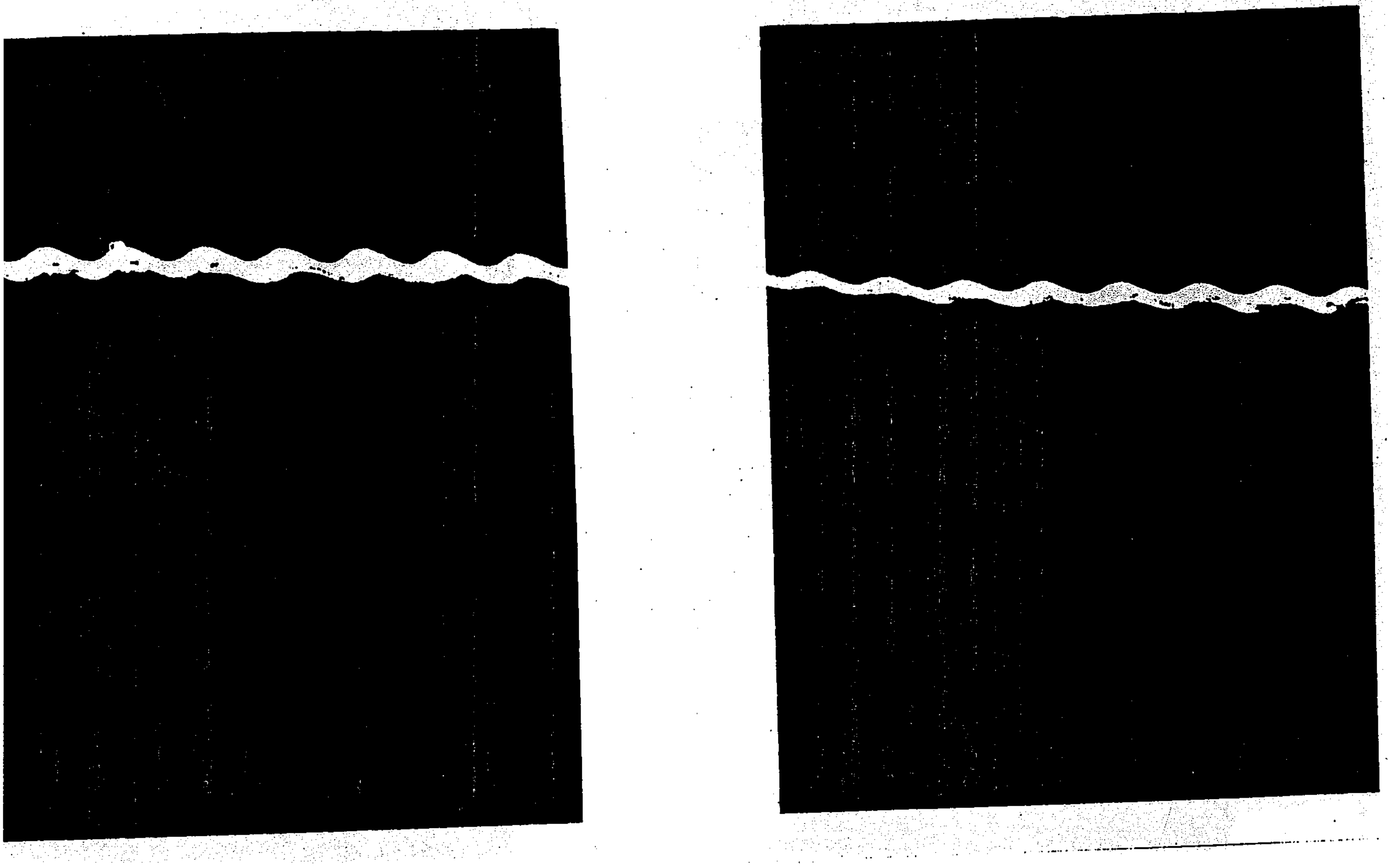

Figs. 5.10a,b. Edge view (90° Tilt) of the grating structure shown in Figs. 5.9a and 5.9b.

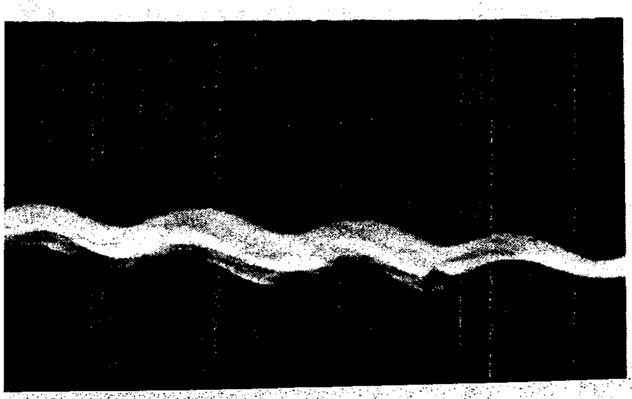

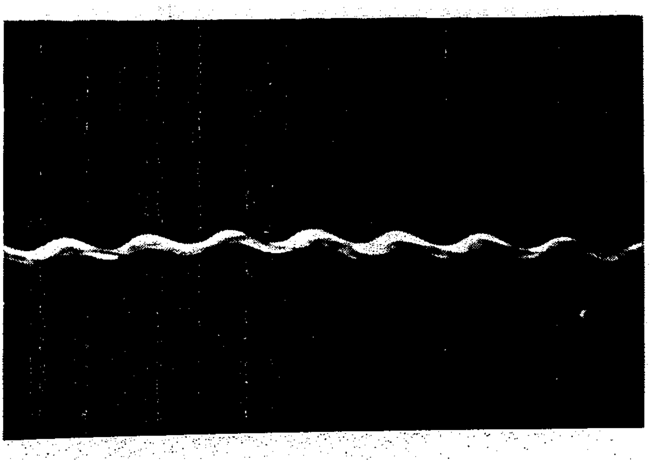

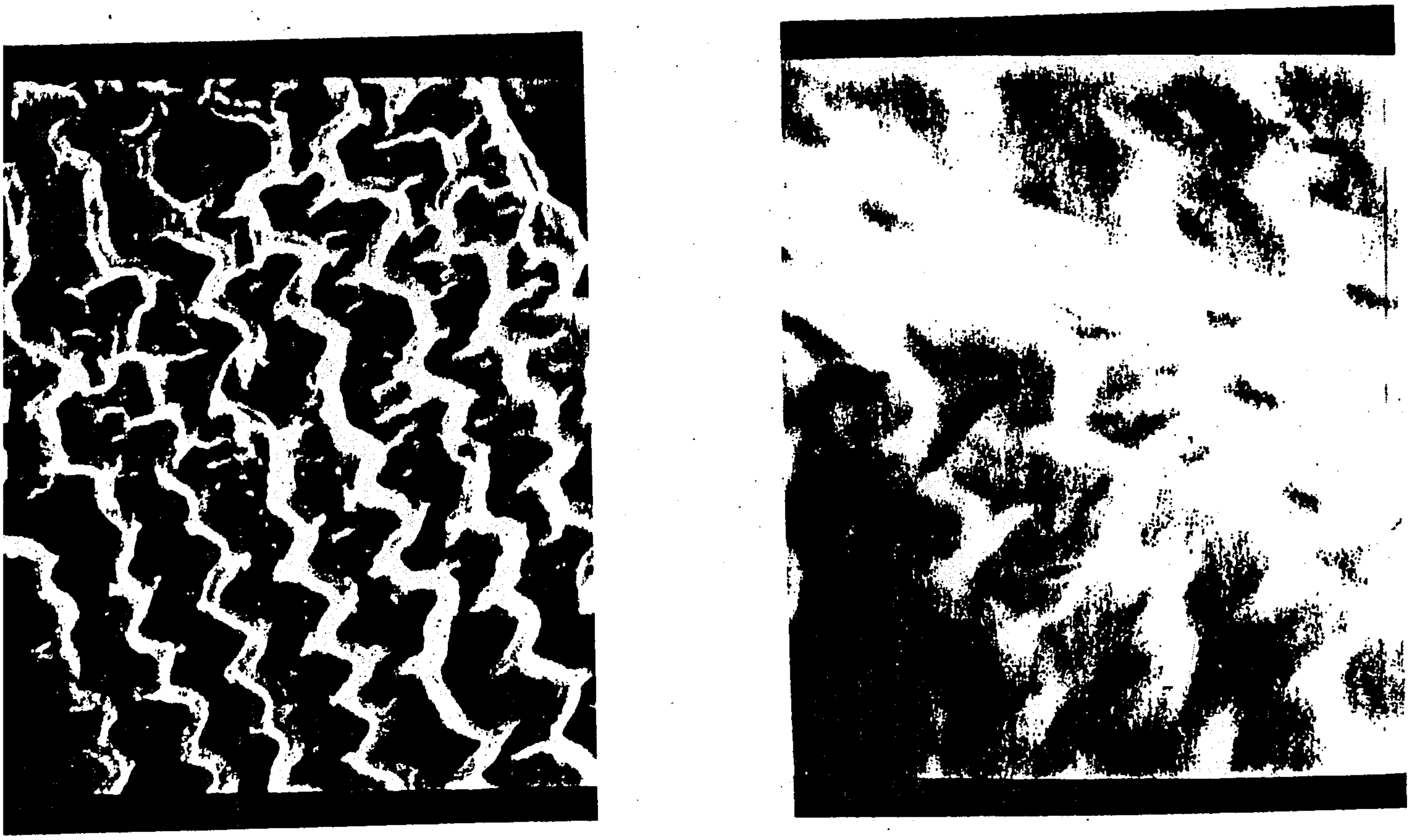

Fig. 5.11a,b. 1 μm grating structures. No substrate cooling during exposure.

In the Appendix the preparation of PMMA and the coating procedure for wafers is described.

CHAPTER VI

SIMULATION OF DEVELOPED RESIST PROFILES - THEORY

A. Theory

6.1. Formulation and Definition of the Problem

With the increasing importance of photoresist and electron beam and x-ray resists in the fabrication of integrated circuits and various devices, modeling of the development process is very useful. For the present work it is desirable to determine groove shapes via simulation when the various parameters (e.g. mask profile, exposure dose, developer, etc.) are given.

PMMA has the desirable property that the development process is a surface-etching phenomenon [14], i.e. there exists a well-defined boundary between the developer front and the undeveloped resist. The development of projection-printed images in positive-type photoresist can, at least to some degree of accuracy, be described by a surface-etching phenomenon [39]. (Another familiar etch-type process is that of etching oxide doped by ion implantation. In this case, also, a surface etching phenomenon may be applied.) The etch rate of the exposed resist at any point in the resist medium is a function of the local exposure dose and the kind of developer used.

With these assumptions we model the resist, with respect to the developer section, as an inhomogeneous and isotropic medium. The etch speed at a particular point in the resist is defined as $R(x,y)$.

Figure 6.1 shows the formulation of the problem: Given a curve Σ_o, the interface between regions ① and ② at time t_o and a velocity field (x,y), find at time t_1 the shape and position of the curve Σ_1, where Σ_1 is the new interface between regions ① and ②. Figure 6.2 shows an

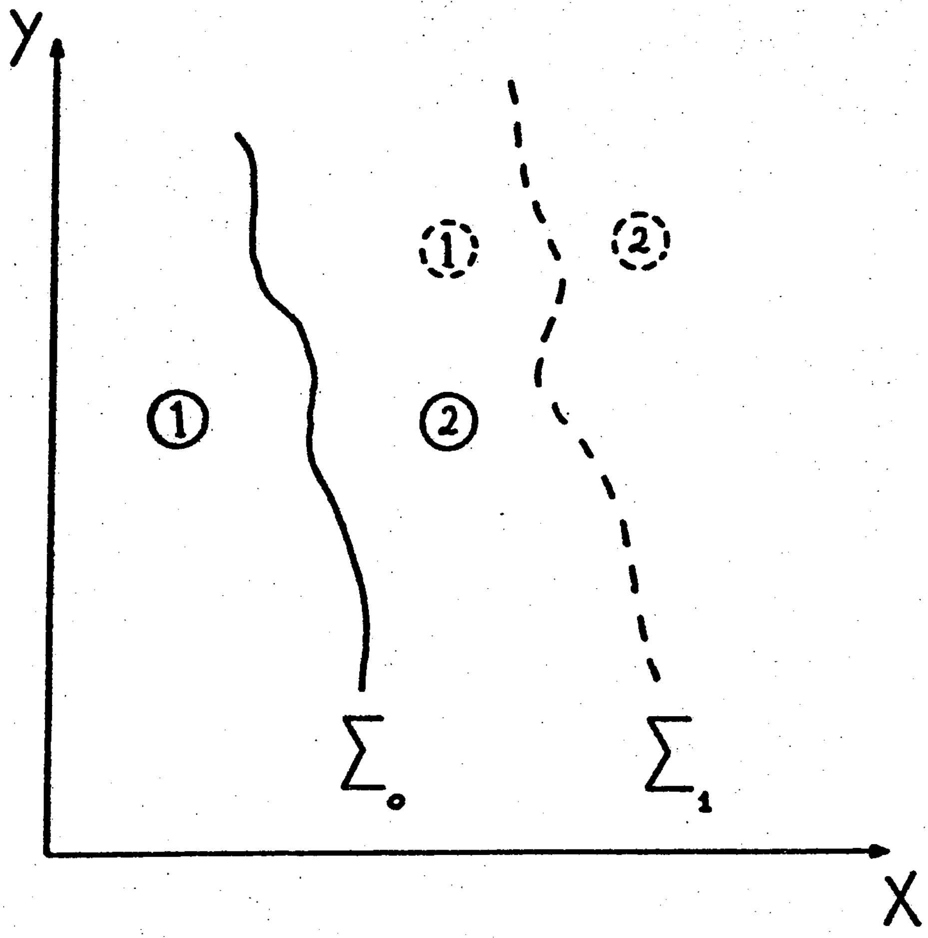

Fig. 6.1. Definition of the etching problem.

etch front with three different approaches that can be used to determine the profile at the next instant of time. All three approaches are the implementation of determining the envelope of instantaneous Huygen's sources (Chapter III) as shown in Fig. 6.2. The first approach uses a string of "cells" to define the profile at any time t. The cells can move in all four directions. The second approach uses a "string" of points to define the profile. A point moves normal to the line joining its adjacent points. The third approach is to follow the normals to the profile at any time. Their end points will define the profile [49]. We will now develop the theory of the ray direction in order to solve the problem as it is defined in both Figs. 6.1 and 6.2.

6.2. Solution Using Ray Equations

The solution of the problem is based on the fact that locally, at every infinitesimal region of the resist, the developer front satisfies Snell's law of refraction. In Fig. 6.3 we have two regions of different etch rate $R_1 > R_2$. From this goemetry, where $\overline{O_1A} = R_1dt$ and $\overline{BO_2} = R_2dt$, we get

$$\frac{R_1}{R_2} = \frac{\sin\theta_1}{\sin\theta_2} \qquad (6.1)$$

We know define an "etch ray" as a ray which is always perfpendicular to the developer front as shown in Fig. 6.3. It is obvious that the etch ray obeys Snell's law of refraction at the interface between two regions of different etch speed. This definition is in analogy to the definition of an optical ray in geometrical optics and it establishes a correlation between the development process and geometrical optics. Important definitions and results of goemetrical optics are specialized to the development case [50].

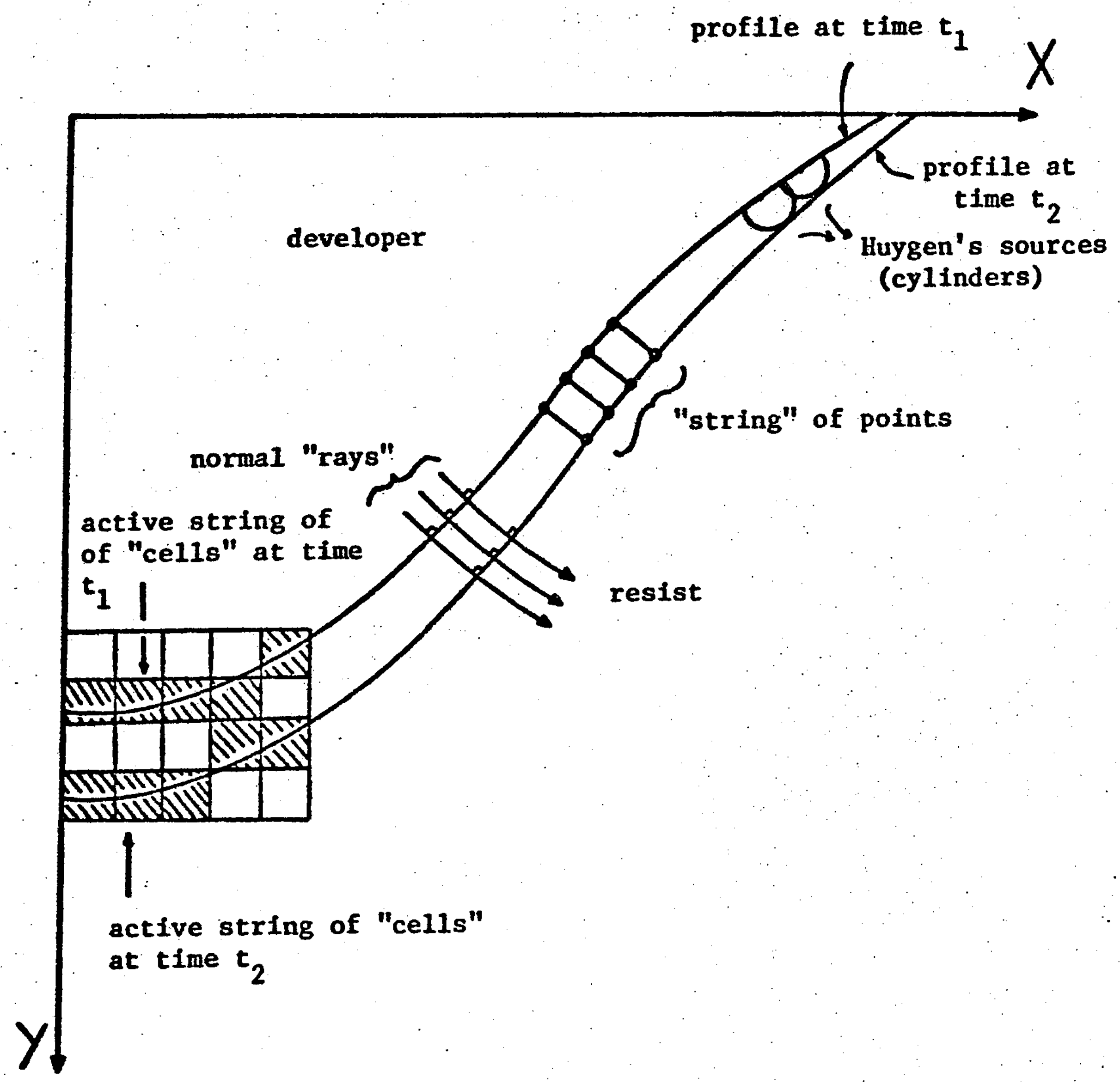

Fig. 6.2. The three different approaches (cell removal, ray-tracing, string) that can be used to determine the resist profile.

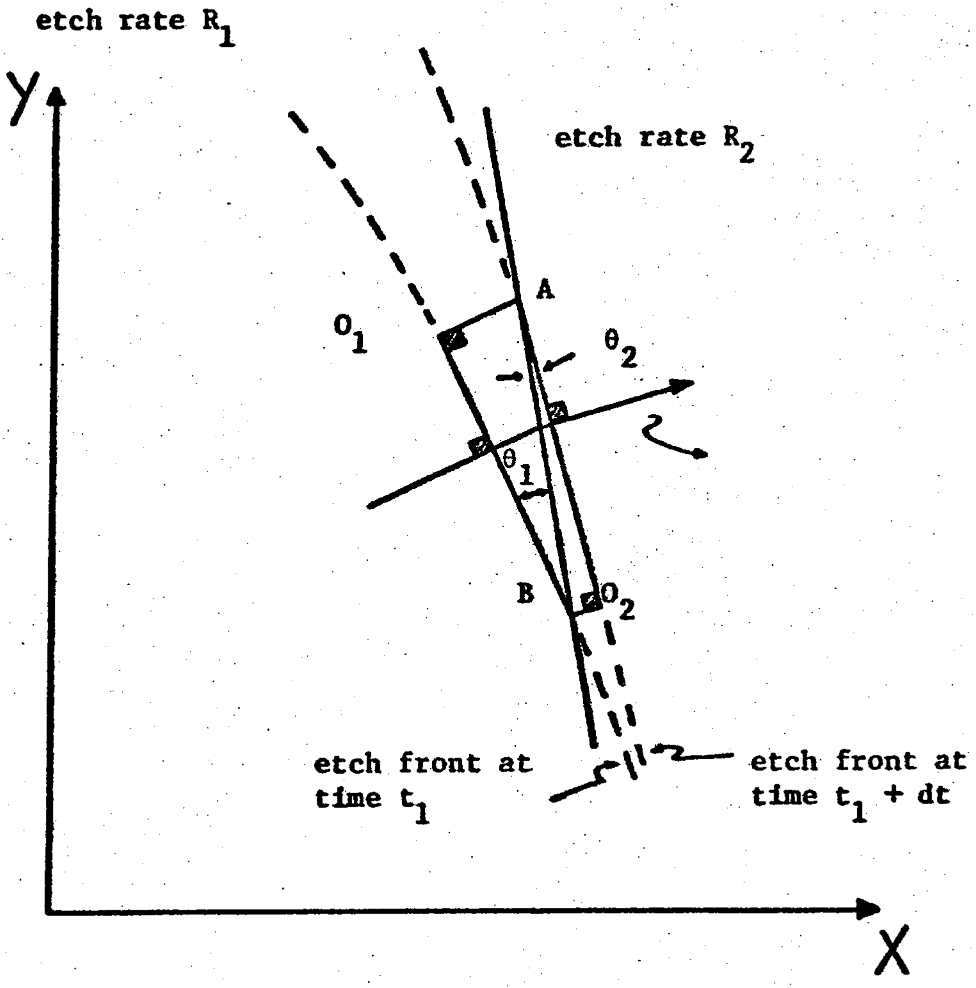

Fig. 6.3. Definition of an etch ray.

We define the resist index of refraction, n_{ph} as

$$n_{ph} = \frac{R_F}{R_s(x,y)} \tag{6.2}$$

where $R_s(x,y)$ is the etch speed at any point in the resist and $R_F = R_{max} = \max R_s(x,y)$ over all points in the resist.

We define the etch length from a point E to a point F along a given path in the resist, which we shall denote by ℓ_e, as the distance that the etch front would progress in a resist medium of constant etch speed R_F during the time it needs to cover the distance E to F along the given path. The etch length is given by

$$\ell_e = \int_E^F n_{ph} ds = \int_E^F \frac{R_F}{R_s(x,y)} ds \tag{6.3}$$

All rays connecting two developer fronts have equal etch lengths. Geometrical optics results may be applied to the resist development model by replacing the optical index of refraction n by the resist index of refraction n_{ph}.

We assume that the etch front at time $t_o = 0$ is represented by a given surface Σ_o as shown in Fig. 6.4 (3-dimensions). We define a function D(x,y,z) such that the value of D at a given point p equals the etch length from Σ_o to p of the etch ray passing through p. The equation of an arbitrary etch front is then

$$D(x,y,z) = \ell_e = \text{constant} \tag{6.4}$$

At a given point, let ds be the distance between the two etch fronts corresponding to ℓ_e and $\ell_e + d\ell_e$ as shown in Fig. 6.4. From (6.4) we obtain

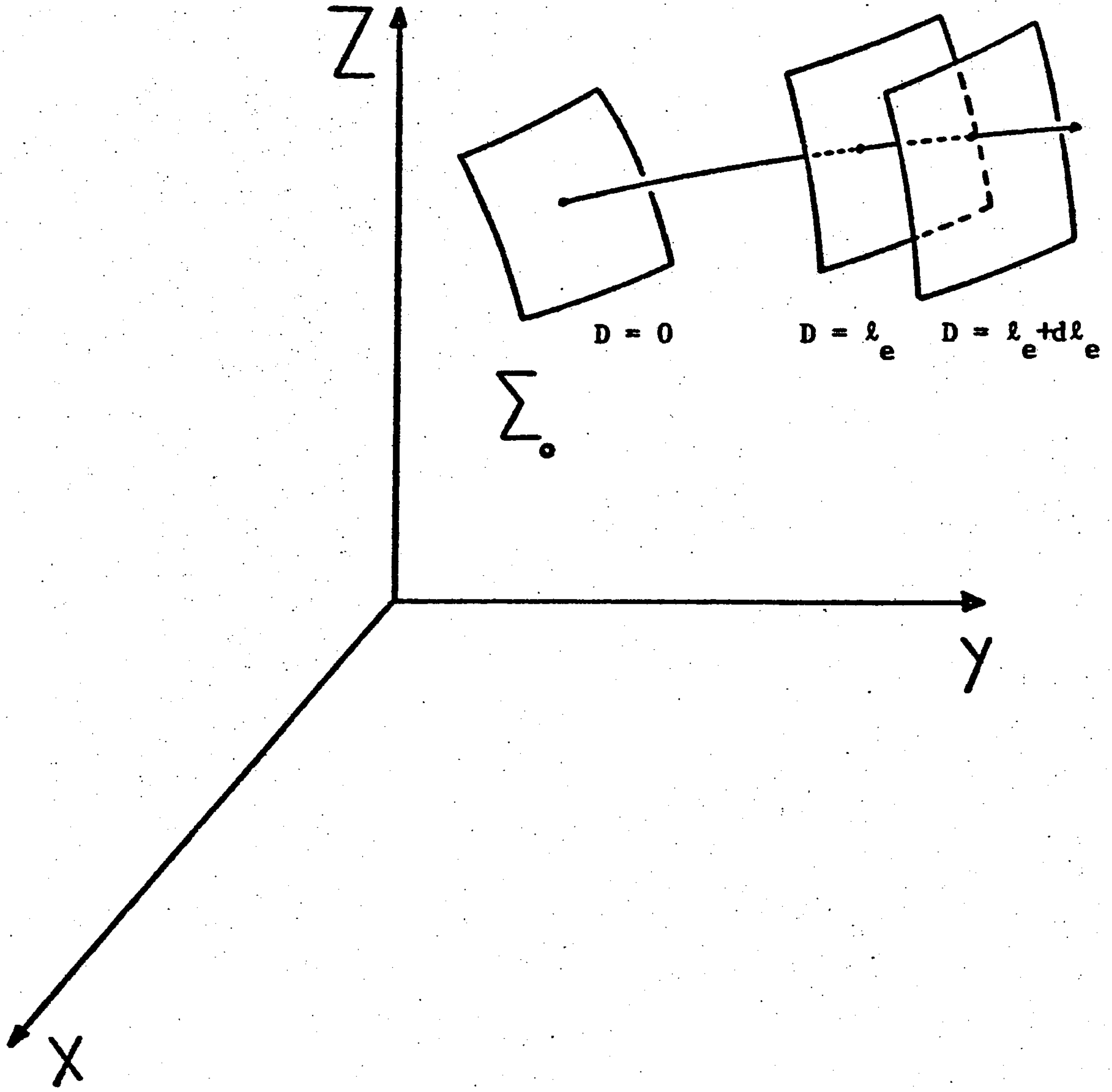

Fig. 6.4. Propagation of a developer front in an inhomogeneously exposed resist.

$$|\vec{\text{grad}}\ D|ds = d\ell_e \tag{6.5}$$

and from (6.3) we obtain

$$\frac{d\ell_e}{ds} = n_{ph} \tag{6.6}$$

and (6.5) becomes

$$|\vec{\text{grad}}\ D|^2 = n_{ph}^2 \tag{6.7}$$

or in Cartesian coordinates,

$$\left(\frac{\partial D}{\partial x}\right)^2 + \left(\frac{\partial D}{\partial y}\right)^2 + \left(\frac{\partial D}{\partial z}\right)^2 = n_{ph}^2 \tag{6.8}$$

Equation (6.8) is the Hamilton-Jacobi equation, better known in optics as the eikonal (εἰκῶν). It is also the mathematical formulation of Huygen's principle. Its solution, subject to the boundary condition that the equation $D(x,y,z) = 0$ represents the initial etch front Σ_o at time $t_o = 0$, determines the etch front at all subsequent times. Indeed, the equation of the etch front at time t is

$$D(x,y,z) = R_F t \tag{6.9}$$

The etch rays are the normal trajectories of the surfaces $D = \text{const}$.

We will now find the equation which governs the trajectory of an etch ray. Let $\vec{\tau}$ be a unit vector tangent to the etch ray as shown in Fig. 6.5 and consider the vector $n_{ph}\vec{\tau}$. From Snell's law it follows that when an etch ray passes across the surface of separation between two resist regions of different etch speed, it changes direction in such a way that the component of $n_{ph}\vec{\tau}$ parallel to the surface remains unchanged. We have

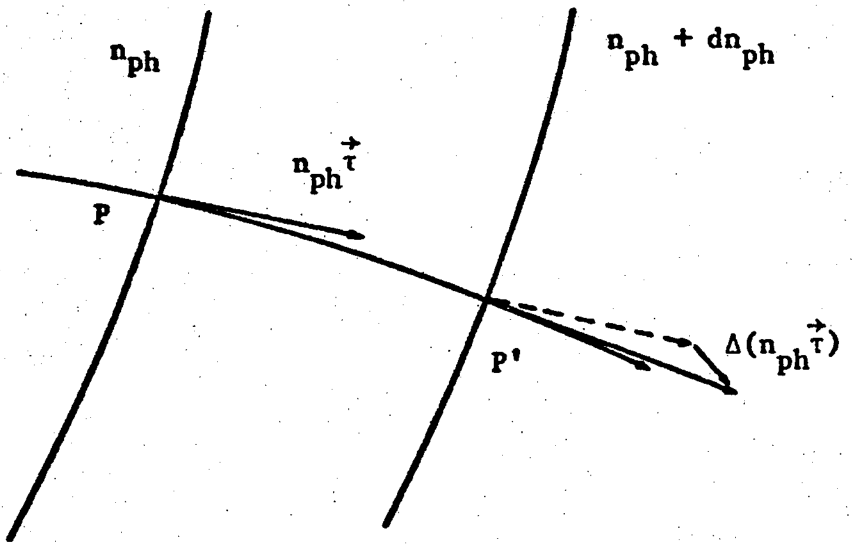

Fig. 6.5. Trajectory of an etch ray in a resist of variable n_{ph}.

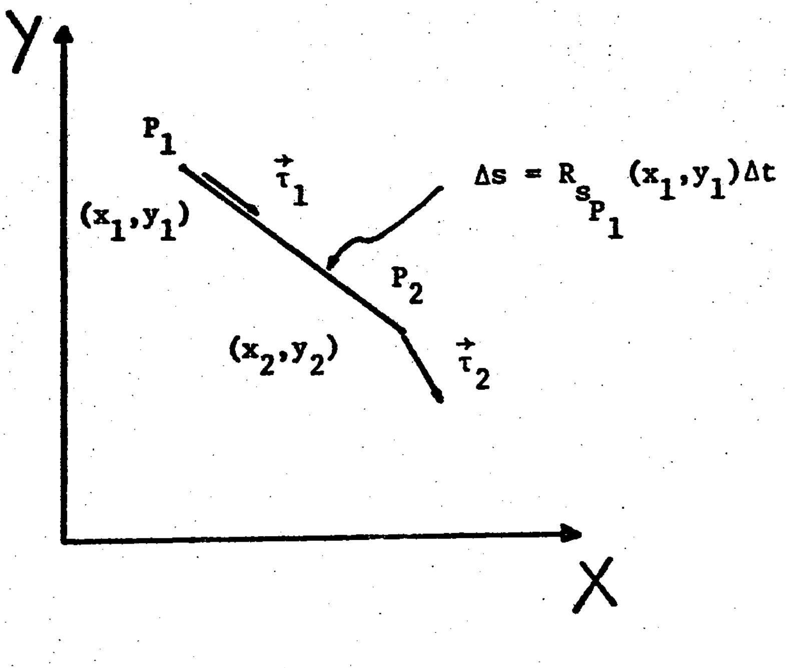

Fig. 6.6. Geometry for numerical calculation of etch ray trajectories.

$$(n_{ph}\vec{\tau}) \cdot (n_{ph}\vec{\tau}) = n_{ph}^2 \qquad (6.10)$$

and by differentiation $\Delta\vec{\tau} \perp \vec{\tau}$ for small steps

$$(n_{ph}\vec{\tau}) \cdot \Delta(n_{ph}\vec{\tau}) = n_{ph}\Delta n_{ph} = n_{ph}\, \overrightarrow{\text{grad}}\, n_{ph} \cdot \Delta\vec{s} = n_{ph}\Delta s\, \overrightarrow{\text{grad}}\, n_{ph} \cdot \vec{\tau} \qquad (6.11)$$

where $\Delta\vec{s}$ is the vector PP', Δs is its magnitude, and $\Delta(n_{ph}\vec{\tau})$ represents the vector difference between the vectors $n_{ph}\vec{\tau}$ at P' and P, respectively from the above equation we obtain

$$\frac{d(n_{ph}\vec{\tau})}{ds} \cdot \vec{\tau} = \overrightarrow{\text{grad}}\, n_{ph} \cdot \vec{\tau} \qquad (6.12)$$

Equation (6.12) indicates that the vectors $d(n_{ph}\vec{\tau})/ds$ and $\overrightarrow{\text{grad}}\, n_{ph}$ have equal projections along the tangent to the ray. Moreover, $\overrightarrow{\text{grad}}\, n_{ph}$ is perpendicular to the surface n_{ph} = constant, and so is the vector $d(n_{ph}\vec{\tau})/ds$, because as it was mentioned above, the component of n_{ph} parallel to a refracting surface is the same on both sides of this surface. Therefore, we obtain

$$\frac{d(n_{ph}\vec{\tau})}{ds} = \overrightarrow{\text{grad}}\, n_{ph} \qquad (6.13)$$

This is the differential equation of the etch ray, in vector form. It is equivalent to

$$\delta\int n_{ph}\, ds = 0 \qquad (6.14)$$

which is the mathematical formulation of Fermat's principle [51]

6.3. Ray Tracing Algorithm

6.3.1. Fundamentals

The ray-tracing algorithm is based on the fact that the locus of the end points of etch rays at the same instant of time form the developer front. In order to derive the equations for the numerical calculation of etch ray trajectories we use the geometry shown in Fig. 6.6. The end point of a ray at time t_1 is at point P_1 with the direction of the ray given by $\vec{\tau}_1$. For a small time interval Δt, the etch speed is considered constant and equal to $R_{s_{P_1}}(x_1,y_1)$. In Δt point P_1 will progress to point p_2 and $\Delta s = R_{s_{P_1}}(x_1,y_1)\Delta t$ where Δs is the distance between points P_1 and P_2. The direction of the ray at point P_2 is given by $\vec{\tau}_2$. First we need to calculate $\Delta\vec{\tau}$ since

$$n_{ph}(x_2,y_2)\vec{\tau}_2 = n_{ph}(x_1,y_1)\vec{\tau}_1 + \Delta(n_{ph}\vec{\tau}) \tag{6.15}$$

as it is shown in Fig. 6.6. A discretization of (6.13) is required. We have the obvious relationship

$$d(n_{ph}\vec{\tau}) = n_{ph}d\vec{\tau} + \vec{\tau}dn_{ph} \tag{6.16}$$

or

$$d\vec{\tau} = \frac{1}{n_{ph}}\,(-\vec{\tau}dn_{ph}+\vec{\text{grad}}\,n_{ph}ds) \tag{6.17}$$

since from Eq. (6.13) we have

$$d(n_{ph}\vec{\tau}) = \vec{\text{grad}}\;n_{ph}ds \tag{6.13a}$$

Let $R_s dt = ds$. Then (6.17) becomes

$$d\vec{\tau} = \frac{1}{n_{ph}}\,(-\vec{\tau}dn_{ph}+R_s\vec{\text{grad}}\,n_{ph}dt) \tag{6.18a}$$

or

$$d\vec{\tau} = R_s\,(-\vec{\tau}d(\frac{1}{R_s}) + R_s\vec{\text{grad}}(\frac{1}{R_s})dt) \tag{6.18b}$$

and retaining only the first term of a Taylor series expansion of (6.18a) we have for a small time step Δt

$$\Delta\vec{\tau} = R_s(-\vec{\tau}d(\frac{1}{R_s}) + R_s\,\vec{grad}\,\frac{1}{R_s}\,\Delta t) \tag{6.19}$$

where the expression on the R.H.S. of (6.19) is evaluated at the starting point P_1.

Let $n_{ph}(x_1,y_1) = n_{ph1}$ and $n_{ph}(x_2,y_2) = n_{ph2}$. Then from Eq. (6.15) we obtain

$$n_{ph2}\vec{\tau}_2 = n_{ph1}\vec{\tau}_1 + \vec{\tau}_1\Delta n_{ph} + n\Delta\vec{\tau} \tag{6.20}$$

where

$$n = \frac{n_{ph2}+n_{ph2}}{2}, \Delta n_{ph} = n_{ph2} - n_{ph1}$$ and $\Delta\vec{\tau}$ is given by

Eq. (6.19). Equation (6.20) may be written as follows:

$$\frac{R_F}{R_{s_{P_2}}}\vec{\tau}_2 = \frac{R_F}{R_{s_{P_1}}}\vec{\tau}_1 + R_F(\frac{1}{R_{s_{P_1}}} - \frac{1}{R_{s_{P_2}}})\vec{\tau}_1 + \frac{R_F}{2}(\frac{1}{R_{s_{P_2}}} - \frac{1}{R_{s_{P_1}}})\Delta\vec{\tau}$$

or $$\vec{\tau}_2 = \vec{\tau}_1 + \frac{1}{2}(1 + \frac{R_{s_{P_2}}}{R_{s_{P_1}}})\Delta\vec{\tau} \tag{6.21}$$

Equation (6.19) together with Eq. (6.23) allow us to calculate trajectories of etch rays. For numerical computations we discretize $d(\frac{1}{R_s})$ to $\Delta(\frac{1}{R_s}) = \frac{1}{R_{sP_2}} - \frac{1}{R_{sP_1}}$.

The etch speed $R_s(x,y)$ may be given either as a continuous function of position in the resist or as discrete data at various points in the resist. In the first case analytical expressions of both the x and y components of $\vec{grad}\,\frac{1}{R_s}$ are found and they are evaluated at discrete points along the trajectory of the etch ray (e.g. points P_1, P_2, etc). For discrete etch-rate data, the resist can be divided into a grid of points as shown in Fig. 6.7. All points on the grid are assigned an etch speed $R_{i,k}$ as shown in Figs. 6.8a and 6.8b. In Fig. 6.8a an individual grid square is shown. $A_{i,k}$, $A_{i,k+1}$, $A_{i+1,n+1}$, $A_{i+1,k}$ are areas. Their sum equals A_T, the total area of one grid square. For a point P_1, the etch speed R_{P_1} is given by

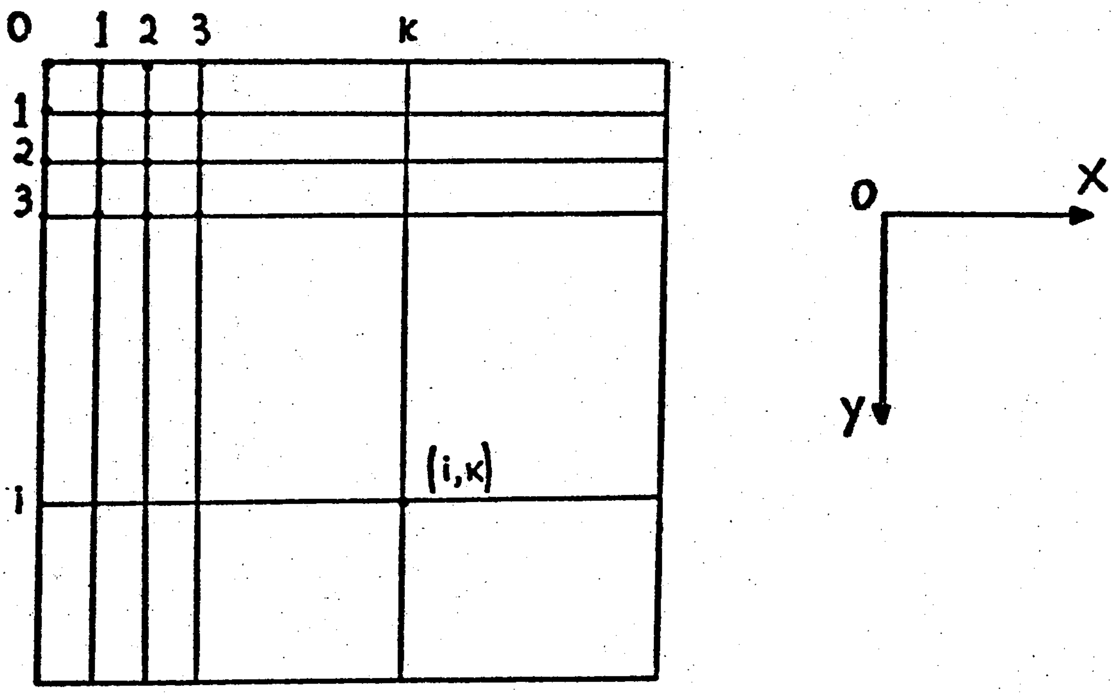

Fig. 6.7. Grid of points for discrete etch-rate data.

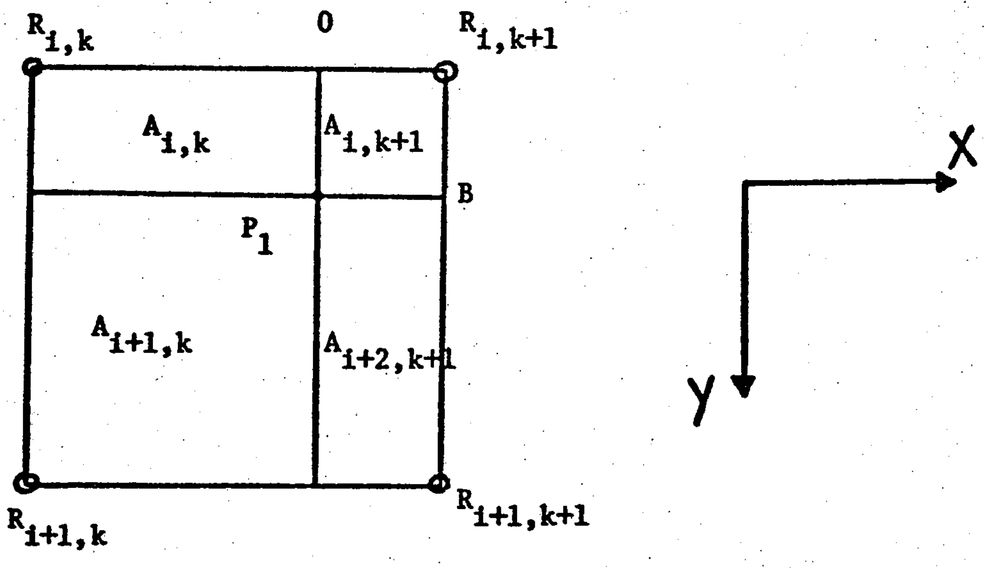

Fig. 6.8a. Definition of R_{P_1}

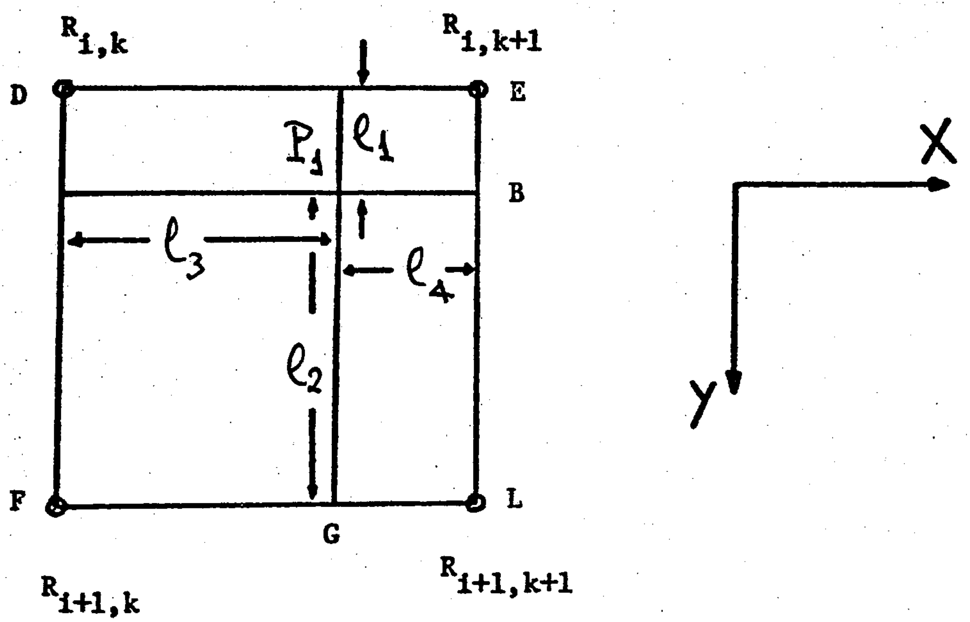

Fig. 6.8b. Definition of $\vec{\text{grad}}(\frac{1}{R})\Big|_{P_1}$

$$R_{P_1} = \frac{(R_{i,k+1})(A_{i+1,k})+(R_{i+1,k+1})(A_{i,k})+(R_{i,k})(A_{i+1,k+2})+(R_{i+1,}{}^{k})(A_{i,}{}^{k}{}_{+1})}{A_T} \tag{6.22}$$

The other two quantities that need to be found are the x and y components of the gradient of $(\frac{1}{R})$. In Fig. 6.8b $\ell_1+\ell_2 = \Delta y = \Delta x = \ell_3+\ell_4 = \ell$. The value of the gradient in the x direction for the side DE is given by (to a linear approximation)

$$\frac{\Delta}{\Delta x}\left(\frac{1}{R}\right) = \frac{1}{\Delta x}\left(\frac{1}{R_{i,k+1}} - \frac{1}{R_{i,k}}\right) = f_1 \tag{6.23}$$

and similarly on FL we have $\frac{\Delta}{\Delta x}(\frac{1}{R}) = f_2$, on DF, $\frac{\Delta}{\Delta y}(\frac{1}{R}) = f_3$ and on EL, $\frac{\Delta}{\Delta y}(\frac{1}{R}) = f_4$.

The components of the gradient of point P_1 are obtained using a length-weighted approximation

$$\frac{\Delta}{\Delta x}\left(\frac{1}{R}\right)_{P_1} = \frac{\ell_2 f_1+\ell_1 f_2}{\ell} \tag{6.24a}$$

and

$$\frac{\Delta}{\Delta y}\left(\frac{1}{R}\right)_{P_1} = \frac{\ell_4 f_3+\ell_3 f_4}{\ell} \tag{6.23b}$$

For both the continuous case and the discrete case, the analysis was carried out in two dimensions. It can be very easily extended to a three-dimensional resist medium with the simple addition of a third coordinate and the third component in all vector equations.

6.3.2. Structure of the Algorithm

Here we discuss briefly the algorithmic approach of determining profiles using the ray-tracing approach.

A. As shown in Fig. 6.9a, k etchs rays are started with direction $\vec{\tau} = \vec{a}_y$ at time t = 0 ($\vec{a}_y$ denotes a unit vector in the y direction).

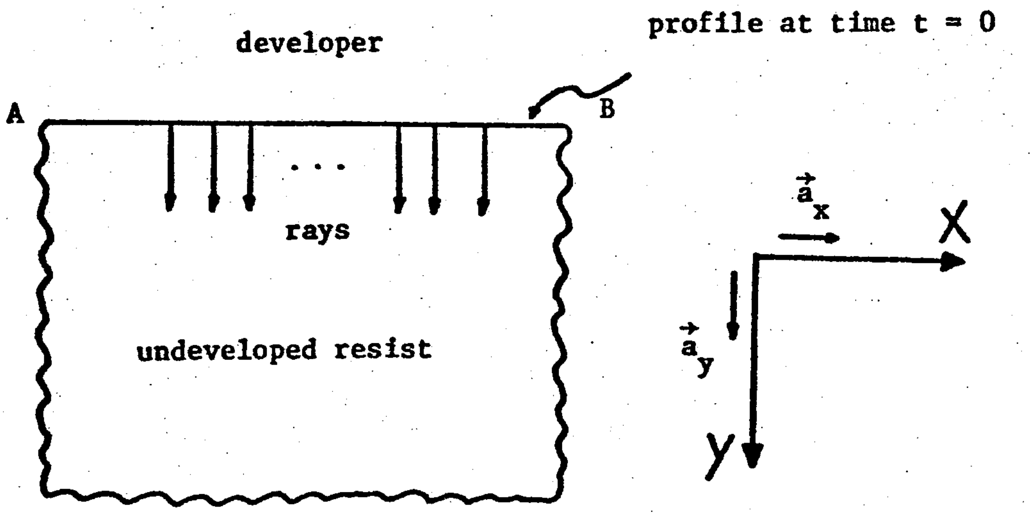

Fig. 6.9a. Initiation of etch rates at time t = 0.

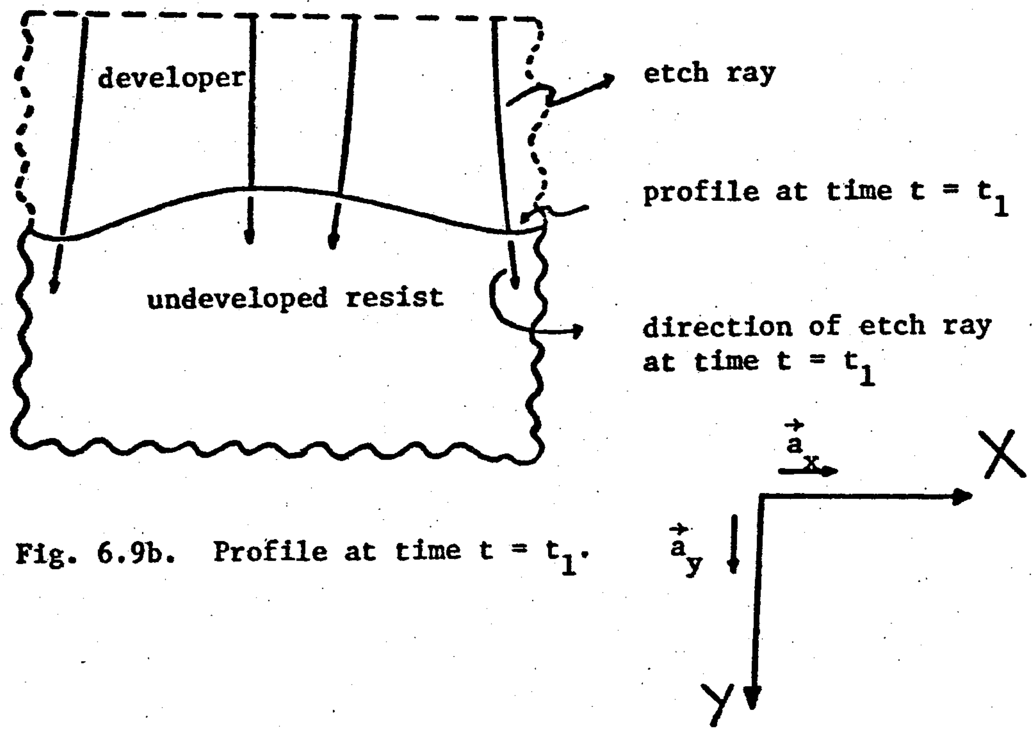

Fig. 6.9b. Profile at time t = t_1.

B. Initially, each ray moves at an etch speed $R_s(x_i^1,0)$ where $(x_i^1,0)$ is the point of origin of the ray on AB. Let t_1 be the total development time and $\Delta t = \frac{t_1}{n}$.

C. Without loss of generality, we consider only one etch ray. In time Δt, the tip of the ray will be at (x_i^2,y_i^2) where $x_i^2 = x_i^1$ and $y_i^2 = R_s(x_i^1,0)\Delta t$ as shown in Fig. 6.10. Using Eqs. (6.19) and (6.21) we obtain $\vec{\tau}_i^2$.

D. As we progress, each time we determine the following

$$x_i^{\ell} = x_i^{\ell-1} + \tau_{ix}^{\ell-1}\, R_s(x_i^{\ell-1},y_i^{\ell-1})\Delta t \tag{6.25a}$$

$$y_i^{\ell} = y_i^{\ell-1} + \tau_{iy}^{\ell-1}\, R_s(x_i^{\ell-1},y_i^{\ell-1})\Delta t \tag{6.25b}$$

and using (6.19) and (6.21) we determine $\vec{\tau}_i^{\ell} = \tau_{ix}^{\ell}\vec{a}_x + \tau_{iy}^{\ell}\vec{a}_y$.

E. At time t_1, the etch ray that originated at $(x_{1,0}^1)$ will have reached point (x_1^{n+1},y_1^{n+1}) will direction $\vec{\tau}_1^{n+1}$. The one that originated at $(x_2^2,0)$ will have reached point (x_2^{n+1},y_2^{n+1}) with direction $\vec{\tau}_2^{n+1}$ and so on. The locus of all the end points of the k etch rays at time t_1 define the developed resist profile at the same time as shown in Fig. 6.9b.

As mentioned in Chapter III and in Section 1 of this chapter (Fig. 6.2), during the actual development of the resist, all points on the developer front act like Huygen's sources of propagating secondary developer fronts, and the new developer front after time dt will be the envelope of all the secondary developer fronts. This means that the developer will act in all directions in the resist at all times; therefore, it is not a necessary condition to start rays normal to the surface as in Step A, but they may be started at any desired direction $\vec{\tau}'$ as shown in Fig. 6.11a. An extention of the above is the branching of rays as shown in Fig. 6.11b.

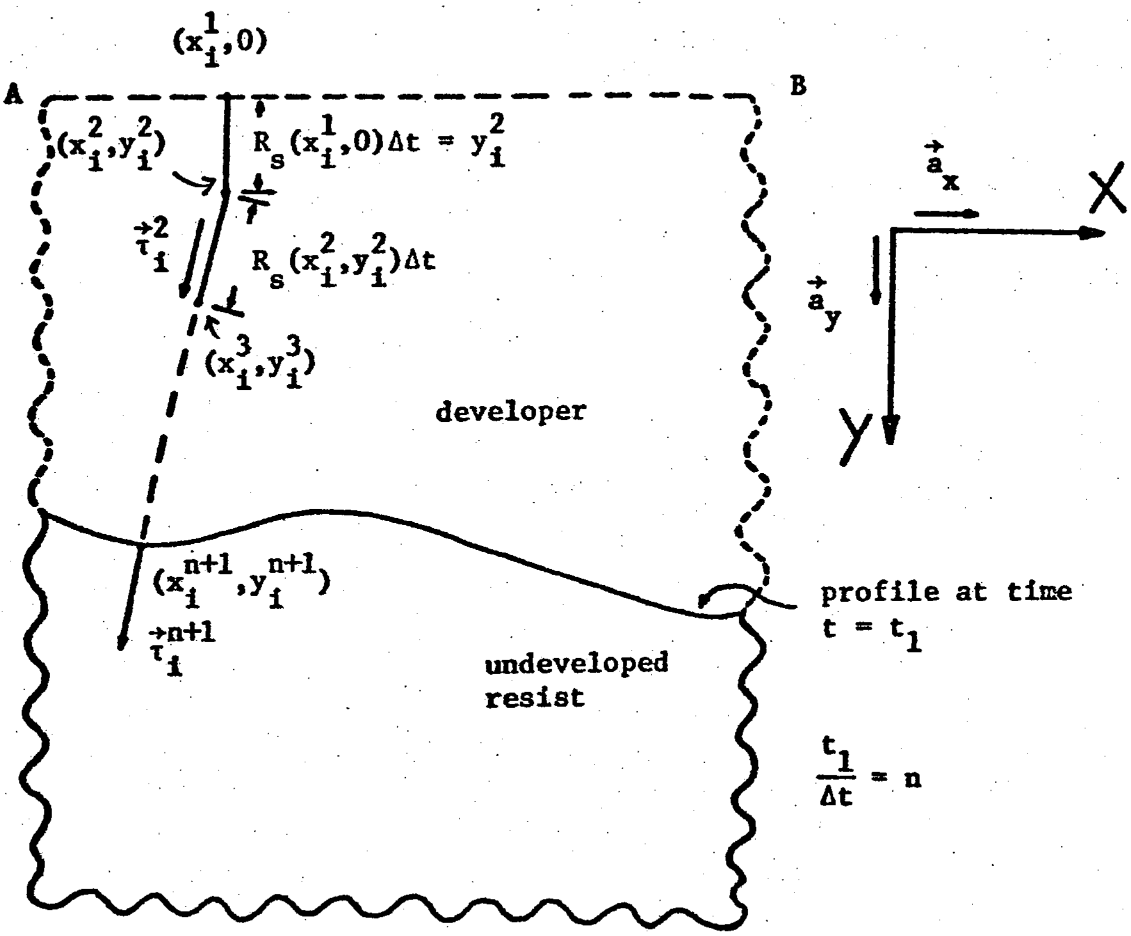

Fig. 6.10. Graphic representation of the ray-tracing algorithm.

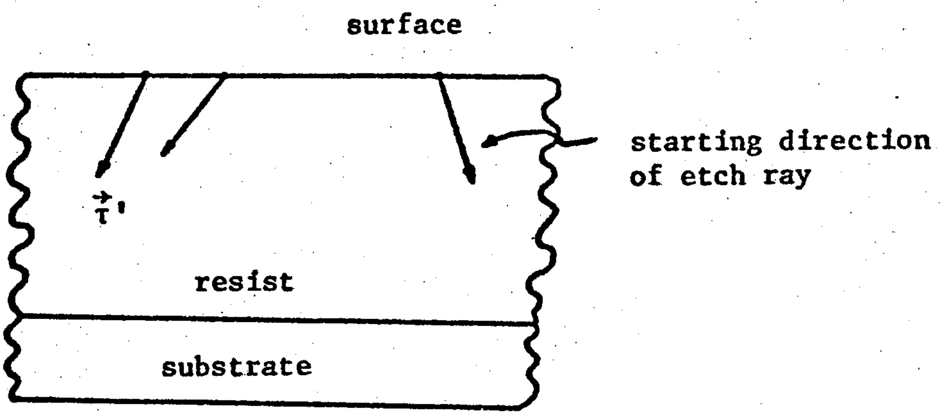

Fig. 6.11a. Initiation of etch rays at a direction other than the normal to the surface.

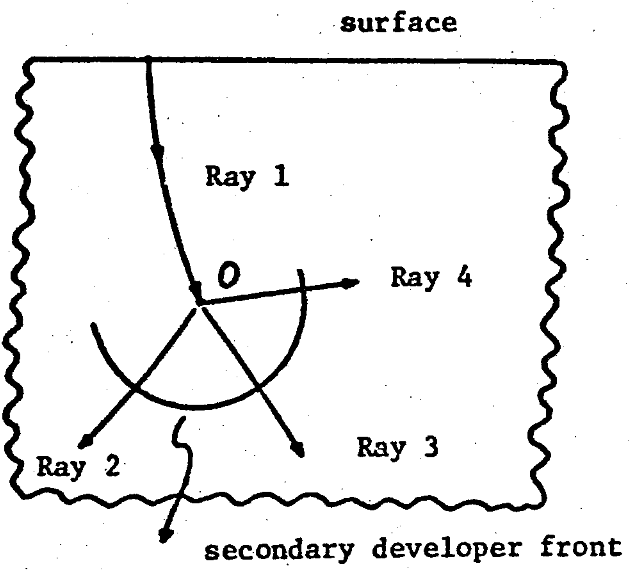

Fig. 6.11b. Branching of a ray.

Due to the discrete time steps used for numerical computation of the trajectories of etch rays and to boundaries where either the etch speed $R_s(x,y)$ or its first derivative vary discontinuously from one side to another, there exists situations where the end points of particular rays have lagged behind the end points of other rays and physically they are now situated in the developer region and not on the developer front. Also, the locus of all the end points might form a profile which contains loops. Since end points of etch rays are on the profile which is ahead of the loop except at the common point A, the loop can be deleted since it was already "etched" by other, faster mvoing rays. Figures 6.12a and 6.12b describe those situations. In Section 6.4 of this chapter, the situation where rays get "trapped" will be discussed in connection with the optical line.

Added features of the ray tracing algorithmic method in predicting resist profiles is its capability to predict 3-dimensional profiles. One feature, particular to this algorithm is its capability of allowing its user to predict only part of the developer front at any time t_1 and not the complete front. This is because each etch ray trajectory does not depend on the trajectories of other etch rays.

B. Results

6.4. Simulation of Developed Resist Profiles: Results

In this part we present our computer simulated results for the cases of x-ray lithographic fabrication of blazed diffraction gratings projection printed images in positive type photoresist, simulated electron-beam exposure with undercutting and etching oxide doped by ion implantation. Results are compared with those obtained using different algorithmic approaches [49] and observations are made concerning the ray-tracing approach.

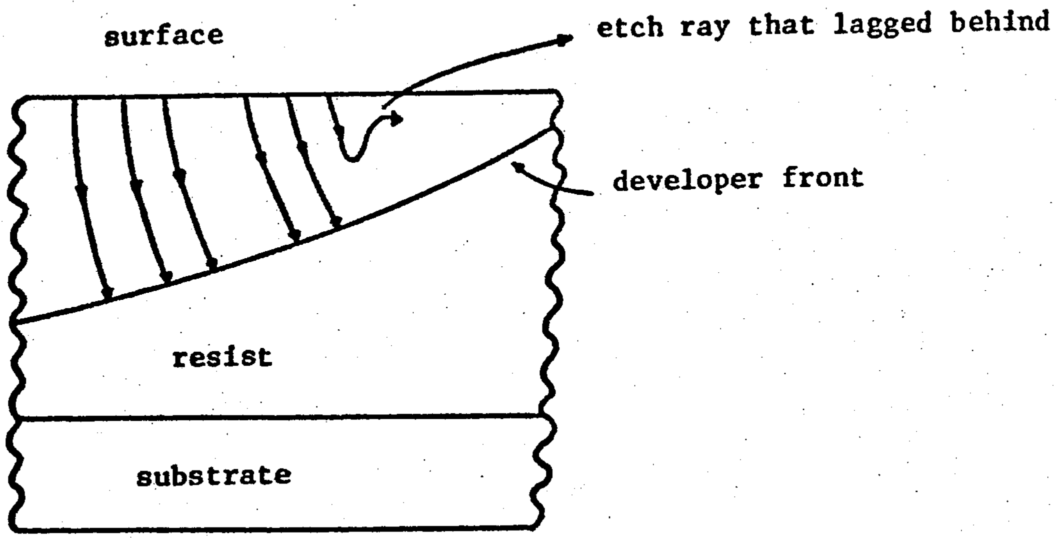

Fig. 6.12a. Lagging of a ray.

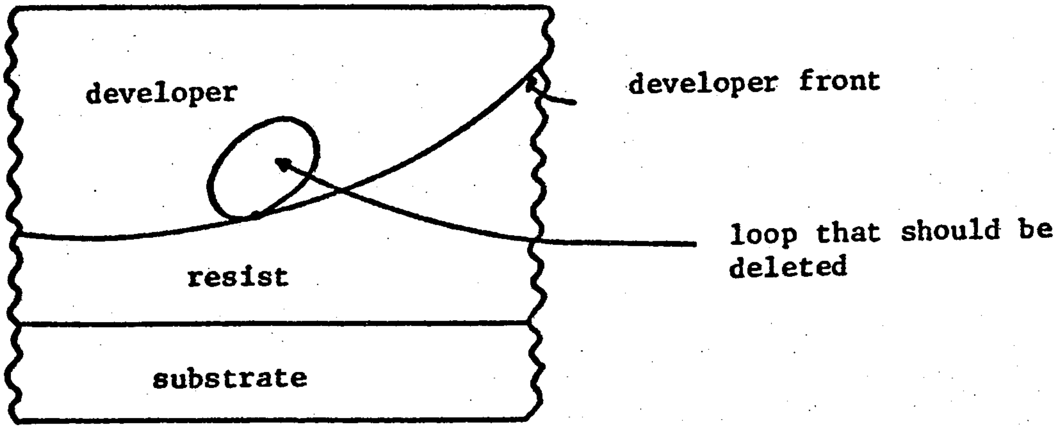

Fig. 6.12b. Loop formation.

6.4.1. Gratings

Figure 6.13 shows the geometry of a two source exposure using a non-planar mask. The mask opening is equal to P/2 where P denotes the grating period; however, it can always be varied. We distinguish five different regions of exposure for the left hand side (the right hand side is the same except that θ_i and θ_R are interchanged). ①, ③ and ⑤ are regions of homogeneous exposure and regions ② and ④ are of inhomogeneous exposure. ① is the region of the fastest etch rate. Using normalized energy dose, ① receives 2 units of exposure and the etch speed is given by $R_1 = 2^\alpha$ where α is the developer exponent (Chapter III). Development time stops when the developer has reached depth h in region ①. Total development time is given by $h/2^\alpha$ where h equals

$$h = \frac{P}{2} \frac{1}{\tan\theta_i + \tan\theta_R} - t \qquad (6.26)$$

In ③ the etch speed is given by $h_3 = [1 + \exp(-\tilde{\alpha}t/\cos\theta_i)]^\alpha$ where $\tilde{\alpha}$ is the linear absorption coefficient of x-rays for gold (4.60517 μm^{-1} for the $A\ell_{k_\alpha}$ line and 13.4798 μm^{-1} for the Cu_{L_α} line). In ⑤, $R_5 = [\exp(-\tilde{\alpha}t/\cos\theta_i) + \exp(-\tilde{\alpha}t/\cos\theta_R)]^\alpha$. In region ②, $R_2(x,y) = [1 + \exp(-\tilde{\alpha}(t-x\cot\theta_i+y)/\cos\theta_i)]^\alpha$ and in ④, $R_4(x,y) = [\exp(-\tilde{\alpha}t/\cos\theta_i) + \exp(\tilde{\alpha}(x+y\tan\theta_R)/\sin\theta_R)]^\alpha$. At this point, it should be emphasized that we assume perfect contact between mask and resist-substrate and a collimated beam of x-rays.

Figure 6.14 shows the results for a 1 μm grating line. They were obtained using a CDC 6400 digital computer. Parameter values are shown on the picture. The development profile is shown for the following times: .2T, .4T, .6T, .8T and T where T denotes total development time. The loops that have formed are mainly due to the strong focusing (i.e. bending

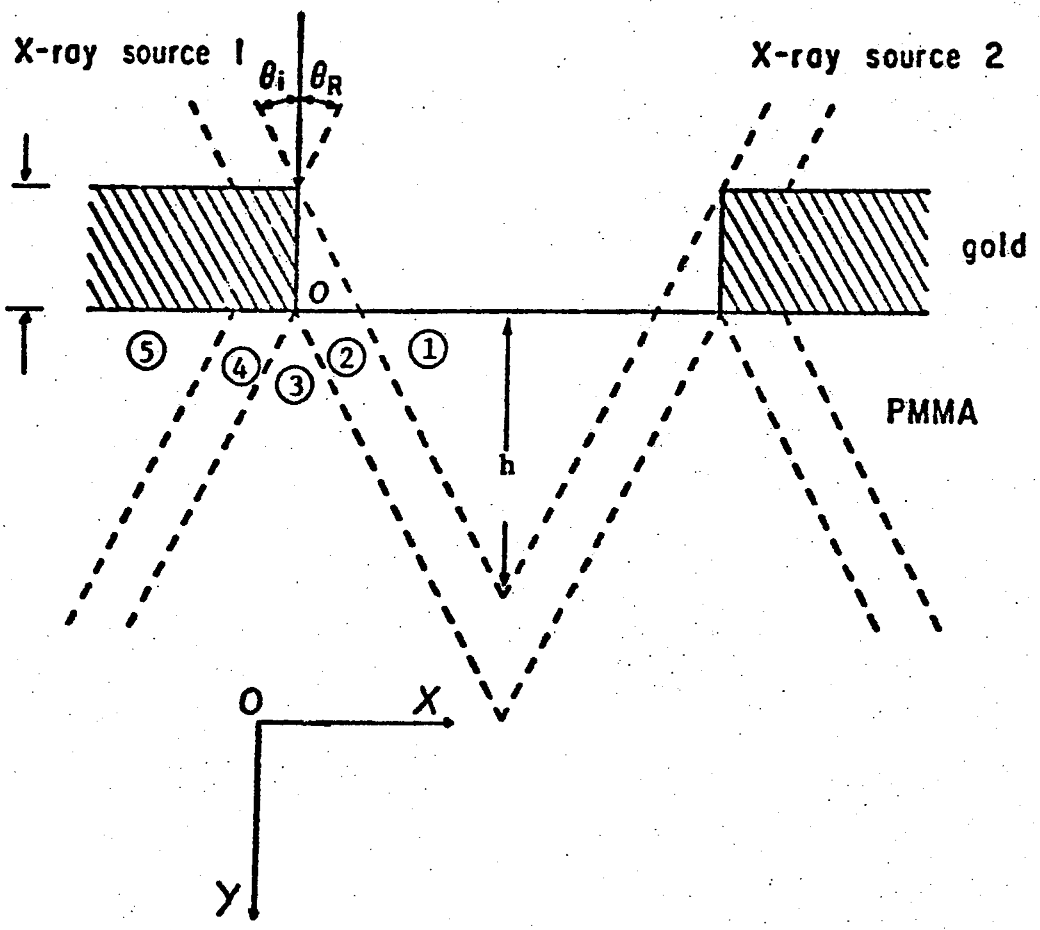

Fig. 6.13. Geometry for a two source exposure.

$\alpha = 3.4$

$\tilde{\alpha} = 4.60517$

$\theta_i = 20°$

$\theta_R = 15°$

$t = 0.2\ \mu m$

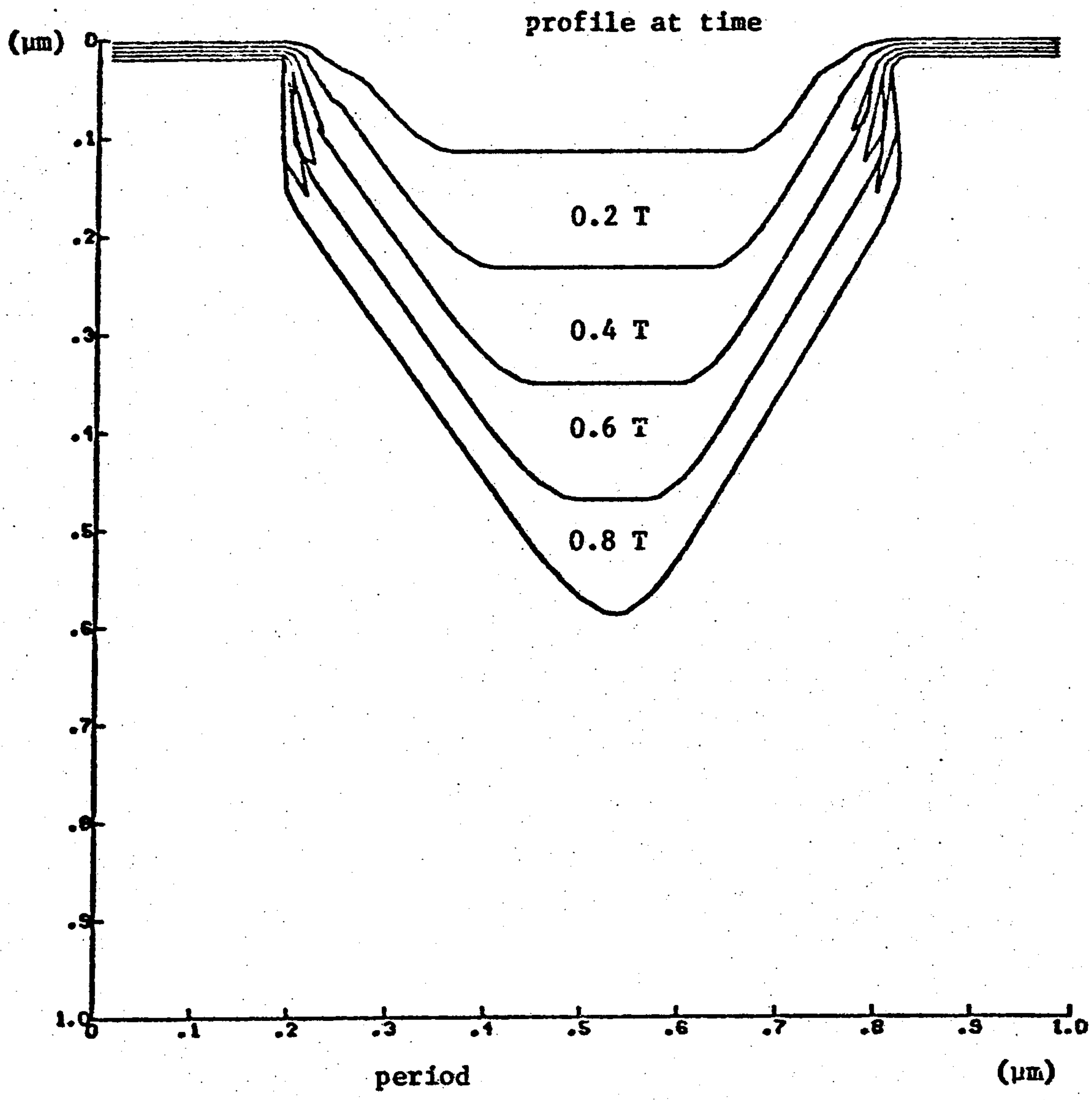

Fig. 6.14. 1 μm grating profile. T is total development time.

of rays) effect of the gradient of $1/R_{21}(x,y)$. They are also partly due to the discontinuity of the etch rate from region ③ to ④. The loops should be disregarded (Chapter VI, Section 6.3.2.). The results indicate that the mask opening may be increased so that two neighboring sloping facets will intersect for a better blazed grating structure.

Figure 6.15 shows the results for a .5 μm grating line. The groove angle has increased as compared to that of the 1 μm line due to a decrease in mask contrast. For a .3 μm line (Fig. 6.16) a further decrease in gold thickness resulted in a still larger groove angle as compared with the two previous cases. This in trun indicates that for a further decrease in gold thickness, the Cu_{L_α} irradiation should be used in order to increase the contrast of a very thin absorbing mask. Figure 6.17 shows the results for a .1 μm grating line where Cu_{L_α} irradiation was used. For both the .3 μm line and the .1 μm line, steep source angles ($\theta_i = 15°$, $\theta_R = 10°$) were used in order to further limit the value of the groove angle.

6.4.2. Optical Line

The development of a projection printed 1 μm line in positive photoresist on a reflecting substrate was examined by Dill, et al. [39]. In this case we assume a 5000 Å thick photoresist layer on top of a reflecting substrate. Due to transverse standing waves in the resist the normalized variation of the etch rate in the y direction is approximated as in Fig. 6.18b. The normalized variation of the etch rate in the x-direction is a gaussian as shown in Fig. 6.18a. This is an approximation of a lens function. X is given by

$$X = \exp(-x^2/5000^2) \qquad (6.27)$$

$\alpha = 3.4$

$\tilde{\alpha}$ 4.60517

θ_i 20°

θ_R 15°

$t = 0.1$ μm

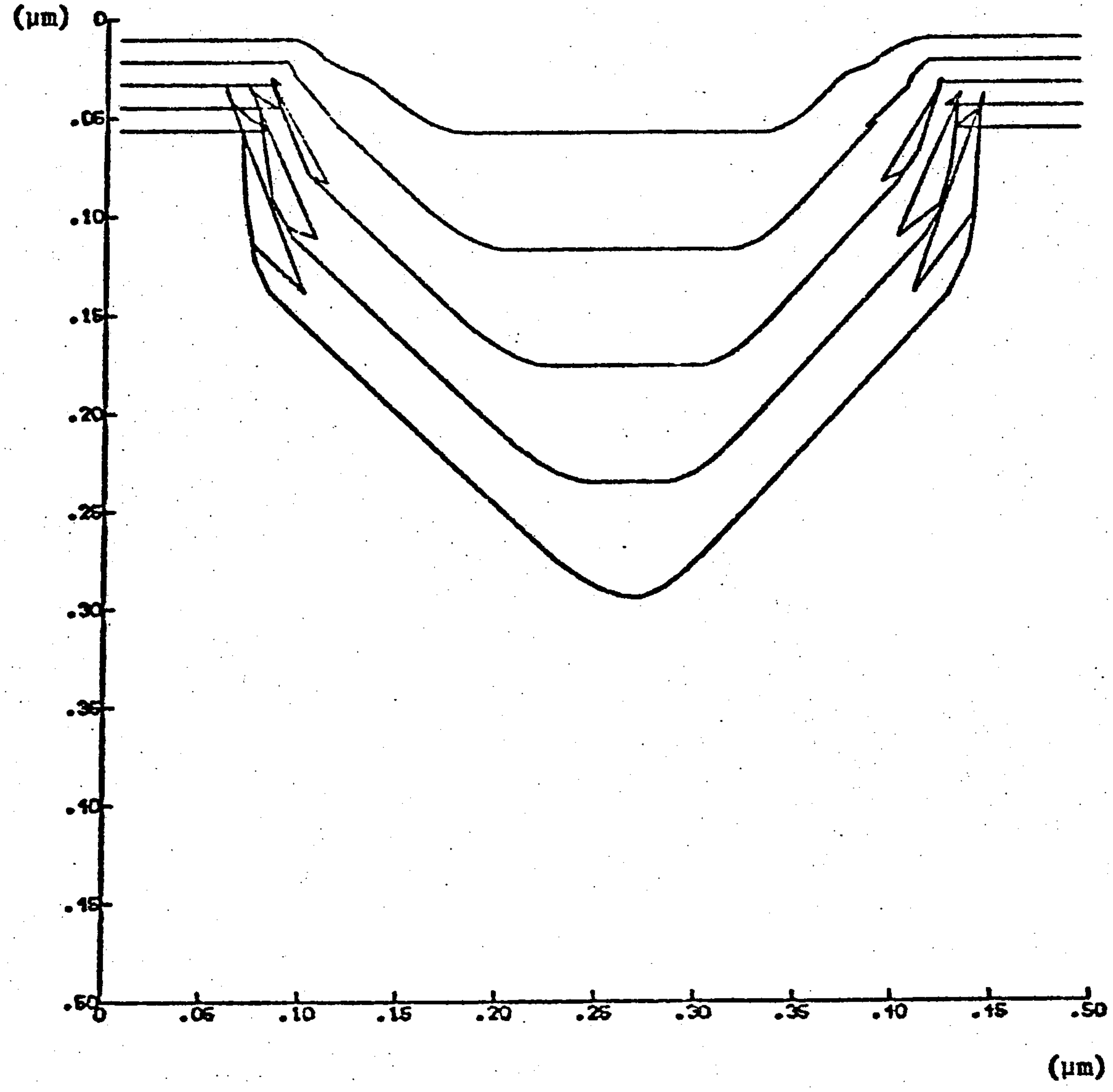

Fig. 6.15. 0.5 μm period grating profile.

$\alpha = 3.4$

$\tilde{\alpha} = 4.60517$

$\theta_i = 15°$

$\theta_R = 10°$

$t = 0.06\ \mu m$

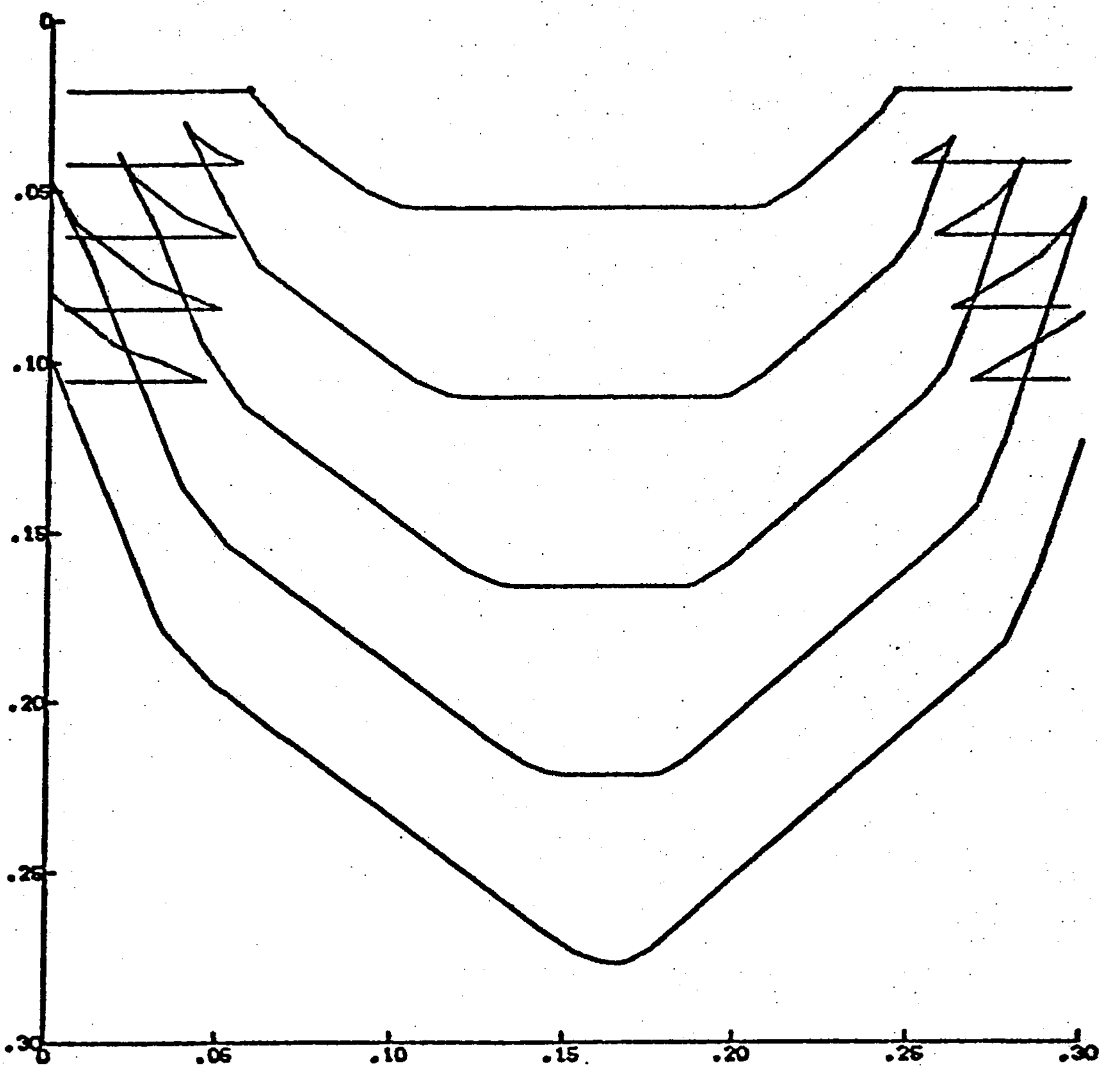

Fig. 6.16. 0.3 μm period grating profile.

$\alpha = 3.4$

$\tilde{a} = 13.4798$

$\theta_i = 15°$

$\theta_R = 10°$

$t = 0.02\ \mu m$

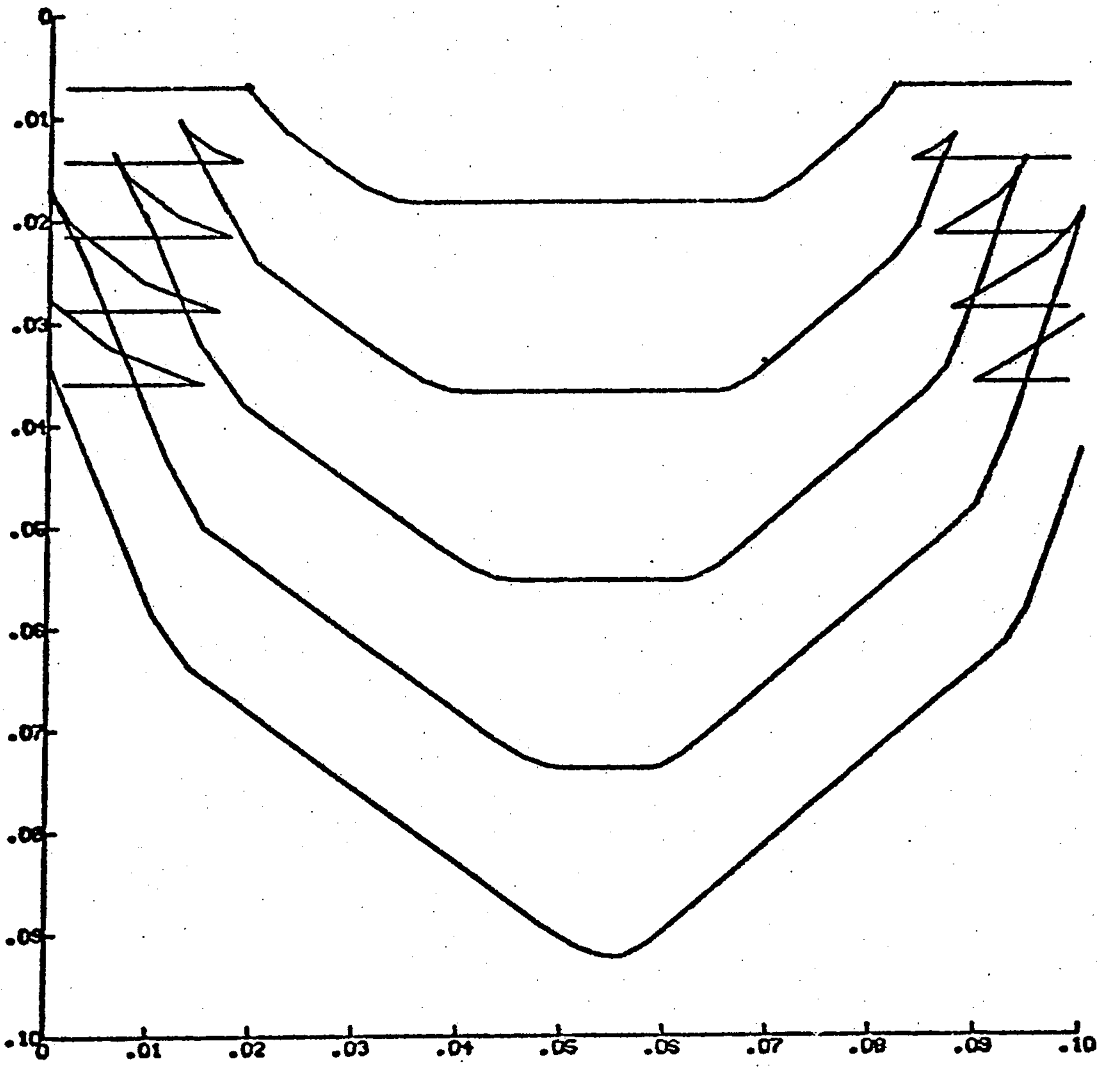

Fig. 6.17. 0.1 μm period grating profile.

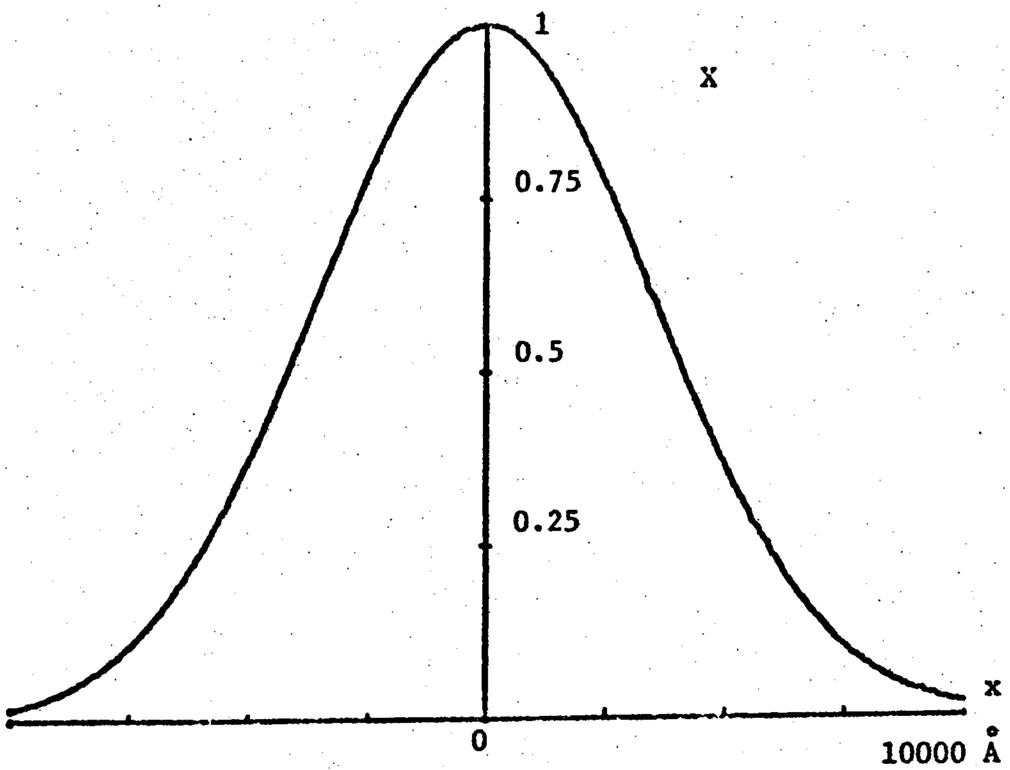

Fig. 6.18a. X vs. x.

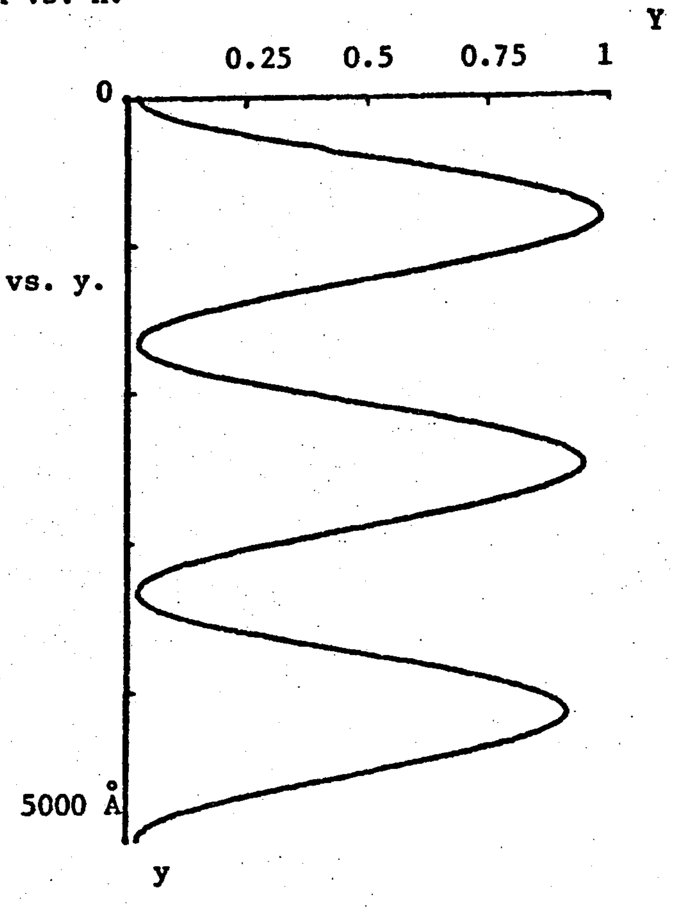

Fig. 6.18b. Y vs. y.

and Y is given by

$$Y = \frac{1}{2.05}(1 - .1 \frac{y}{5000})(1.05 - \cos(2\pi \frac{y}{1667})) \quad (6.28)$$

The etch rate R(x,y) is given by R(x,y) = 400 XY Å /second. The ray calculations were done interactively on a desk calculator (HP9820) due to little memory nned. Figure 6.19 shows ray trajectories for a total development time of 120 seconds. We notice ray-scarce regions (between 403 and 404 and between 860 and 870 where the numbers indicate the initial x-coordinate of the ray (time t = 0)) and ray-crossing regions. The later is an example of ray "trapping" [52]. In this particular case both the ray-scarce regions and the ray-crossing regions are due to the fact that the curvature of a ray is directly proportional to the gradient of the inverse etch rate (Chapter VI, Sections 6.1-6.3) [53]. The gradient variations in this case are large. The ray always curves toward a region of minimum etch rate; such a region will tend to form a "wave" guide for developer propagation. Notice that the ray-crossing regions correspond to the valleys of the Y function. Interacting with the calculator we determined the initial x-coordinates of rays so that information for the ray-scarce regions was obtained. In particular we noticed that information for the fingers corresponding to fast regions of development (and also ray-scarce), was obtained from rays which originated in a .01 Å interval for the deepest finger, in a .1 Å interval for the middle finger and a .2 Å interval for the shallowest finger. Figure 6.20 shows our results. Tick marks indicate both the end points of rays corresponding to 120 seconds development time and the intermediate results for 30 seconds, 60 seconds and 90 seconds. Figure 6.21 shows the end result when the end points of the rays are joined with a smooth curve. Development times

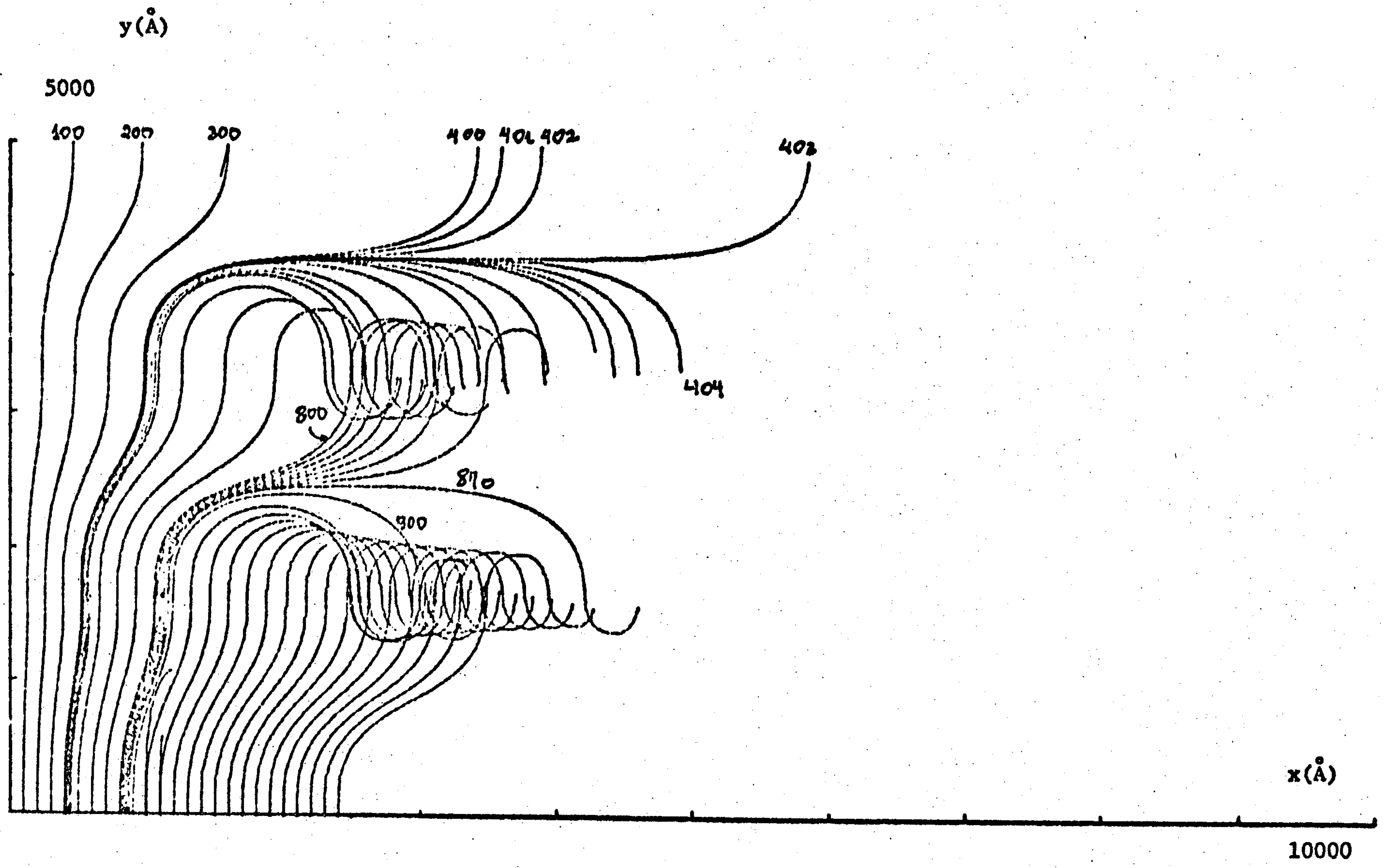

Fig. 6.19. Ray-tracing of the optical line with both ray-scarce and ray-crossing regions.

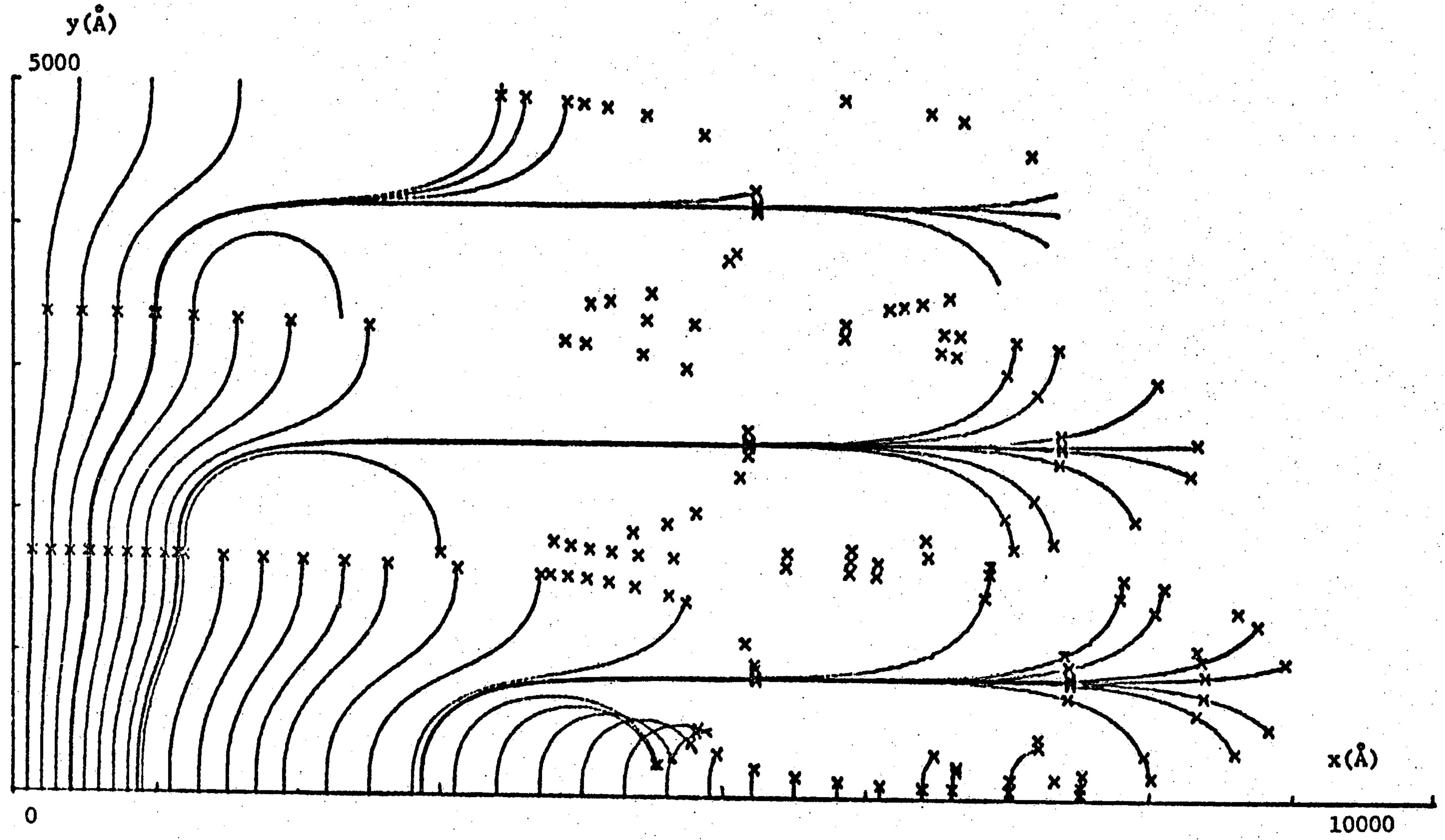

Fig. 6.20. Ray-tracing of the optical line. The tick masks define the profile for four different development times (30, 60, 90, and 120 seconds).

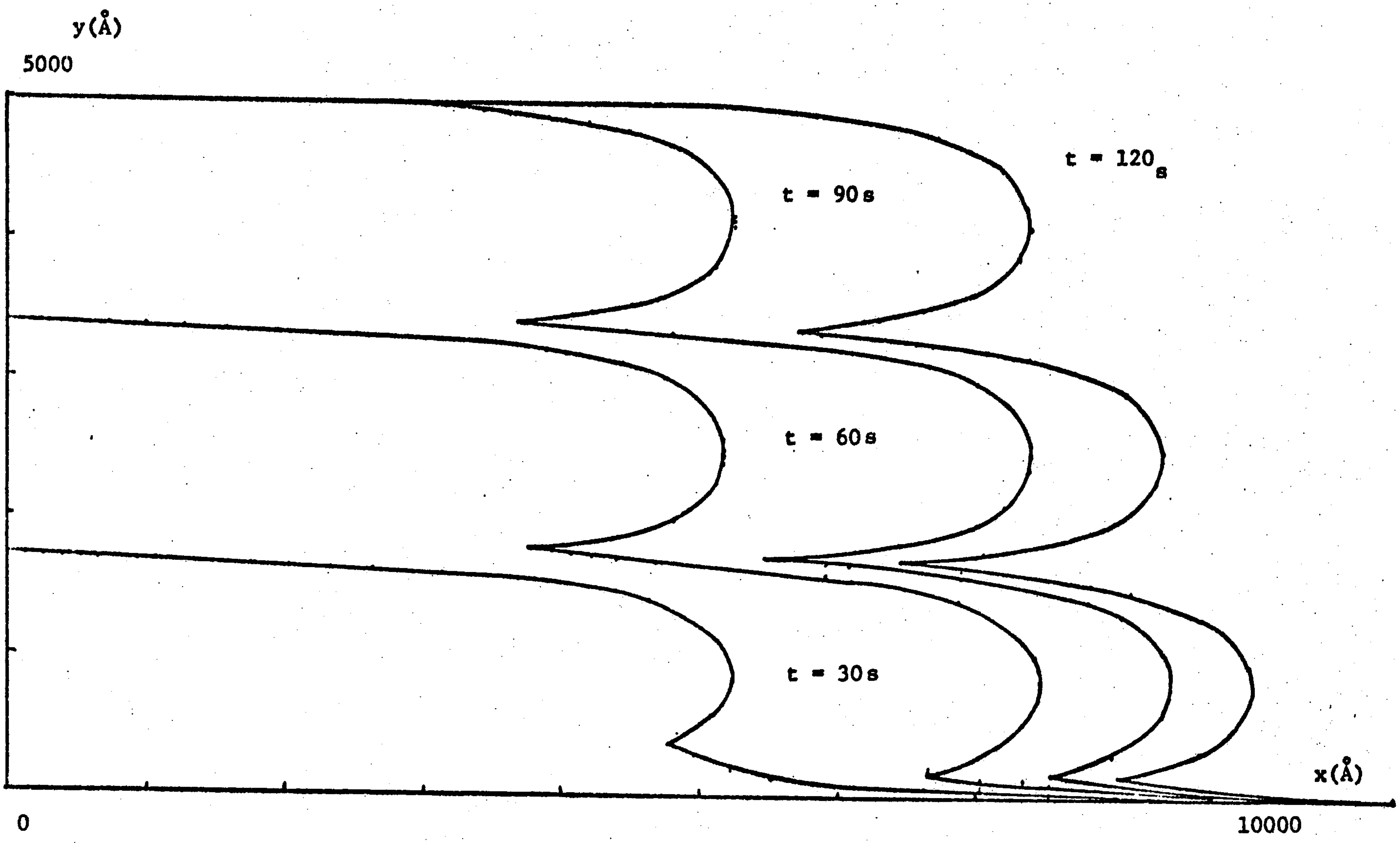

Fig. 6.21. Profiles for 30, 60, 90 and 120 s for the optical projection printened 1 μm line.

are indicated on the graph. Except for a very small portion of only one of the curves, our results agree exactly with those obtained using the string model [49]

6.4.3. Simulated Electron-Beam with Undercutting

Figure 6.22 shows the results of a simulated electron-beam exposure. The etch rate $R(x,y)$ is given by

$$\left.\begin{aligned} R(x,y) &= 10-(x^2)\,\frac{1}{1+y/8} \\ R_{\text{minimum}} &= 0.5 \end{aligned}\right\} \qquad (6.29)$$

where $R = 0.5$ if $R(x,y) \leq 0.5$. The developed resist profiels are shown for five normalized times. The loops at the corners are due to the discontinuity of the first derivative of $R(x,y)$ at points where R becomes equal to 0.5. They should again be disregarded. They were not deleted for information purposes. A "loop deleter" developed by Jewett [54], used in conjunction with the main calculating program would remove the loops. The computations were carried out using a digital computer (CDC 6400). Our results agreeded exactly with those obtained using the string model.

6.4.4. Ion-Implantation Doped Oxide

For the case of an oxide doped by ion implantation, the configuration is shown on the top right part of Fig. 6.23. For the unmasked region the etch rate is given by $R(x) = \left(5 - \frac{(x-.15\ \mu\text{m})^2}{(.15\ \mu\text{m})^2}\right) \text{x}\ 2.4$ Å/second for $x \in [0, .45\ \mu\text{m}]$ and 2.4 Å/second for all other x. (Note: Here x denotes depth). The etch rate in the masked region is 2.4 Å/second. Figure 6.23 shows the profiles in the masked region for two development times (1000 seconds and 500 seconds). The results are obtained by taking the

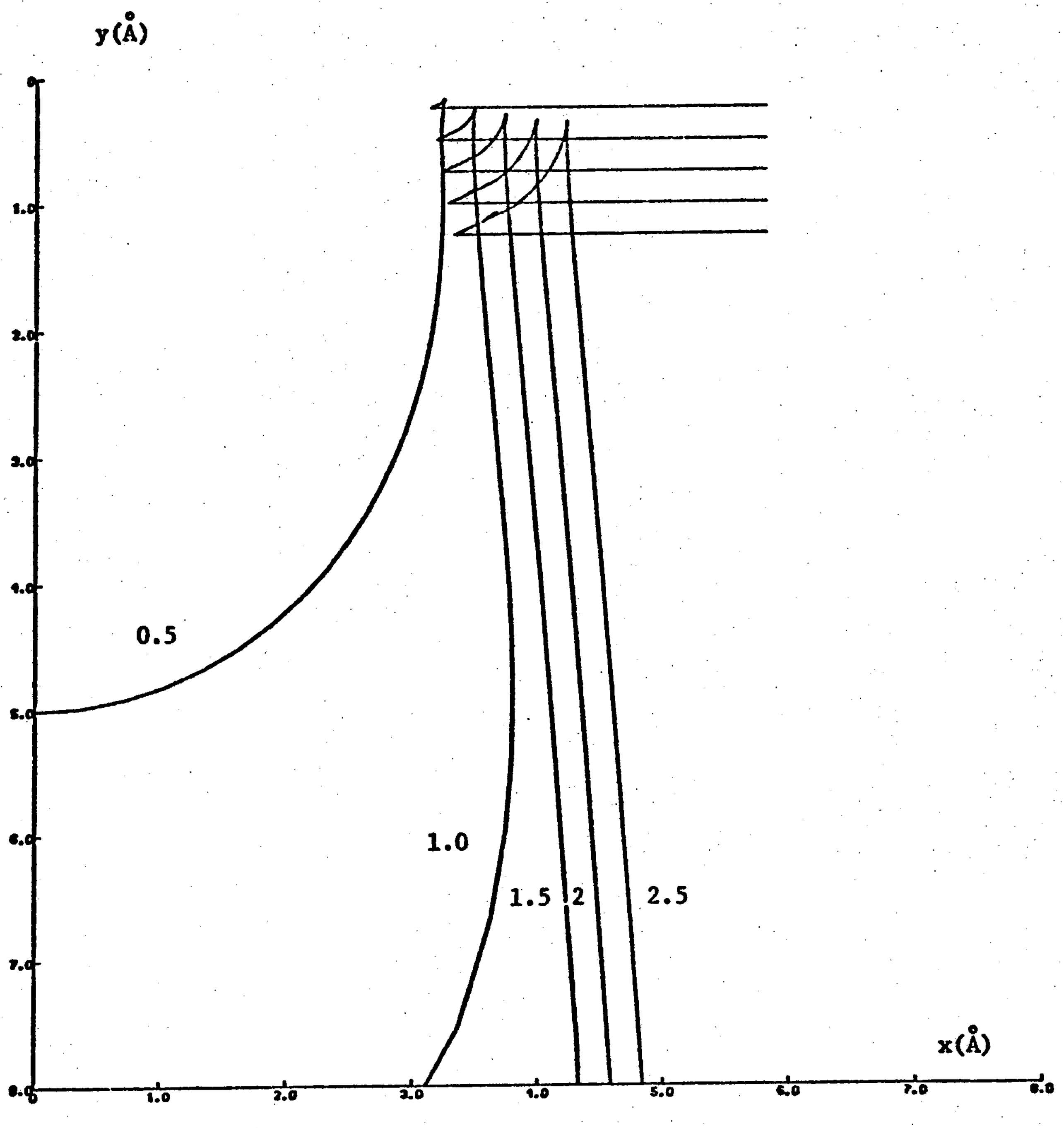

Fig. 6.22. Simulated electron-beam exposure profiles for times indicated.

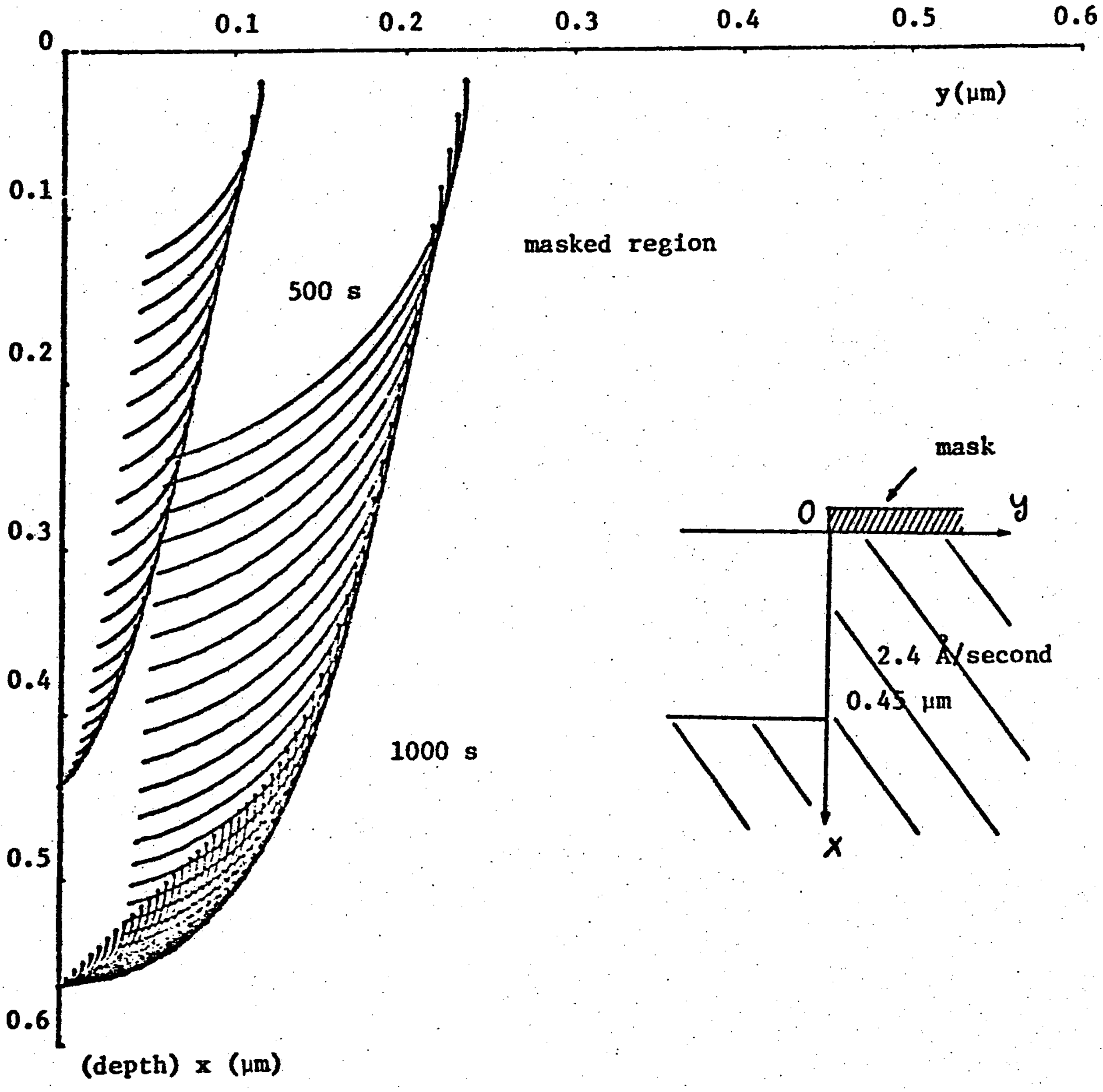

Fig. 6.23. Profiles in the masked region of ion-implanted oxide.

envelope of all the secondary developer fronts originating at points on the axis $y = 0$. This is an example of branching of rays. A ray is started at (0,0) and at regular intervals as it progresses down the axis $y = 0$, secondary rays are started at various angles from the same point on the axis. They are allowed to progress for the remaining development time. It should be noted that the same results may be obtained much more quickly with single branching, where the initial direction of the branching ray makes an angle of $90° - \text{arc}\sin(\frac{2.4}{R(x,y)})$ degrees with the positive x-axis. This corresponds to the optical case of a ray incident at an angle of 90° in the interface between two media of different light speed and refracted according to Snell's law. The above demonstrates the close relation that the development process bears with geometrical optics. Figure 6.24 shows the actual profiles for various times. Our results agree to within a time step (10 seconds) with the ones obtained using the string model. Another approach shows that our results are exact. This approach consists of the application of Fermat's principle starting at the end point of the profile situated at the axis $y = 0$ and working backwards [54].

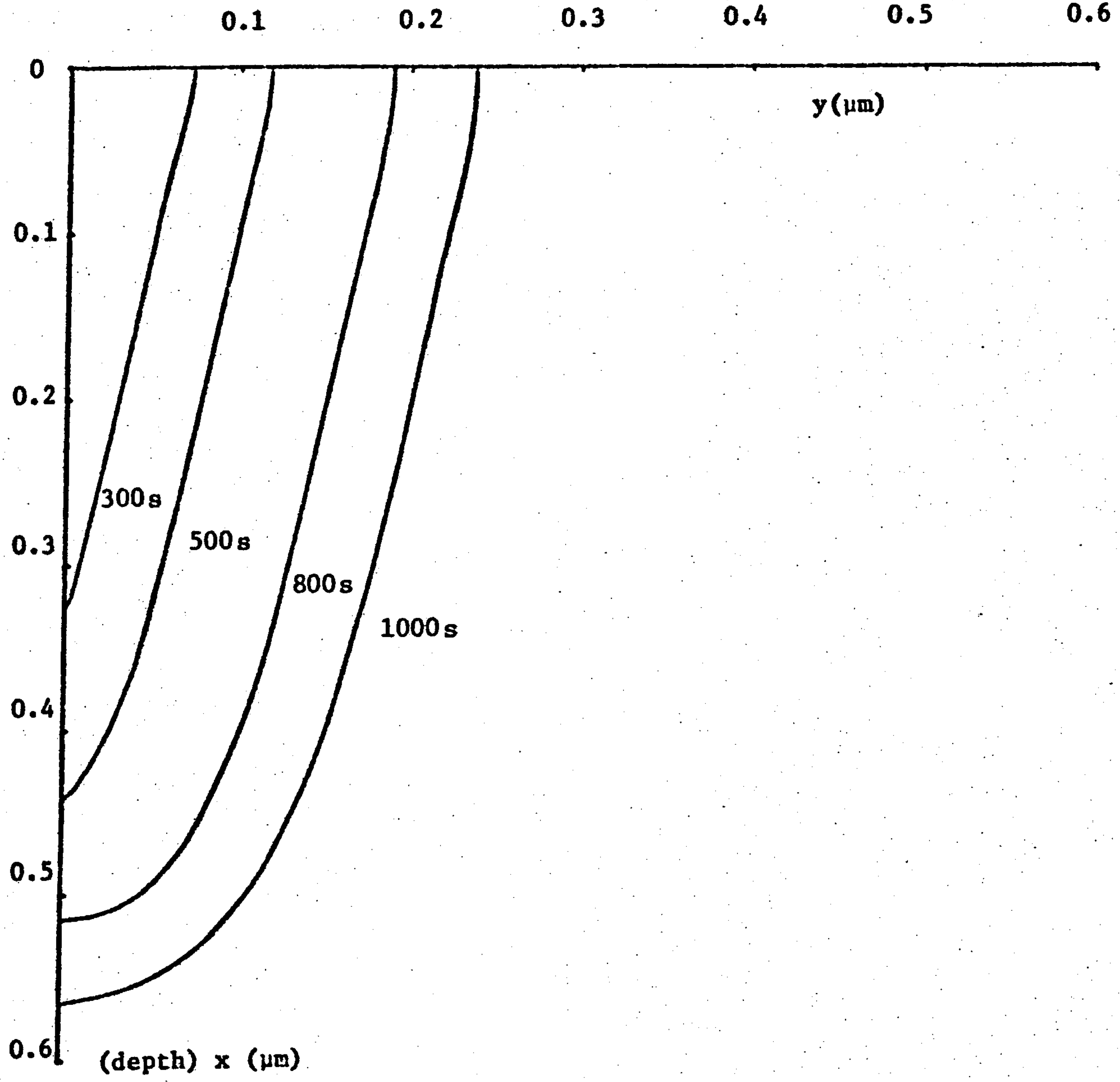

Fig. 6.24. Profiles in the masked region of the ion-implanted oxide for four different times.

CHAPTER VII

CONCLUSIONS AND DISCUSSION OF RESULTS

The feasibility of making small-period blazed diffraction gratings with x-ray lithography was explored both theoretically and experimentally. Using both a simple algebraic model and a more rigorous simulation approach, very promising results have been predicted. Experimental results have been achieved, but further technological development in several areas are needed to realize the gratings of the quality of the theoretical prediction. The theoretical and experimental prognosis will now be discussed in detail.

Using a simple algebraic model and assuming a planar mask (Chapter III) we have shown that for a mask to period ratio of .2, it is possible to make a .1 μm grating with a minimum groove angles of 100° using $A\ell_{k_\alpha}$ irradiation. More rigorous simulation of the etching process validated the above conclusion. It is certainly possible to make gratings with periods about a factor of 3 smaller with blazed profiles similar to those of ruled gratings at 3600 lines/mm. Resolution of .1 μm geometry using $A\ell_{k_\alpha}$ irradation was reported [28].

In Chapter VI we have shown that for a two-source exposure, the $A\ell_{k_\alpha}$ irradiation is sufficient to produce a .3 μm blazed grating of acceptable groove angle (~ 110°). However, for fabrication of .1 μm gratings longer wavelength x-ray irradiation is needed both for increased contrast and for lower photoelectron range. The maximum range of secondary electrons (photoelectrons) generated by the Cu_{L_α} line in PMMA is 500 Å [11]; therefore, for .1 μm gratings Cu_{L_α} irradiation is needed along with a lower absorption mask support than the 3 μm silicon membrane.

An aluminum-oxide mask should be considered. Carbon K_α (44.8 Å) irradiation should also be considered for even finer resolution and detail for .1 μm geometries. Further theoretical and simulation studies should involve the incorporation of a suitable model for the photoelectron range in the exposure model for increased accuracy of simulation results for small geometries (.3 μm to .1 μm).

One of the most important technical problems we have is that of the penumbra. Large penumbras washed out our gratings and severly limited the resolution of our system [55]. The actual penumbra of our system is calculated to vary from around .2 μm to .4 μm. It is obvious that such large values defeat our efforts of groove shape control even for 1 μm period gratings as results indicate (Chapter V). For a .5 μm mask opening and a gold thickness of .2 μm (40% transmission for $A\ell_{k_\alpha}$), the results of simulating the effects of the penumbra are shown in Fig. 7.1. A line source and normal incidence are assumed. Parameter values are shown on the figure. The line shapes are symmetrical with respect to the vertical axis.

The penumbra equation (Chapter III) implies that in order to minimize it, good contact and a small source spot size is required if the source to substrate distance is assumed fixed. For a 1 mm spot size and a source to substrate distance of 100 mm, the maximum (mask to substrate) gap that can be tolerated for a .3 μm grating is 2.5 μm for a .025 μm penumbra and for a .1 μm grating a 1 μm gap for a .01 penumbra.

Good contact between mask and substrate is closely related to mask fabrication. A smooth gold mask surface with no irregularities such as gold grain nodules is of prime importance if good contact should be achieved. The quality of gold evaporated films is difficult to control.

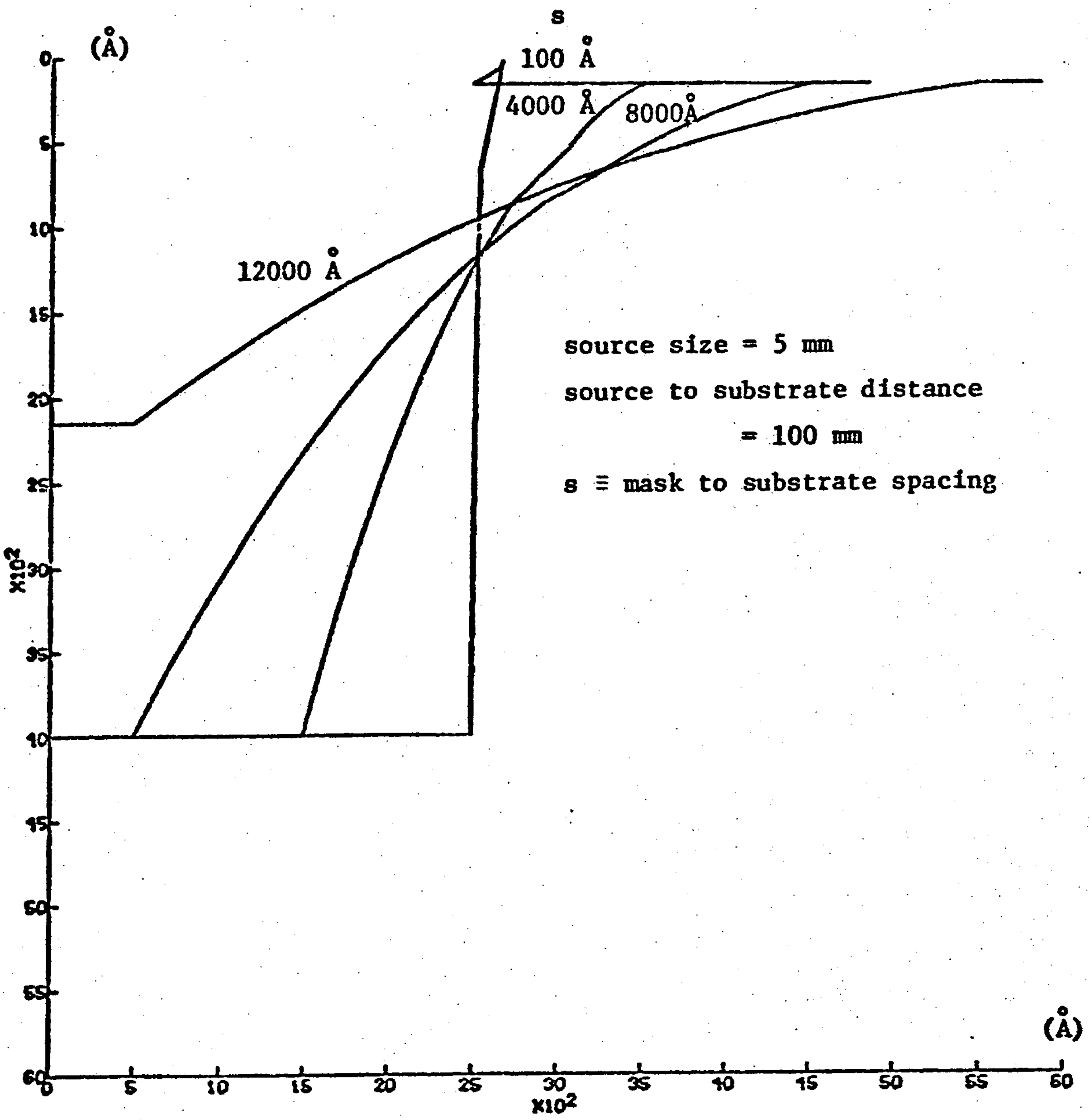

Fig. 7.1. The penumbra effect on a 1 μm line for various s. Half of the line is shown. Mask opening is 0.5 μm.

Further study is needed of the quality of both evaporated and r.f. sputter deposited gold films. Also, for intimate contact, an electrostatic scheme should be studied [30].

The fabrication of the gold mask pattern is closely related to that of the holographic fabrication of photoresist gratings on top of the gold reflecting layer. Further studies are needed in order to better control the resist profiles for various grating periods, resist thicknesses and postbaking conditions so that the final gold grating bars have no depression in the center such as shown in Chapter IV. For .3 μm grating periods and lower, ion-beam sputter etching is a must for better control of the gold etching and for mask-edge resolution. Sloping mask sidewalls are controllable only to the extent that the liftoff of the photoresist etch mask is controllable especially at the edges. The relative etch rates of gold and AZ1350J positive photoresist during r.f. sputter etching if the substrate cooling, input power and the argon gas pressure are varied should be determined experimentally. Due to both thin resist films required for the holographic fabrication of small period gratings that open to the gold surface and liftoff during sputter etching, gold layer thickness will be limited, therefore the Cu_{L_α} line may even be needed in order to fabricate .3 μm gratings.

Improvement of the x-ray source (smaller spot size, no or low tungsten target contamination, higher power output) is of importance for submicron resolution lithography. Good x-ray sources have been reported [23] [17] [56].

We believe that further work in order to produce results comparable to the theoretically predicted ones is worth the effort. The direction is clear where progress should be made and new approaches to that end are available as mentioned above. In many cases the technological development parallels that needed in other applications of high resolution lithography such as IC fabrication. Technological advances realized in the application of x-ray lithography to both diffraction grating and IC fabrication will be mutually beneficial.

APPENDIX

PREPARATION OF THE X-RAY RESIST

Here we briefly describe the steps involved in preparing our PMMA resist solution, and the preparation of resist coated flexible glass substrates.

A.1. Preparation of the Resist Solution

Initial preparation of the PMMA powder (leaching) follows the steps described by Greeneich [57]. The preparation of the resist solution is done as follows:

1. Mix PMMA power with trichloroethylene by weight for desired solution concentration.

2. Stir the mixture for an hour using a magnetic spinner. After one hour the solution will look clear.

3. Centrifuge the solution for an hour. Pour the solution into a tightly covered container.

4. Refrigerate in order to inhibit thermal degradation of the resist. Remove the container from the refrigerator at least an hour prior to resist application, in order for the resist temperature to reach ambient temperature.

A.2. Preparation of the PMMA Coated Substrate

This involves cleaning flexible glass mask substrates, coating them with PMMA and prebaking them. The steps are as follows:

1. Clean the substrate by degreasing in 60°C trichloroethylene for 10 minutes, by dipping in cold acetone for 1 minute, by rinsing in Di H_2O for 1 minute and by immersion in a 75°C solution of 5:1:1, $H_2O:NH_4OH,H_2O_2$

for 12 minutes. Rinse in DI H_2O for 2 minutes. The flexible glass substrate should be hydrophylic at this stage. Blow dry with N_2.

2. For an extra dry surface for good resist adhession, drying under an infrared lamp immediately before coating is recommended.

3. Flood the substrate with PMMA. A spinning speed of 3000 rpm for a 6% solution of PMMA gives a coating around 1.4 μm thick.

4. Prebake at 165°C for 15 minutes.

5. Avoid exposing the substrate to light in order to inhibit ultraviolet degradation.

BIBLIOGRAPHY

1. S. Hayat and G. Pieuchard, Handbook of Diffraction Gratings, Ruled and Holographic, Jobin Yvon Optical Systems, 1973.
2. E. W. Palmer, M. C. Hutley, A. Franks, J. F. Verrill and B. Gale, "Diffraction Gratings," Rep. Prog. Phys., 1975, vol. 38, pp. 975-1048.
3. C. V. Shank and R. V. Schmidt, "Optical Technique for Producing 0.1 μm Periodic Surface Structures," Appl. Phys. Lett., vol. 23, no. 3, Aug. 1973, pp. 154-155.
4. L. Levi, Applied Optics, vol. 1, John Wiley & Sons, Inc. New York, 1968.
5. D. L. Spears and H. I. Smith, "X-Ray Lithography - A New High Resolution Replication Process," Solid State Technology, vol. 15, no. 7, July 1972, pp. 21-26.
6. R. M. Eisberg, Fundamentals of Modern Physics, John Wiley & Sons, Inc., New York, 1961.
7. N. A. Dyson, X-Rays in Atomic and Nuclear Physics, Longman Group Limited, London, 1973.
8. A. H. Compton and S. K. Allison, X-Rays in Theory and Experiment, D. Van Nostrand Company, Inc., New York, 1935.
9. V. E. Cosslett and W. C. Nixon, X-Ray Microscopy, Cambridge at the University Press, 1960.
10. M. Green, "The Target Absorption Correction in X-Ray Microanalysis," X-Ray Optics and X-Ray Microanalysis, edited by H. H. Pattee, V. E. Cosslett and A. Engström, Third International Symposium, August 1962, Academic Press, New York, 1963.

11. D. L. Spears, H. I. Smith and E. Stern, "X-Ray Replication of Scanning Electron Microscope Generated Patterns," Proceedings of the Fifth International Conference on Electron and Ion Beam Science and Technology, edited by R. Bakish, The Electrochemical Society, Inc., Princeton, 1972.

12. P. A. Sullivan and J. H. McCoy, "Determination of Wavelength and Excitation Voltage for X-Ray Lithography," IEEE Trans. Electron Devices, vol. ED-23, no. 4, April 1976, pp. 412-418.

13. T. Conley, editor Thermal Stability of Polymers, vol. 1, Marcel Dekker, Inc., New York, 1970.

14. R. F. Herzog, J. S. Greeneich, T. E. Everhart and T. Van Duzer, "Computer-Controlled Resist Exposure in the Scanning Electron Microscope," IEEE Trans. Electron Devices, vol. ED-19, no. 5, May 1972, pp. 635-641.

and J. S. Greeneich, "Developer Characteristics of Poly-(Methyl Methacrylate) Electron Resist," J. Electrochem. Soc., vol. 122, n. 7, July 1975, pp. 970-976.

15. M. Hatzakis, C. H. Ting and N. Viswanathan, "Fundamental Aspects of Electron Beam Exposure of Polymeric Resist System, "Proceedings of the Fifth International Conference on Electron and Ion Beam Science and Technology, edited by R. Bakish, The Electrochemical Society, Inc., Princeton, 1974.

16. F. Asmussen and K. Vebeneiter, J. of Pol. Sci., v. 57, 1962, pp. 199-208.

17. S. E. Bernacki and H. I. Smith, "X-Ray Lithography Applied to Silicon Device Fabrication," Proceedings of the Sixth International Conference on Electron and Ion Beam Science and Technology, edited by R. Bakish, The Electrochemical Society, Inc., Princeton, 1974.

18. "Elvacite" Acrylic Resin, grade 2041, E. I. DuPont de Nemours & Co. (Inc.), Los Angeles, California 90022.

19. H. I. Smith, Private Communication.

20. BTI, Brad Thompson Industries, Inc., Indio, California 92201.

21. Edwards, Grand Island, New York.

22. Ventron Corporation, Alfa Products, San Leandro, California 94577.

23. P. A. Sullivan, *X-Ray Lithograph System Complete with Interdigital Transducer Master*, Hughes Research Laboratories Report, November 1975.

24. S. M. Sze, *Physics of Semiconductor Devices*, Wiley-Interscience, New York, 1969.

25. United Detector Technology, Inc., *Planar Diffused Silicon PIN Photodiodes*, Prospectus, Santa Monica, California 90404.

26. L. H. Fong and S. G. Tomlin, "Absolute Intensities of Some L and M Characteristic X-Rays from Solid Targets," *Aust. J. Phys.*, vol. 23, 1970, pp. 17-21.

27. J. H. McCoy and P. A. Sullivan, "Progress in X-Ray Lithography," *Proceedings of the Sixth International Conference on Electron and Ion Beam Science and Technology*, edited by R. Bakish, The Electrochemical Society, Inc., Princeton, 1974.

28. R. Feder, E. Spiller and J. Topalian, "Replication of 0.1 μm Geometries with X-Ray Lithography," RC5445 (#23782) 6/5/75, *Engineering Technology*, IBM Research, Yorktown Heights, New York.

29. J. S. Greeneich, "X-Ray Lithography: Part I - Design Criteria for Optimizing Resist Energy Absorption; Part II - Pattern REplication with Polymer Masks," *IEEE Trans. Electron Devices*, vol. ED-22, no. 7, July 1975.

30. D. C. Flanders, H. I. Smith and S. E. Bernacki, "X-Ray Lithographic Replication of 1000 Å Linewidth Patterns using Cu_L Radiation," Extended Abstracts, vol. 76-1, The Electrochemical Society, Inc., Spring Meeting, Washington, D.C., May 2-7, 1976.

31. R. A. Cohen, R. W. Mountain, D. L. Spears, H. I. Smith, M. A. Lemma and S. E. Bermacki, "Fabrication Procedure for Silicon Membrane X-Ray Lithography Masks," Technical Note, 1973-38, MIT Lincoln Laboratory, 20 September 1973.

32. RCA Review, New Process Technologies for Microelectronics, vol. 31, no. 2, June 1970.

33. C.-L. Huang, "Schottky and Josephson Devices on Thin Silicon Membranes," Ph.D. Dissertation, University of California, Berkeley, 1975.

34. A. S. Grove, Physics and Technology of Semiconductor Devices, John Wiley and Sons, Inc., New York 1967.

35. S. Maekawa and T. Oshida, "Diffusion of Boron into Silicon," Journal of the Physical Society of Japan, vol. 19, no. 3 March 1964.

36. S. Y. Wang, Private Communication.

37. Handbook of Chemistry and Physics; 54 th Edition, CRC Press, Cleveland, Ohio 44128, 1973.

38. American Institute of Physics Handbook, Third Edition, McGraw-Hill Book Company, San Francisco, 1972.

39. F. H. Dill, A. R. Neureuther, J. A. Tuttle and E. J. Walker, "Modeling Projection Printing of Positive Photoresists," IEEE Trans. Electron Devices, vol. ED-22, no. 7, July 1975, pp. 456-464.

40. M. O'Toole, Private Communication.

41. R. M. Finne and D. L, Klein, "A Water-Amine-Complexing Agent System for Etching Silicon," J. Electrochem. Soc., vol. 114, no. 9, Sept. 1967, pp. 965-970.

42. J. C. Greenwood, "Ethylenediamine-Catechol-Water Mixture Shows Preferential Etching of p-n Junction," J. Electrochem. Soc., vol. 116, no. 9, Sept. 1969, pp. 1325-1326.

43. A. Bohg, "Ethylene Diamine-Pyrocatechol-Water Mixture Shows Etching Anomaly in Boron-Doped Silicon," J. Electrochem. Soc., vol. 118, no. 2, Feb. 1971, pp. 401-402.

44. R. M. White and L. Figueroa, Jr., Memo to File, Semiconductor Laboratory, University of California, Berkeley, 1975.

45. H. I. Smith, "Fabrication Techniques for Surface Acoustic-Wave and Thin-Film Optical Devices," Proceedings of the IEEE, vol. 62, no. 10, October 1974.

46. Yoshio Hatano, Hajime Morishita and Saburo Nonogaki, "A Modified Methyl Methacrylate Positive Resist," Coatings and Plastics Preprints, American Chemical Society, 170 th Meeting, August 25-29, 1975.

47. H. G. Jellinek, "Some Aspects of Polymer Degradation Process," The Effects of Polymer Degradation of Flow Proeprties of Fluids and Lubricants Containing Polymers, American Society for Testing and Materials, 1967.

48. M. Green, "The Efficiency of Production of Characteristic X Radiation," X-Ray Optics and X-Ray Microanalysis, edited by H. H. Pattee, V. E. Cosslett and Arne Engstrom, Third International Symposium, August 1962, Academic Press, New York, 1963.

49. R. E. Jewett, P. I. Hagouel, A. R. Neureuther and T. Van Duzer, "Line-Profile Resist Development Simulation Techniques," Fourth

Technical Conference on Photopolymers, "Photopolymers: Principles, Processes and Materials," Ellenville, New York, October 13-15, 1976.

50. B. Rossi, Optics, Addison-Wesley, Palo Alto, 1960.

51. Born and Wolf, Principles of Optics, Pergamon Press, New York, 1975.

52. M. S. Wong, "Ionospheric Ray Tracing with Analogue Computer," Electromagnetic Wave Propagation, International Conference Sponsored by the Postal and Telecommunications Group of the Brussels Universal Exhibition, Academic Press, New York, 1960.

53. C. B. Officer, Introduction to the Theory of Sound Transmission with Application to the Ocean, McGraw-Hill Book Company, New York, 1958.

54. R. E. Jewett, Private Communication.

55. A. R. Neureuther, R. E. Jewett, P. I. Hagouel and T. Van Duzer, "Surface Etching Simulation and Applications in IC Processing," Kodak Microelectronics Seminar, Interface '76, October 3-5, 1976, Monterey, California.

56. R. M. White, Private Communication.

57. J. S. Greeneich, Master's Thesis, unpublished, University of California, Berkeley, 1971.

Paul Isaac Hagouel
Πωλ Ισαάκ Χάγουελ

Διάφορες Εργασίες
Publications originating from Research Work

hagouel@eecs.berkeley.edu

Modeling of X–Ray Resists for High Resolution Lithography

Paul Isaac Hagouel & Andrew R. Neureuther
Department of Electrical Engineering & Computer Sciences
and the Electronics Research Laboratory
University of California, Berkeley, California 94720

Coatings and Plastics Preprints
American Chemical Society
Division of Organic Coatings and Plastics Chemistry
170th Meeting
Chicago, Illinois
August 25-29, 1975

Paul Isaac Hagouel
Thessaloniki, Greece
Tel + 30 2310270886
Mob +30 6974389086
Facsimile +30 2310238449
hagouel@ieee.org

COATINGS and PLASTICS PREPRINTS

OF PAPERS PRESENTED AT THE CHICAGO MEETING

170th MEETING
August 25-29, 1975

VOLUME 35—NUMBER 2

AMERICAN CHEMICAL SOCIETY
DIVISION OF
ORGANIC COATINGS
AND PLASTICS CHEMISTRY

COATINGS and PLASTICS
PREPRINTS

OF PAPERS PRESENTED AT THE CHICAGO MEETING

170th MEETING
August 25-29, 1975

VOLUME 35—NUMBER 2

AMERICAN CHEMICAL SOCIETY
DIVISION OF
ORGANIC COATINGS
AND PLASTICS CHEMISTRY

MODELING OF X-RAY RESISTS FOR HIGH RESOLUTION LITHOGRAPHY

P.I. Hagouël and A.R. Neureuther
Department of Electrical Engineering and Computer Sciences
and the Electronics Research Laboratory
University of California, Berkeley, California 94720

I. INTRODUCTION

Modeling techniques developed for optical resists and extended to e-beam resists can also be applied to X-ray resists. The effect of X-ray exposure of the resist is similar to that of e-beam irradiation. Many quantitative values developed by e-beam lithography [1] are used to establish the exposure-development model applicable at any point in the resist. In the interest of exploring high resolution for IC and gratings microfabrication, this model is used to study contrast, development time and minimum line edge angle as a function of exposure energy density, mask transmission and developer mixture. An algebraically tractable model has been developed for the case of planar (two-dimensional) masks which results in planar facets. For more complicated geometries such as those involving mask edge profiles a development algorithm based on an analogy to geometrical optics (ray tracing) has been found. This algorithm has been used in a simulation program to explore nonplanar facet effect in line edge profiles.

II. LOCAL DEVELOPMENT MODEL

During irradiation, positive working X-ray resist will degrade from a high average molecular weight $\bar{M}_n$ to a lower one $\bar{M}_f$. The dependence of $\bar{M}_f$ on the absorbed energy density ε has been shown to be [1,2]:

$$\bar{M}_f = \frac{\bar{M}_n}{1+\frac{g\varepsilon\bar{M}_n}{\rho A_0}} \tag{1}$$

where g is the efficiency factor proportional to the radiation chemical yield, A_0 is Avogadro's number and ρ is the resist density. For PMMA (poly-methylmethacrylate) $\rho = 1.2\ \mathrm{gm/cm^3}$ and $g = 1.9 \times 10^{-2}$ events/eV.

The surface etching rate during development depends on the developer used and it is a function of the average molecular weight $\bar{M}_f$. The rate R is given by [1,3]

$$R = R_0 + \beta\bar{M}_f^{-\alpha} \tag{2}$$

(usually in Å/min) where R_0 is the background etch rate and β and α are characteristic constants of the developer used. For developers with $R_0 = 0$ note that R is inversely proportional to the average fragmented molecular weight $\bar{M}_f$. Data reported [1,4] for a number of developers is summarized below.

	Developer	α	β
1:3	MIBK:IPA	3.86	9.332×10^{14}
1:2	MIBk:IPA	3.4	5.24423×10^{14}
1:1	MIBK:IPA	1.188	6.645×10^{6}
	MIBK	1.5	3.14×10^{8}

MIBK denotes Methyl isobutylketone and IPA denotes isopropyl alcohol. The above values are given for room temperature (21°C). The above relation (2) is valid over a large range of molecular weights and only β is temperature dependent [3].

The X-ray flux at the resist substrate surface is given by

$$\phi = I\varepsilon' h\nu/gr^2 \tag{3}$$

where I is the cathode ray current, r is the distance of the substrate from the source, ε' is proportional to the X-ray yield per incident electron per steradian, g is the electronic charge and ν is the frequency of radiation. The absorbent energy density ε is given by

$$\varepsilon = \phi\mu T \tag{4}$$

where μ (= 1000 cm^{-1} for PMMA) is the absorption coefficient of the resist and T is total exposure time. Typical values for our system [5] are 60-100 mA for cathode ray current, 7-10 cm for substrate to source distance and 13.5Å for the wavelength of the $Cu_{L\alpha}$ line. The resulting X-ray flux is about .1521 mW/cm^2. Higher values 1.3 mW/cm^2 have been reported [4] and 5 mW/cm^2 is possible from a small source diameter.

From (1) and (2) the dependence of R on ε is given by

$$R = R_0 + \frac{\beta}{(\bar{M}_n)^\alpha}\left(1+\frac{g\varepsilon\bar{M}_n\sigma}{\rho A_0}\right)^\alpha \tag{5}$$

where σ is the transmission factor of the absorbing mask. σ varies from 0 (perfect mask) to 1 (no mask). A contrast ratio Γ is defined as $\Gamma = 1 - R_s/R_f$ where R_s is defined as the slow etch rate $(0 \leq \sigma < 1)$ and R_f is the fast etch rate $(\sigma = 1)$. Γ varies from 0 to 1. We note that

$$\frac{R_s}{R_f} = \frac{R_0 + \frac{\beta}{(\bar{M}_n)^\alpha}\left(1+\frac{g\varepsilon\bar{M}_n\sigma}{\rho A_0}\right)^\alpha}{R_0 + \frac{\beta}{(\bar{M}_n)^\alpha}\left(1+\frac{g\varepsilon\bar{M}_n}{\rho A_0}\right)^\alpha} \;. \tag{6}$$

Note that for a given resist and exposure conditions (i.e. constant g and ε), decreasing σ higher values of contrast Γ can be achieved.

For e-beam exposure, ε is given by

$$\varepsilon = (Q/q)(E_0/R_G)\lambda(f) \tag{7}$$

[1] where Q is the total incident charge per unit area, E_0 is the beam energy and $\lambda(f)$ is a normalized depth dose function. Due to $\lambda(f)$, ε is non-uniform with depth except for high incident energies (E_0) and thin resist films. The non-uniform absorption of energy is mainly due to the finite range of electrons in the resist and the back scattering of electrons from both the substrate and the resist film. However, this problem is not present in X-ray exposure where to a good approximation the dose is independent of the distance the ray has traveled in the resist. To explore the effects of X-ray exposure on contrast Γ and development time it is convenient to use the exposure energy in J/cm^3. In Fig. 1 the contrast Γ is plotted vs. ε for the developers MIBK and 1:3 MIBK:IPA. The nonzero background development rate for MIBK makes Γ less than one even for a perfect mask. Reasonable contrast $\Gamma = .5$ requires an exposure of about 250 J/cm^3. For a thin mask allowing up to 50% transmission the required exposure can be as large as 600 J/cm^3 for $\Gamma = .5$. The time required to develop a 3000 Å film is also shown in Fig. 1. For MIBK, contrast imposes the primary consideration on exposure. For developer mixtures having $R_0 = 0$ such as 1:3 MIBK:IPA the contrast Γ for a perfect mask is always equal to one. However, even for moderate development times (10 to 20 minutes for a 3000 Å film) the energy required for exposure will require long exposure times. The primary constraint on exposure for these developers is the development rate. In Fig. 2 the development rate vs. ε is shown for the three developers: MIBK, 1:1 MIBK:IPA and 1:3 MIBK:IPA. MIBK is the obvious choice for developer for moderate contrast. For thin masks the use of $Cu_{L\alpha}$ (13.5 Å) instead of $Al_{K\alpha}$ (8.3 Å) X-rays will reduce mask transmission and increase the contrast.

III. ANALYSIS OF DEVELOPED RESIST PROFILES

The model of the development process as a local surface etching phenomena can be used to evaluate developed line edge profiles. For the special simplified assumptions of a zero thickness but finite absorption mask the developed profile will consist of connected planar facets.

The angles of the facets have been described previously [5]. The minimum sidewall angle for IC lithography or minimum groove half angle $\theta G/2$ for diffraction grating fabrication is shown in Fig. 3. Fig. 3 shows a complete line shape where the absorbing mask has not been removed for clarity. Normal incidence of X-ray has been assumed. This angle ($\theta G/2$) is given by $\theta G/2 = \arcsin R_s/R_f$ or $\arcsin(1-\Gamma)$. Through Γ mask absorption can be related to the minimum feature resolution. The minimum sidewall angle vs. ε for various developers and different σ is shown in Fig. 4. For the replication of periodic structures, limitations in the mask fabrication process force us to limit the thickness of the absorbing mask to approximately 10-30% of the period of the pattern that is replicated. For .1 micron lines and mask thickness of 200 Å we get the following values for σ for an Au mask and normal incidence: 95.5% transmission if the $Al_{K\alpha}$ line is used and 87.9% transmission if the $Cu_{L\alpha}$ line is used. The above numbers demonstrate the fundamental limitation in fabricating sub-micron periodic structures using X-ray lithography. If MIBK is used, then for $\theta G/2 = 45°$ and for $\sigma = .2$ and .5 we get the following information from Fig. 4. For $\sigma = .2$ and for $Al_{K\alpha}$ irradiation $t = .7\mu$ and for $Cu_{L\alpha}$ irradiation $t = .25\mu$. For both cases $\varepsilon = 170$ J/cm^3. For $\sigma = .5$ we have respectively .301µ and .108µ. ε equals 250 J/cm^3. If we assume a maximum gold thickness to period ratio $t/p = .3$ then we have the following minimum periods:

t (µm)	P_{min} (µm)
.7	2.333
.25	.833
.301	1.003
.108	.36

As an alternative developer 1:1 MIBK:IPA can be used for $\varepsilon = 480$ J/cm^3 giving R = 100 Å/min (Fig. 2) and $\theta G/2 = 27°$ for $\sigma = .5$ (Fig. 4). Therefore the fabrication of a 2000 Å deep I.C. line would require 20 minutes of development time if 1:1 MIBK:IPA is used. Furthermore the minimum period of the corresponding grating would be .36 µm with a minimum sidewall angle of 27°. In allowing a decrease in gold thickness with a concurrent increase in minimum sidewall angle to about 45° it appears that blazed gratings of period as small as .1 µ can be fabricated.

IV. SIMULATION OF DEVELOPED RESIST PROFILES - GEOMETRICAL OPTICS (RAY TRACING)

For more general cases, including non-planar mask profiles of special geometries and finite X-ray source size, we anticipate some problems where the planar model is not tractable. For those cases we have found a method of simulating development profiles, based on an analogy to geometrical optics. At points where $\bar{M}_f$ is maximum we know that R_s is minimum. At those points the medium is dense (in analogy to optically dense medium). At points where $\bar{M}_f$ is minimum, the etch rate R_f is maximum. We define the resist index of refraction $n_{Ph}(x,y) = R_f/R_s(x,y)$ for all points in the resist. It is easily shown that rays perpendicular to etch fronts satisfy Snell's law of refraction. Therefore, an analogy exists between etch fronts perpendicular to rays and wavefronts in geometrical optics perpendicular to light rays. Geometrical optics results may be applied to the resist development model by simply replacing the optical index of refraction n by n_{Ph}.

In theory all development profiles may be found analytically if the etch rate R_s is known as a function of position and if we can solve the following equation:

$$|\vec{\mathrm{grad}}\, L|^2 = n_{Ph}^2 \tag{8}$$

where $L(x,y,z) = 0$ represents the etch front at time $t = 0$. The equation of the etch front at time t is equal to $L(x,y,z) = R_f t$. The above PDE (8) is known as the Hamilton-Jacobi equation or the eikonal equation of geometrical optics [6]. In practice (8) is unsolvable except for very specialized cases. An equation more easily solved is the ray equation given by [6]

$$\frac{d(n_{Ph}\vec{\tau})}{ds} = \vec{\mathrm{grad}}\, n_{Ph} \tag{9}$$

where $\vec{\tau}$ is a unit vector tangent to the ray of every point (Fig. 5). In solving numerically the above equation we define small time steps Δt such that $\Delta s = (R_{s_{P'}} + R_{s_P})\frac{\Delta t}{2}$. Then (9) becomes:

$$\Delta\vec{\tau} = R_{s_P}\left(-\vec{\tau}_P \Delta\left(\frac{1}{R_s}\right) + R_{s_P}\ \vec{\mathrm{grad}}\left(\frac{1}{R_s}\right)\Delta t\right) \tag{10}$$

and $\vec{\tau}_{P'}$, i.e. the unit tangent vector at point P' is given by

$$\vec{\tau}_{P'} = \vec{\tau}_P + \frac{1}{2}\left(1 + \frac{R_{s_P}}{R_{s_{P'}}}\right)\Delta\vec{\tau} \tag{11}$$

The simulation algorithm can be used to explore the effects of mask geometry which is very important when we have double source exposure of the resist at different angles of incidence, θ_i and θ_R as shown in Fig. 6. Notice that the mask is non-planar and a mask slant angle of 45° anticipated in chemical etching is included. The etch rates for regions ①, ② and ③ are as follows: For region ① $R_{fast} \equiv R_f = 2^{\alpha}$. For region ②, $R_{s_2} = \{\exp\left(\frac{-\tilde{\alpha}(y \tan\theta_i - x)}{\cos\theta_i(1 - \tan\theta_i)}\right) + 1\}^{\alpha}$ and for region ③, $R_{s_3} = \{\exp\left(\frac{-\tilde{\alpha}t}{\cos\theta_i}\right) + 1\}^{\alpha}$. α was defined earlier (equation (2)) and $\tilde{\alpha}$ is the attenuation coefficient. For Al (8.3 Å) irradiation, $\tilde{\alpha} = 2.3025\ \mu^{-1}$ and for Cu (13.5 Å), $\tilde{\alpha} = 6.4473\ \mu^{-1}$. The total time of development is equal to h/R_f.

The algorithm was applied to various cases of interest and the simulated profiles of some typical geometries are shown in Figs. 7, 8 and 9. In Fig. 7, successive etch fronts are shown for increasing time. The period of the mask is 1μ, $d = .5\mu$, $t = .2\mu$, $\theta_i = 20°$ and $\theta_R = 15°$, $a = 3.0$ (1:2 MIBK:IPA) and $\tilde{\alpha} = 2.3025$. The broken curve is the final development profile when the $Cu_{L\alpha}$ line is used in exposing the resist. As expected, the groove angle for the latter case is smaller than the one for the preceeding case where the resist was exposed with Al characteristic radiation. For the same geometry, the profile which is based on the algebraic (planar mask) model [5] is also shown. The algebraic model does not predict any curvature around the appex of the groove angle. However, θ_G and the blaze angle θ_B are the same for both the algebraic profile and the simulated one. The above observation demonstrates that the algebraic model can give fairly accurate initial results especially if the effective width of the mask opening is adjusted.

The final groove angle θ_G depends on θ_i, θ_R, t, $\tilde{\alpha}$ and α. In order to use MIBK ($\alpha = 1.5$) to obtain $\theta_G \doteq 110°$, θ_i and θ_R should be decreased while t and $\tilde{\alpha}$ should be increased. The development profile of a 1μ period grating, where $\theta_i = \theta_R = 10°$, $\tilde{\alpha} = 6.4473$, $t = .2\mu$ and $d = .5\mu$ is shown in Fig. 8 (solid line). If t is changed to $.5\mu$ then the profile is as shown (broken line). Note that because θ_i and θ_R are small, h is large and the grating is created rather deep in the resist.

For a 3600 lines/mm grating a simulated profile is shown in Fig. 9 for $t = .08325\mu$, $\theta_i = 20°$, $\theta_R = 15°$, $\alpha = 3.86$ (1:3 MIBK:IPA), $\tilde{\alpha} = 6.4473$ and $d = .13887\mu$. Other developers with reasonable exposure and development times can be used to obtain approximately the same profile. As mentioned previously, blazed diffraction gratings with periods as small as .1µm appear feasible.

V. CONCLUSION

X-ray resist modeling techniques are useful in realizing the advantages and limits of the X-ray lithography for microfabrication. For general cases such as non-planar mask geometries, an algorithm based on ray optics can be conveniently used for simulation. The previous algebraic model is generally valid, especially if the mask opening d_{eff} is adjusted, but the simulation of resist profiles showed details, such as small curvature effects. Much steeper sidewalls and small grating groove angles can be achieved with 1:1 MIBK:IPA using 480 J/cm^3 instead of MIBK with 200 J/cm^3. The characteristic $Cu_{L\alpha}$ (13.5 Å) irradiation is preferable over the $Al_{K\alpha}$ (8.3 Å) for high resolution and .1µm period gratings with 100° groove angle are feasible.

ACKNOWLEDGMENT

Research sponsored by the Joint Services Electronics Program, Contract F44620-71-C-0087.

REFERENCES

1. James S. Greeneich, "Developer Characteristics of Poly-(Methyl Methacrylate) Electron Resist." Preprint of paper prepared for publication in the J. Electrochem. Soc.
2. M. Hatzakis, C.H. Ting, N. Viswanathan, "Fundamental Aspects of Electron Beam Exposure of Polymeric Resist System," Proceedings of the Sixth International Conference on Electron and Ion Beam Science and Technology, edited by R. Bakish (The Electrochemical Society, Princeton 1974).
3. F. Asmussen, K. Vebeneiter, J. of Pol Sci. 57, 199-208 (1962).
4. Stephen E. Bernacki and Henry I. Smith, "X-Ray Lithography Applied to Silicon Device Fabrication," Proceedings of the Sixth International Conference on Electron and Ion Beam Science and Technology, edited by R. Bakish (The Electrochemical Society, Princeton 1974).
5. A.R. Neureuther, P.I. Hagouel, "X-Ray Lithographic Fabrication of Blazed Diffraction Gratings," Proceedings of the Sixth International Conference on Electron and Ion Beam Science and Technology, edited by R. Bakish (The Electrochemical Society, Princeton 1974).
6. Rossi, Optics, Addison Wesley, Palo Alto, 52-60 (1960).

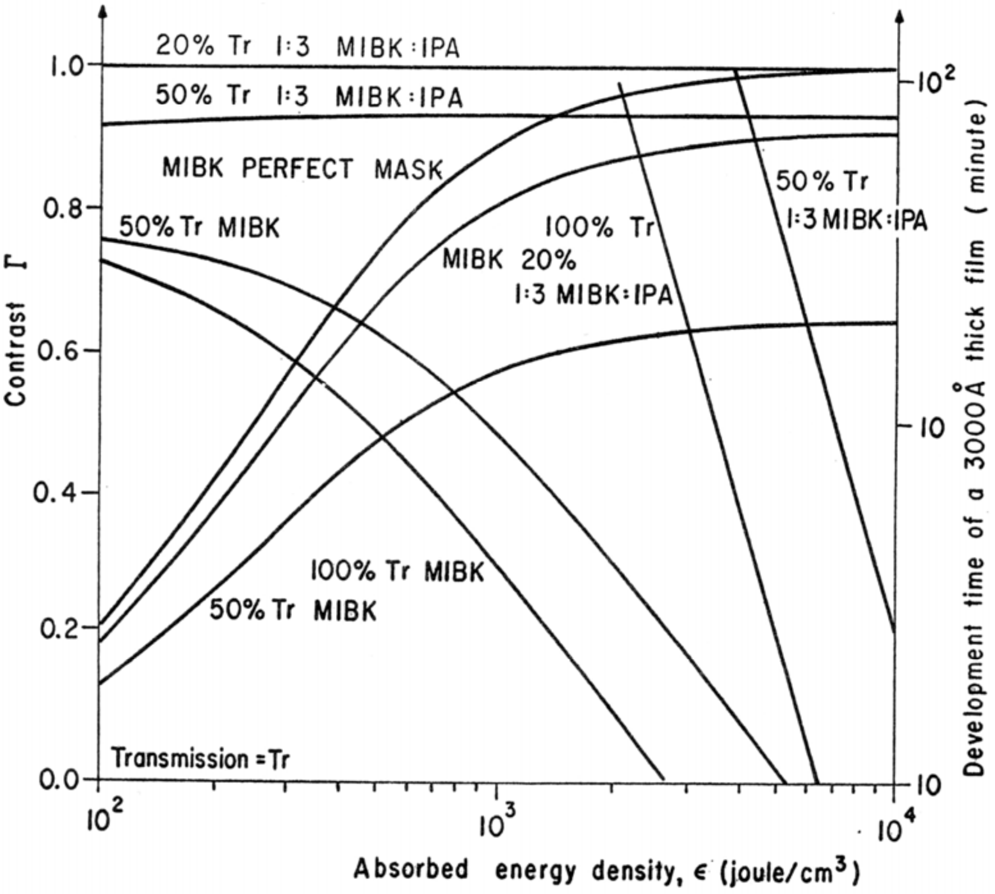

Fig. 1 The contrast Γ vs. absorbed energy density ε (positive slope) for two developers and three transmission factors. The development time for a 3000 Å film vs. ε (negative slope) for two developers and two transmission factors.

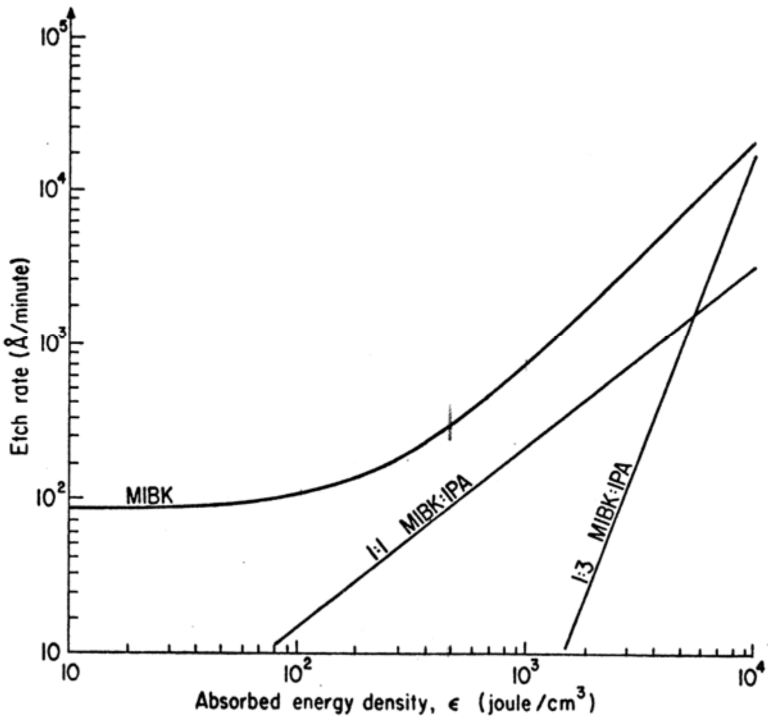

Fig. 2 The solubility rate vs. absorbed energy density ε for three different developers.

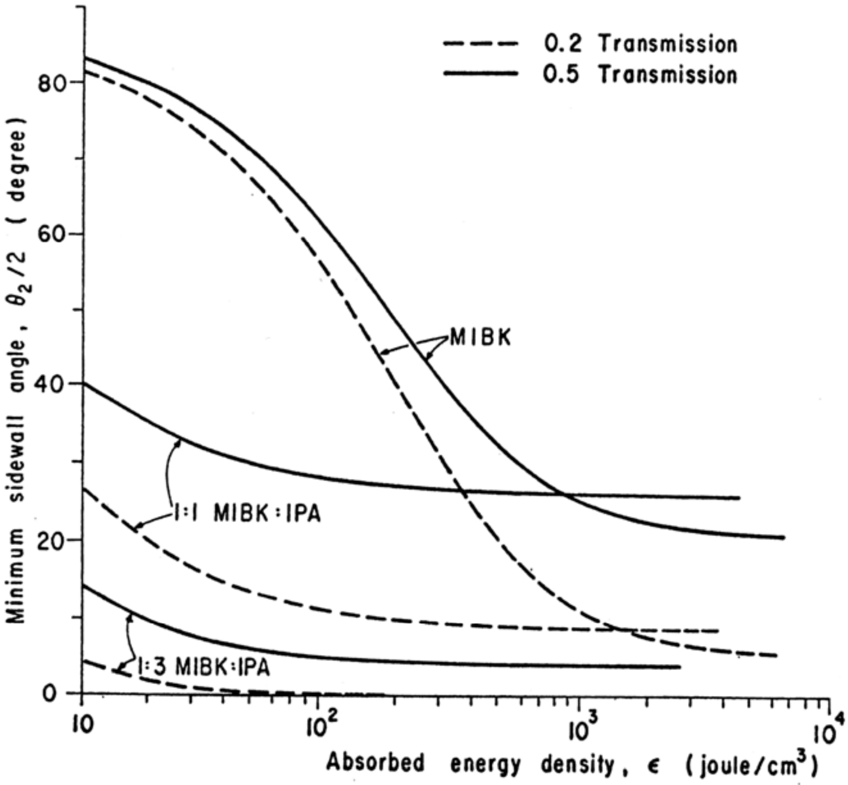

Fig. 4 The minimum side wall angle, $\frac{\theta G}{2}$ vs. absorbed energy density ε for three developers and two transmission factors.

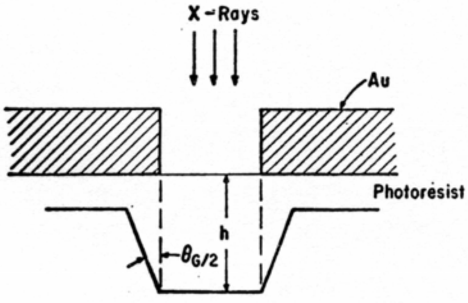

Fig. 3 Mask-resist system with a characteristic development profile.

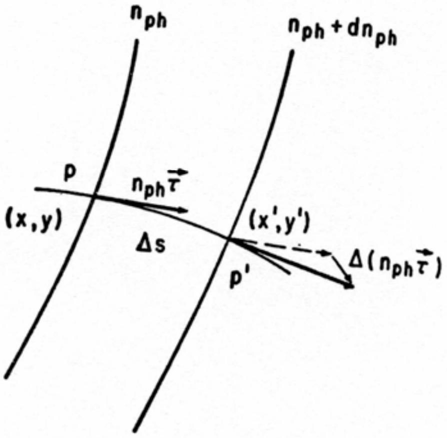

Fig. 5 Ray bending as it traverses an inhomogeneous medium.

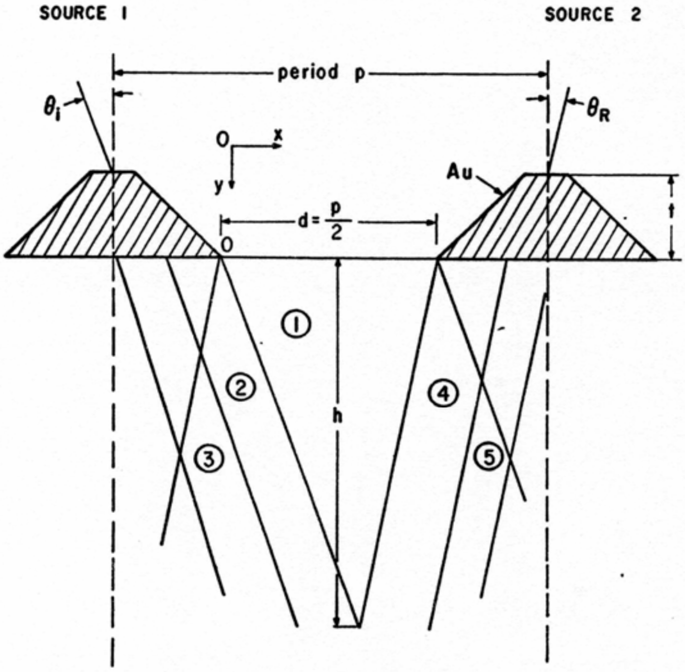

Fig. 6 Exposure and masking geometry for producing blazed diffraction gratings. The different regions of exposure in the resist are shown.

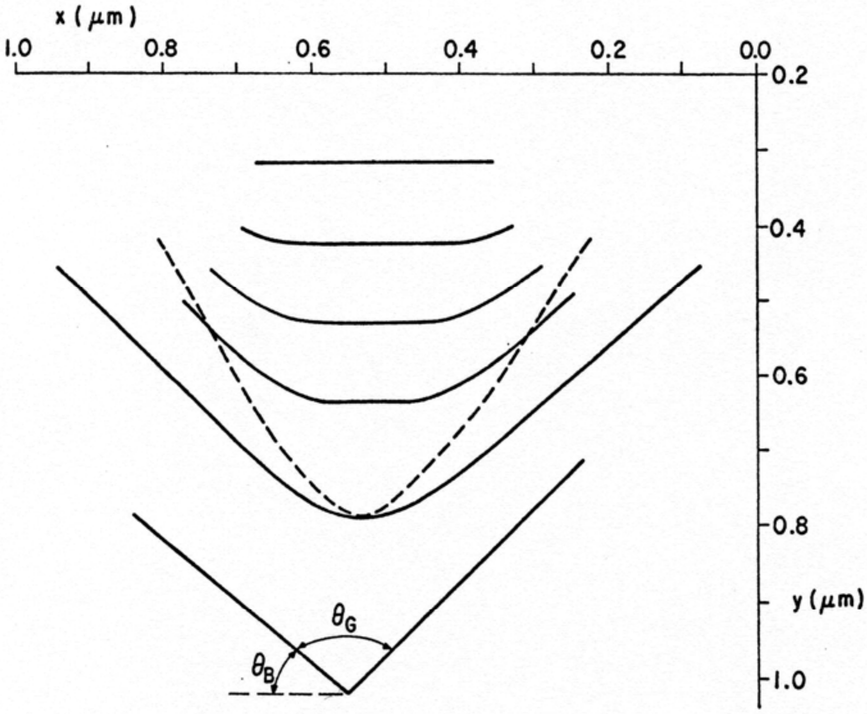

Fig. 7 Etch fronts for 40, 53, 66, 80 and 100% of total development time T, for a 1μm period grating. Development profile (dashed line) for Cu$_{L\alpha}$ exposure. The algebraically predicted profile is also shown. In all cases $\theta_i = 20°$, $\theta_R = 15°$, $\alpha = 3.0$, $t = .2\mu m$ and $d = .5\mu m$.

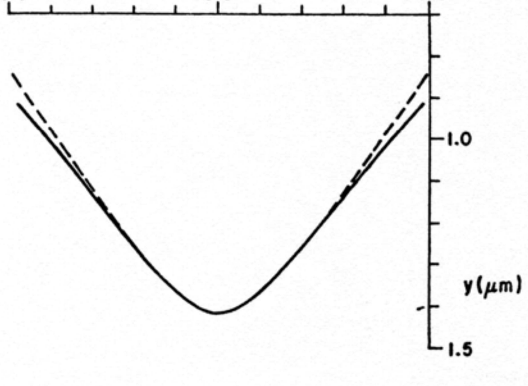

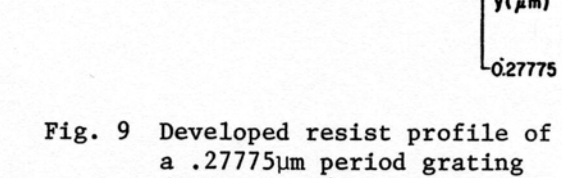

Fig. 9 Developed resist profile of a .27775μm period grating (3600 lines/mm). $\theta_i = 20°$, $\theta_R = 15°$, $\alpha = 3.86$, $\tilde{\alpha} = 6.4473\mu m^{-1}$ and $d = .13887\mu m$.

Fig. 8 Developed resist profiles for different mask thickness, $t = .2\mu m$ (solid line) and $.3\mu m$ (dashed line), $p = 1\mu m$, $\theta_i = \theta_R = 10°$, $\tilde{\alpha} = 6.4473\mu m^{-1}$, $\alpha = 3.86$ and $d = .5\mu m$.

Line-Profile Resist Development Simulation Techniques

R. E. JEWETT,* P. I. HAGOUEL,** A. R. NEUREUTHER, *and* T. VAN DUZER

Department of Electrical Engineering and Computer Sciences
and The Electronics Research Laboratory
University of California, Berkeley, California 94720

The relative advantages and disadvantages of three different algorithms are compared for simulating the time evolution of two-dimensional line-edge profiles produced by a locally rate dependent surface etching phenomenon. Simulated profiles typical of optical projection printing and electron-beam and X-ray lithography of micron-sized lines in resist and etching of ion-implanted SiO_2 are used as a basis of comparison. One of the algorithms is a cell-by-cell removal model used earlier by Neureuther and Dill. One of the newly developed algorithms employs ray tracing; it can be shown that the path followed by a point on a front between the developed and undeveloped regions can be calculated using ray-optic equations. The other new algorithm uses a string of points initially on the surface of the exposed resist. The points on the string advance perpendicular to the local direction of the string; with time the string of points moves down into the resist, replicating the action of a developer. We compare the computing cost, convenience, and accuracy of the algorithms.

INTRODUCTION

It is desirable for the lithographic fabrication of devices and circuits of microscopic dimensions that techniques for modeling cross-sectional profiles of lines be established. Such modeling requires that the distribution of energy absorption be calculated, the effect of absorbed energy on rate of etching by a developer be known, and the dynamics of the etching be simulated. There are various ways to calculate the absorbed energy, depending on the type of radiation used for the exposure. The relation between absorbed energy and etch rate has been determined for certain kinds of resists. The simulation of the development etching itself has been considered by Dill, *et al.* (1) using a rectangular array of cells, each having a specified etch rate. This paper presents two other algorithms for calculating the effect of the developer and compares the three regarding cost, convenience, and accuracy. All the numerical calculations presented here assume that a distribution of etch rates in a resist layer has been obtained in some previous calculation. It is of importance to point out that the work presented here employs the assumption that all the etching action takes place only on the surface of a time-varying front.

In developing and comparing these algorithms, we have studied several types of problems which serve as examples of situations that are encountered in practice but which are somewhat stylized. That is, we have used parameters which could come up in practice but which have not been taken from actual experiments. One of the test cases for comparison of the algorithms is calculable analytically and thus provides an absolute test as well as a comparison. The most complicated case is the development of an optically projection-printed line which contains a periodic variation of developer rate perpendicular to the resist-substrate interface because of the standing light wave during exposure. This particular example makes a sensitive test because it has strong variations of etch rate over short distances and a complex pattern of etch rates. Somewhat simpler is an etch-rate distribution which simulates an electron-beam-exposed resist layer. The developer action in a pattern of etch rates produced by X-ray absorption is also studied. Calculations were also made of the etching of SiO_2 which is nonuniformly ion-implanted to enhance etching. This is not a resist problem but is presented to show another possible application of the algorithms.

DESCRIPTION OF ALGORITHMS

The three algorithms are based on the cell-removal, ray-tracing, and string models. The cell-removal model evolved from a collaborative effort by Tuttle and Walker (2) on simulating projection printing of lines in a positive-type photoresist. The ray-tracing model and string model were developed as a part of the present project.

The initial work on the cell-removal model divided the resist layer into cells similar to those shown in *Fig. 1* and used a logic matrix to characterize the state of each cell as developed or undeveloped. The reason for this approach was that a simple APL matrix-shift operation could be used to locate the boundary between the developed and undeveloped regions. The algorithm was

---

* Present address: Hewlett Packard, Santa Rosa, California 90406.
** Present address: 85 Metropoleos Street, Thessaloniki, 14, Greece.

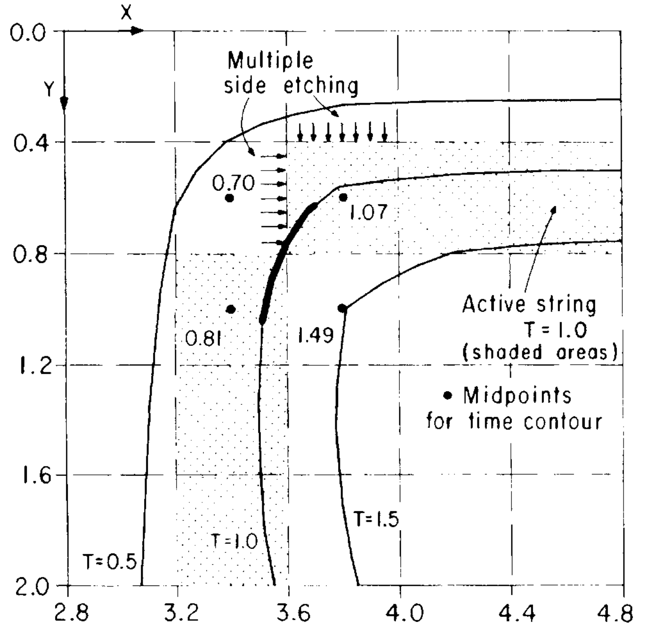

Fig. 1. Cell-removal model. The contours shown are ones calculated for a simulated electron-beam exposure. The numbers shown at the centers of the cells are the times (T) of dissolution of the cells. The contours are interpolated from these numbers. The time and distances shown have been normalized by use of a rate function $R(x,y)$ = larger of [$10 - x^2(1 + y/8)^{-1}$ or 0.5] units/time step.

subsequently modified extensively as described below for both improved accuracy and running time (1).

The basic features of the cell-removal model are shown in *Fig. 1*, which shows the detailed results for a simulated electron-beam exposure. The etching process is started along the top surface. The rate of dissolution of the resist in each cell that is in contact with the developer is determined by the etch rate previously assigned to that cell. Correction factors are used to adjust the cell-removal rate to account for the number of sides exposed to the developer and whether or not these sides are adjacent. Nonsquare cells can be used to account for situations where there are significantly slower etch-rate variations in one direction. A continuous developed contour can be calculated for any specified developing time by interpolating between recorded times of dissolution of the various cells. Some consideration was given to further improving the algorithm by using more than the four nearest neighbors to correct the etch rate but it was apparent that it would be easier to go to a string model.

The ray-tracing algorithm is based on the fact that a vector perpendicular to the boundary between developed and undeveloped regions, defined as an etch ray, is refracted at boundaries between regions having different etch rates (R and $R + dR$ in *Fig. 2(a)*) according to Snell's law of refraction. In analogy to geometrical optics, we can define a resist index of refraction as

$$n_R \equiv \frac{R_{max}}{R(x,y)} \tag{1}$$

where R_{max} is the maximum value of the etch rate $R(x,y)$ that appears in the problem under consideration. This index of refraction can then be used for ray tracing according to the laws of geometrical optics. In that discipline, the end points of a set of rays at a particular time define a phase front. In the resist problem, they define the advanced boundary between the developed and undeveloped regions. At $t = 0$, rays are started perpendicularly from the surface of the resist; then their trajectories are calculated using the ray equation. The end points of the rays are joined after some particular time to form a developed contour, as shown in *Fig. 2(b)*.

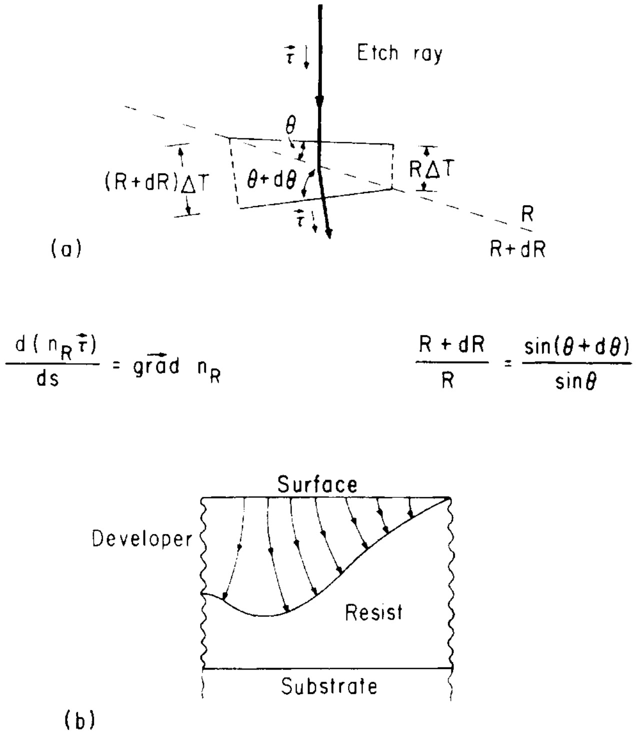

Fig. 2 Ray-tracing algorithms. (a) Etch ray is refracted at a boundary between regions having etch rates R and R + dR according to Snell's law. The effective refractive index for the resist is $n_R = R_{max}/R$ = (maximum etch rate)/(local etch rate). (b) Rays are started at the surface and the contour joining their end points after a given time is an etch front.

In the string model, the etching boundary between developed and undeveloped regions is approximated by a series of points joined by straight line segments. Each point advances along the angle bisector of the two adjoining segments according to the local value of etch rate, as shown in *Fig. 3(a)*. A typical string, composed of 40-100 line segments, is started on the resist surface and, as time proceeds, its position always defines the etch front. During the simulation, the segments are kept roughly equal in length by adding points in regions of expansion of the etch front and deleting points in regions of contraction. The process used for deleting points is illustrated in *Figs. 3(b)* and *3(c)*. The adjustment of segment length maintains good resolution and prevents certain computational difficulties.

DISCUSSION OF RESULTS

We have studied the application of the three algorithms to several different kinds of problems. *Figure 4* shows a comparison of the results achieved in the case of a simulated electron-beam exposure. The contours of equal etch rate are described by $R = 10 - x^2 (1 + y/8)^{-1}$ for etch rates of 0.5 or greater. A constant etch rate of 0.5

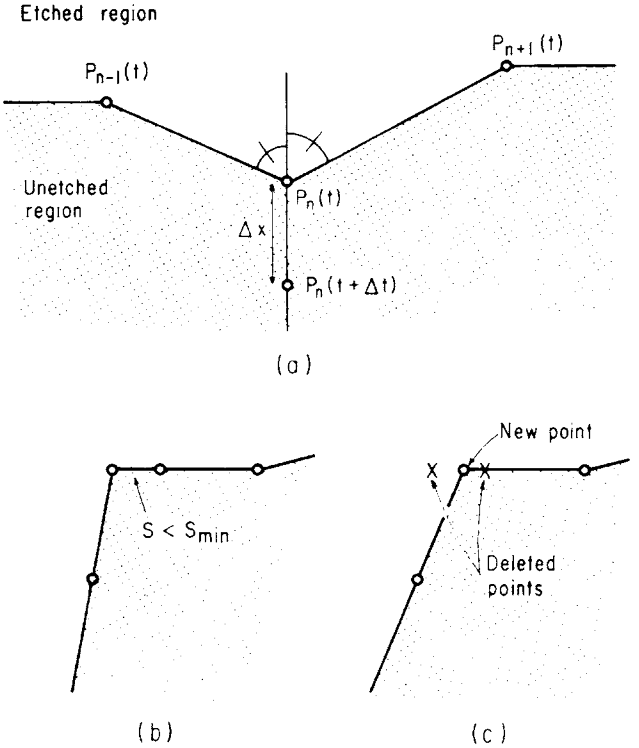

Fig. 3. Algorithm for the string model. (a) The advancement of a point by a distance Δx in a time Δt is along the bisector of the angle between the segments of the line at point $P_n(t)$. The distance $\Delta x = \Delta t\, R(P_n(t))$ where R is the rate. All points along the string are advanced in this manner. (b) The string where a point is about to be eliminated. (The segment length is S and the minimum allowed value is S_{min}.) (c) The string after change that eliminated one point.

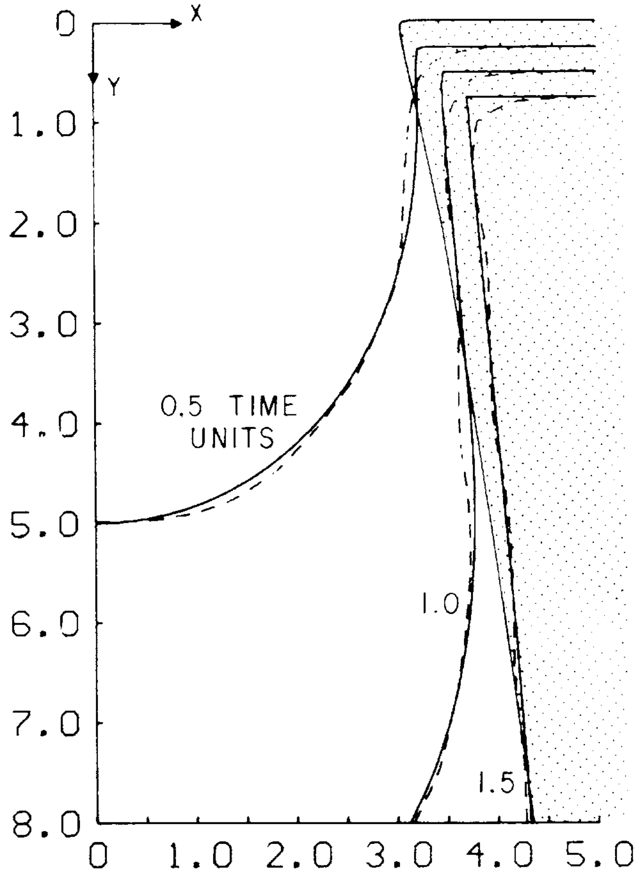

Fig. 4. Comparison of the results obtained using the three algorithms for a simulated electron-beam exposure. The solid lines were obtained with the string and ray methods and the broken lines were found with the cell-removal algorithm. The normalized etch rate and distances are the same as for Fig. 1. In the shaded region the etch rate is constant (0.5).

is assumed for the shaded region. The boundary shows the shape of the profile that would be expected if equal energy absorption lines were thought to bound the developed line. The solid lines show the developed fronts at three different (normalized) times for both the ray and string algorithms; for the given discreteness of the Cal Comp plotter, there is no difference of the results. The broken lines show the fronts calculated using the cell-removal algorithm. The accuracy is clearly less with the cell-removal scheme. Similar effects of the discreteness of the cells are observed in other problems. The discreteness problem can be alleviated by choosing a finer grid of cells, but the cost of computation is also increased. Even with smaller cells, there is a fundamental accuracy problem that has to do with the direction of movement of the developer front relative to the cell orientation; this can lead to errors of several percent in the effective etch rate.

Cost is an important factor in comparing algorithms as it is often necessary to calculate a large number of profiles. Good accuracy can be achieved with any of the three with sufficient expenditure. The cell-removal model has been written in APL (for the IBM 360/91) while the others were done in Fortran (for the CDC 6400) so the comparison is difficult. We found that the cell-removal model required about twenty times as many cpu operations as the string model. Much of this, and possibly all, could be eliminated by using a compiled language. However, judging from the number of operations in the algorithms, the cell-removal model would probably require several times the number of cpu operations for the same accuracy. Ray calculations cost about the same as those using the string model.

We have also found certain other advantages in using the ray method. It could be adapted to 3-d problems more conveniently than the others. Also, the accuracy of the position of the end point of a ray at a given time can be increased arbitrarily by taking smaller time steps. The ray method will also allow finding the position of one part of a front without doing the whole problem. Little memory is needed for the ray calculation so it can be done interactively on a desk calculator, as we did for a number of cases. There is a weakness of the ray method in that certain regions may not be reached by the first choice of initial ray locations on the surface; some kind of interactive computation is needed.

In summary, we believe the string model to be the most versatile for line profiles and of about equal cost with the ray method. For the same accuracy, the cell-removal algorithm would probably be at least a factor of two slower than the others if implemented in the same language. The ray method will have its main advantage when only a part of a development profile is desired or when one wishes to use a desk calculator.

ACKNOWLEDGMENT

Research sponsored by the Joint Services Electronics Program, contract F44620-71-C-0087, Air Force Office of Scientific Research, grant 71-2113 and the U.S. Army Research Office grant DA-ARO-D-31-124-73-G165.

REFERENCES

1. F. H. Dill, A. R. Neureuther, J. A. Tuttle, and E. J. Walker, "Modeling Projection Printing of Photoresists," IEEE Trans. on Electron Devices, vol. ED-22, pp. 456-464 (July 1975).
2. J. A. Tuttle and E. J. Walker, Private communication, Jan. 1972.

PERGAMON

Microelectronics Reliability 43 (2003) 249–258

MICROELECTRONICS RELIABILITY

www.elsevier.com/locate/microrel

Blazed diffraction gratings fabricated using X-ray lithography: fabrication, modeling and simulation

Paul Isaac Hagouel *

Optelec, 11, Chrys. Smyrnis Street, GR-546 22 Thessaloniki, Greece

Received 10 May 2002; received in revised form 15 August 2002

Abstract

Diffraction gratings are used in optical communications devices, spectrographs, optical scanners, monochromators, and in other instances. Diffraction gratings are either transmission or reflection. Reflective gratings are, usually, either ruled or holographic. Blazed gratings (step-echelette or phase gratings) are non-planar gratings. We present the fabrication of blazed diffraction gratings using X-ray lithography. We model, theoretically, the development process of X-ray exposed X-ray sensitive resist material (polymethyl methacrylate), and we establish a simulation algorithm, the ray-tracing algorithm based on the Hamilton–Jacobi equation. Theoretical predictions based on simulation results validate fully the fabricational results.

---

1. Introduction

Diffraction gratings are used in optical communication devices (e.g. optical couplers), in spectrographs and spectroscopy in general, in monochromators etc. The theory of diffraction gratings, as the name implies, is, basically, the theory of diffraction. For the case of light diffraction, the theory of gratings is given in [1–4]. The definition of a diffraction grating is any arrangement of parallel and equidistant diffracting elements of the same width where the period is comparable to the wavelength of the incident radiation.

Blazed gratings are capable of diverting the major part of the incident energy into a single spectrum of a given order of diffraction on one side and to suppress almost completely all other spectra, in particular that of the zero order [1,3]. Fig. 1 shows the general blazed grating profile.

In a blazed grating the grooves of the diffraction grating are controlled to form orthogonal triangles with a "blaze angle" φ. The peak angle may vary from the ideal 90°. The equation that holds for the Littrow condition where the incident and diffracted (or scattered) rays are in autocollimation (as in Fig. 1) is:

$$2\sin\varphi = k(1/\alpha)\lambda_B, \quad k = 1, 2, 3, \ldots \tag{1}$$

where λ_B is the blaze wavelength. Given the blaze wavelength, the blaze angle can be computed from the above equation [3,5].

Ruled gratings are time consuming in fabrication and thus costly. An alternative technique is the recording on radiation sensitive material the holographic interference pattern of two intersecting laser beams. Unfortunately, this very accurate grating generation technique suffers from lack of capability of groove profile (shape) control. Another technique involves the patterning of an interferometrically produced grating onto and into special $\langle 111 \rangle$ silicon wafers, cut around 1° off the $\langle 111 \rangle$ plane. Then, using a silicon anisotropic etching solution (e.g. potassium hydroxide—KOH) which etches $\langle 111 \rangle$ planes much more slowly than other crystallographic planes, the result is a smooth silicon blaze surface [6,7]. This method is constrained by the inherent crystallography and molecular silicon dimensions.

The fabrication of blazed diffraction gratings via X-ray lithography offers more versatility in groove shape profiles. The first step of the fabricational process is the

---

* Tel.: +30-2310-270886; fax: +30-2310-238449.

E-mail address: hagouel@cal.berkeley.edu (P.I. Hagouel).

0026-2714/03/$ - see front matter © 2003 Elsevier Science Ltd. All rights reserved.
PII: S0026-2714(02)00265-2

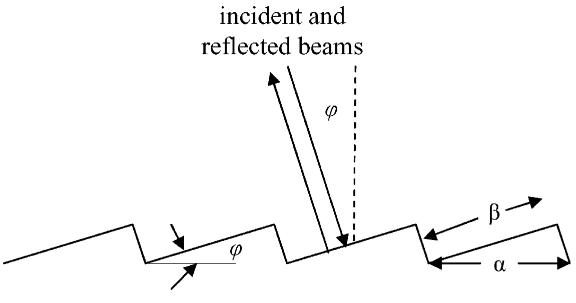

Fig. 1. Blazed grating profile.

transferring of the pattern of a holographically recorded grating onto and into the gold plated surface of a silicon wafer. Then, the substrate layer of silicon is thinned, from its backside, to a few microns that offer just the needed structural support for the gold grating structure. This thin silicon window attenuates negligibly the X-rays used subsequently. Lastly, the gold grating structure, in intimate contact with an X-ray sensitive resist coated planar substrate, is exposed with an X-ray beam, where the gold grating serves as an attenuator mask for the X-rays and thus we fabricate the blazed grating.

2. X-ray mask fabrication

One key step for the fabricational process is the gold grating mask structure fabrication on top of a thin silicon window that serves as an X-ray mask during exposure with an X-ray beam.

The first step in mask fabrication is the diffusion of boron into the front surface of a ⟨1 0 0⟩ n-type silicon wafer. This is done at an elevated temperature (1100 °C) for 6 h, and a subsequent drive-in diffusion at 950 °C for 3 h. This will provide a heavily, p-type (donor), doped ($>= 5 \times 10^{+19}$ atoms/cm^3) layer. This is needed since the use of the anisotropic silicon etching solution consisting of ethylenediamine, pyrocatechol and water shows preferential etching of a p^+n junction (the etching via the n doped side stops abruptly at the p^+n junction interface), and anisotropic etching of bulk silicon (the etch ratios for ⟨1 1 1⟩, ⟨1 1 0⟩, and ⟨1 0 0⟩ oriented silicon are approximately 3:30:50). The above procedure yields thin silicon windows of a thickness between 2.5 and 3 μm. The solution etches SiO_2 films very slowly (~200 Å/h) so they are used as etching masks.

A 12 000 Å film of SiO_2 is sputter deposited on the back side of the wafer and 1500 Å of SiO_2 is deposited on the front. A thin layer of nichrome (~300 Å) is then evaporated on the front surface followed by the evaporation of a 2000 Å gold film. Then, we spin coat the wafer with 3000 Å of Shipley positive photoresist and expose interferometrically using a helium–cadmium laser (3250 Å wavelength). The resulting resist grating structure, after development and post baking, serves as an etching mask for the transferring of the grating structure onto and into the gold layer via rf sputter etching.

The last step involves the actual fabrication of the thin silicon window. The aforementioned solution is very potent and attacks the gold relief grating structure. The following technique is used for masking:

We evaporate a thin nichrome (~300 Å) film on top of the gold grating. This film provides a convenient adhesive interface between Au and SiO_2.

We then sputter deposit a 1.2 μm film of SiO_2 on top of the Nichrome. This film will protect the gold pattern during the preferential etching of Si.

We coat both sides of the wafer with photoresist and then open a window (photolithographically) on the back side of the wafer directly beneath the gold pattern. The photoresist envelope coating acts as a mask when we etch through the SiO_2 layer, opening up a window beneath the gold pattern.

We then immerse the wafer in the preferential etchant (the etchant solution is heated up to 110–115 °C) and

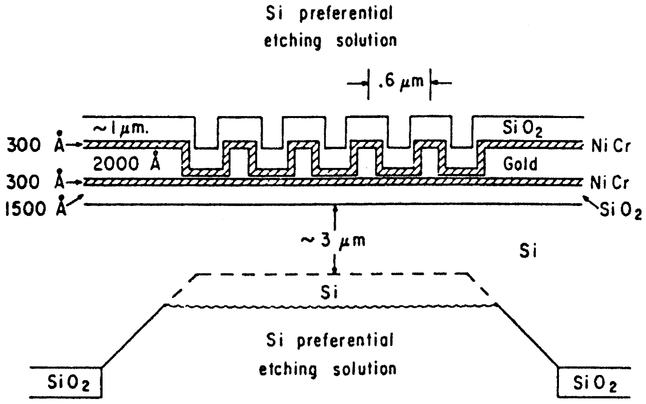

Fig. 2. Wafer topology for nichrome–SiO_2 protection of Au mask during thin silicon window etching.

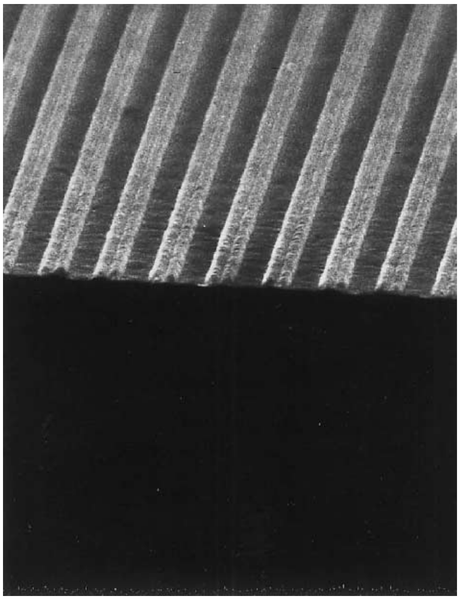

Fig. 3. 1 μm period Au grating.

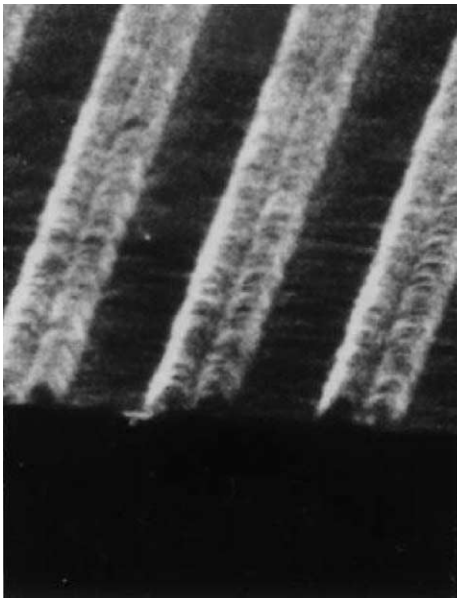

Fig. 4. Larger magnification of 1 μm period Au grating.

upon completion of the silicon etch up to the boron doped layer (this step takes from 3 to 5 h depending on the thickness of the wafer the exact composition of the etchant solution), we remove the wafer and strip the SiO_2 films on both sides by immersion in buffered HF.

A sketch of the topology of this process is shown in Fig. 2. Figs. 3 and 4 show SEM pictures of a 1 μm gold grating mask structure in two magnifications.

Fig. 5. 1 μm period Au grating (90° edge view).

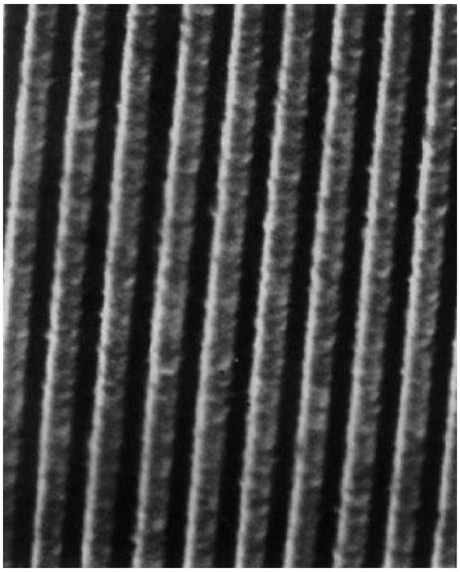

Fig. 6. 600 nm period Au grating.

Fig. 5 shows a SEM picture of the 1 μm period Au grating viewed at a 90° angle (edge view). The depression at the center of the gold bars is, most probably, due to the photoresist profile after development. Fig. 6 shows a SEM picture of a 600 nm period gold grating.

3. X-ray lithography, angle exposure, blazed diffraction gratings

The X-ray exposure system consists of a horizontal evaporation gun and a water cooled target at an angle of

45° with interchangeable target material. The electron beam diameter size is 4 mm and the target is capable of dissipating the heat produced by a 200 mA current beam. The source to substrate distance is 8 cm and typical exposure time for a 100 mA beam current is an hour. The main X-ray line for the aluminum target we used is the Al_{K_α} line (8.34 Å). For a thin silicon membrane (which supports the gold mask structure), a thin aluminum foil-filter, and polymethyl methacrylate (PMMA) resist, the optimum wavelength for the shortest exposure is the AL_{K_α} line. The thin silicon window absorbs (attenuates) the continuum X-rays below and above this line, thus the radiation incident on the X-ray resist is almost entirely the above line.

We use PMMA, a polymer, as the X-ray resist. It is positive acting and irradiation with X-rays (or energetic electrons) initiates a polymer chain scission. Subsequent immersion into a discriminative solvent developer (in our case a 60:40 mixture of IPA (isopropyl alcohol) and methyl isobutyl ketone (MIBK)) will etch more rapidly the areas where the exposure has produced macromolecule chain scission and thus has lowered the average molecular weight, as compared to areas that absorbed very little energy and thus retain a high average molecular weight and resist etching.

A lab made PMMA solution is spin coated on a plane glass substrate. After a prebake step, the PMMA film on glass is ready for exposure. In order to avoid penumbra and geometric distortion effects the X-ray mask (the gold grating pattern on the thin silicon window) should be in close contact with the PMMA film. We lay the PMMA coated glass substrate on top of the gold grating structure (the PMMA film faces the gold grating), and this "sandwich" arrangement is clamped on a water cooled mask substrate—PMMA substrate holder.

We perform an angle X-ray exposure (either single or double one) in order to achieve the desired groove profile (slanted ridge groove wall and blaze angle). The multiple angle exposure technique for groove shape control is shown in Fig. 7. A more general exposure and masking geometry for producing blazed diffraction gratings is shown in Fig. 8 (as is the case if wet chemical etch of the gold is used since it produces lines with angled side walls). The geometry is crucial since it provides both, the desired mask profile for exposure of the X-ray resist and, the basis for the theoretical calculation of the absorbed energy density profile inside the "bulk" of the PMMA resist. The absorbed energy profile inside the X-ray resist depends on the number of exposure doses (cumulative effect), the angle(s) of exposure (profile shape effect), and gold mask geometry (resist regions of different and/or variable energy dose density absorbed).

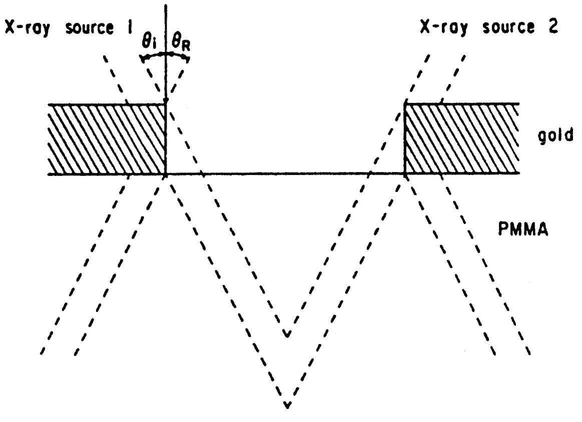

Fig. 7. Multiple angle exposure technique for groove shape control of blazed gratings.

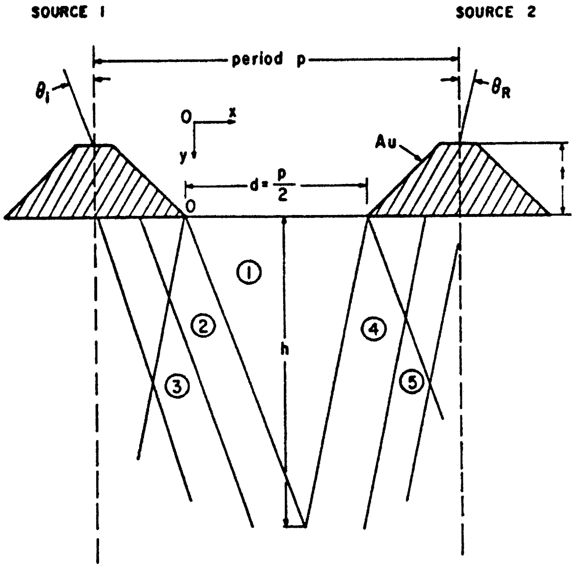

Fig. 8. General exposure and masking geometry for producing blazed gratings. Different regions of exposure in the resist are shown.

We performed a single angle exposure of the 1 μm gold grating mask pattern where we positioned the mask substrate—resist substrate system at an angle of 30° with respect to the horizontal during exposure. Typical exposure and development parameters are as follows: total exposure time 120 min, source to substrate distance 10 cm, and total development time 16 min. The total energy density absorbed by the resist during exposure was approximately 900 J/cm^3. The development rate of the fully exposed PMMA is around 130 Å/min.

Fig. 9 shows a SEM picture of the PMMA blazed grating after exposure and development. Fig. 10 shows an edge view (90° tilt) of the same grating. Note that one of the groove facets is longer than the other one. It is the one that corresponds to the angle exposure. We note

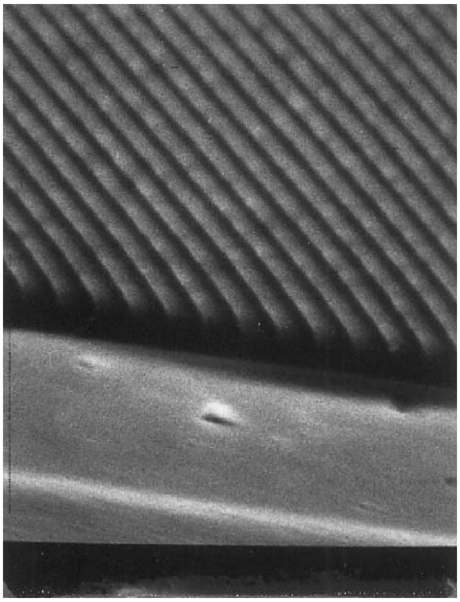

Fig. 9. PMMA 1 μm blazed grating.

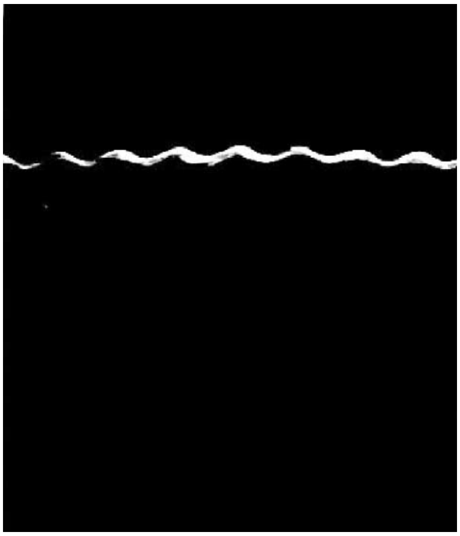

Fig. 10. 90° edge view of the blazed 1 μm PMMA grating.

that the depression in the middle of the gold mask rib (Figs. 3 and 4) had negligible effect on the developed profile.

Measurement of the 1 and −1 orders of diffraction when the grating was positioned perpendicularly to the path of an argon laser beam ($\lambda = 4880$ Å) showed the intensities to be different by 25%. The mechanism of PMMA development process produced a rounded apex angle instead of the desired pointed one. This we explain theoretically in the next section.

4. Modeling and simulation (TCAD)—comparison with experimental results

4.1. Physical and mathematical principles—modeling

Predicting theoretically, by modeling and simulation, the experimental outcome of various process steps involved in nano- and micro-lithography and fabrication, as well as nanoelectronics and microelectronics, is both desirable and extremely useful. Etching (including resist development, ion-implanted oxide etching among others) and deposition of various substances are processes that we encounter extensively in IC and other nano- and micro-devices fabrication.

Resist development or etching is just a special case of the general field of the etching and deposition processes of various substances. Therefore, we use the modeling simulation of resist development as vehicle for the development of the physical and mathematical principles involved, as well as for the development of the algorithms that are an offspring and realize the mathematical equations that will describe the processes. These algorithms form a potent and versatile set of tools for TCAD.

Resist etching involves mass transfer operations. In the case of a liquid developer, the etchant attacks the exposed resist surface (positive resist) and starts dissolving the resist material in contact with the liquid. If we assume an abundant supply of developer (e.g. immersion of the resist coated substrate), then the dissolved substances are immediately separated from the remaining resist. This process continues till either we stop the development or the developer reaches resist areas that have not been exposed and, thus, are unsolvable. Another case involves reaching the substrate surface.

In most cases the etching process is a surface etching phenomenon. This implies, by definition, that there exists, at any period of time, a well defined boundary (or interface) between the developer and the undeveloped resist. The shape and position of the boundary at a particular moment is determined by the geometrical (and physical) interface between the liquid etchant and the undeveloped resist bulk. This boundary progresses in time into the resist as development continues.

Thus we establish that we may visualize the bulk of the resist as a medium where the interface between the developer and undeveloped resist is a surface front that, at every point, moves with a velocity dependent on position. The velocity (speed) at any point in the resist is determined by the correlation of the locally absorbed energy density as it applies to etching speed by the developer used. Thus we model the resist, in general, as an inhomogeneous and isotropic medium where fronts can propagate and assume shapes dependent on the speed, which is a function of position. Since the medium is finite in volume, we can measure or calculate maximum and minimum development (etching) speeds.

Therefore, the problem posed is how to model the advancement of the etchant-bulk resist interface in time and predict its shape (profile) and position at any moment in time.

The notions that we expounded lead to geometrical optics. Its principles and notions may be applied in the case of a material medium (e.g. polymeric resist) being etched since it shows the same principal characteristics with an optics medium. The solution of the problem is based on the fact that locally, at every infinitesimal region of the resist, the developer front satisfies Snell's law of refraction. All laws of geometrical optics are derived from Snell's law [8].

We now define an *etch ray* as a ray which is always perpendicular to the developer front (the interface). The etch ray obeys Snell's law of refraction at the interface between two regions of different etch speed. This definition is in analogy to the definition of an optical ray in geometrical optics and it establishes the correlation between the development process and geometrical optics, especially in what concerns wave front advancement. Important definitions and results of geometrical optics are specialized to the development case.

We define the *resist index of refraction*, n_{ph} as

$$n_{\mathrm{ph}} = \frac{R_{\mathrm{F}}}{R_{\mathrm{s}}(\mathbf{r})} \tag{2}$$

where $R_{\mathrm{s}}(\mathbf{r})$ is the etch speed at any point $\mathbf{r}$ in the resist and $R_{\mathrm{F}} = R_{\max} = \max R_{\mathrm{s}}(\mathbf{r})$ for all points $\mathbf{r}$ in the resist.

We define the *etch length* from point P_1 to a point P_2 along a given path in the resist, which we shall denote by ℓ_{e}, as the distance that the etch front will advance in a resist medium of constant etch speed R_{F}, during the time it needs to cover the distance P_1 to P_2 along the given path. The etch length is given by

$$\ell_{\mathrm{e}} = \int_{P_1}^{P_2} n_{\mathrm{ph}}\,\mathrm{d}s = \int_{P_1}^{P_2} \frac{R_{\mathrm{F}}}{R_{\mathrm{s}}(\mathbf{r})}\,\mathrm{d}s \tag{3}$$

All rays connecting two developer (etch) fronts have equal etch lengths. We apply all geometrical optics principles to the resist development model by replacing the optical index of refraction n by the resist index of refraction n_{ph}.

We assume that the etch front at time $t_0 = 0$ is represented by a given surface S_{o} as shown in Fig. 11 (3-dimensions). We define a function $D(\mathbf{r})$ such that the value of D at any given point p in the resist equals the etch length from S_{o} to p of the etch ray passing through p. The equation of an arbitrary etch front is then

$$D(\mathbf{r}) = \ell_{\mathrm{e}} = \text{Constant} \tag{4}$$

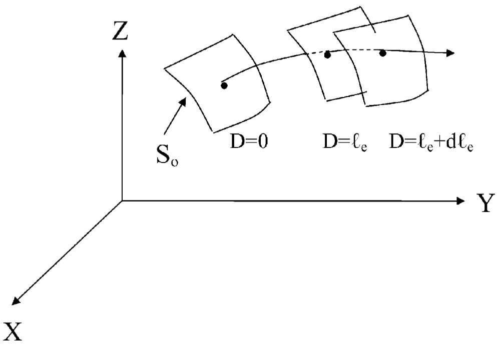

Fig. 11. Propagation of a developer front in an inhomogeneous and isotropic medium—advancement of the developer front (developer-bulk resist interface) in an exposed resist medium.

At a given point, let ds by the distance between the two etch fronts and corresponding to ℓ_{e} and $\ell_{\mathrm{e}} + \mathrm{d}\ell_{\mathrm{e}}$ as shown in Fig. 11. From (4) we obtain

$$|\mathrm{grad}\, D(\mathbf{r})|\,\mathrm{d}s = \mathrm{d}\ell_{\mathrm{e}} \tag{5}$$

and from (3) we obtain

$$\frac{\mathrm{d}\ell_{\mathrm{e}}}{\mathrm{d}s} = n_{\mathrm{ph}} \tag{6}$$

and (5) becomes

$$|\mathrm{grad}\, D(\mathbf{r})|^2 = n_{\mathrm{ph}}^2 \tag{7}$$

or in Cartesian coordinates,

$$\left(\frac{\partial D}{\partial x}\right)^2 + \left(\frac{\partial D}{\partial y}\right)^2 + \left(\frac{\partial D}{\partial z}\right)^2 = n_{\mathrm{ph}}^2 \tag{8}$$

Eq. (8) is the Hamilton–Jacobi equation better known in optics as the eiconal (from the greek *εικών*) equation [1,2,4,8–10]. It is also the mathematical formulation of Huygen's principle. Its solution, subject to the boundary condition that the equation $D(x,y,z) = 0$ represents the initial etch front S_{o} at time $t_0 = 0$, determines the etch front at all subsequent times. Indeed, the equation of the etch front at time t is

$$D(x,y,z) = R_{\mathrm{F}}t \tag{9}$$

The etch rays are the normal trajectories of the surfaces $D =$ constant.

Huygen's principle leads to two equivalent descriptions of propagation (in our case front advancement), namely we either observe and follow the (wave) front or we may observe and follow the path or rays, i.e. (in geometrical optics) the paths of shortest time of light propagation.

Other etching and deposition algorithms, as well as spin-off and specialized cases for different kinds of resists and/or exposure and development (etching) parameters have been described. The basics of the *ray-tracing algorithm* along with its *physical–mathematical foundation* was briefly described in [11]. The various simulation techniques including the *string* and *cell removal* models are included in [12]. Ref. [13] modeled and adapted the string algorithm to the case of *anisotropic etching*. Simulation of *multiple etch fronts* is described in [14]. The basics of a *cellular automata* based etching and deposition algorithm is given in [15]. *Negative resist corner rounding* is described in [16]. The effect that the *developer temperature* has on the profiles is described in [17], and the effect of *exposure energy dose* in [18]. The intricacies of *packed* (close-spaced) *parallel and isolated lines* are expounded in [19]. The *CA photoresist developer simulator* is described in [20]. The importance of using simulation tools and techniques for the advancement of nanotechnology cannot be overemphasized [21].

We will now find the equation that governs the trajectory of an etch ray.

Let $\boldsymbol{\tau}$ be a unit vector tangent to the etch ray as shown in Fig. 12 and consider the vector $n_{\text{ph}}\boldsymbol{\tau}$. From Snell's law it follows that when an etch ray passes across the surface of separation between two resist regions of different etch speed, it changes direction, in such a way, that the component of $n_{\text{ph}}\boldsymbol{\tau}$ parallel to the surface remains unchanged. We have

$$(n_{\text{ph}}\boldsymbol{\tau}) \cdot (n_{\text{ph}}\boldsymbol{\tau}) = n_{\text{ph}}^2 \tag{10}$$

and by differentiation ($\Delta\boldsymbol{\tau} \perp \boldsymbol{\tau}$ for small time steps)

$$\begin{aligned}(n_{\text{ph}}\boldsymbol{\tau}) \cdot \Delta(n_{\text{ph}}\boldsymbol{\tau}) &= n_{\text{ph}}\Delta n_{\text{ph}} = n_{\text{ph}}\,\text{grad}\, n_{\text{ph}} \cdot \Delta\mathbf{s} \\ &= n_{\text{ph}}\Delta s\, \text{grad}\, n_{\text{ph}} \cdot \boldsymbol{\tau}\end{aligned} \tag{11}$$

where $\Delta\mathbf{s}$ is the vector PP', Δs is its magnitude, and $\Delta(n_{\text{ph}}\boldsymbol{\tau})$ represents the vector difference between the vectors $n_{\text{ph}}\boldsymbol{\tau}$ at P' and P. From the above equation we obtain

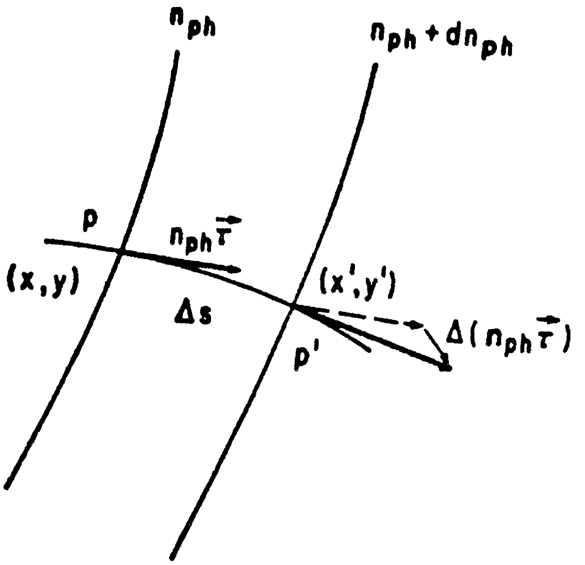

Fig. 12. Trajectory of an etch ray in a resist of variable n_{ph}.

$$\frac{\text{d}(n_{\text{ph}}\boldsymbol{\tau})}{\text{d}s} \cdot \boldsymbol{\tau} = \text{grad}\, n_{\text{ph}} \cdot \boldsymbol{\tau} \tag{12}$$

Eq. (12) indicates that the vectors $\text{d}(n_{\text{ph}}\boldsymbol{\tau})/\text{d}s$ and $\text{grad}\, n_{\text{ph}}$ have equal projections along the tangent to the ray. Moreover, $\text{grad}\, n_{\text{ph}}$ is perpendicular to the surface $n_{\text{ph}} = \text{constant}$, and so it the vector $\text{d}(n_{\text{ph}}\boldsymbol{\tau})/\text{d}s$, because as we mentioned above, the component of n_{ph} parallel to a refracting surface is the same on both sides. Therefore we obtain

$$\frac{\text{d}(n_{\text{ph}}\boldsymbol{\tau})}{\text{d}s} = \text{grad}\, n_{\text{ph}} \tag{13}$$

This is the differential equation of the etch ray in vector form. It is equivalent to

$$\delta \int n_{\text{ph}}\, \text{d}s = 0 \tag{14}$$

This is the mathematical formulation of Fermat's principle.

4.2. Ray-tracing algorithm

The *ray-tracing algorithm* is based on the fact that the locus of the end points of the etch rays at the same instant of time form the developer front. In order to derive the equations for the numerical calculation of etch ray trajectories we use the geometry shown in Fig. 13. The end point of a ray at time t_1 is at point P_1 with the direction of the ray given by $\boldsymbol{\tau}_1$. For a small time interval Δt, we assume the etch speed to be constant and equal to $R_{sP_1}(x_1, y_1)$. In Δt point P_1 will advance to point P_2 and $\Delta s = R_{sP_1}(x_1, y_1)\Delta t$ where Δs is the distance between points P_1 and P_2. The direction of the ray at point P_2 is given by $\boldsymbol{\tau}_2$. We need to calculate the vector $\Delta\boldsymbol{\tau}$ since

$$n_{\text{ph}}(x_2, y_2) \cdot \boldsymbol{\tau}_2 = n_{\text{ph}}(x_1, y_1) \cdot \boldsymbol{\tau}_1 + \Delta(n_{\text{ph}}\boldsymbol{\tau}) \tag{15}$$

as we show in Fig. 13. Therefore, a discretization of Eq. (13) is required.

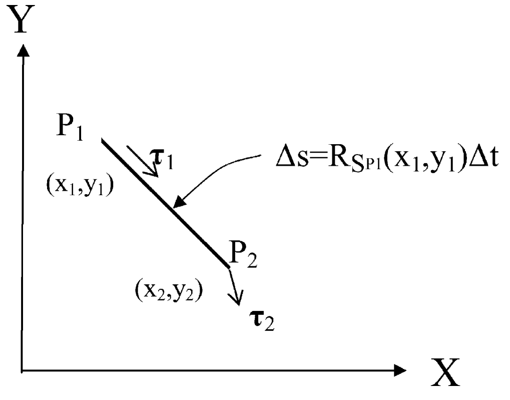

Fig. 13. Geometry for numerical calculation of etch ray trajectories.

We have the obvious relationship

$$\mathrm{d}(n_{\mathrm{ph}}\tau) = n_{\mathrm{ph}}\,\mathrm{d}\tau + \tau\,\mathrm{d}n_{\mathrm{ph}} \tag{16}$$

or

$$\mathrm{d}\tau = \frac{1}{n_{\mathrm{ph}}}(-\tau\,\mathrm{d}n_{\mathrm{ph}} + \mathrm{grad}\,n_{\mathrm{ph}}\,\mathrm{d}s) \quad \text{(using Eq. (13))} \tag{17}$$

Let $R_{\mathrm{s}}\,\mathrm{d}t = \mathrm{d}s$. Then Eq. (17) becomes

$$\mathrm{d}\tau = \frac{1}{n_{\mathrm{ph}}}(-\tau\,\mathrm{d}n_{\mathrm{ph}} + R_{\mathrm{s}}\,\mathrm{grad}\,n_{\mathrm{ph}}\,\mathrm{d}t) \tag{18a}$$

or

$$\mathrm{d}\tau = R_{\mathrm{s}}\left(-\tau\,\mathrm{d}\left(\frac{1}{R_{\mathrm{s}}}\right) + R_{\mathrm{s}}\,\mathrm{grad}\left(\frac{1}{R_{\mathrm{s}}}\right)\mathrm{d}t\right)$$
$$\text{(by definition of } n_{\mathrm{ph}} \text{ Eq. (2))} \tag{18b}$$

Retaining only the first term of a Taylor series expansion of Eq. (18b) we have for a small time step Δt such that $\Delta s = ((R_{\mathrm{s}P_2} + R_{\mathrm{s}P_1})/2)\Delta t$

$$\Delta\tau = R_{\mathrm{s}}\left(-\tau\,\mathrm{d}\left(\frac{1}{R_{\mathrm{s}}}\right) + R_{\mathrm{s}}\,\mathrm{grad}\left(\frac{1}{R_{\mathrm{s}}}\right)\Delta t\right) \tag{19}$$

where the expression on the right hand side of the above equation is evaluated at the starting point P_1.

Without loss of generality, we continue the analysis in two dimensions.

Let $n_{\mathrm{ph}}(x_1, y_1) = n_{\mathrm{ph}1}$ and $n_{\mathrm{ph}}(x_2, y_2) = n_{\mathrm{ph}2}$. Then from Eq. (15) we obtain

$$n_{\mathrm{ph}2}\tau_2 = n_{\mathrm{ph}1}\tau_1 + \tau_1\Delta n_{\mathrm{ph}} + n\Delta\tau \tag{20}$$

where

$$n = \frac{n_{\mathrm{ph}2} + n_{\mathrm{ph}1}}{2}, \quad \Delta n_{\mathrm{ph}} = n_{\mathrm{ph}2} - n_{\mathrm{ph}1},$$

and $\Delta\tau$ is given by Eq. (19).

Again, by definition, we may write Eq. (20) as follows

$$\tau_2 = \tau_1 + \frac{1}{2}\left(1 + \frac{R_{\mathrm{s}P_2}}{R_{\mathrm{s}P_1}}\right)\Delta\tau \tag{21}$$

Eq. (19) together with Eq. (21) allow us to calculate trajectories of etch rays. For numerical computations we discretize $\mathrm{d}(1/R_{\mathrm{s}})$ to $\Delta(1/R_{\mathrm{s}}) = (1/R_{\mathrm{s}P_2}) - (1/R_{\mathrm{s}P_1})$ and the x and y components of the gradient of $(1/R_{\mathrm{s}})$, $\{\mathrm{grad}(1/R_{\mathrm{s}})\}$, are given by (to a linear approximation) as, for the x component,

$$\frac{\Delta}{\Delta x}\left(\frac{1}{R_{\mathrm{s}}}\right) = \frac{1}{\Delta x}\left(\frac{1}{R_{\mathrm{s}P_2|_x}} - \frac{1}{R_{\mathrm{s}P_1|_x}}\right)$$

where $R_{\mathrm{s}P_2|_x}$ denotes the x-axis component of R_{s} at Point P_1 etc.

The etch speed $R_{\mathrm{s}}(x, y)$ may be given either as a continuous function of position in the resist or as discrete date at various points in the resist. In the first case analytical expressions of both the x and y components of $\mathrm{grad}(1/R_{\mathrm{s}})$ are found and evaluated at discrete points along the trajectory of the etch ray (e.g. points P_1, P_2, etc.). For discrete etch-rate data, the resist can be divided into a grid of points with assigned etch speeds. We compute the speed at any arbitrary point in the resist by weighted inference from the etch speeds of the nearest surrounding grid points.

4.3. Simulation

We use the ray-tracing algorithm to explore the effects of mask geometries (such as mask opening d, mask period p, mask thickness t_{mask} as shown in Fig. 8), different angles of incidence θ_{i} and θ_{R} (again as shown in Fig. 8) of the exposing X-ray beam, different compositions of developers (e.g. 1:3 MIBK:IPA or 1:2 MIBK: IPA etc.), different X-ray characteristic lines used for exposure {such as the $\mathrm{Al}_{\mathrm{K}_\alpha}$ line (8.34 Å) or the $\mathrm{Cu}_{\mathrm{L}_\alpha}$ line (13.5 Å)} for which characteristic lines gold exhibits different attenuation coefficients when they traverse the mask thickness, and different exposure times.

The etch rate of the resist during development depends on the exposing X-ray energy dose and all the above parameters. By varying any combination of the above parameters at will, we can predict the profiles after development and, by careful selection of the parameters, we can synthesize desired profiles.

The etch rate at any point in the resist depends on the local energy dose absorbed and is given by

$$R_{\mathrm{s}} = R_{\mathrm{o}} + \frac{\beta}{(\overline{M_{\mathrm{n}}})^{\alpha}}\left(1 + \frac{g\varepsilon\overline{M_{\mathrm{n}}}\sigma}{\rho A_0}\right)^{a} \tag{22}$$

where σ is the transmission factor of the absorbing mask (it depends on mask material, thickness, and X-ray characteristic line). σ varies from 0 (perfect mask) to 1 (no mask) that is $0 \leqslant \sigma < 1$ and R_{F}, the fast etch rate is the rate for $\sigma = 1$. g is the efficiency factor of energy absorption in the resist, ε is the total absorbed energy density dose (no mask), $\overline{M_{\mathrm{n}}}$ is the average molecular weight before irradiation, ρ is the resist density, A_0 is Avogadro's number, and α and β are characteristic constants of the developer used. R_{o} is the background etch rate (i.e. no exposure, usually extremely small). For computational purposes, we may replace the transmission factor with σ the attenuation coefficient $\tilde{\alpha}$ (units μ^{-1}), particular to the characteristic X-ray line used and the mask material. We may also neglect the term $\beta/(\overline{M_{\mathrm{n}}})^{\alpha}$ compared to $(g\varepsilon\overline{M_{\mathrm{n}}}\sigma/\rho A_0)^{a}$. For Au, $\tilde{\alpha} = 2.3025$ μ^{-1} for the $\mathrm{Al}_{\mathrm{K}_\alpha}$ line (8.34 Å), and $\tilde{\alpha} = 6.4473$ μ^{-1} for the $\mathrm{Cu}_{\mathrm{L}_\alpha}$ line (13.5 Å).

The simulated profiles of some typical geometries and parameter sets are shown in Figs. 14–16. In Fig. 14, successive etch fronts are shown for increasing development time. The period of the mask p is equal to 1 μ,

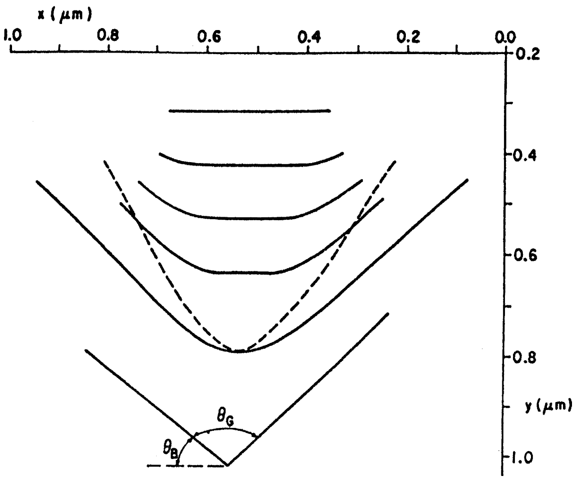

Fig. 14. Etch fronts for 40%, 53%, 66%, 80% and 100% of total development time T, for a 1 μm period grating. Development profile (- - -) for $\mathrm{Cu}_{\mathrm{L}_\alpha}$ exposure. The algebraically predicted profile is shown. In all cases $d = 500$ nm, $t_{\mathrm{mask}} = 200$ nm, $\theta_{\mathrm{i}} = 15°$, $\theta_{\mathrm{R}} = 20°$, $\alpha = 3.0$.

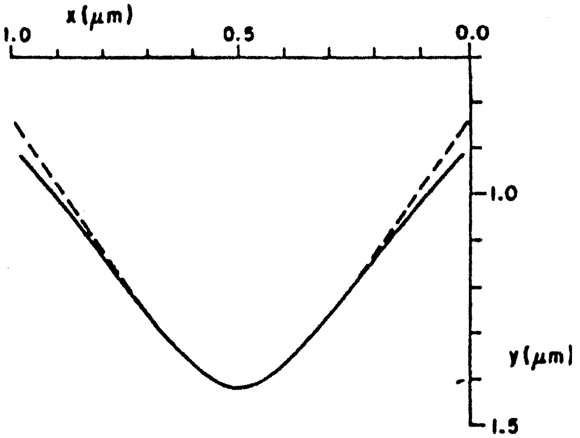

Fig. 15. Developed resist profiles for different mask thicknesses, $t_{\mathrm{mask}} = 200$ nm (—) and $t_{\mathrm{mask}} = 300$ nm (- - -). Other parameters are $p = 1$ μm, $\theta_{\mathrm{i}} = \theta_{\mathrm{R}} = 10°$, $\tilde{\alpha} = 6.4473$, $a = 3.86$, and $d = 500$ nm.

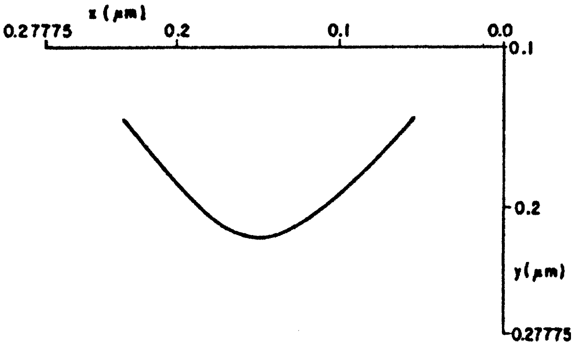

Fig. 16. Developed resist profile of a 280 nm period grating (3600 lines/mm). Other parameters are $\theta_{\mathrm{i}} = 20°$, $\theta_{\mathrm{R}} = 15°$, $\tilde{\alpha} = 6.4473$, $\alpha = 3.86$, and $d = 140$ nm.

$d = 500$ nm, $t_{\mathrm{mask}} = 200$ nm, $\theta_{\mathrm{i}} = 15°$ and $\theta_{\mathrm{R}} = 20°$, $\alpha = 3.0$ (1:2 MIBK:IPA), and $\tilde{\alpha} = 2.3025$ μ^{-1}. The dashed curve is the final development profile when the $\mathrm{Cu}_{\mathrm{L}_\alpha}$ line is used for exposure. As expected, the groove angle for the latter case is smaller than the one for the preceeding case where the resist was exposed with Al characteristic line radiation. For the same geometry, the profile which is based on the algebraic (planar mask) model is also shown. It is based on the simplified assumption of a mask of zero thickness but of finite absorption. The algebraic model does not predict any curvature around the apex of the groove angle. However, θ_{G} and the blaze angle θ_{B} are the same for both the algebraic profile and the simulated one. This observation demonstrates that the algebraic model can give fairly accurate initial results.

The final groove angle θ_{G} depends on, t_{mask}, θ_{i}, θ_{R}, α, and $\tilde{\alpha}$. In order to use only MIBK ($\alpha = 1.5$) to obtain $\theta_{\mathrm{G}} \cong 110°$, θ_{i} and θ_{R} should be decreased while t_{mask} and $\tilde{\alpha}$ should be increased. The development profile of a 1 μm period grating, where $\theta_{\mathrm{i}} = \theta_{\mathrm{R}} = 10°$, $\tilde{\alpha} = 6.4473$, $t_{\mathrm{mask}} = 200$ nm, and $d = 400$ nm is shown in Fig. 15 (solid line). If t_{mask} is changed to 300 nm then the profile is as shown (dashed line). We note that because θ_{i} and θ_{R} are small, h (Fig. 8) is large and the grating is created rather deep in the resist.

For a 3600 lines/mm grating a simulated profile is shown in Fig. 16. The parameters are $\theta_{\mathrm{i}} = 20°$, $\theta_{\mathrm{R}} = 15°$, $\alpha = 3.86$ (1:3 MIBK:IPA), $\tilde{\alpha} = 6.4473$, $t_{\mathrm{mask}} = 83$ nm, and $d = 140$ nm. Other developers with reasonable exposure and development times can be used to obtain approximately the same profile.

5. Conclusions

The goal of fabricating non-planar blazed diffraction gratings using X-ray lithography was realized. Blazed diffraction gratings were fabricated using X-ray lithography. A theoretical model for the development process of X-ray exposed X-ray sensitive resist material (PMMA) was developed. Based on this model, a general, three dimensional etching and deposition simulation algorithm, the ray-tracing algorithm, has been developed. Simulation results validate fully the fabricational results. More intense X-ray beam sources and/or more absorbing masks will improve the procedure. With the availability of other X-ray sources, 100 nm period gratings fabricated with X-ray lithography are feasible.

References

[1] Sommerfeld A. Optics. New York, NY: Academic Press; 1954.

[2] Landau LD, Lifshitz EM. The classical theory of fields. 3rd ed Reading, MA: Addison-Wesley; 1971.

[3] Jenkins F, White H. Fundamentals of optics. 4th ed New York, NY: McGraw-Hill; 1976.

[4] Jones DS. The theory of electromagnetism. Oxford, UK: Pergamon; 1964.

[5] Optics tutorial—diffraction gratings ruled and holographic, Jobin Yvon-Horiba, UK, 2002.

[6] Chen C, Fleming RC, Hindle P, McGuirk M, Murphy E, (Schattenburg ML, Canizares CR, Smith HI). Super-smooth X-ray reflection gratings. Submicron and nanometer structures report. Massachusetts Institute of Technology, Cambridge, MA, 1999. p. 139–40.

[7] Fleming RC, Heilmann R, Murphy E, (Schattenburg ML, Canizares CR, Smith HI). Super-smooth X-ray reflection gratings. Space nanotechnology laboratory progress report. Center for Space Research, Massachusetts Institute of Technology, Cambridge, MA, 2001. p.14–6.

[8] Rossi BB. Optics. Reading, MA: Addison-Wesley; 1957.

[9] Goldstein H. Classical mechanics. Reading, MA: Addison-Wesley; 1965.

[10] Arnold V. Méthodes Mathématiques de la Mécanique Classique. Moscow, Russia: Mir; 1976.

[11] Hagouel PI, Neureuther AR. Modeling of X-ray resists for high resolution lithography. In: 170th Meeting, American Chemical Society, Organic Coatings and Plastics, Preprints, Chicago, IL, vol. 35, no. 2, 1975. p. 298–305.

[12] Jewett RE, Hagouel PI, Neureuther AR, VanDuzer T. Line profile resist development simulation techniques. Polym Eng Sci 1977;17(6):381–4.

[13] Tassopoulos N, Hagouel PI, Kriezis EE. Modeling and simulation of anisotropic etching. In: Proceedings of the Microcircuit Engineering 83 Conference, Cambridge, England, Microcircuit Engineering 1983. London: Academic Press; 1983. p. 421–6.

[14] Karafyllidis I, Hagouel P. Simulation of multiple etch fronts. Microelectron J 1991;22:97–104.

[15] Karafyllidis I, Thanailakis A. Simulation of two-dimensional photoresist etching process in integrated circuit fabrication using cellular automata. Model Simul Mater Sci Eng 1995;3:629–42.

[16] Hagouel PIL, Neureuther AR, Zenk AM. Negative resist corner rounding. Envelope volume modeling. J Vac Sci Technol B (Microelectron Nanometer Struct) 1996;14(6): 4257–61.

[17] Hagouel PI, Karafyllidis I, Neureuther AR. Developer temperature effect on negative deep ultraviolet resists: characterization, modeling and simulation. J Vac Sci Technol B (Microelectron Nanometer Struct) 1997;15(6): 2616–20.

[18] Hagouel PI, Karafyllidis I, Neureuther AR. Dependence of developed negative resist profiles on exposure energy dose: experiment, modeling and simulation. Microelectron Eng 1998;41/42:351–4.

[19] Karafyllidis I, Hagouel PI, Neureuther AR. Negative resist profiles of close-spaced parallel and isolated lines: experiment modelling and simulation. Microelectron Eng 1999; 45:71–84.

[20] Karafyllidis I, Hagouel PI, Thanailakis A, Neureuther AR. An efficient photoresist development simulator based on cellular automata with experimental verification. IEEE Trans Semicond Manuf 2000;13(1):61–75.

[21] Cole DC, Barouch E, Conrad EW, Yeung M. Using advanced simulation to aid microlithography development. Proc IEEE 2001;89(1):1194–213.

Nanofabrication Simulation as a Processes Research Tool

P. I. Hagouel

Abstract – Nanofabrication Simulation is evolving continuously. Ever higher and faster digital computer calculating and processing power automates further the algorithms. General simulators can tackle mainstream processes. Special cases call for individualized simulation approach. Information of the physical process and initial conditions of the optical line of positive photoresist on reflective substrate is derived by using the X-Ray tracing algorithm that demonstrates initial value starting surface segment widths for etch ray "launching" in the sub Ångstrom region; Furthermore, ray-crossing and ray-scarce regions delineate the feed through pathways for the etchant to reach the final profile. In another case, that of exposed cluster of lines in negative resist where the developer [etchant] is heated up, by validating the experimental results via the calibrated simulator, we validate also the initial hypothesis of the physical and chemical processes that come into play such as he thermodynamics of the resist – etchant medium front that produce negative slant angle line walls.

I. INTRODUCTION

Nanofabrication Simulation is evolving continuously. Ever higher and faster digital computer calculating and processing power automates them further; However, all encompassing nanofabrication programs are inherently restricted in generating simulation results for only the most common fabrication process steps incorporated into them; Furthermore, the end result (e.g. simulation profile) sometimes deprives us of information on the process mechanism and / or on the initial conditions that come into "play" in the physical–chemical process.

In other instances, simulations of a nanofabrication process validate physical and / or chemical phenomena that play a role in the fabrication result. Physical and / or chemical equations describe the phenomenon, but it is only through simulation that we establish the effect on the process in time progression.

A. Initial Conditions and Progression

In the first instance we will present the development of a projection printed optical line in positive resist on a reflecting substrate [1]. The Ray – Tracing algorithm will be used [2] and initial conditions and time incremental progression mechanism will be shown and described [3]. Standing wave effects due to the interference of the incident and the reflected beams result in areas of heavy exposure (and, hence, polymeric chemical reactions), and areas where the cancellation of the beams results in minimal exposure energy dose and minute polymeric chemical alterations.

The Ray – Tracing algorithm in its pristine form shows that the etchant – developer liquid needs to attack the resist surface at very particular points congregated in sub–Ångstrom width regions! (in order to reach the final etch front and shape the final resist profile). Furthermore, the physics of ray advance coupled with the resist index of refraction [2] for this medium lead to areas where there is entrapment of rays, hence ray–dense (or ray–crossing) areas as shown in Fig 5. Only ray–scarce areas facilitate the etching – development process and contribute to the final profile shape {delineate the feed through pathways for the etchant progression}.

B. Physical and Chemical Phenomena

In the second instance, we validate the hypothesis of the role that thermodynamics play in the final shape of developed negative photoresist lines where we vary the developer temperature [4] – [7]. The physics and chemistry of polymers play also an important role [8], [9]. The simulator in based on Cellular Automata [10].

We are faced with the fact that an inescapable characteristic of most commercially available positive and negative resists is their polymeric constitution. Nanolithography demands that we take into account formative details of the composition of the resist films together with other parameters that are crucial in explaining subsequent developed profile details. We consider the effect of both elevated and depressed (as compared to room temperature) developer (etchant) temperatures in the dissolution of both the exposed and unexposed parts of the resist. We guess that the spin formatted resist film tends to have macromolecules oriented parallel to the substrate surface (Fig. 1). The probability of finding more readily dissolvable low molecular weight (MW) chains and oligomers is higher at the "exposure" interface (i.e. interface between exposed and unexposed resist) and this also contributes to the inhomogeneity of the region. Increased developer temperature causes an increase in vibrations of bound molecules of resist at the exposed-unexposed region interface, which most of the time, coincides also with the developer front in that region. The solvent molecule experiences, therefore, more collisions

Paul Isaac Hagouel, 11 Chrysostomou Smyrnis Street, GR-546 22 Thessaloniki, Greece, e-mail: hagouel@ieee.org

moving perpendicularly down, something that retards its advance. On the other hand, increased mobility of the solvent molecule coupled with an apparent bigger solid angle presented in the horizontal and slanted directions (Fig. 2) facilitates the penetration of the solvent molecules (horizontal-diagonal percolation) in between two or more molecules.

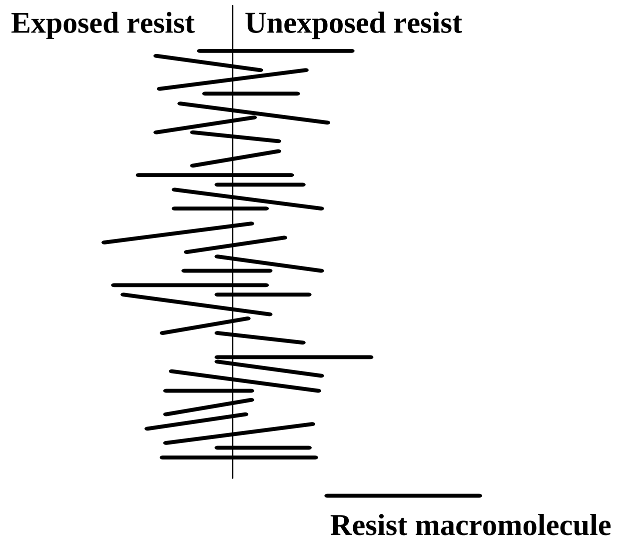

Fig. 1. Resist macromolecules at the exposed-unexposed resist interface.

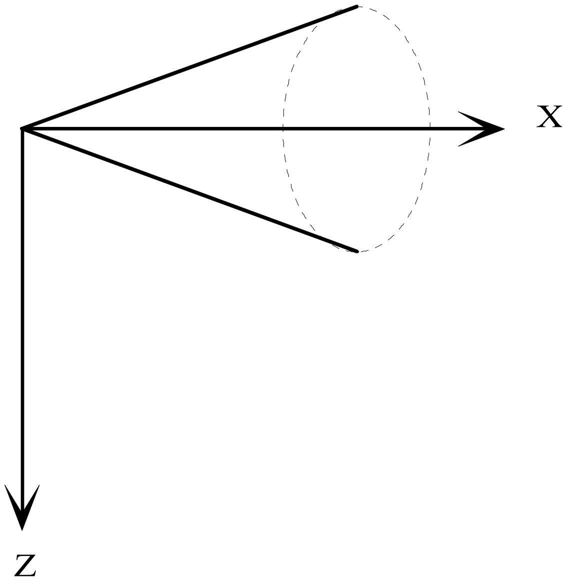

Fig. 2. The solid angle presented in the horizontal and slanted directions.

Elevated temperatures enhance mechanical vibrations of the resist molecules and *hammer* like activity of the solvent molecules attacking the resist. The orientation of the resist macromolecules introduces an anisotropic component to the etch rate: higher in the direction parallel to the substrate surface and lower in the perpendicular one. The effect has also a spatial parameter, more pronounced at the exposure interface.

We performed a series of experiments on resist coated Si wafers using a stepper and a Deep UV source at 0.248 μm. The mask had a set of periodic and isolated lines. We used SNR-248 negative resist. We obtained SEMs for various developer temperatures. The enhancement of the lateral etch rate manifested itself in sidewall slope. The sidewall slope is positive in the case where the developer temperature is equal to 0 °C, becomes almost zero when the developer temperature is equal to room temperature and becomes negative when the developer temperature is 80 °C.

We simulated the experimental results by characterizing the dissolution process as a chemical-thermodynamic process where the Gibbs free energy gives a relative (normalized) measure of the developer speed. We modeled the inherent anisotropy in etch rates due to the entropy directional flow by incorporating it into the local rule of the Cellular Automata model. In this simulation we introduced the temperature effect as anisotropy to the Cellular Automaton local rule. The simulation results are in very good agreement with experimental results for all developer temperatures.

II. OPTICAL LINE – INITIAL RAY “LAUNCH”

A. Etch Rate

The development of a projection printed 1 μm line in positive photoresist on a reflecting substrate was examined by Dill, et al. [1]. In this case we assume a 5000 Å thick photoresist layer on top of a reflecting substrate. Due to transverse standing waves in the resist, the normalized variation of the etch rate Y in the y-direction is approximated as in Fig. 3. The normalized variation of the etch rate X in the x-direction is a Gaussian as shown in Fig. 4. This is an approximation of an (optical) lens function. X is given by

$$X = \exp\left(\frac{-x^2}{5000^2}\right) \tag{1}$$

and Y is given by

$$Y = \frac{1}{2.05}\left(1 - 0.1\frac{y}{5000}\right)\left(1.05 - \cos\left(2\pi\frac{y}{1667}\right)\right) \tag{2}$$

The etch rate R(x,y) is given by

$$R(x,y) = 400XY\left(\frac{\text{Å}}{\text{sec}}\right) \tag{3}$$

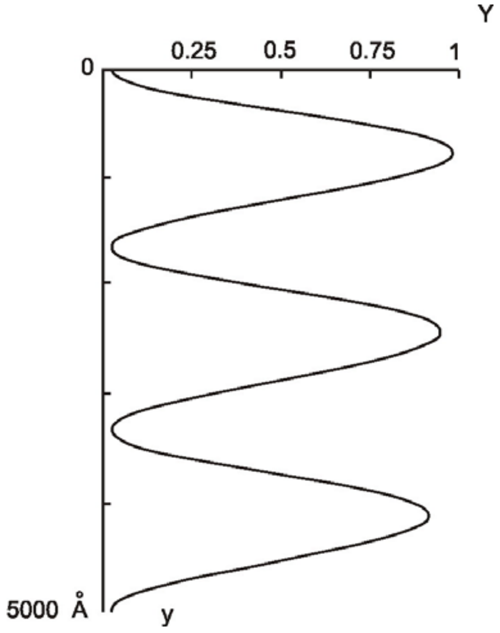

Fig. 3. The normalized variation of the etch rate Y in the y-direction.

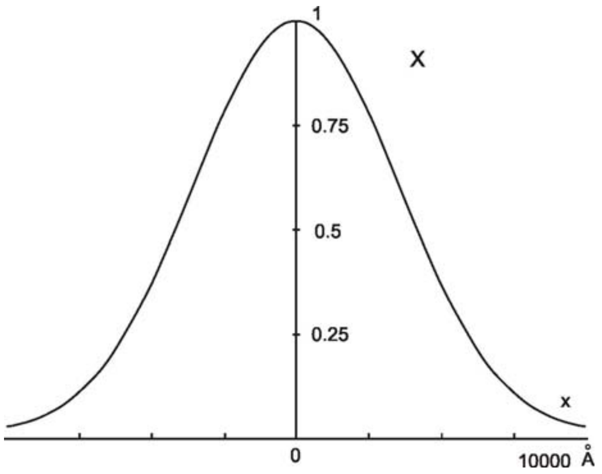

Fig. 4. The normalized variation of the etch rate X in the x-direction.

B. Simulation

The Ray calculations were done interactively. Fig. 5 shows ray trajectories for a total development time of 120 seconds. We notice ray–scarce regions (between 403 and 404 and between 860 and 870 where the numbers indicate the initial x–coordinate of the ray (time t=0)) and ray–crossing regions. The later is an example of ray "trapping" [11]. In this particular case both ray–scarce regions and the ray–crossing regions are due to the fact that the curvature of the ray is directly proportional to the gradient of the inverse etch rate [12]. The gradient variations in this case are large. The ray always curves toward a region of minimum etch rate; such a region will tend to form a "wave" guide for developer propagation. Notice that the ray-crossing regions correspond to the valleys of the Y function.

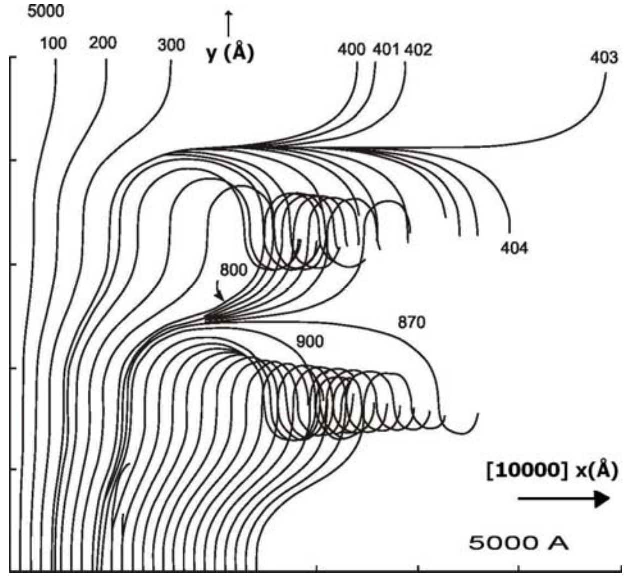

Fig. 5. Ray–tracing of the optical line with both ray–scarce and ray–crossing regions.

Interacting with the simulator we determined the initial x-coordinates of rays so that information for the ray-scarce regions was obtained. In particular we noticed that information for the fingers corresponding to fast regions of development (and also ray-scarce) was obtained from rays that originated in a 0.01 Å interval for the deepest finger, in a 0.1 Å interval for the middle finger and a 0.2 Å interval for the shallowest finger. Fig. 6 shows the results. Tick marks indicate both the end points of rays corresponding to 120 seconds development time and the intermediate results for 30 s, 60 s, and 90 s. Fig. 7 shows the final profile where the ray end points are joined with a smooth curve.

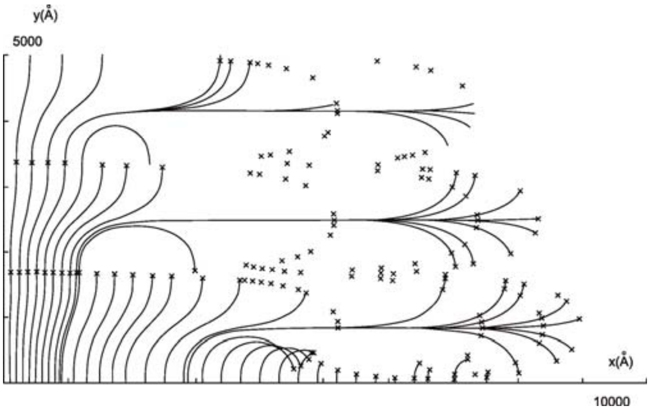

Fig. 6. Ray–tracing of the optical line. The tick marks define the profile for four different development times (30, 60, 90, and 120 seconds).

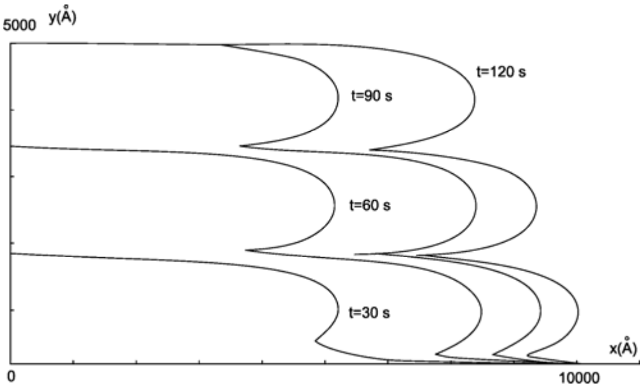

Fig. 7. Profiles for 30, 60, 90, and 120 seconds for the optical projection printed 1 μm line.

II. NEGATIVE RESIST – NEGATIVE WALL SLOPE

A. Temperature Effect

Temperature increment causes more intense molecular vibrations which results in faster dissolution rates of polymers. It is therefore expected that an increment in developer temperature will result in faster dissolution of both exposed and unexposed parts of the resist. Increased developer temperature causes an increase in vibrations of bound molecules of resist at the exposed-unexposed region interface. The solvent molecule experiences, therefore, more collisions moving perpendicularly down, something that retards its advance. On the other hand, increased mobility of the solvent molecule coupled with an apparent bigger solid angle presented in the horizontal and slanted directions facilitates the penetration of the solvent molecules (horizontal-diagonal percolation) in between two or more molecules. This effect can be modeled by an increment of the etch rate in both exposed and unexposed parts of the resist. This effect of the temperature is homogeneous and isotropic because the etch rate will vary proportionally at all points of the resist. Suppose that in the case where the developer temperature is equal to room temperature (20 ^{o}C) R(x,y) is the etch rate at the various points of the unexposed part of a negative resist and that R_{bg} is the etch rate at the exposed part (background etch rate). We model the homogeneous temperature effect using the following equations:

$$R'(x,y) = (1+r)\ R(x,y) \qquad -1 < r < 1$$
$$R'_{bg} = (1+b)R_{bg} \qquad -1 < b < 1 \qquad (4)$$

R´(x,y) and R'_{bg} are the etch rates at the unexposed and exposed parts, respectively, in the case that the developer temperature is different from 20 ^{o}C. In the case that the developer temperature is greater than room temperature r and b are positive. If the developer temperature is less than room temperature then r and b are negative. The case of room temperature is represented by letting r and b to be equal to zero. Etch rates at room temperature are calculated using the ABC parameter model [13]. We assume that r and b are not equal, i.e. the etch rates at the exposed and unexposed parts do not vary proportionally. Furthermore, the temperature increment increases the difference of etch rates between the exposed and unexposed parts of the resist. This is made clear by the following inequality:

If $T_1 < T_2 < T_3$, then

$$R^{T_1}(x,y) - R^{T_1}{}_{bg} < R^{T_2}(x,y) - R^{T_2}{}_{bg} < R^{T_3}(x,y) - R^{T_3}{}_{bg}$$
$$\left|\forall\ x,y \in R\right| \qquad (5)$$

R^{T_1}, R^{T_2}, and R^{T_3} correspond to the etch rates (both in exposed and unexposed parts) at temperatures T_1, T_2, and T_3. In other words, according to the proposed model, the difference in etch rates at the two sides of the boundary between the exposed and unexposed parts increases with temperature.

The orientation of the resist macromolecules introduces an anisotropic component to the etch rate: higher in the direction parallel to the substrate surface and lower in the perpendicular one.

By the second law of thermodynamics, dissolution proceeds only when the change in Gibbs free energy or the energy of dilution is negative [8] [9].

$$\Delta G_{sol} = \Delta H_{sol} - T\,\Delta S_{sol}\ <\ 0 \qquad (6)$$

where G is the Gibbs free energy, H is the enthalpy and S is the entropy. The value of $|\Delta G_{sol}|$ is, therefore, a measure and indication of the speed of dissolution as long as $\Delta G_{sol} < 0$. If the reaction is endothermic ($\Delta H_{sol} > 0$ and if $\Delta H_{sol} < T\Delta S_{sol}$) then an increase in temperature increases the speed of dissolution provided ΔH_{sol} and ΔS_{sol} remain virtually unperturbed for the range of temperatures.

The spatial and temporal dependence of this equation introduces a dynamic inhomogeneity and anisotropy in the dissolution process at interfaces between exposed and unexposed regions of the resist as well as at the (1)etch front and adjacent region. The mobility of the solvent affects the speed with which the molecules of the solvent associate with the molecules of the solute.

Entropy is a measure of ordering. Therefore, a region of extended structural variations, such as the neighborhood of the exposed-unexposed interface introduces a propensity for large change in entropy that depends also on the direction chosen, hence the anisotropy. Entropy has a tendency to increase in the case of dissolution of resists and for the structure presented in Figure 1 the increase is more pronounced towards the x axis and around it in a solid shown in Fig. 2.

Even though entropy is usually a scalar quantity, its change occurs with a flow of entropy. In regions of rapidly varying structural changes, such as interfaces of exposed-unexposed regions and in regions of time varying structural changes such as the etch front (dissolution front) neighborhoods, the propensity or potential for change in S (ΔS) endows ΔS with inhomogeneous and anisotropic characteristics. Cellular Automata lend themselves naturally for the solution of such problems.

B. Etching Anisotropy

In order to model this anisotropic temperature effect we incorporate the anisotropy into the Cellular Automaton local rule [13]. This is accomplished by introducing the normalized "weight" parameters that incorporate the thermal effect on the etch speed for the vertical (perpendicular), horizontal (parallel), and diagonal directions. These are denoted with *v, h, d* where

$$\begin{aligned} -1 &< v < 1 \\ -1 &< h < 1 \\ -1 &< d < 1 \end{aligned} \tag{7}$$

Note that for $T \geq 20\ {}^{o}C \Rightarrow v<d<h$. For $T \leq 20\ {}^{o}C \Rightarrow h<d<v$. We assume that the temperature increment increases the effect of the vertical, horizontal and diagonal cells, but not by the same amount and not the same way, i.e.:

If $T_1 < T_2 < T_3$, then

$$\begin{aligned} & v^{T_1} > v^{T_2} > v^{T_3} \\ & But \\ & h^{T_1} < h^{T_2} < h^{T_3} \\ & d^{T_1} < d^{T_2} < d^{T_3} \end{aligned} \tag{8}$$

Where

$$\begin{aligned} \left|h^{T_1} - v^{T_1}\right| < \left|h^{T_2} - v^{T_2}\right| < \left|h^{T_3} - v^{T_3}\right| \\ \left|d^{T_1} - v^{T_1}\right| < \left|d^{T_2} - v^{T_2}\right| < \left|d^{T_3} - v^{T_3}\right| \end{aligned} \tag{9}$$

The indices (superscripts) in (8) and (9) correspond to temperatures T_1, T_2, and T_3 respectively.

C. Simulation and comparison to experimental results

We performed a series of experiments on resist coated Si wafers using a stepper and a Deep UV source at 0.248 µm. The mask had a set of periodic and isolated lines. We used SNR-248 negative resist. We obtained SEMs for various developer temperatures. The enhancement of the lateral etch rate manifested itself in sidewall slope. The sidewall slope is positive in the case where the developer temperature is equal to 0 °C, becomes almost zero when the developer temperature is equal to room temperature and becomes negative when the developer temperature is 80 °C. Figures 8, 10 & 12 show the SEMs we obtained for developer temperatures equal to 0 °C, 20 °C, and 80 °C, respectively. The line pitch in Figures 8, 10, & 12 is 0.5 µm, 0.4 µm, and 1 µm, respectively.

Figures 9, 11 & 13 show the simulation results which we obtained using the model described in [13]. The values of the parameters used to obtain the simulation results are shown in Table I.

TABLE I
VALUES OF *v, h, d*

T {°C}	*v*	*h*	*d*
$T_1 = 0$	0.90	0.70	0.75
$T_2 = 20$	0.80	0.90	0.85
$T_3 = 80$	0.60	1.00	0.90

The variation of the sidewall slope with temperature has been successfully reproduced strengthening, thus, the proposed model for the temperature effects.

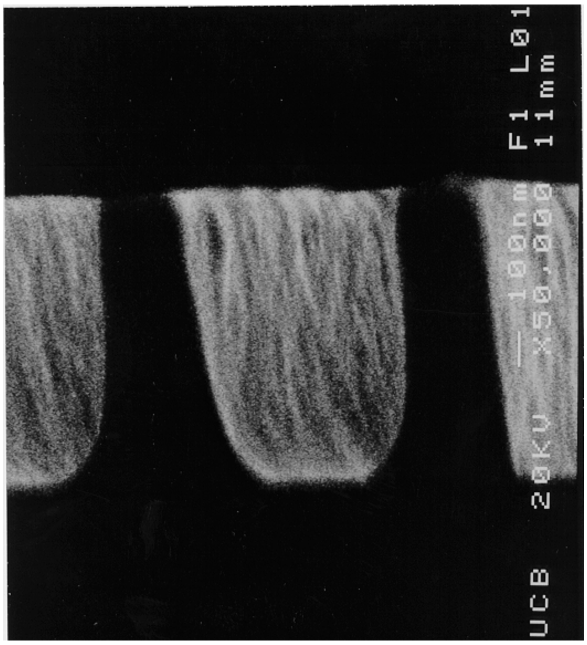

Fig. 8 SEM of periodic isolated lines with pitch 0.5 µm obtained using SNR 248 resist at 0 °C.

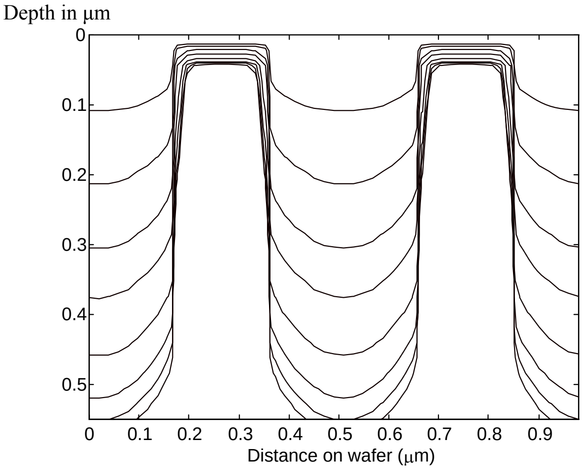

Fig. 9. Simulation results for T= 0 $^{\mathrm{O}}$C.

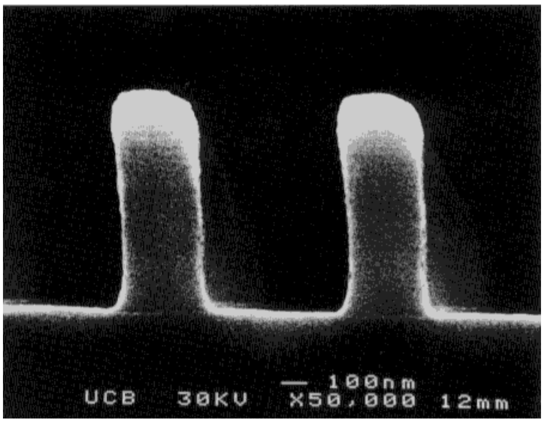

Fig. 10. SEM of periodic isolated lines with pitch 0.4 µm obtained using SNR 248 resist at 20 $^{\mathrm{O}}$C.

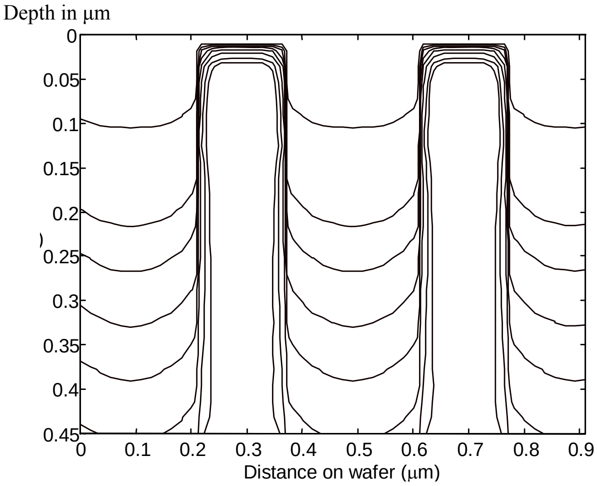

Fig. 11. Simulation results for T= 20 $^{\mathrm{O}}$C.

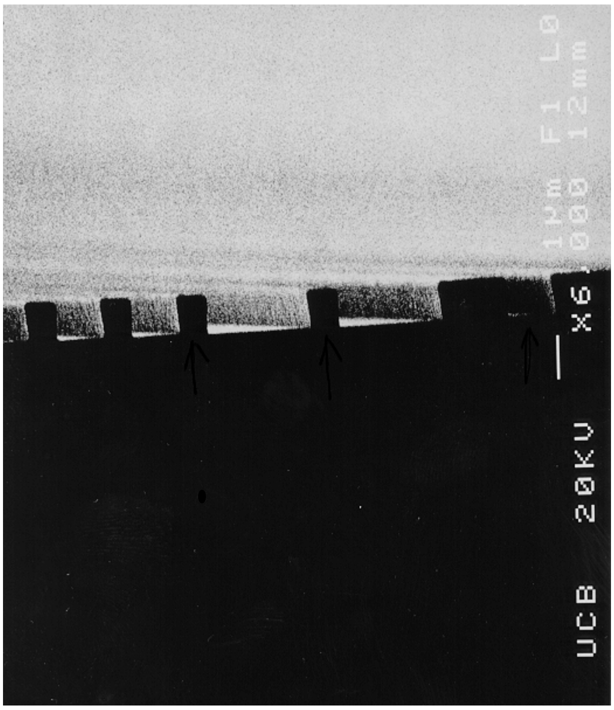

Fig. 1. SEM of periodic isolated lines with pitch 1 µm obtained using SNR 248 resist at 80 $^{\mathrm{O}}$C.

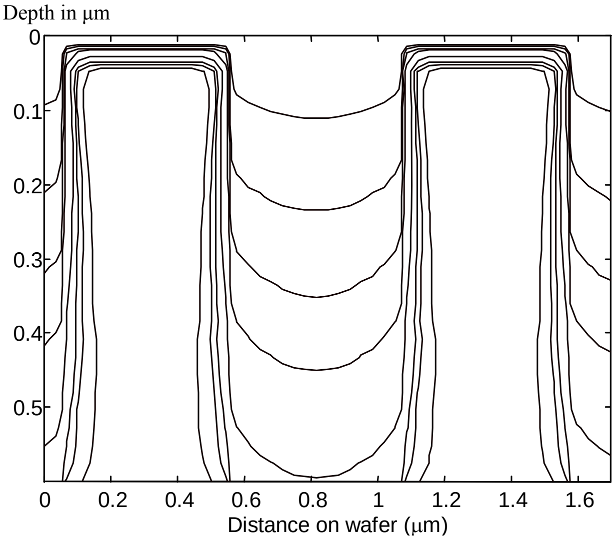

Fig. 13. Simulation results for T= 80 $^{\mathrm{O}}$C.

III. CONCLUSION

Initial Conditions (Launch surface coordinates and direction) of etch rays and their progression in the medium demonstrate the innate atomic structure of matter. The inverse problem (i.e. to “trace–back” the ray) may be used to plan fabrication procedures via simulation and study the processes involved. Another area that might benefit is medical drug delivery. Such a case might be to find the best penetration point for an intra–ocular injection in order to optimize in maximum and fastest delivery of the medical fluid to its intended target point – areas [14] – [16].

The effect of the developer temperature on the dissolution of negative resists has been investigated using experiment and simulation. The temperature has a homogeneous and an anisotropic effect on the dissolution of both exposed and unexposed parts of negative resists. The variation of the lateral etch rate manifested itself in sidewall profile slopes and is compatible with the entropy directional flow. We performed a series of experiments on resist coated Si wafers at three different developer temperatures. These experiments unveiled the effect of the developer temperature on sidewall slopes given the physical – chemical characteristics of the resist. We introduced temperature effect parameters into the Cellular Automata model and the simulation results that we obtained reproduced successfully the temperature effect on sidewall slopes and thus validated the model.

ACKNOWLEDGEMENT

I thank Professor Ioannis Karafyllidis of the Democritus University of Thrace, Xanthi for stimulating discussions and Cellular Automata Simulation.

I thank Professor Theodoros Tsiboukis for the hospitality of the Computational Electromagnetics Group of the Aristotle University of Thessaloniki and, in particular, Dr. Nikolaos Kantartzis, Vassilis Papantoniou, and Dimitrios Sounas.

The support over the years of the Electronics Research Laboratory at the University of California, Berkeley is acknowledged.

REFERENCES

[1] F. H. Dill, A. R. Neureuther, J. A. Tuttle, and E .J. Walker, “Modeling Projection Printing of Positive Photoresists”, *IEEE Transactions on Electron Devices,* vol. 22, pp. 456-464, 1975.

[2] P. I. Hagouel, “Blazed diffraction gratings fabricated using X-Ray lithography: fabrication, modeling and simulation”, *Microelectronics Reliability*, vol. 43, pp. 249–258, 2003.

[3] P. I. Hagouel, “X-ray lithographic fabrication of blazed diffraction gratings” Ph.D. Dissertation, University of California, Berkeley, 1976.

[4] P. J. Flory, *Principles of Polymer Chemistry,* Cornell University Press, Indiana, 1953.

[5] Arnold Sommerfeld, *Thermodynamics and Statistical Mechanics* (Lectures on Theoretical Physics) vol. 5, Academic Press, New York, 1956.

[6] L. Sédov, *Méchanique des Milieux Continus*, Éditions Mir, Moscou, 1975.

[7] L. D. Landau, E. M. Lifshitz, *Méchanique des Fluides*, Éditions de Moscou, Moscou, 1971.

[8] B. Akhmetov, Yu. Novichenko, and V. Chapurin, *Physical and Colloid Chemistry*, Mir Publishers, Moscow, 1989.

[9] M. Kambouris and C. Papaspyridis, *Technology of Polymers – Structure and Properties*, 5th edition, NTUA Press, Athens, 1994.

[10] I. Karafyllidis, and A. Thanailakis, “Simulation of Two-Dimensional Photoresist Etching Process in Integrated Circuit Fabrication Using Cellular Automata”, *Modeling and Simulation in Materials Science and Engineering,* vol. 3, pp. 629–642, 1995.

[11] M. S. Wong, “Ionospheric Ray Tracing with Analogue Computer”, *Electromagnetic Wave Propagation*, International Conference sponsored by the Postal and Telecommunications Group of the Brussels Universal Exhibition, Academic Press, New York, 1960.

[12] C. B. Officer, *Introduction to the Theory of Sound Transmission with Application to the Ocean*, McGraw–Hill Book Company, New York, 1958.

[13] P. I. Hagouel, I. Karafyllidis, and A. R. Neureuther, “Developer temperature effect on negative deep ultraviolet resists: characterization, modeling, and simulation” *Journal of Vacuum Science and Technology B,* vol. 15, pp. 2616-2620, 1997.

[14] Napoleone Ferrara & Robert S. Kerbel, “Angiogenesis as a therapeutic target”, *Nature* Insight Review, vol. 438, No. 15, pp. 967–974, December 2005.

[15] Booth, Blake A; Vidal Denham, Lori; Bouhanik, Saadallah1; Jacob, Jean T; Hill, James M, “Sustained-Release Ophthalmic Drug Delivery Systems for Treatment of Macular Disorders: Present and Future Applications”, *Drugs and Aging* , vol. 24(7), pp. 581–602, 2007.

[16] Robert Steinbrook, “The Price of Sight — Ranibizumab, Bevacizumab, and the Treatment of Macular Degeneration”, *New England Journal of Medicine*, Perspective, vol. 355, No. 14, pp. 1409–1412, October 5, 2007.

Πωλ Ισαάκ Χάγουελ, Ph.D.

Περίληψη Διδακτορικής Διατριβής

Μικροκατασκευή Γωνιακών Φραγμάτων Παράθλασης με Λιθογραφία Ακτίνων–Χ

Τμήμα Ηλεκτρολόγων Μηχανικών
και Επιστημών Υπολογιστών

Πανεπιστήμιο της Καλιφόρνιας, Μπέρκλεϋ

Τριμελής Επιτροπή

Andrew R. Neureuther
Theodore VanDuzer
Paul L. Richards

1976

hagouel@eecs.berkeley.edu

ΔΙΔΑΚΤΟΡΙΚΗ ΔΙΑΤΡΙΒΗ

Paul Isaac Hagouel
Πωλ Ισαάκ Χάγουελ
"X-Ray Lithographic Fabrication of Blazed Diffraction Gratings"
Μικροκατασκευή Γωνιακών Φραγμάτων Παράθλασης
με Λιθογραφία Ακτίνων–Χ
University of California, Berkeley, 1976

Φράγματα παράθλασης χρησιμοποιούνται σε φασματοφωτόμετρα υψηλότατης ακρίβειας, σε διατάξεις για οπτικές τηλεπικοινωνίες, σε οπτικούς σαρωτές (optical scanners), ως φράγματα αστρικής αστρονομίας, σε μονοχρωμάτορες φασματοσκοπίας Raman, κ.α. Μέχρι τούδε τα φράγματα παράθλασης κατασκευάζονταν με την μέθοδο της χάραξης η οποία ήταν χρονοβόρα, ακριβή και επιρρεπής σε σφάλματα. Από τα μέσα της δεκαετίας του 60, κατασκευάζονται με την ολογραφική μέθοδο, λόγω ανάπτυξης των λέϊζερ (laser). Τα πλεονεκτήματα είναι η ταχύτητα κατασκευής, το μικρό κόστος και η δυνατότητα κατασκευής φραγμάτων με πολύ μικρή περίοδο (0.1 μm). Το κύριο μειονέκτημα είναι η αδυναμία ελέγχου του σχήματος της διατομής (groove profile).

Σκοπός της διατριβής ήταν η κατάδειξη ότι είναι δυνατή η κατασκευή **γωνιακών φραγμάτων παράθλασης** με **Λιθογραφία Ακτίνων Χ**. Με την προτεινόμενη μέθοδο επιζητείται η επίτευξη αυτού του ελέγχου σε συνδυασμό με τα υπόλοιπα πλεονεκτήματα των ολογραφικών φραγμάτων παράθλασης. Η ανάπτυξη της Λιθογραφίας Ακτίνων Χ μαζί με άλλες μεθόδους κατασκευής Ολοκληρωμένων Κυκλωμάτων, οι οποίες δεν χρησιμοποιούν ως εκθέτουσα ακτινοβολία το φάσμα του ορατού φωτός και της υπεριώδους ακτινοβολίας, είναι αναγκαία λόγω των απαιτήσεων για Ολοκληρωμένα Κυκλώματα στη Μικροηλεκτρονική με όλο και μικρότερες γεωμετρικές διαστάσεις. Η Ολοκλήρωση Πολύ Μεγάλης Κλίμακας (**VLSI**) υπαγορεύει την ανάπτυξη νέων τεχνικών για την κατασκευαστική διαδικασία της αποτύπωσης των κυκλωματικών λεπτομερειών πάνω στις πλακέτες (wafers) Πυριτίου (Si), Γαλλίου-Αρσενικού (GaAs) κα. Όμως, οι κυματικές ιδιότητες του ορατού φωτός και της μαλακής υπεριώδους ακτινοβολίας, με κατώτερο μήκος κύματος γύρω στο 0.1 μm, έχουν ως αποτέλεσμα έντονα φαινόμενα παράθλασης. Τα φαινόμενα παράθλασης εμφανίζονται κατά τη διάρκεια αναπαραγωγής μιας μάσκας, με σχεδιασμένο κύκλωμα ελαχίστων γεωμετρικών διαστάσεων γύρω στο 1 μm, με έκθεση της "φωτοευαισθητοποιημένης" επιφάνειας δια μέσου της μάσκας η οποία βρίσκεται σε στενή επαφή μαζί της (contact printing).

Φαινόμενα παράθλασης δεν επηρεάζουν τη Λιθογραφία Ακτίνων Χ (ΛΑΧ). Θεωρητικά, η Λιθογραφία Ακτίνων Χ μπορεί να αναπαράγει με μεγαλύτερη ευκολία υπομικρές (submicrometer) διαστάσεις λόγω του μικρού μήκους κύματος της ακτινοβολίας (η χαρακτηριστική γραμμή $Al_{K\alpha}$ έχει μήκος κύματος λ=8.34 Å) έτσι ώστε, για τα γεωμετρικά μεγέθη τα οποία ενδιαφέρουν, τα φαινόμενα παράθλασης είναι ανύπαρκτα και ισχύουν οι κανόνες της γεωμετρικής οπτικής. Η αρχή της Λιθογραφίας Ακτίνων Χ στηρίζεται: α) στη κατασκευή κατάλληλων μασκών, τέτοιων ώστε τα σημεία της ευπαθούς στην ακτινοβολία ακτίνων Χ επιφάνειας τα οποία δεν θέλουμε να εκτεθούν, να αντιστοιχούν σε εκείνα τα σημεία της μάσκας τα οποία είναι μη διαπερατά ("αδιαφανή") ως προς τη χρησιμοποιούμενη ακτινοβολία ακτίνων Χ, και β) στην ύπαρξη ευπαθών στις ακτίνες Χ resists (X-ray resist). Ως τέτοιο χρησιμοποιήθηκε το PMMA (Polymethyl Methacrylate).

Η διατριβή χωρίζεται σε επτά κεφάλαια. Το πρώτο κεφάλαιο είναι εισαγωγικό. Το δεύτερο κεφάλαιο αναφέρεται στα βασικά των ακτίνων Χ και στις αρχές της Λιθογραφίας με Ακτίνες Χ με έμφαση την κατασκευή γωνιακών φραγμάτων παράθλασης. Το τρίτο κεφάλαιο περιγράφει την κατασκευή του συστήματος παραγωγής ακτίνων Χ για τους σκοπούς της εργασίας. Το περιεχομένο του τέταρτου κεφαλαίου, δηλαδή αυτού που περιγράφει την κατασκευή της μάσκας για την κατασκευή γωνιακών φραγμάτων παράθλασης με Λιθογραφία Ακτίνων Χ, αναπτύσσεται περιληπτικά στην επόμενη παράγραφο.

Η μέθοδος στηρίχθηκε στην υπό γωνία έκθεση της πλακέτας, που είναι επιστρωμένη με ευπαθές σε ακτίνες Χ πολυμερές (**X-ray resist**), μέσω μιας μάσκας με αποτυπωμένο ένα χρυσό φράγμα παράθλασης. Ο χρυσός είναι το υλικό που αποσβαίνει τις διερχόμενες ακτίνες Χ και παίζει το ρόλο του "αδιαφανούς" μέρους της μάσκας. Η κατασκευή της μάσκας ξεκινάει από την ολογραφική αποτύπωση των κροσσών συμβολής δυο δεσμών ακτίνων laser υπεριώδους ακτινοβολίας, που ξεκινούν από την ίδια πηγή, με αποτέλεσμα να παράγεται ένα φράγμα παράθλασης στο φωτοευπαθές υλικό (photoresist) με το οποίο είχε επιστρωθεί, με φυγοκεντρική μέθοδο, μια πλακέτα πυριτίου. Η επιφάνεια της πλακέτας είχε επιστρωθεί προηγουμένως με ένα στρώμα χρυσού με τη μέθοδο της εξάχνωσης χρυσού μέσα σε κενό (Au Evaporation in Vacuum). Κατόπιν η όλη διάταξη βυθίζεται σε εμφανιτικό υγρό (διαλύτη) και τα μέρη του πολυμερούς που αντιστοιχούν στους μέγιστους κροσσούς συμβολής διαλύονται ("σκάβονται") με ταχύτητα ανάλογη με την ενέργεια που έχουν απορροφήσει [θετικό photoresist]. Το αποτέλεσμα είναι το τρισδιάστατο φράγμα παράθλασης από πολυμερές (resist). Με ακόλουθο σκάψιμο με sputtering ("sputter etching") το αποτέλεσμα είναι ένα τρισδιάστατο φράγμα παράθλασης από χρυσό. Κατά την διάρκεια του σκαψίματος με sputtering, το φράγμα από photoresist λειτουργεί ως προστατευτική μάσκα έτσι ώστε να σκάβεται μόνο το μέρος του χρυσού που δεν καλύπτεται από photoresist. Τοιουτοτρόπως έχουμε σαν αποτέλεσμα ένα χρυσό φράγμα παράθλασης πάνω σε μια πλακέτα πυριτίου. Το τελικό στάδιο της κατασκευής της μάσκας επιτυγχάνεται με το ανισοτροπικό σκάψιμο της πλακέτας του πυριτίου, από την πίσω πλευρά, έτσι ώστε το χρυσό φράγμα να «υποστηρίζεται» δομικά μόνο από ένα λεπτό υμένιο πυριτίου πάχους 3μm περίπου, τέτοιο ώστε να είναι διαπερατό από την ακτινοβολία ακτίνων Χ. Το σχήμα 1 περιγράφει την τοπολογία της μάσκας, το σχήμα 2 δείχνει το χρυσό φράγμα παράθλασης περιόδου 1 μm σε μικρή κλίση (α) και σε κλίση (τομή) 90° (β), και το σχήμα 3 το χρυσό φράγμα παράθλασης περιόδου 0.6 μm σε μικρή κλίση.

Διάλυμα για ανισοτροπικό σκάψιμο του πυριτίου (Si)

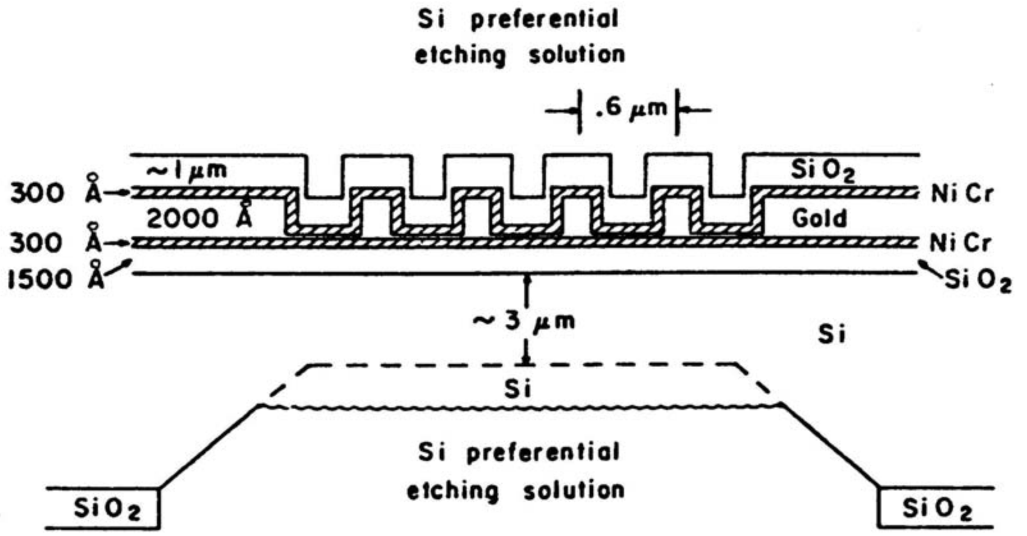

Διάλυμα για ανισοτροπικό σκάψιμο του πυριτίου (Si)

Σχήμα 1. Τοπολογία πλακέτας [το NiCr και το SiO$_2$ χρησιμοποιούνται για προστασία της χρυσής μάσκας από σκάψιμο κατά τη διάρκεια του ανισοτροπικού σκαψίματος του πυριτίου με υγρό]

Στο πέμπτο κεφάλαιο περιγράφονται τα αποτελέσματα της καθεαυτής έκθεσης με ακτίνες Χ, μέσω χρυσών μασκών, που έδωσαν πολύ καλά αποτελέσματα. Η υπό γωνία έκθεση αποδείχθηκε, όπως προβλέφθηκε θεωρητικά, ότι μας δίνει τη δυνατότητα ελέγχου της μορφής του καναλιού. Κατασκευάστηκε γωνιακό φράγμα παράθλασης περιόδου 1 μm και αναπαράχθηκε φράγμα περιόδου 0.6 μm. Σημαντικά προβλήματα υπάρχουν, κυρίως αυτό της σκίασης λόγω της παρασκιάς των ακτίνων Χ (X-Ray Penumbra Shadowing) η οποία οριοθετεί και την διαχωριστική ικανότητα (resolution) αλλά και την αντίθεση (contrast) ενός συστήματος έκθεσης με ακτίνες Χ. Για τις φωτογραφίες χρησιμοποιήθηκε Ηλεκτρονική Μικροσκοπία Σάρωσης (SEM). Το σχήμα 4 δείχνει ένα γωνιακό φράγμα παράθλασης περιόδου 1 μm όπου η απουσία “μυτερής” γωνίας στο βάθος [κορυφή] της περιόδου είχε προβλεφθεί με την προσομοίωση που περιγράφεται παρακάτω. Το αποτέλεσμα αυτό επιβεβαιώνει και το μοντέλο απορρόφησης ενέργειας από το resist.

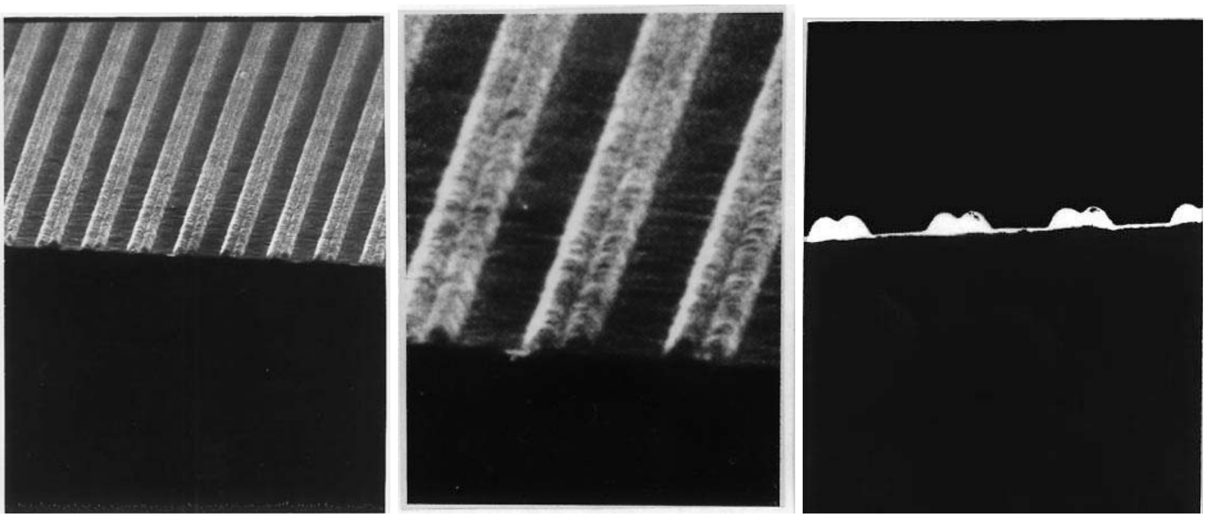

(α) μικρή κλίση (β) κλίση 90°

Σχήμα 2. Χρυσό φράγμα παράθλασης περιόδου 1 μm.

μικρή κλίση

Σχήμα 3. Χρυσό φράγμα παράθλασης περιόδου 0.6 μm.

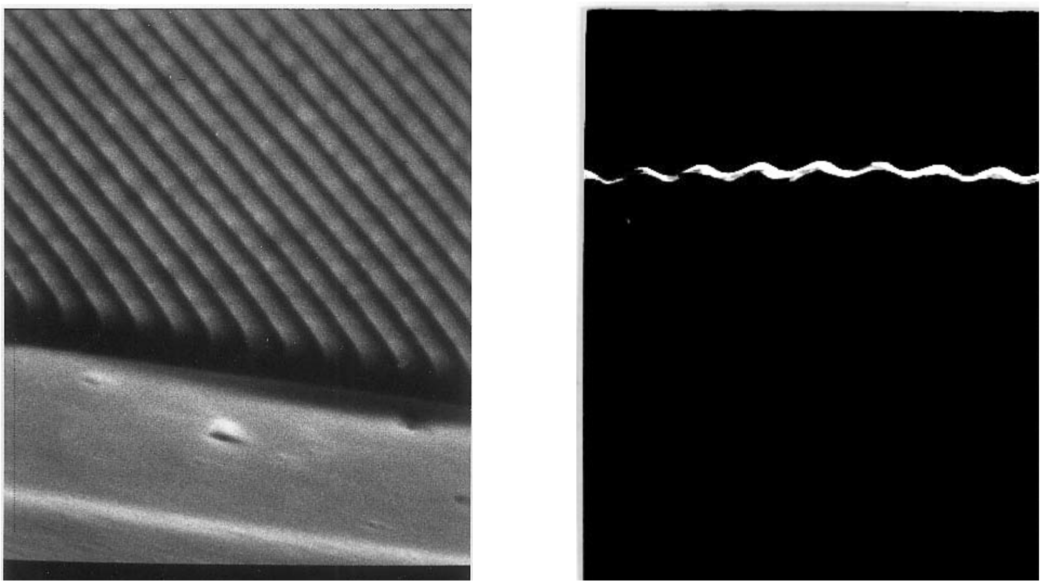

(α) μικρή κλίση (β) κλίση 90°

Σχήμα 4. Γωνιακό φράγμα παράθλασης περιόδου 1μm κατασκευασμένο με λιθογραφία ακτίνων Χ.

Στο έκτο κεφάλαιο αναπτύσσεται ένα μοντέλο και ένας αλγόριθμος προσομοίωσης της διαδικασίας εμφάνισης ή σκαψίματος. Με μια αλγεβρική μέθοδο έγινε αρχικά μια πρώτη προσέγγιση του προβλήματος, δηλαδή ότι είναι εφικτή η κατασκευή των γωνιακών φραγμάτων παράθλασης με τη μέθοδο της ΛΑΧ. Αναπτύχθηκε επίσης, και αποδείχθηκε θεωρητικά, μια μέθοδος προσομοίωσης του σχήματος (προφίλ) του διαχωριστικού μετώπου καθώς αυτό κινείται στο χρόνο και στο χώρο μεταξύ του υλικού που σκάπτεται και του υγρού ή άλλου σκαπτικού μέσου (π.χ. ιόντων κ.λπ.) που «σκάβει». Στη περίπτωση του resist (μια γενική περίπτωση) θεωρήθηκε το υλικό ώς ανομοιογενές και ισότροπο. Αφού η ταχύτητα σκαψίματος (δηλαδή η ταχύτητα με την οποία κινείται το μέτωπο ή η ταχύτητα με την οποία "σκάβει" ή "τρώει" το σκαπτικό υγρό το resist σε κάθε σημείο) ικανοποιεί το Νόμο της Παράθλασης του Snell, τότε ισχύουν όλα όσα ισχύουν για τη Γεωμετρική Οπτική, όπου η ταχύτητα σκαψίματος σε κάθε σημείο του resist, αντιστοιχεί με την ταχύτητα μετάδοσης του φωτός στους χώρους της Γεωμετρικής Οπτικής. Ετσι ορίζεται και ένας δείκτης παράθλασης του resist, κατά πλήρη αντιστοιχία με τον τρόπο που ορίζεται στην Οπτική. Για την έρευνα αναπτύχθηκε κυρίως η μέθοδος της *προσομοίωσης της ιχνηλάτησης χρονικά και χωρικά της «ακτίνας» σκαψίματος* (**Ray Tracing**) έτσι ώστε η περιβάλλουσα των άκρων όλων των ακτίνων σε μια ορισμένη χρονική στιγμή να δίνει το μέτωπο, και κατ' επέκταση το τελικό προφίλ (απεικόνιση του μετώπου–διατομής) μετά το πέρας της εμφάνισης. Η ακριβής λύση του προβλήματος δίνεται από τη λύση της εξίσωσης **Hamilton–Jacobi**, η οποία στην Οπτική αποκαλείται και «απεικονιστική» (**eikonal**). Στην εξίσωση αυτή αντικαθίσταται ο οπτικός δείκτης παράθλασης με το **δείκτη παράθλασης του resist** ή οποιουδήποτε άλλου μέσου που σκάπτεται. Ορίζεται ως δείκτης παράθλασης του μέσου (λχ. photoresist, X-Ray resist κ.λπ.), σε τυχόν σημείο του, το κλάσμα με αριθμητή τη μέγιστη ταχύτητα σκαψίματος στο μέσο και παρονομαστή την ταχύτητα σκαψίματος στο σημείο. Η μέθοδος προσομοίωσης προσφέρεται και για τη λύση **τρισδιαστάτων** απεικονιστικών προβλημάτων. Τα αποτελέσματα του αλγορίθμου βρέθηκαν σε άριστη συμφωνία με τα αντίστοιχα πειραματικά αποτελέσματα.

Η προσομοίωση της διαδικασίας σκαψίματος με το μοντέλο της ιχνηλάτησης ακτίνας (ray tracing) δίνει μια πολύ καλύτερη αντίληψη και γνώση της φυσικής διεργασίας του σκαψίματος. Παρατηρείται ότι η τελική διατομή (προφίλ) επηρεάζεται αρκετές φορές από ακτίνες (δηλαδή σκαπτικό υγρό) που ξεκινούν από την επιφάνεια του υλικού που σκάβεται, από μια ορισμένη περιοχή σημείων τα οποία απέχουν μεταξύ τους λίγα Å! Αυτό δείχνει ότι η διεργασία σκαψίματος λειτουργεί μικροσκοπικά σε ατομικές διαστάσεις. Η πλήρης ιχνηλάτηση δείχνει ποιες ακτίνες θα ακολουθήσουν ποιο δρόμο έτσι ώστε μετά από ορισμένο χρονικό διάστημα να μορφοποιείται η τελική διατομή.

Με γνώμονα τη μελλοντική ύπαρξη πιο ισχυρών πηγών ακτινοβολίας παράλληλης δέσμης ακτίνων X, και υποθέτοντας «τέλεια» επαφή μάσκας–υποστρώματος με resist ακτίνων X, παρουσιάζονται αποτελέσματα προσομοίωσης για διάφορα πάχη μασκών και διάφορες περίοδους φραγμάτων. Ενα συμπέρασμα είναι ότι φράγματα με περίοδο 0.1 μm είναι εφικτά. Επίσης προσομοιώθηκαν διατομές (προφίλ), τυπικές για Οπτική Προβολική Εκτύπωση (Optical Projection Printing), και γραμμών 1 μm σε resist κατασκευασμένες με Λιθογραφία Ηλεκτρονικής Δέσμης (Electron Beam [E-Beam] Lithography), καθώς και για σκάψιμο ιοντικά εμφυτευμένου SiO_2 (ion-implanted SiO_2). Σύγκριση με πειραματικά αποτελέσματα, καθώς και με αποτελέσματα άλλων αλγορίθμων προσομοίωσης επιβεβαιώνουν την ακρίβεια του αλγόριθμου.

Τέλος στο έβδομο κεφάλαιο αναφέρονται περιληπτικά τα αποτελέσματα και οι τελικές παρατηρήσεις.